Damage Characterization and Modelling of Composite Plates Subjected to High-Speed Oblique Impacts

Developing a Robust Simulation Methodology

Thesis Aerospace Structures & Materials

Daniele Accomazzo

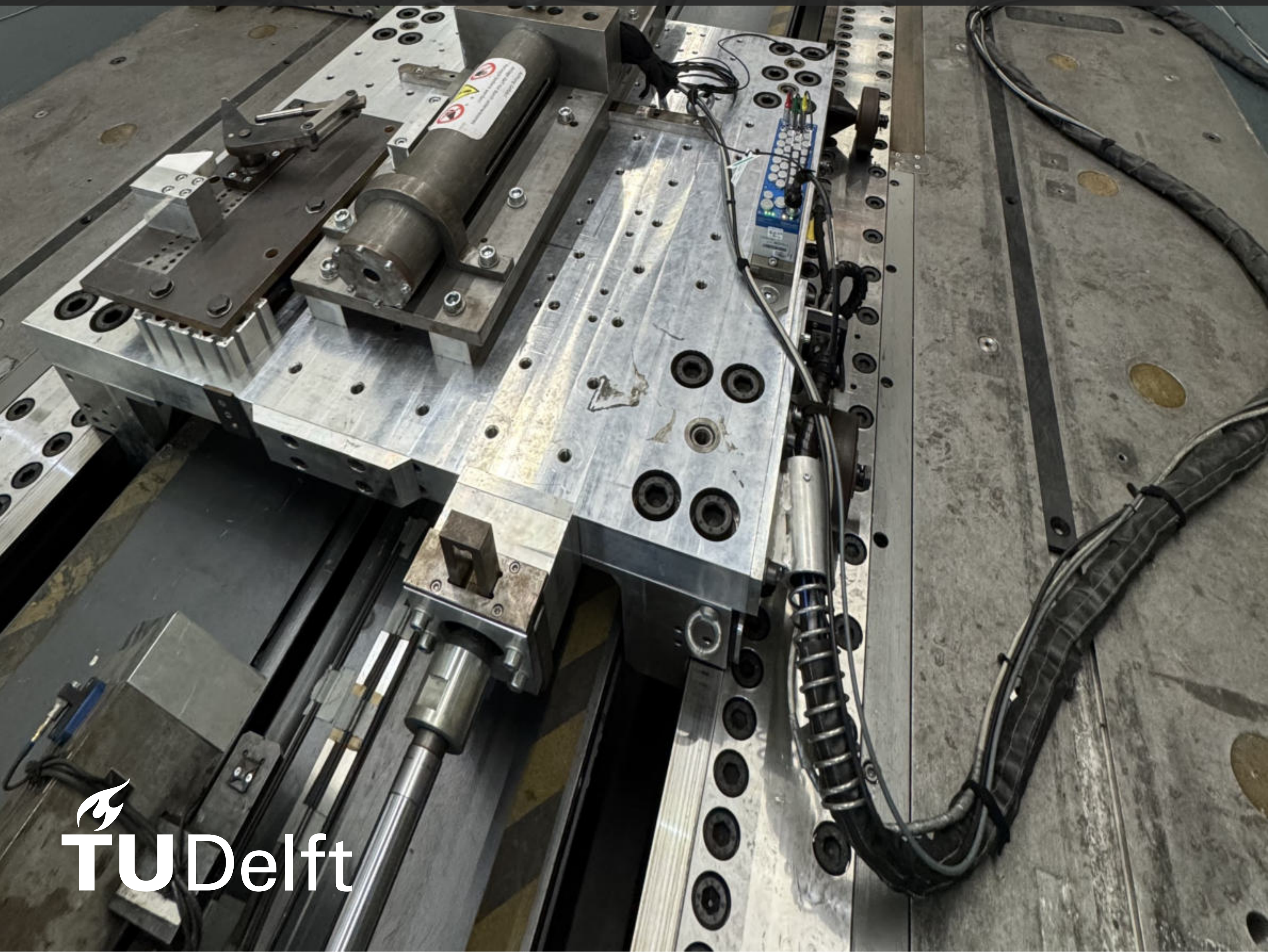

TU Delft

Damage Characterization and Modelling of Composite Plates Subjected to High-Speed Oblique Impacts

Developing a Robust Simulation Methodology

by

Daniele Accomazzo

to obtain the degree of Master of Science

at the Delft University of Technology,

to be defended publicly on Wednesday February 18, 2026 at 09:30 AM.

Student number:	5906512	
Project duration:	May 15, 2025 – December 12, 2025	
Thesis committee:	Prof. Daniël Peeters,	TU Delft, Chair
	Prof. Otto Bergsma,	TU Delft, Examiner
	Prof. C. Kassapoglou,	TU Delft, Supervisor
	Ir. T. Schäfer,	External, Supervisor

Cover: Impact test set-up used for the Project (Photograph by author)

Style: TU Delft Report Style, with modifications by Daan Zwaneveld

An electronic version of this thesis is available at `http://repository.tudelft.nl/`.

TU Delft

Preface

This thesis is the result of my research project at an undisclosed company, external to TU Delft. It has been an incredible journey that I will remember for the rest of my life. Many thanks to everyone at the company who supported me professionally and personally, making my staying far from home a bit less harsh.

My most sincere gratitude goes to Professor Christos Kassapoglou, for helping me in finding the topic for my project, and for going above and beyond supervising me, always being there for feedback and guidance. Finally, thanks to everyone from TU Delft, from the technicians who helped me setting up the experiments for this project, to the friends I made throughout the years, who always had time for sharing ideas and for a laugh over a bad coffee.

Ai miei genitori, che sono la ragione per cui ho potuto fare tutto questo, e che mi hanno sostenuto a ogni passo lungo il percorso. *E' la fine di un viaggio iniziato ormai tanti anni fa su un banco di scuola a Palera, c'eravate allora come ora, grazie*.

Ad Arianna, senza cui non avrei mai avuto il coraggio di cambiare vita. *Grazie per avermi aspettato tutto questo tempo e aver creduto in me*.

Daniele Accomazzo
Delft, February 2026

Abstract

Simulating high-speed oblique impacts on composites remains a critical engineering challenge, as the monolithic shell models preferred in the industry often fail to accurately reproduce the diverse failure mechanisms typical of composite materials, such as fibre failure and delamination, whose interplay with inertial effects is essential for an accurate modeling of the event. To address this, a discretized modeling approach was developed with the explicit finite element software LS-Dyna, representing a composite laminate as a stack of shell elements connected via tiebreak contacts to allow for inter-laminar failure via a purely strength-based criterion. Validation against experimental data revealed that the plate response was governed by the mutual interaction of delamination, inter-ply friction and impactor kinematics. Using maximum out-of-plane intrusion as a benchmark, the newly developed model showed a discrepancy with the test data of -2.9%, against the +17.7% of the monolithic model baseline provided by the company at the beginning of the project. Furthermore, great qualitative correlation has been observed w.r.t. the delamination morphology when compared with C-scans of the tested samples. This study demonstrates that high-fidelity prediction of both intrusion and delamination shape and size in the proposed high-speed oblique impact event can be obtained through a strength-based discretized framework without the need for complex energy parameters or computationally expensive solid elements, offering a robust and efficient solution for industrial safety analysis.

Contents

List of Figures

List of Tables

1
Introduction

This chapter first establishes the context and scope of the research. Then, a research question is formulated and research objectives are defined, and last, an outline of the thesis is presented.

1.1. Context

1.1.1. Crash Safety in Electric Vehicles

Accounting for crashes and impacts is a fundamental aspect of the design of all means of transportation, as passengers' safety always represents the top priority for manufacturers. In this context, experimental tests represent the standard, as they enable validation of the implemented safety features and identification of the main weak points in the vehicle design; furthermore, many of these tests are highly regulated and standardized by control bodies, and passing them represents a necessary step to obtain authorization to manufacture and ultimately sell the final product. The significance of impact tests is amplified for electric vehicles (EVs), due to the potential hazards associated with their high-voltage battery systems: new designs need to be conceived to ensure safety of the battery packs, and the absence of extensive data on their effectiveness, due to the technology being relatively new and constantly evolving, makes testing all the more important.

The company department within which this project took place is responsible for designing the battery cells housing of the brand's EVs, where a critical role is played by the under-ride car protection plate (hereinafter referred to as UFS), whose function is to protect the battery cells from impacts coming from underneath the car (e.g., loose vehicle part or truck cargo laying on the highway), which could cause severe damage.

To assess the impact protection capabilities of the UFS in different scenarios, two tests have been devised inside the company: the ”Poller” test, for low-speed vertical impacts, and the ”Beschuss” test, for high-speed angled impacts (see Section 2.1).

1.1.2. Simulations vs Testing

Striving for optimal performances, fibre-reinforced composites have been chosen for the manufacturing of the UFS. With composites, given a certain plate thickness, a virtually endless number of combinations can be explored compared to more traditional materials (e.g., steel, aluminum), due to additional parameters such as multiple available fibres and patterns, fibre orientation and stacking sequences.

Safety requirements and the certainty which only experimental testing can give must, naturally, coexist with the fast pace of R&D projects, where ideas need to be quickly evaluated and iterated. This is particularly problematic for composites, where even though guidelines exist to streamline the design process, many promising candidates often need to be experimentally tested, with great expenditure of time and resources.

To solve the issue, simulations come into play, representing a quick and cheap alternative to experimental testing, while still being able to direct preliminary designs. Numerous efforts were made by the company in this area, beginning from simulations of the Poller test: the experimental set-up has been replicated in a simulative environment with a high-degree of fidelity, and material calibration has been performed[1] to achieve convergence with test results.

When the same process was repeated for the Beschuss test, convergence couldn't be obtained. Specifically, a big residual discrepancy between model output and available test results was measured, with the model largely overshooting the plate deformations (see Figure 1.1[2]) and showing different damage patterns than the tests.

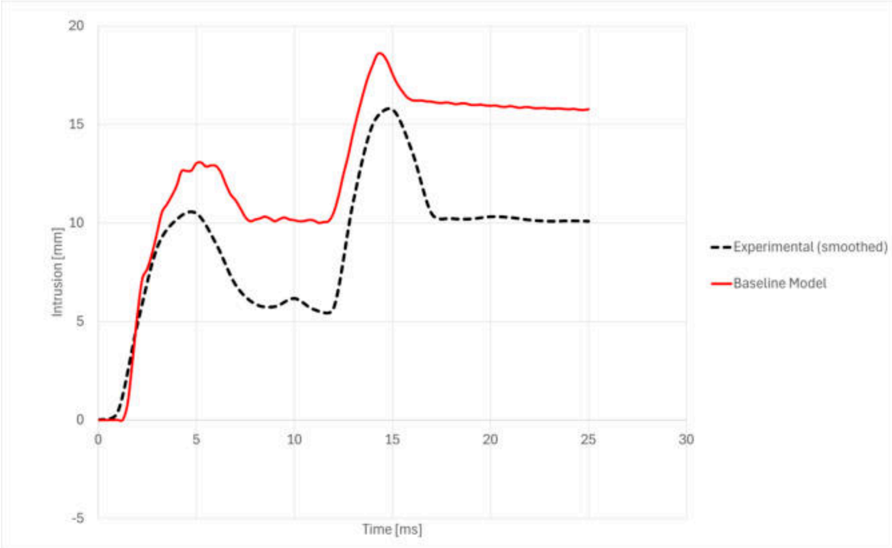

Figure 1.1: Maximum Intrusion over time, test vs baseline model

1.2. Possible Reasons for the Test-Simulation Discrepancy

There are multiple reasons that could explain the discrepancy between tests and simulation for the Beschuss load-case, and the most prominent ones will be addressed in the following.

Since each of the proposed implementations would steer the research in a unique direction, and given the time limit imposed by both the company and university regulations, it is necessary to focus the scope of the project to a limited number of aspects. Therefore, each one will be assessed based on the following parameters: 1) Required effort. 2) Research orientation. 3) Generality of the solution. 4) Chance of improving the test-simulation match. 5) Chance of original contribution.

At the end of the section, a final comparison taking all the aforementioned parameters into account is performed, and the most promising implementation(s) will be identified.

1.2.1. Material Card Calibration

Hypothesis

By performing a re-calibration of the material cards specific to the Beschuss load-case, accurate and reproducible results could be obtained. Yet, this would result in a new set of material cards, making the model limited to a certain case, and losing generality. Therefore, it is advisable to determine a series of implementations that could result in a general modeling approach that works for a variety of load-cases with a unified set of material cards.

For this reason, the Poller-calibrated cards are used as a baseline for the project. As delamination and strain-rate effects are not a factor in the Poller load-case (due to low speed and smooth stress distribution), these cards shouldn't be integrating any calibration to account for these mechanisms, avoiding the risk of accounting for them twice (both via modeling implementation and pre-existing card calibrations).

[1] Material cards definition and calibration has been performed by an external company.

[2] The test-simulation pair in the figure is taken as an example, and it is representative of the general behaviour of the model

Considerations on implementation

Material card calibration generally requires a medium effort, due to a mostly iterative approach where parameters are tweaked until convergence; as an advantage, it would definitely influence the results as that's the intended effect of the approach, but there is a high risk of it being specific of the load-case used for calibration. Furthermore, no actual research is required to take on this approach, which is mostly iterative, and chances of an original contribution to the academia or the industry are non-existent. Therefore, it is not well suited for a MSc thesis research topic.

1.2.2. Strain Rate Sensitivity

Hypothesis

The main differences between the Beschuss and the Poller load-cases lie in the impactor's shape and speed. The Beschuss presents a parallelepiped impactor hitting with one of its corners, opposed to the hemispherical impactor of the Poller. The difference in shape results in higher stress concentrations in the Beschuss, hence higher localized strains, and premature failures compared to the Poller.

This is particularly important when paired with the increased impact speed of the impactor in the Beschuss, as not only the strains are higher, but also the speed at which those strains are reached (i.e., the strain-rate). Strain-rate sensitivity is a well documented phenomenon, in which high strain rates result in a variation (usually an increase) of the instantaneous mechanical properties of a material. In fibre-reinforced composites, this variation can be considerable, making it an important phenomenon to account for when modeling high-speed impacts.

The material cards used in the simulative environment allow for strain-rate dependent curves to be defined for each relevant mechanical property, making this a viable approach to obtain test-simulation improvements after getting the necessary additional material properties via a characterization campaign.

Considerations on implementation

Strain rate sensitivity implementation also requires a medium effort, as it is mostly based on already existing standardized testing. Its chances of influencing the results are based on the actual strain rates registered during experimental testing, but since impact speeds and geometries are known to be high and complex, it is legitimate to suppose that it would have at least a moderate influence on the results. As per the generality of the approach, that will of course depend on the range of strain rates analyzed during testing. Finally, the chances of an original contribution to the research environment are low, as the implementation is mostly based on standardized tests.

1.2.3. Element Formulation & Material Model

Hypothesis

Plies are currently modeled with shell elements with a fully-integrated shell formulation[3], which is considered the standard for many internal applications at the company. Notably, this formulation doesn't allow for any thickness stretch, which is instead advisable when the shell surface shows an out-of-plane load/contact. For example, in sheet metal forming applications, modeling normal stresses in thickness direction improves the accuracy of the solution and its contact response, while also enhancing the instability characteristic of the model.

Additionally, changing the element formulation, going as far as switching to solid elements, opens up a variety of possibilities and combinations on how to model the whole UFS (e.g. different contact types and material models). Still, it is important to consider that this sometimes requires the definition of new parameters through experimental testing, besides the calibration of the already existing ones, making the process quite complex.

Considerations on implementation

Investigating the element formulation and material model would require a rather high amount of work, as each option could dramatically change the whole simulative setup, from the material cards to the contacts in use, even though this could pay off as for very complex formulations, highly general and

[3]This formulation is based on the Reissner-Mindlin kinematic assumption, and even though it is around 2-3 times more expensive than the Belytschko-Tsay shell, it still is the least expensive of all the 2x2 integrated elements.

adaptable solutions can be obtained. Surely, research would be necessary to determine in which direction to steer the modeling efforts, and to find the best compromise between accuracy, robustness and computational efficiency; nevertheless, chances of original contributions are rather low, as most of the material models have already been defined and a general consensus has been reached on which ones have the best predictive capabilities for impact load-cases. As an alternative, trying to define a new comprehensive custom material model altogether represents a challenge too great, both time- and knowledge-wise. Last, chances of influencing the final result are variable, depending on the performance of the final formulation.

1.2.4. Delaminations Modeling

Hypothesis

In the current simulative approach, the layup is modeled as a single equivalent shell; this means that phenomena such as delamination cannot be simulated, as they require individual modeling of each ply, and of the inter-laminar interfaces.

It is well known that the process of creating and propagating delaminations in a composite plate absorbs a certain amount of energy, therefore it is possible that by implementing them into the simulation, part of the impactor kinetic energy, that would otherwise all go into payload (i.e. the battery packs) indentation and damage, will end up in the delamination process. Naturally, the trade-off between stiffness reduction and energy absorption needs to be accounted for, making the final effect of the implementation unpredictable and subjected to a case by case evaluation.

To assess the effect of delamination implementation for the project load-case and plate configuration, it would be advisable to perform C-scans on the impacted samples in order to determine the size of the delaminated area and understand whether it could have a significant influence on energy absorption and structural compliance.

Considerations on implementation

Delamination modeling would require a considerable effort in terms of rethinking the whole simulative approach, as a new way to model the UFS is required. Most probably, plies and matrix need to modeled separately, and a new material card for the matrix, which implies the definition of specific inter-laminar failure criteria, needs to be defined. The high number of available methods with their specific advantages and disadvantages and the need to adapt them to the industry environment (i.e. computational efficiency and integration into models with complex and realistic geometries with different other loads and contacts) would also ensure plenty of research opportunities and chances of an original contribution. As per generality, it will totally depend on the chosen modeling framework, although it would surely represent a desirable characteristic. Finally, chances of influencing the test-simulation mismatch are highly dependent on the actual size of delaminations, as previously mentioned.

1.2.5. Experimental Test Errors

Hypothesis

Since the experimental setup used for the load-case (see Section 3.1.1) cannot guarantee granular control over the impact dynamics, deviations from the test standard for a variety of parameters (e.g., impact speed and position, impactor rotations along its axes) are expected.

By measuring these deviations with dedicated high-speed camera systems, it is possible to explicitly model them into the simulations to reproduce the impact event with higher fidelity. This is important as during preliminary studies, test results have shown very high sensitivity to the impactor's positional and rotational variations. Therefore, regardless of their individual effect on the improvement on test/simulation match, accurately modeling the impactor's kinematics is most probably required to establish a solid model baseline.

Considerations on implementation

Although implementing test errors which have been already recorded during tests would be a trivial task, a comprehensive investigation on the matter would require to analyze the available data, determine their accuracy and possibly identify parameters that weren't directly measured during testing but that could have an influence on the impact dynamics, developing a method to retrieve their values from available sources. Finally, the interplay between different parameters needs to be analyzed (e.g., a measured shift in the impact position could be caused by a measured full body rotation of the impactor, thus implementing both into the model would be incorrect, as the latter would automatically include the former). Due to these considerations, this ”forensic investigation” would therefore be a medium effort task, possibly supplementing a main topic, and it could result in an original contribution in the form of a detailed generalized approach for kinematic boundary conditions modeling.

1.2.6. Summary and Final Considerations

A summary of the considerations for each implementation is presented in Table 1.1, from which a choice for the project's principal area of research can be made.

Even though it doesn't ensure an improvement on the test-simulation discrepancy, the delamination modeling implementation represents the most interesting topic to focus on from a research point of view. Furthermore, if results end up showing that delaminations don't play a major role in the improvement on the simulation accuracy, their implementation would still be a general result that can be used as a tool for future applications where delamination is in fact a critical factor.

For these reasons, developing a modeling framework to account for delamination effects is selected as the main research objective for this thesis; along with it, other aspects such as accurate impactor kinematics representation (i.e., accurate test errors implementation) and material characterization (e.g., custom material cards, strain-rate effects implementation) will potentially be explored to further improve on the simulation accuracy.

Implementation	Effort	Research vs Iteration	Generality	Chances of Influencing Results	Chances of Original Contribu-tion
Material card calibration	Medium	Iterative	Specific	High	Low
Strain rate sensitivity	Medium	Iterative	Variable	Variable	Low
Element formulation	High	Research	Variable	Variable	Low
Delaminations modeling	High	Research	General	Variable	Medium/High
Test errors	Medium	Research	General	Variable	Medium

Table 1.1: Comparison between the proposed implementations to improve on the test-simulation match for the Beschuss load-case.

1.3. Formulation of the Research Proposal

1.3.1. Research Question

From the conclusions of Section 1.2.6, the following research question can be formulated:

”*How can the predictive accuracy of the company's simulative framework for high-speed oblique impact tests on composite plates be enhanced by developing a generalized delamination modeling solution and improving the fidelity of the impactor's kinematic representation?*”

1.3.2. Research Objectives

To answer the research question effectively, the project is divided into four primary objectives, each addressing a specific aspect of the simulation-experiment discrepancy:

1. **Evaluate the limitations of the current industrial baseline.** First, it is necessary to quantify the predictive error of the existing monolithic shell model, hereinafter referred to as ”baseline model”,

in use at the company. This involves both quantitative measurements of deformation and qualitative observations on damage morphology. Furthermore, the model needs to be prepared for the planned delamination implementation via a series of minor updates, so that a fairer comparison can be performed later on.

2. **Develop a robust ”discretized” modeling strategy.** To overcome the baseline framework's incapability of modeling delaminations without incurring the high computational cost of solid elements, a discretized modeling architecture must be defined, relying on the implementation of a stack of shell elements, representing the plies, connected via tiebreak contacts, which model the interfaces. This objective, which represents the core of the thesis, includes:
    - Determining the validity of a simplified strength-based failure criterion versus an energy-based approach for high-speed impact regimes.
    - Calibrating the inter-laminar shear and normal strength parameters to account for mesh sensitivity.
    - Investigating the influence of inter-ply friction on the post-failure impact kinematics.
3. **Implement a ”forensic” kinematic reconstruction.** After the main objective is achieved, the fidelity of the impactor kinematics is addressed. Available test results and high-speed video footage are used to quantify all the unmeasured inertial deviations of the projectile, which are then included in the new model to assess their effect on the simulation results.
4. **Validate the coupled simulation framework.** The final objective is to verify the predictive accuracy of the new methodology against experimental data. This is done via a multi-metric validation including:
    - **Intrusion Plots:** Matching magnitude and timing of experimental deformation plots on the plates.
    - **Damage Morphology on the composite plates:** Correlating the simulated delamination patterns with C-scan envelopes[4] to ensure the model correctly captures the inter-laminar failure mode.
    - **Damage Morphology on the aluminum plates:** Visually correlating the simulated damage patterns with damage on test specimens.
    - **Kinematic validation:** Correlating test and simulation footage, analyzing the trajectory and body rotations of the impactor in a frame-by-frame fashion.

1.4. Thesis Outline

The thesis is organized in 6 chapters:

- **Chapter 1: Introduction** outlines the context, defines the engineering problem and establishes a research proposal.
- **Chapter 2: Theoretical Framework** provides the necessary background on composite impacts and introduces the simulative environment, ending with a critical review of the available modeling solutions and the proposal of a preferred candidate.
- **Chapter 3: Experimental Methodology** describes the impact test experimental set-up and all the additional tests performed to build the validation database (DIC uncertainty quantification, C-scans, fibre volume determination, microscopy) and improve the material cards fidelity (aluminum characterization).
- **Chapter 4: Numerical Analysis** details the development of the new simulation framework in LS-Dyna, documenting the transition from the baseline monolithic model all the way to the finalized version implementing delamination and precise impactor kinematics.
- **Chapter 5: Results and Discussion** compares numerical predictions with experimental data, focusing on reduction of deformation error and correlation of deformation morphology.

[4]Verified through microscopy performed on section cuts of the test specimens.

- **Chapter 6: Conclusions and Recommendations** summarizes the project's findings, outlining the contributions of the work and proposing future developments for the simulation framework and for design optimization.

2
Theoretical Framework

This chapter deals with the theoretical foundations of the project, providing a systematic critical review of the available scientific literature in the field of composite impact modeling.

First, the load-case is presented and relevant failure mechanisms in a composite material are discussed; then, a distinction is made between low- and high-speed impacts, and the importance of delamination in the Beschuss load-case is advocated for.

Then, after introducing a simulation environment suitable for the project requirements, the baseline and state-of-the-art modeling solutions for composite delamination are presented, and their main characteristics and limitations are discussed.

Alternative solutions are introduced, and a final comparison is performed, advocating for a preferred candidate. The nuances of the selected approach are then discussed, highlighting the benefits of a strength-based approach over a fracture mechanics one, and finally an literature-based estimation of the required parameters for the model is preformed.

2.1. Experimental Tests

Two tests have been internally developed at the company to assess the performances of the under-ride car protection[1] in a variety of impact scenarios.

The first, called ”Poller”[2] load-case, aims at determining the UFS response in case of vertical low-speed impacts with an hemispherical object; due to the favorable loads distribution (given the impactor’s shape) and speed, this test doesn’t pose a significant challenge from a simulative perspective, and it has been accurately modeled with the company’s current approach.

The second, called ”Beschuss”[3] load-case, represents instead a more complex problem, as the goal of the test is to determine the protective capabilities of the UFS in cases of high-speed angled impacts (for a complete description of the test set-up and procedure, see Section 3.1.1). Given the higher speeds and the concentrated loads (since the impactor hits with one of its corners, as seen in Figure 3.2), this load-case results in much more varied forms of damage than the Poller, and the current models at the company are incapable of reproducing all of them. In the following sections, the most important impact-related failure mechanisms in composite plates will be detailed, and the available modeling solutions to account for them will be presented.

2.2. Failure Mechanisms During Impact of Composite Parts

Composite materials subjected to impact events fail through various damage mechanisms; depending on the load-case, different mechanisms can have more or less prominence in the failure event but

[1] Henceforth called ”UFS”, which stands for ”Unterfahrschutz” and translates to ”under-ride car protection”.
[2] which translates to ”Bollard”.
[3] ”Beschuss” roughly translates to ”Bombardment”, meaning ”Projectile Impact” in this context.

generally ”damage mechanisms such as fiber breakage, matrix cracking and delamination occur under the impact and have great effects on the impact absorption energy” [1].

In a broader sense, due to the inherent structure of composite materials, failure modes can be classified into intra-laminar and inter-laminar modes.

2.2.1. Intra-Laminar Modes

The intra-laminar failure modes, as the name suggests, happen within a single composite ply. They can be further categorized in fibre-related modes, matrix-related modes and fibre-matrix interaction modes.

The main fibre-related modes are:

- **Tensile/shear failure:** This mode occurs due to high tensile stresses along the fibre direction and associated shear strains [2] [3].
- **Compressive failure:** This mode is the result of in-plane compression along the fibre direction, and it can result in the global micro-buckling behaviour or in the local kinking phenomenon [3].
- **Crush failure:** This highly localized damage mode is the result of high through-the-thickness compressive loads in the impact area [4] [5].
- **Punch shear damage:** This phenomenon is the result of a combination of fibre failure modes of punch shear, crush and tension, and it is generally localized around the impact area [6].

The matrix-related modes are usually originated from crack or void formations between fibres [3], and the most important are:

- **Transverse/in-plane failure:** This mode involves cracking within a ply, caused by shear stress or transverse tension, without fibre breaking; they can develop as through-the-thickness cracks or stacking parallel cracks [3].
- **Micro-cracking:** Localized micro-cracks, often associated with localized buckling under compressive loading [7].

Last, there are intra-laminar failure modes that develop from the interaction between fibres and matrix, such as **fibre-matrix de-cohesion** [6] [8]; generally, they are rather complex phenomena to describe.

2.2.2. Inter-Laminar Modes

The inter-laminar failure modes, naturally, happen between two different composite plies. The most notable failure of this kind is **delamination**, which is defined as the separation of two or more laminate plies, usually due to high inter-laminar (i.e., through-the-thickness) stresses that exceed the strength of the thin matrix layer between the plies [9].

There are multiple reasons why this happens: ”One reason for this is that the strength in this direction is typically very low and the other reason is that few reliable data on inter-laminar tensile strength (ILTS) are available and the methods of analysis are complex and time-consuming making it difficult to perform during typical design cycles. Therefore, it is difficult for designers to design against delamination failure” [10].

Borrowing from the nomenclature of crack propagation modes in fracture mechanics, the delamination regulated by ILTS takes the name of ”mode I” delamination, or ”opening mode” delamination. The other 2 existing modes are the ”mode II” (”sliding mode”, or ”in-plane shear”) and the ”mode III” (”tearing mode” or ”out-of-plane shear”), and their onset is governed by the inter-laminar shear strength (ILSS). It must be noted that in most real-world applications, the three modes happen simultaneously, in what is called ”mode mixity” [11].

2.3. Delamination in High-Speed Impacts

As delamination implementation is the main focus of the project, it is imperative to advocate for its importance in determining the laminate impact response in high-speed load-cases.

In high-speed impact events like the Beschuss load-case, the mechanical response of the material is governed by inertial effects and characterized by fast-developing highly localized damage. This most times results in penetration-induced fibre breakage damage patterns, often described as plugging, which is a combination of local-crush and out-of-plane shear [6] [4].

As velocity increases, failure becomes more brittle and there is no time for delamination to form and influence the impact dynamics, hence omitting its implementation in perpendicular high-speed impact simulations introduces negligible accuracy errors [12].

The fundamental difference of the Beschuss load-case, compared to standard high-speed impacts, is the non-perpendicular impact angle. Under normal impact, stresses through the thickness are mostly compressive, thus incapable of causing delaminations (or actively suppressing Mode I separation), but as incidence angle increases, shear stresses become significant and shear-driven delamination becomes prominent [13]. This, paired with the additional contact surface and contact time provided by the altered impact angle increases the absorbed energy, enhancing delamination-driven energy dissipation and making the phenomenon non-negligible in determining the material response.

2.4. Introduction to the Modeling Environment

Implementing one or multiple damage mechanics in impact calculations and analytical models represents a considerable challenge, mostly due to the non-linearity they involve, which can be ascribed to complex contacts, large deformations and interacting material failures.

An analytical model addressing the structural response is detailed in Appendix F, which presents an original derivation of a closed-form solution to the 1st von Karman equation for anisotropic plates. This methodology introduces a monolithic formulation to directly resolve the geometric nonlinearity induced by oblique loads, bypassing the need for standard iterative numerical schemes. However, as this analytical framework remains constrained by idealized boundary conditions and static point-load assumptions, it cannot capture the transient dynamics, evolving contact interfaces, and complex damage mechanisms inherent to the impact event. Consequently, high-fidelity numerical models are required to simulate the load-case.

To perform such simulations, an appropriate software must be chosen, specifically concerning the solution approach used for time integration methods. In the following, a distinction is made between implicit and explicit integration methods, and explicit methods are advocated for. Subsequently, the chosen simulation software is presented, along with the pre-processor used to prepare the relevant input.

2.4.1. Implicit and Explicit Integration Methods

High-speed impact simulations, and crash simulations in general, are usually performed with software based on explicit time integration methods. To understand why, it is necessary to explain the difference between implicit and explicit approaches.

In numerical analysis, implicit and explicit methods ”are approaches used for obtaining numerical approximations to the solution of time-dependent differential equations” [14].

While implicit methods solve an equation involving both the current and future state of a system (i.e., the solution is implicit in the final equation), explicit ones calculate the state at a time t from its state at the time $t-1$ (i.e., the solution is directly obtained, or explicit) [15];

Naturally, implicit methods require extra computational effort to get to a solution, and in specific practical application finding it can be extremely hard. Moreover, in non-linear problems (like high-speed impacts) a Newton iteration is needed to find the solution in each time-step. This doesn’t happen in explicit formulations, but still, in case the chosen time-step is too big, stability issues may arise: for this reason, explicit methods are optimal for short duration events, where a small time-step won’t render the simulation prohibitive from a computational point of view [16]. Furthermore, choosing a small enough time-step plays favorably into the possibility of comprehensively describing a short-lived event, where the larger time-steps typical of implicit methods would likely miss the details of it. As a summary, a comparison of the two methods is presented in Table 2.1.

	Implicit	Explicit
Stability	Unconditionally stable	Depends on time-step size
Time-step size	Large	Very small
In non-linear problems	Needs iterations	Does not need iterations
Solving speed for one step	Slow	Fast

Table 2.1: Comparison between implicit and explicit methods. Elaboration from [16]

2.4.2. Mass Scaling

Based on these considerations and given the nature of the Beschuss load-case, explicit time integration methods are selected; therefore, the issue of time-step related instability must be addressed. A well known criterion in this regard is the ”Courant-Friedrichs-Lewy (CFL) condition”, which states that:

”to enforce stable results, a stress wave cannot travel farther than the smallest element characteristic length in a single time step”, i.e.:

$$\Delta t \leq \left[\frac{h}{c}\right]_{min} \tag{2.1}$$

with Δt the time step, h the characteristic length and c the speed of sound in the material. In many large-scale engineering application, the CFL condition imposes really small time-steps, which result in very high simulation times. A solution to the issue, which has been adopted in the project, is mass scaling: the mass of the smallest elements of the model is artificially increased in order to increase the density and in turn reduce the speed of sound in the material (as $c = \sqrt{\frac{E}{\rho}}$), increasing the minimum time-step threshold. This technique is based on the assumption that only a small portion of the model will be subject to mass scaling, thus keeping the global accuracy of the simulation within a reasonable range [16]; to this end, the artificial mass added to the model must be checked at the beginning of every simulation, adjusting the relevant parameters in case it falls outside of reasonable ranges.

2.4.3. Introduction to LS-Dyna

Among the commercially available explicit integration software, LS-Dyna has been selected for this project due to several reasons: first, even though it evolved to become a general-purpose multiphysics simulation software package, its ”origin and core-competencies lie in highly non-linear transient dynamic finite element analysis, using explicit time integration” [17], which in 2.4.1 were shown to be the best fit for the Beschuss load-case. Second, in the department of the company where the project took place, plenty of LS-Dyna related resources were readily available, in the form of industrial-level licenses, expert supervision and a direct contact line to modeling support from Ansys, the company which develops the software.

At its core, LS-Dyna uses spatial discretization to model structures via a wide array of elements such as solids, shells, thick shells, beams and specialized elements, which then interact via robust contact algorithms. Material behaviour is governed through a broad library of pre-defined or custom material models [18].

Input is supplied through a flexible and logically organized database called Keyword Input, which defines model geometry, simulation type, control parameters and constitutive properties. Each input section begins with a keyword followed by the data pertaining to it, which can be provided in free or fixed format; apart from the *END keyword which specifies the end of the input stream, input is order independent. To manage large input files, the input information can be split into multiple sub-files (with extension ”.k”) and then called for in the main input file (with extension ”.i1”) via the *INCLUDE keyword.

A last note should be made concerning the possibility for users to specify numerical values for named parameters referenced throughout the input file through the *PARAMETER keyword, in order to enhance model maintainability and adaptability [18].

2.4.4. Introduction to Ansa

Input is supplied through a single ASCII text file, which can be prepared with any generic text editor, even though many third-party pieces of software are available to this end. Ansys provides its one license-free pre-processing software, ”LS-PrePost”, but the availability within the company of a more comprehensive option in ”Ansa” made it the chosen pre-processor. The software allows for a vast array of solutions such as CAD-input and cleanup, advanced meshing and morphing, model integrity checks and includes configurator[4] [19].

In uniformity to the workflow adopted in the company, Ansa has been used to set up and ”write” the includes (.k files), while the main input file (.i1) has been written through a regular text editor in order to enhance readability and intelligibility, as the Ansa-generated or modified files lose all previous formatting.

2.5. Modeling Solutions

Having introduced the simulation environment, it can now be explained how it can be used to model the damage mechanisms discussed in 2.2 to simulate the Beschuss load-case described in 3.1.1, with a focus on delamination implementation, as argued in 2.3. First, a general framework is established to classify the available solutions, then the baseline implementation provided by the company is presented, highlighting its main features and limitations. Improving on those, alternative implementations are proposed, starting from the current state-of-the-art. Finally, a comparison between all the approaches is performed, and the most promising candidate is selected.

2.5.1. Overview of the Available Solutions

The existing approaches to damage modeling in LS-Dyna can be divided in two big groups, depending on their capability of simulating delaminations. The ones which have this option can be further divided in all-in-one material formulations, where fibre failure and delaminations are internally handled via complex 3-d stress fields, and ”discretized” formulations, where plies are modeled through material models which handle fibre failure, and the interfaces between them are modeled through tiebreak contacts or cohesive elements, whose failure results in delamination.

A summary of the available solutions are presented in Figure 2.1. In the following, some of them will be explained further; specifically:

- **the baseline solution** provided at the beginning of the project, using shell elements and MAT_58 to model a single equivalent laminate for the whole laminate, thus incapable of modeling delaminations.
- **the state-of-the-art solution** available in the form of MAT_161 (and MAT_162), an all-in-one formulation.
- **the chosen solution for the project**, which re-uses the same shell formulation and material card as the baseline model for the plies, though modeling them individually and connecting them with a tiebreak contact formulation, which fails at predefined stresses, hence simulating interface failure and delaminations.

[4] which allows to set-up different files for each part, leveraging the *INCLUDE keyword discussed before.

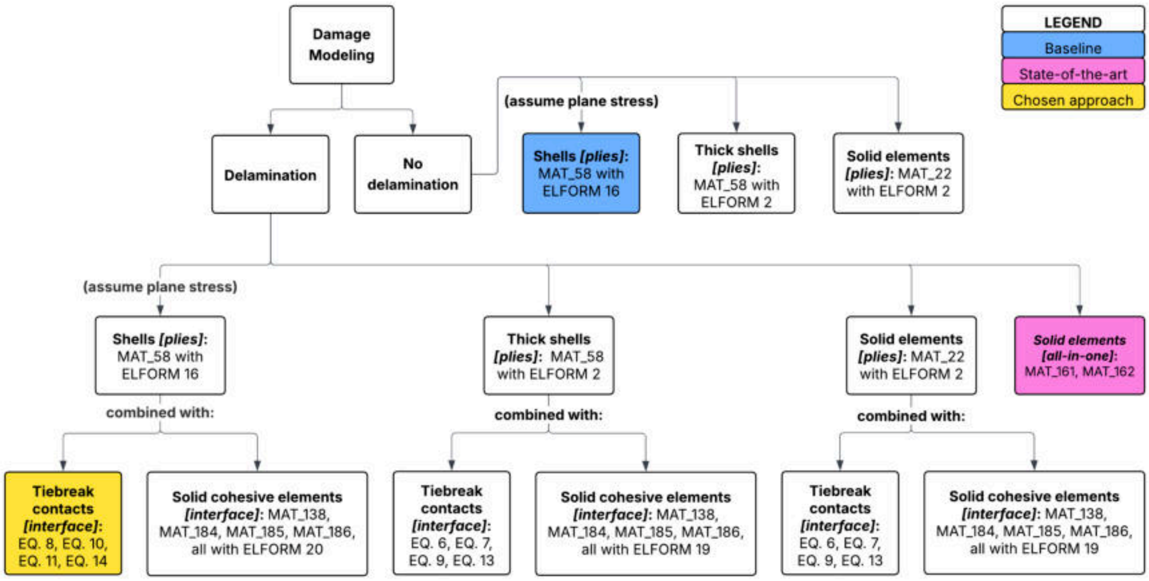

Figure 2.1: Summary of the available modeling approaches to damage modeling in composites in LS-Dyna [20][21][22]. Note that the reported examples are representative of the modeling strategies they refer to, but not comprehensive.

2.5.2. Baseline Solution

As mentioned in the introduction, the company provided a starting model, which will be thoroughly discussed in all its components and settings in 4.2.2. In this section the modeling approach to the laminate will be introduced; furthermore, the constitutive material model chosen for the laminate will be described, highlighting its capabilities and limits.

Features

In the baseline solution, given the large aspect ratio of the plate compared to its thickness, plane stress approximation is adopted, and the laminate is modeled as a single layer of shell elements.

Still, no CLT[5]-based smearing of the single plies properties is performed. Instead, by invoking the *PART_COMPOSITE card, different material properties, fibre orientation and thicknesses can be assigned to multiple integration points distributed through the thickness of the shell, hence enabling failure of individual plies [20]. By default, each layer is numerically integrated with a one-point trapezoidal rule, which is deemed to be sufficient for most composite layups and it is the recommended setting; still, if necessary, a 3-point Simpson integration rule can be chosen by flagging the IRPL parameter [18].

Note that since the laminate is treated as a single shell, the integration points through the thickness are enough to properly compute its bending stiffness as long as the number of plies is ≥ 2, as 2 points are necessary to differentiate tension and compression (the shell would otherwise be a membrane). As per the number of integration points per layer, element formulation ELFORM_16 is used, meaning 4 integration points per element are used (i.e., fully integrated formulation); since high deformations are expected, hourglass control (TYPE_8) is required. Although ELFORM_16 uses approx. 2.5 times more CPU than ELFORM_2 shell, it has been proven to be much more accurate and resistant to locking and hourglassing [23], hence being the preferred formulation at the company for basically all crash simulations.

As per the material model, MAT_LAMINATED_COMPOSITE_FABRIC (MAT_58) has been used: it supports shell, thick shell and solid elements, and can model composite materials with UD layers, woven fabrics and complete laminates, like in this project's case. Maximum effective strain controls the failure of an element layer, which is completely removed when the specified value is reached (note that maximum allowed value for the effective strain is 1, equaling to 100% strain) [21].

[5] Classical Laminate Theory

Limitations

First, since the whole laminate is modeled as a single shell, no interface failure is possible. Hence, delamination cannot be modeled by this approach, and impact dynamics cannot be represented with a high degree of fidelity, as the reduction in bending stiffness and the increase in energy absorbed by the plate cannot be computed.

Second, since plane stress approximation is adopted, no through the thickness stresses are computed. This limits the accuracy of the solution in case of transverse impacts, like the Beschuss.

2.5.3. State of the Art

Material models MAT 161 (MAT_COMPOSITE_MSC) and MAT 162 (MAT_COMPOSITE_DMG_MSC) are computational constitutive material models implemented in LS-Dyna. They were developed by Materials Sciences Corporation (MSC) to characterize the progressive failure behavior of fiber-reinforced composite laminates consisting of uni-directional and woven fabric layers, particularly under high strain rate and pressure loading conditions like ballistic impact [21][4][24].

Features

By computing the entire 3D stress field (i.e., 6 components) of the elements, and adopting a set of progressive failure criteria based on the methodology developed by Hashin (with a generalization to account for the effects of highly constrained pressure), these material modes are able to accurately simulate fibre failure, matrix damage and delaminations (any mode). Specifically, ply level stresses are computed and used as input for individual criteria for fibre tensile/shear, compressive and crush failures, along with perpendicular and parallel (delamination) matrix failures [21].

The _DMG keyword of MAT 162 enables a generalization of the basic layer failure mode of MAT 161 by adopting a fracture mechanics approach for characterization of the softening after damage initiation. Furthermore, it implements strain rate sensitivity [21].

Limitations

The main disadvantages of these material models are their complexity, data requirements and mesh dependency, along with sub-optimal accuracy/cost ratio for delamination modeling and extra licensing requirements.

First, they only work with solid elements, making the simulations computationally expensive and hard to integrate in existing models.

As per the data requirements, MAT 162 necessitates a large number of parameters (34), many of which are quite difficult to obtain experimentally (damage parameters, residual strengths, rate constants) and are usually determined and tuned through calibration, requiring extensive effort and computational modeling comparison with test data [1].

Concerning the mesh dependency, it has been proven that mesh refinement doesn't lead to convergence, as smaller elements fail earlier, dissipating less energy. Optimal mesh size has therefore to be obtained through comparison with test data, and it has been observed to be dependent on a variety of parameters, such as laminate thickness and material, but also on projectile size, shape and speed, making it necessary to repeat the tuning process if any of those change [25].

Furthermore, it has been observed that the through-the-thickness tensile and shear failures, which are used to model delaminations, show reduced accuracy/cost ratio compared to other implementations. Some authors obviated to this issue by setting the through-the-thickness strengths to artificially high values to prevent failure, and then adopting a separate routine to handle delamination, based on special tiebreak (tie-break, option 9) contacts mimicking cohesive element formulations without the need of modeling zero-thickness solid elements [25].

Last, as the models are developed and updated by MSC (an external company), they require a separate additional license to be implemented in any simulation.

2.5.4. Combo 1: Shells + Cohesive Elements

As explained, even with state-of-the-art material models, delaminations are more efficiently handled by dedicated solutions. Doing so opens up a vast array of combinations, as either shells, thick shells and solid elements can be used to model the plies individually, combined with cohesive elements or tiebreak contacts to handle interface modeling.

First, a combination of shell and cohesive elements is explored.

Features: Plies Modeling

Since the available MAT_58 presented in 2.5.2 is already calibrated on shells elements and has proven to work effectively for various load cases, it has been selected as the starting point for the combination approach.

Each ply is therefore modeled as a shell element with surface offsets matching its thickness, and the various plies are then stacked together, distanced so that the upper offset surface of the first ply lies on the same plane as the lower offset surface of the second one, and so on (see Figure 2.2).

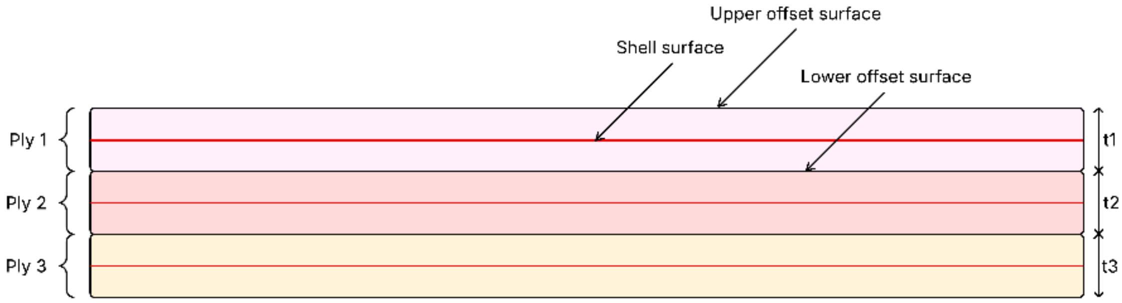

Figure 2.2: Representation of the shell stacking modeling approach.

Keeping the *PART_COMPOSITE card would represent an advantage as it allows to model woven fabric by defining more than one layer per ply and assigning appropriate material properties (UD layers) and orientations, when dedicated material cards are not available. Furthermore, it can be used to group plies where delaminations are not expected, reducing the computational cost of the model.

As mentioned before, the *PART_COMPOSITE has one integration point per ply by default, therefore using it to model a single ply could represent an issue, as the individual shells will only have one integration point through the thickness, falling in the membrane category and resulting in 0 bending stiffness.

This could be solved by interface models constraining rotations, letting the membranes handle bending through their own in-plane tension and compression, but as interfaces fail, each delaminated ply would have 0 residual stiffness (non-physical). Alternatively, as most contact formulations typically used for interface modeling are incapable of constraining rotations[6], a Simpson integration rule[7] can be implemented for each ply, so that ply-level bending stiffness is restored.

Features: Interface Modeling

Cohesive elements with ELFORM_20 or ELFORM_22 can be used to model the cohesive interface between the faces of shell elements, and are typically used to implement delaminations. Unlike continuum elements, they don't model bulk physical material properties, but rather a non-linear dissipative spring-based force response depending on the separation distance between neighboring faces through a traction-separation law. Therefore, they can remain stable under zero or negative volumes, enabling both finite and zero thickness formulations [26], which would be required along with tie contacts when using shell offsets as presented in Figure 2.2.

The constitutive law determines the normal and shear stress as functions of the separation vector: after an initial elastic response up to a critical separation distance δ_0 and stress σ_c, the damage commences

[6] This is due to the penalty-based nature of most contact formulations, opposed to full nodal constraints which would instead be able to inhibit rotations.

[7] 3 through-the-thickness integration points per ply.

and reaches failure at a certain separation distance δ_F, as shown in Figure 2.3, along with the corresponding points in the delamination process. Note that the unloading is typically elastic (”unloading” arrow in the figure) [11].

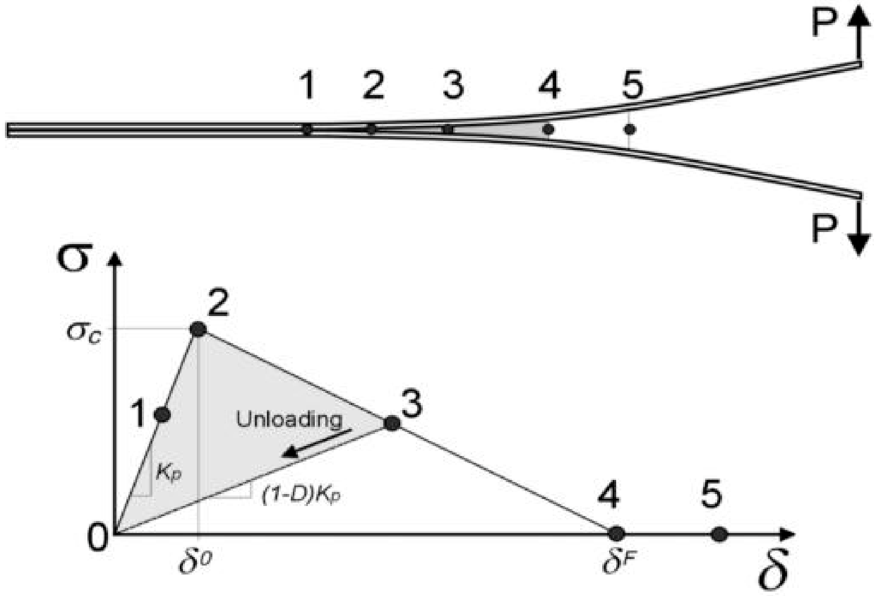

Figure 2.3: Bilinear constitutive model (Mode I), and corresponding points in the delamination process [11]

The same curve can be defined for Mode II, and mixed modes can be handled by extending the law for 3-dimensional deformations, as shown in Figure 2.4.

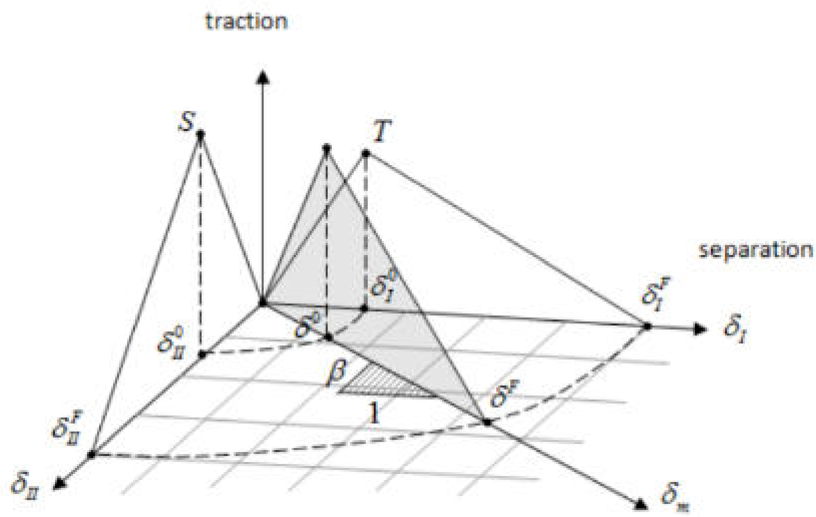

Figure 2.4: Mixed modes traction-displacement interaction [11]

In high-speed applications, the sharp corners in the law may introduce numerical instabilities, known as ”ringing”[8], caused by sudden damage growth at point 2 and sudden failure at point 4. To avoid this, specific material models (MAT_184, MAT_185 and MAT_186) allow to define a load curve for a general separation law, and some authors have rounded the corners with a cubic curve, while keeping the area under the curve (i.e., the total fracture energy) constant; although a viable solution, doing so

[8]Spurious high-frequency oscillation due to instantaneous relaxation of contacts which sends shockwaves through the mesh.

is a complex operation, due to the lack of reliable data and user experience, as really advanced users are necessary to determine the correct shape of the separation law [11].

Limitations

To ensure accurate solutions, cohesive elements require the following input: initial stiffness K_p, fracture energies G_{Ic}, G_{IIc} and G_{IIIc}, and corresponding inter-laminar tensile and shear strengths T and S. Among them, the fracture energies are not readily available and might be difficult to acquire, due to high scatter (up to 20%) of the experimental results and to the absence of a standard ASTM specification.

Furthermore, cautious definition of the optimal mesh size is required, as numerical studies have suggested that at least 3 elements are needed to span the area in front of the crack tip where delamination is happening (called ”cohesive zone”) in order to properly compute the fracture energy, resulting in an element size of around 0.5 mm, making cohesive element formulations impractical for industrial applications [11].

Interestingly, a workaround to obtain a mesh-independent solution has been found [11], hence allowing for coarser meshes and more efficient simulations.

In short, it is based on the fact that only G_{Ic} and G_{IIc} (i.e., the area under the curve in Figure 2.3) are important for a successful analysis, while the interface stiffness and peak tractions in tension and shear are not; therefore, they can be varied freely as long as the release rates (i.e., the areas) are kept constant (see Figure 2.5).

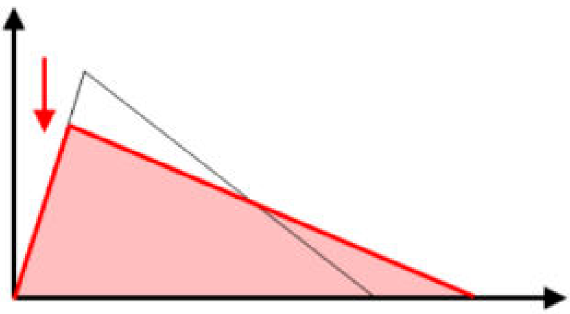

Figure 2.5: Decrease in the peak traction to increase element length [11]

Since the cohesive zone length can be estimated as:

$$l_{cz} = ME\frac{G_c}{\tau^2} \tag{2.2}$$

where M is a multiplier depending on the author and τ is the peak traction, by reducing τ (and increasing the failure strain to keep the area constant) the length can be increased, allowing for higher element sizes and faster computational times. Although powerful, this method requires additional test results, plus some trial and error.

As per the interface stiffness K_p, which is not necessary to solve the mesh-related issue per se, some authors have proposed equations to determine it based on the interface (i.e., resin) properties, but as mentioned its value is not important as long as the G_c are accurate; hence, a constant value of $10^6 N/mm^3$ has been proposed, and it has been found through extensive numerical testing that it would produce essentially the same results for all modes, without leading to the numerical issues encountered with greater values [27].

A second limitation is represented by the fact that cohesive elements are effectively solid elements, which in general correspond to higher CPU effort compared to shells, and even with 0-thickness definition, layers of cohesive elements need to be modeled between the plies, increasing the effort required to convert existing models [20][25].

Last, once cohesive elements fail, for most formulations a separate contact must be defined between the plies in order to avoid inter-penetration [3].

2.5.5. Combo 2: Shells + Tiebreak Contacts

Alternatively to cohesive elements, tiebreak contact formulations can be used to model the plies interfaces.

Features: Plies Modeling
The plies formulation remains the same as presented in the previous combination, due to the reasons already explained.

Features: Interface Modeling
In cases where the bonding layer is thin enough to ignore its own mass (which is true in most cases), it is possible to use *CONTACT_TIEBREAK formulations (OPTION = 6 through 14, referred to as "Combo 2.1"), which can even have traction-separation laws built into their formulations. These laws aim at describing the cohesive zone behaviour, and the most commonly used are based on a linear elastic softening (bilinear) model, similar to the one showed in Figure 2.3 [11]; note that mixed modes can be handled like for cohesive elements.

As mentioned in 2.5.4, ringing may happen in high-speed scenarios, making it necessary to switch to cohesive element formulations that allow for general separation laws.

Notably, some tiebreak options (OPTION = 6, 8, referred to as "Combo 2.2") have a full strength based formulation, where delamination happens when a combination of shear and normal stress reaches user specified values, according to the well known equation:

$$\left(\frac{|\sigma_n|}{NFLS}\right)^2 + \left(\frac{|\sigma_s|}{SFLS}\right)^2 \geq 1 \tag{2.3}$$

where SFLS is the shear strength, NFLS is the normal strength, σ_s is the shear stress and σ_n is the tensile stress, which is taken as 0 if compressive. This is considered a rather crude approximation[11], and should be treated with caution, even though a case for it will be made in the following sections.

The "Combo 2.2" can be enhanced with the definition of a third parameter called PARAM, which represents the critical distance at which the interface failure is complete, and is therefore often labeled CCRIT. As soon as Equation 2.3 is satisfied, damage initiates; then, the damage function linearly scales the stress until failure is reached, as shown in Figure 2.6, where

$$S = \sqrt{max(\sigma_{nf}, 0)^2 + \sigma_{sf}^2} \tag{2.4}$$

with σ_{nf} and σ_{sf} the stresses at damage initiation.

Assuming no load reversals, the energy released to the interface failure is approximately equal to the area under the curve, i.e.

$$Energy = \frac{1}{2} * S * CCRIT \tag{2.5}$$

Note that the curve in Figure 2.6 assumes infinite contact stiffness for explanatory purposes, hence the infinite slope ramp-up which result in S being reached at d=0. In real-case scenarios, the slope must be steep enough for σ to reach S before d reaches CCRIT, i.e., $d_{peak} < CCRIT$. The LS-Dyna Keyword Manual [18] states that for meaningful energy calculations, the contact stiffness must be much large than

$$\frac{min(NFLS, SFLS)}{CCRIT} \tag{2.6}$$

without elaborating further. This most probably comes from

$$S = K_c d_{peak} \rightarrow S/K_c < CCRIT \rightarrow K_c > \frac{S}{CCRIT} \tag{2.7}$$

and to capture at least the weakest failure mode, S can be substituted with $min(NFLS, SFLS)$.

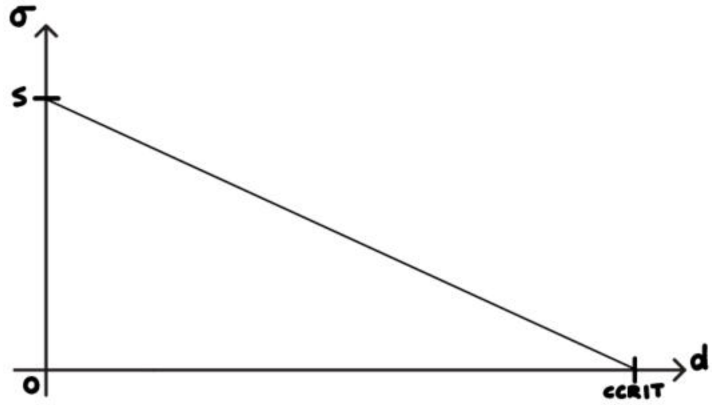

Figure 2.6: Stress scaling in tiebreak contacts with OPTION = 6, 8

In case of CCRIT = 0, the area under the curve collapses to 0, and contact failures don't dissipate any additional energy[9]. With this setting though, no fracture energies need to be determined.

Note that after failure tiebreak contacts revert to surface-to-surface contacts with thickness offsets, therefore no additional contacts are required to handle post-failure dynamics [22].

Limitations

Naturally, the options based on traction-separation laws ("Combo 2.1") have the same disadvantages of their cohesive elements counterparts.

As per OPTION = 6, 8 ("Combo 2.2"), defining the critical distance CCRIT represents a challenge as its value is derived from the fracture energy, (since it dictates the area under the curve, see Figure 2.6), effectively presenting the same limitations as the other options. On the other hand, leaving CCRIT undefined would result in no additional energy dissipated by the delamination process, with the added risk of causing ringing due to the absence of a nodal forces ramp-down. A good solution would be to set CCRIT to an arbitrarily low value, enough to prevent ringing through numerical damping without significantly altering the energy balances. In any case, it must be noted that the relaxed rotational constraints of tie-break formulations already discussed help reducing this specific issue, as more compliance eases the "snap-back" effect of contact failure.

Last, tie-break contacts in MPP[10] need to be manually oriented, even when the "AUTOMATIC" keyword is active; specifically, segment normal vectors should always point towards the opposing contact surface, in order to properly distinguish tension and compression [18]. This creates a layer of added complexity in setting up the contacts, addressed in Appendix E.2.

2.5.6. Comparison Between the Available Solutions

The proposed solutions' features presented in this section are summarized in Table 2.2, for reference. As per their limitations, they are reported in Table 2.3 instead, and each feature is color-coded to help identify the most suitable candidate for the project. By observing the table, "Combo 2.2" (i.e., shell elements + strength-only tiebreak contacts) emerges as the clear winner, as it is able to integrate delaminations into the company's existing modeling environment with a great deal of flexibility. If energy dissipation is important, like it would happen for extensive delaminations, defining CCRIT is enough to account for it with reasonable accuracy, while in cases where it plays a secondary role, CCRIT can be ignored (or kept to a low value to ensure ringing prevention, as discussed before) for an even faster implementation.

Clearly, more refined solutions, like MAT_161/MAT_162 are expected to produce more accurate results, but this project aims at improving current results in a pre-existing industrial context, hence other

[9] In real applications, since the contact stiffness cannot be infinite, only the ramp up energy, which is very small and non physical, would be calculated.

[10] Massively Parallel Processing, version of LS-Dyna that runs on multiple computers connected in a network to reduce simulation time.

aspects such as ease of integration, limited one-time calibration, and computational efficiency have to be considered.

Currently, no publications have been found where the chosen approach has been successfully used to predict delaminations, especially for a high-speed angled impact such as the Beschuss load-case, hence the selection also has significant academic relevance.

2.5.7. Estimation of Model Parameters

Given the high-speed nature of the impact, and the chosen layups stacking sequences, small delaminations are expected around the contact area between plate and impactor: hence, CCRIT could be initially set to 0, assuming negligible energy dissipation (this assumption will be validated in Section C.2.4). Then, its value could be varied in a pre-defined range in different simulations and the impactor's residual kinetic energy can be tracked to determine its influence.

Therefore, in the first iteration of the model, only shear (SFLS) and normal (NFLS) strengths for the tie-break contacts have to be determined.

At first, one could think to determine them from experimental tests on specimens of the expected interface material (epoxy resin in this case). For this, ASTM D2344[28] allows to determine inter-laminar shear strength ILSS (i.e., SFLS), while ASTM C297[29] is used for inter-laminar tensile strength ILTS (i.e., NFLS). Alternatively, various sources in the available scientific literature provide experimental results for these properties for similar ply-matrix combinations as the ones used in this project, and will therefore be used as a first estimation.

NFLS Estimations

For a glass[11]-polyester interface, NFLS is reported to be at around 9.78 MPa [10]. This is most probably a lower value than the one of the glass-epoxy and carbon-epoxy plates, as polyester is expected to give lower strength than epoxy. For a carbon-epoxy interface, NFLS is in fact reported to go up to 51.76 MPa for 4-plies laminates, decreasing to around 43.23 MPa for 12-plies laminates [30], highlighting inverse relationship between inter-laminar normal strength and number of plies. For a glass[12]-epoxy interface, NFLS reaches instead 40 MPa, and no mention of dependency on the number of plies is made [31].

Given these results, the expected NFLS value that provides the most realistic results concerning the delamination pattern should fall in the 40-50 MPa range.

SFLS Estimation

For a glass[13]-epoxy interface, SFLS has been reported to fall within 24 and 24.6 MPa [8]. Another source places SFLS at 25.01 MPa for the same plies-interface combination [32]. A third source recorded a SFLS of around 16.5 MPa, again for the same combination [7].

Hence, the expected SFLS can be confidently placed in the 16-25 MPa range for glass-epoxy laminates.

Additional Considerations

The choice of having delamination models depending on stress limits only can be problematic, as in FEA stresses are averaged over each element's area, hence coarser meshes will result in lower stresses being computed, which could fail to trigger failure altogether, while finer meshes could end up computing stresses so high that all contacts undergo premature failure as soon as the impactor touches the plate.

In principle, selecting a mesh size equal to the physical cohesive zone length of the material (around 2 mm in typical composites) could align the numerical discretization with the material physical failure scale, ensuring that the element's averaged stress capability creates a force balance equivalent to the physical crack tip, allowing for the direct application of standard literature strength values without the need for artificial scaling (this concept will be validated in Section C.2.4).

[11] woven
[12] UD
[13] woven

Unfortunately, this is not always possible due to computational efficiency requirements or mesh-dependent material calibrations (i.e., when a material card has been defined to be representative of the material only for a specific mesh size); therefore, while the literature values previously discussed provide a strong physical baseline, the dependency of the stress-based criterion on mesh size will most probably require phenomenological calibration, where NFLS and SFLS will be tuned until the simulated delamination area correlates with the damage pattern observed in the experimental Beschuss tests (this will be shown in Section 5.3.2, see ”Damage Pattern (Protection Plate)”).

As contact stresses are computed from nodal forces and tributary areas automatically assigned to each node, the contact stiffness doesn't play a direct role in their calculation. Still, since $F = K_c x$, the contact stiffness regulates how much the contact deforms before the required reaction force F is reached, therefore it must have a reasonably high value to simulate a rigid contact until damage initiation. This doesn't imply the need for a realistic contact stiffness value; in fact, as already mentioned in 2.5.4, when dealing with different contact options (e.g., OPTION=9), some authors choose a completely arbitrary contact stiffness for all models, and then scale the strengths (i.e., peak stresses of the traction-separation laws) to match the areas under the curve.

Note that for OPTION=6 and OPTION=8 the contact stiffness is calculated automatically by the solver based on the material moduli and element dimensions; for composites, this calculation is typically dominated by the in-plane fibre moduli (the minimum between E_1 and E_2 is taken [22]), resulting in a high contact stiffness. This is advantageous as it helps enforce a quasi-rigid bond prior to failure without the need for stiffness scaling.

Solution	Element type (plies)	Material model (plies)	Modeling approach (plies)	Integration points through t (plies)	Stress field calculation (plies)	Governing failure mechanism (plies)	Modeling approach (interface)	Governing failure mechanism (interface)
Baseline	Shell elements	MAT_58	Single equivalent laminate (via ”PART COM-POSITE” card)	1 per ply	plane stress	Maximum effective strain	-	-
State of the art	Solid elements	MAT_161 / MAT_162	All-in-one	Depends on meshing (min 3 rec-ommended)	Full 3D stress field	Hashin-based	All-in-one	Hashin-based, or dedicated separate solution
Combo 1	Shell elements	MAT_58	Individual stacked plies	3 per ply	plane stress	Maximum effective strain	Cohesive elements	Traction-separation law
Combo 2.1	Shell elements	MAT_58	Individual stacked plies	3 per ply	plane stress	Maximum effective strain	Tie-break contacts (options 6 through 14)	Traction-separation law
Combo 2.2	Shell elements	MAT_58	Individual stacked plies	3 per ply	plane stress	Maximum effective strain	Tie-break contacts (options 6, 8)	Only strength-based (unless CCRIT is defined)

Table 2.2: Features comparison between the proposed solutions.

Solution	Computational effort	Required characterization	Handles post-delamination contacts?	Does de-lamination dissipate energy?	Easy to integrate in existing models	Can currently available material cards be used for the plies?	Additional steps required?	Additional license required?
Baseline	Low	Card available (otherwise standard material tests)	-	-	Coincides with the existing models	Yes	No	No
State of the art	High	34 required parameters, some of them hard to determine	Yes	Yes	No, switch to solid elements required	No	Dedicated delam. solution for improved results	Yes
Combo 1	High	Fracture energies required (hard to get and high scatter)	No	Yes	No, introduction of 0-thickness cohesive elements required	Yes	Trial and error to achieve mesh indep. behaviour, handling of ringing	No
Combo 2.1	Medium	Fracture energies required (hard to get and high scatter)	Yes	Yes	Yes	Yes	Trial and error to achieve mesh indep. behaviour, handling of ringing	No
Combo 2.2	Medium	Normal and shear interface strengths (and optionally CCRIT)	Yes	Only if CCRIT is defined	Yes	Yes	No (unless CCRIT is defined)	No

Table 2.3: Limitations comparison between the proposed solutions.

3
Experimental Methodology

This chapter establishes the empirical foundation required to validate the numerical models developed in this thesis. First, the Beschuss load-case is described in detail, with a focus on the test set-up; then, available test results are presented, and based on a series of defined variables, the most adequate for the project scope are selected.

Uncertainty quantification on the experimentally measured parameters is performed, and confidence intervals are determined, while proposing possible explanations for variability.

As acquiring additional insights on the delamination extent has been deemed critical, C-scans are performed on selected laminates, and the results validated through indirect fibre-volume determination and section-cut microscopy.

Finally, to minimize input uncertainties in the numerical model, a specific tensile characterization campaign was conducted on the aluminum alloy used in the experiments to update the baseline material card.

3.1. Impact Tests and DIC Measurements

3.1.1. Set-Up and Test Description

As mentioned in Section 2.1, the Beschuss test aims at determining the protective capabilities of the UFS in cases of high-speed angled impacts. The standard set-up is schematically presented in Figure 3.1.

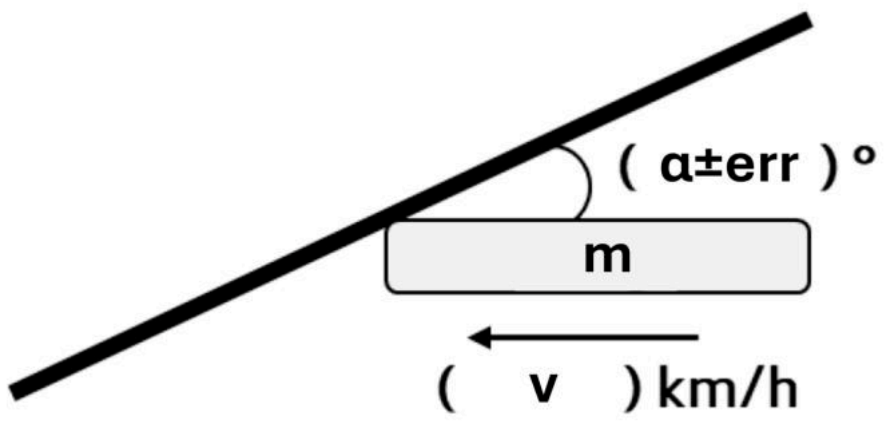

Figure 3.1: Synthetic representation of the Beschuss load-case

The payload to be protected, which in a real vehicle are the battery cells, is represented by an aluminum plate (in red in Figure 3.2), which is bolted to two fixtures (in blue in Figure 3.2) along its longer edges, via 3 bolts per side (in red in Figure 3.2). Between it and the impactor, distanced through solid aluminum spacers (in yellow in Figure 3.2), the protection plate (in green in Figure 3.2) is bolted to the fixtures in the same way.

A steel parallelepiped of dimensions $a \times b \times c$ mm and mass of m kg (in pink in Figure 3.2) is then shot at the protection plate, which absorbs part of its kinetic energy; if not halted, it then hits the aluminum plate, intruding into it. To measure the magnitude of such intrusion, which is used as the principal measure of the protection plate effectiveness, an advanced DIC[1] set-up is used; hence, the back of the aluminum plate is painted with the characteristic black-and-white speckles pattern typically used with this tracking technology.

The impact dynamics typically involve an initial contact made by the anterior face of the projectile, hereinafter referred to as the ”impactor head”. Upon contact, this interface acts as a momentary pivot point; consequently, the projectile retains its translational momentum while simultaneously acquiring rotational velocity. This results in a subsequent collision involving the posterior section, hereinafter referred to as the ”impactor tail”. This sequence generates two distinct loading events, classified in this study as the ”first impact” and ”second impact”, respectively.

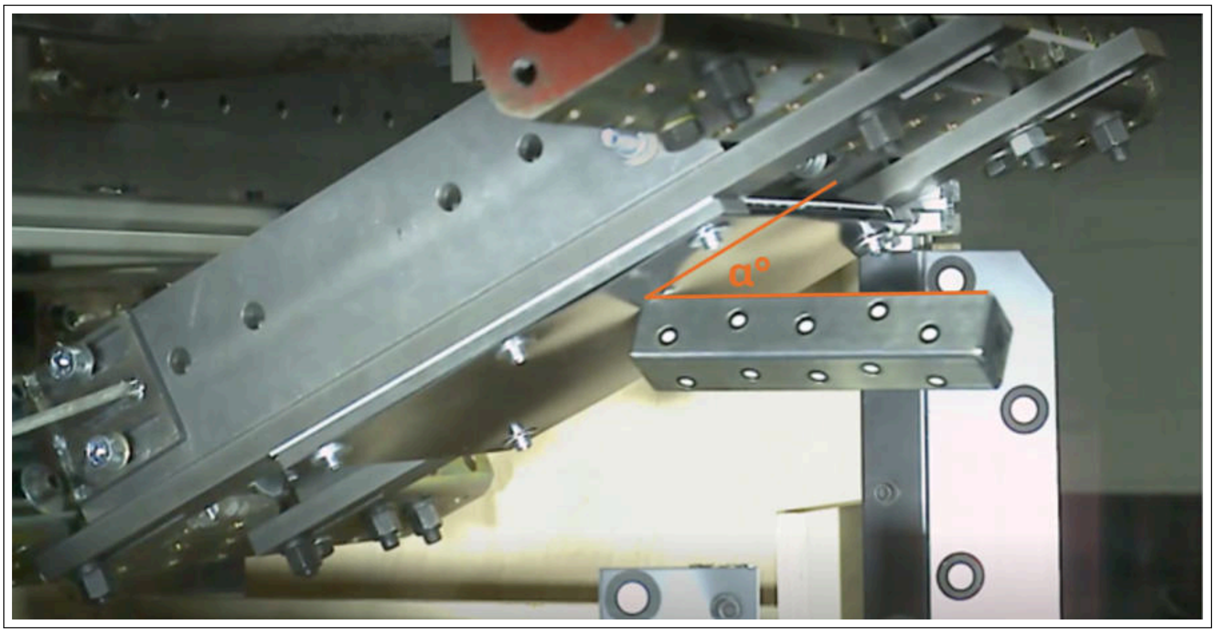

(a) Experimental setup

Continued on next page...

[1]Digital Image Correlation

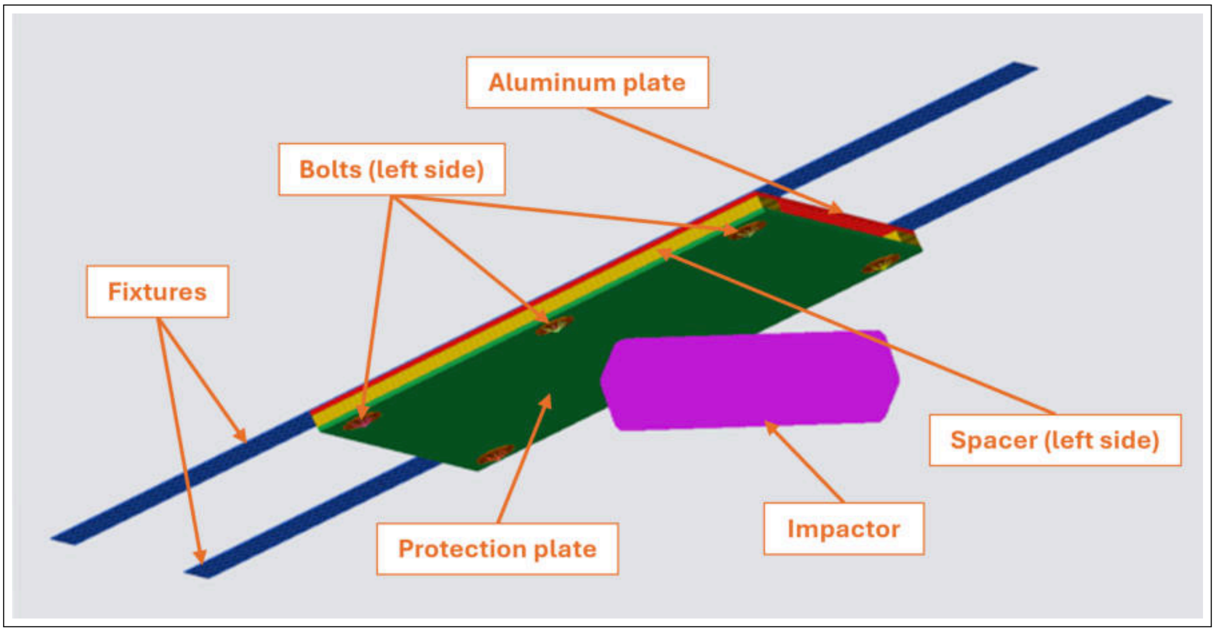

(b) LS-Dyna model

Figure 3.2: Close-up of the Beschuss test set-up, with a corresponding LS-Dyna model for clarity in distinguishing its components

To impart an initial speed to the impactor, a special method is adopted: instead of using a pressure cannon at point-blank distance, the projectile is mounted on a ”cart” which can slide on a rail aligned with the mounted plates (see Figure 3.3a). The cart is suddenly accelerated via a pressurized system (see Figure 3.3b), and forcefully halted after a certain distance. The impactor, guided through a custom-shaped opening, keeps moving due to inertia and ends up hitting the target. An issue with this solution is that the maximum speed allowed by the setup is lower ($\approx 60\%$) than the speed of v [m/s] required by the test specifications.

Hence, a clever workaround has been devised: on top of the cart a spring mechanism (see Figure 3.3c) is loaded and released at the end of the cart's path (i.e. its maximum speed) to further accelerate the projectile to the intended speed. The projectile then has to travel an additional horizontal distance before it can hit the plate at its mid-length with an intended impact angle of $\alpha°$, achieved by rotating the plates themselves.

This specialized approach achieves remarkably accurate speeds, but lacks precision with respect to the impact position and angle, making it difficult to re-produce the load-case in simulations. Hence, additional high-speed cameras, tracking these variables so that they can be accounted for at later stages of the project, have been introduced in the set-up.

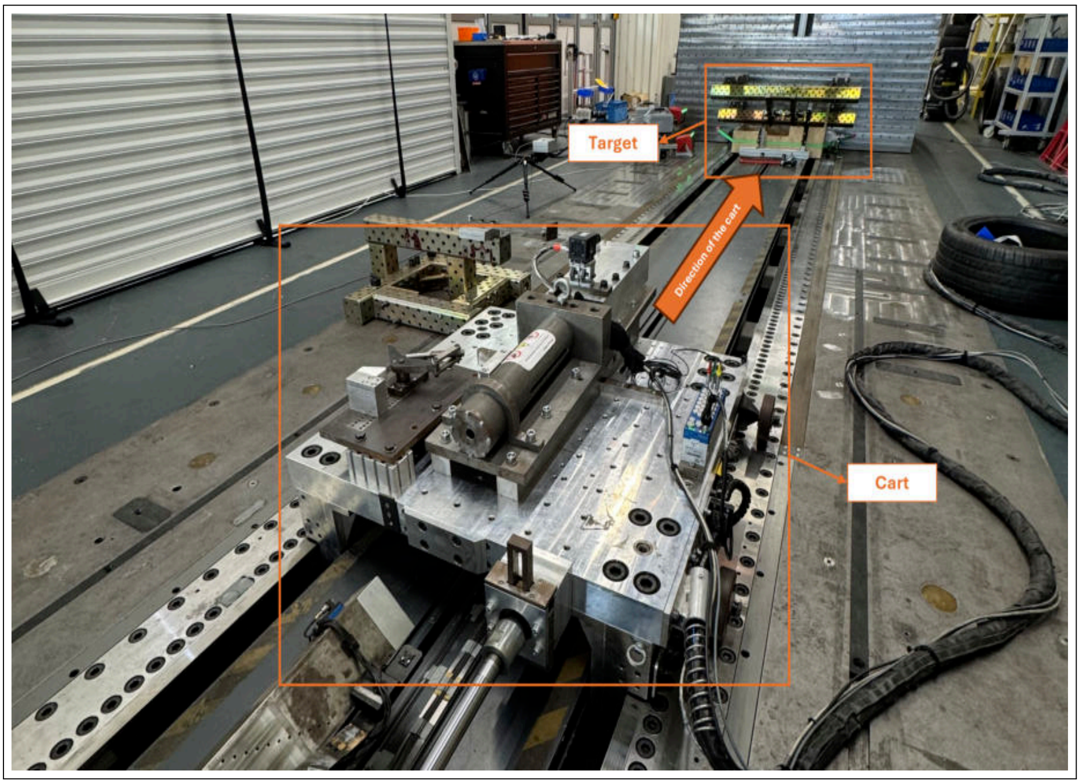

(a) Picture of the cart, rails and target

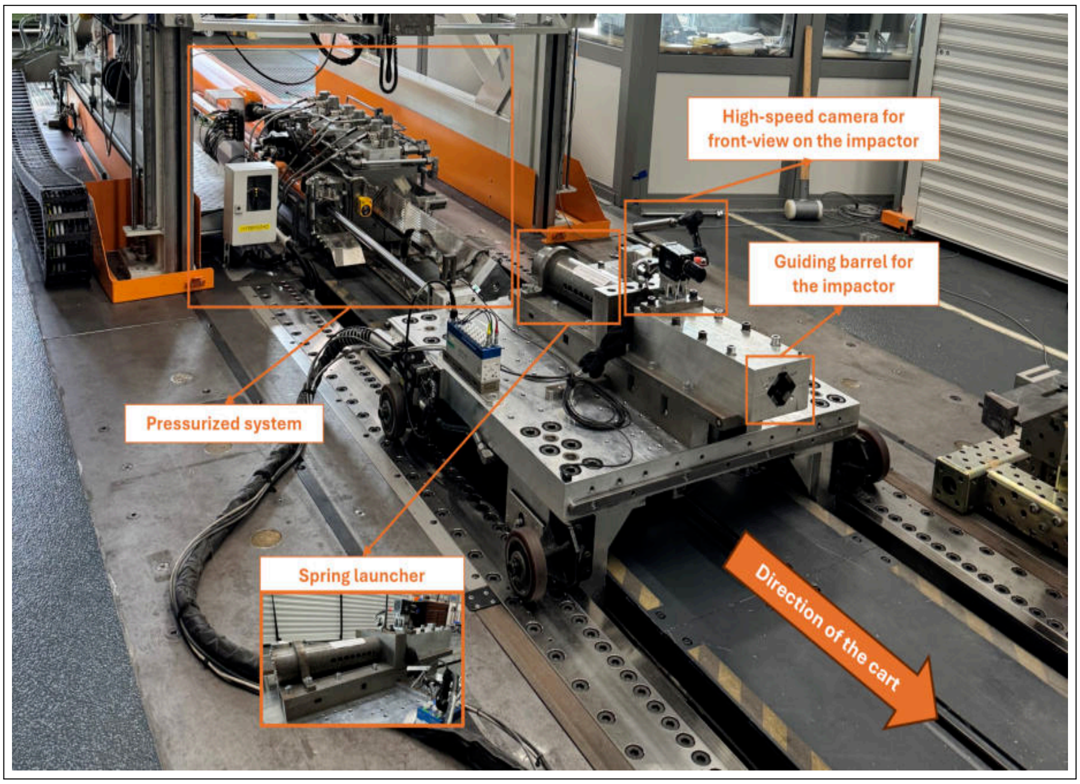

(b) Picture of the cart, primary (pressure) and secondary (spring) launching systems

Continued on next page...

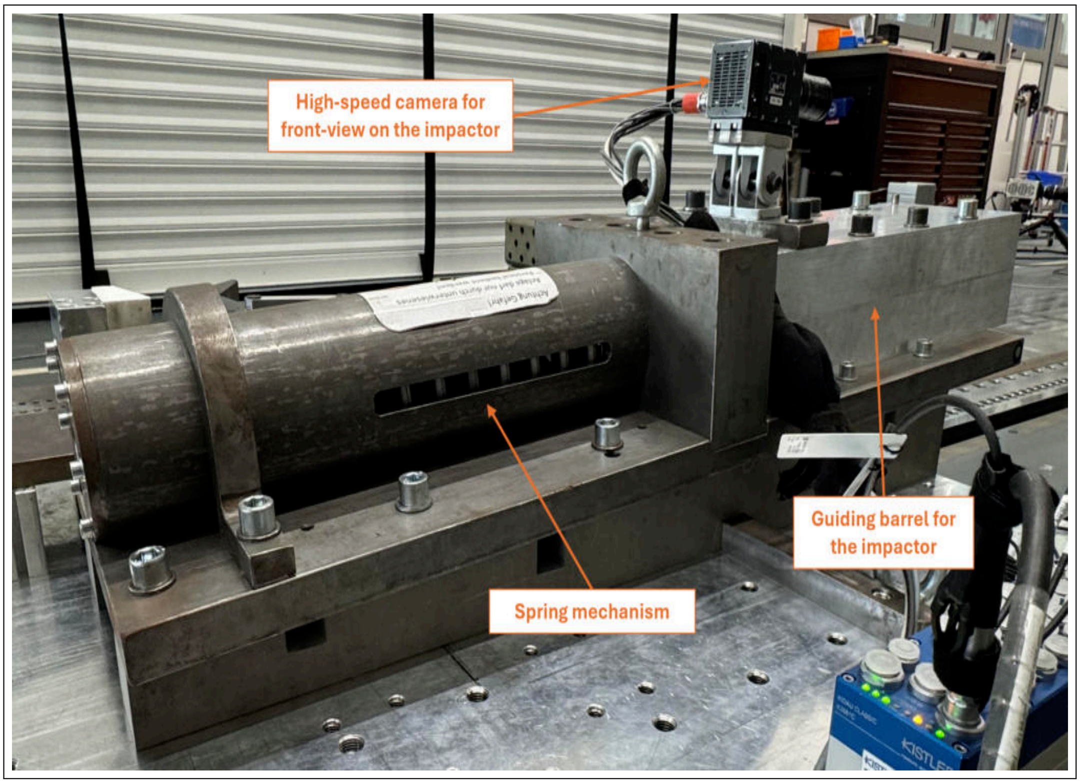

(c) Close-up of the secondary (spring) launching system

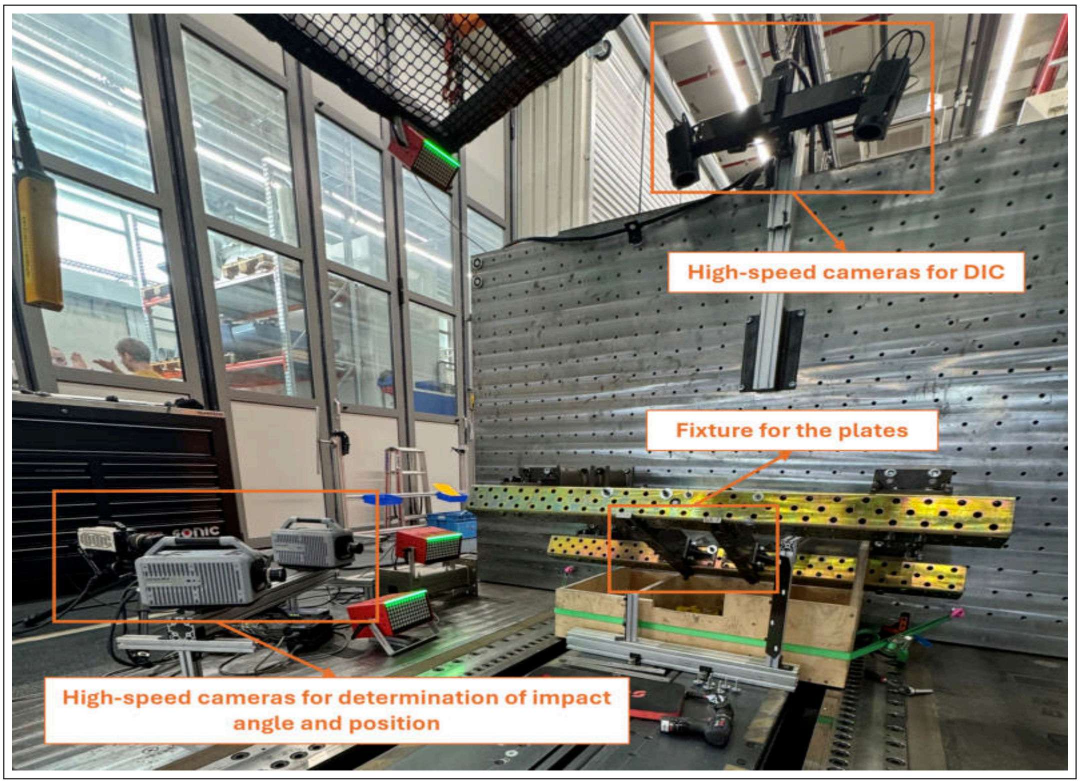

(d) Picture of the cameras set-up

Continued on next page...

Figure 3.3: Pictures of the Beschuss test set-up

3.1.2. Selection of Test Results

Multiple impact test results have been performed for a variety of layups and have been made available to the author. In the section ”Measured variables” below, the variables tracked by the experimental set-up, along with auxiliary variables defined during the project, are explained.

A selection has been performed while trying to capture as many aspects of the whole pool of available layups and materials, with a focus on layups currently in use or about to be used at the company; the chosen test versions and the respective results are presented below in Sections ”First Layup” and ”Second Layup”.

Measured Variables

The high-speed cameras to the side of the plate are measuring both ”pitch” (i.e., rotation around b-axis in Figure 3.4) and ”roll” (i.e., rotation around a-axis in Figure 3.4) angles[2] of the impactor, so that experimental deviations from the intended values of the test standard can be detected and reproduced in simulations. A review of the recorded angles highlighted a discrepancy with what can be observed in the test footage of some results for the ”pitch” angle, therefore a manual re-evaluation has been performed, and both the initial and updated angles are reported for completeness.

The same aforementioned cameras are responsible for measuring the impact position of the impactor in both x and y-directions (see Figure 3.4); note that the origin of the reference system is in the plate’s center.

Note that all the measurements refer to the time of first contact.

The intrusion (i.e., the displacement along the z-axis in Figure 3.4) over time for a certain node is instead tracked by the DIC-system. From the plots (which are extensively used in Chapter 5), along with maximum and plastic intrusions, contact times for both first and second impact can be inferred.

[2] Here, pitch and roll have analog meanings as in the aeronautical context.

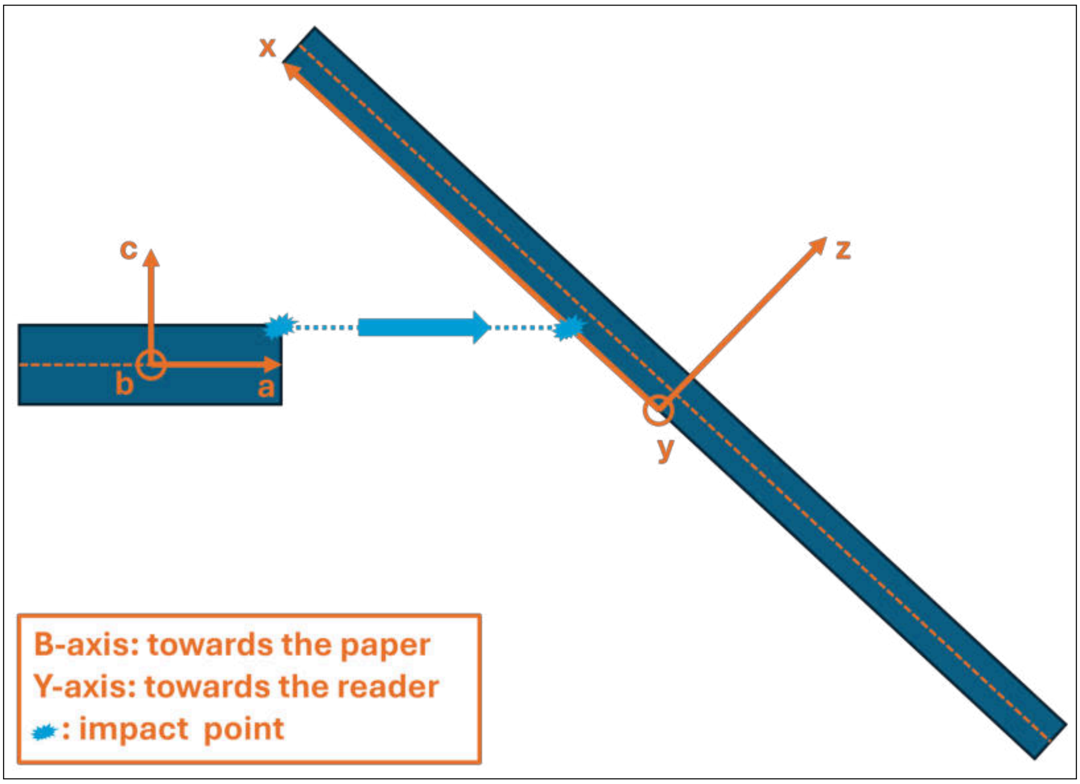

Figure 3.4: Impactor and plate's coordinate systems, side view

In an ideal scenario, the maximum intrusion node is tracked, but in the available test results, in most cases, a node around the first impact position is tracked instead; this is still quite close to the maximum, therefore it will be used for the project, but this discrepancy should be addressed in future experimental campaigns.

To ensure a valid comparison with simulation results, it is imperative to identify the coordinates of the tracked node, so that the corresponding point can be monitored in the numerical model. To achieve this goal, the node's position is identified from the video footage of the test by associating it to specific and recognizable speckle patterns, which are then pinpointed on the real plate, where the coordinates of the node can be measured. Then, the corresponding node ID in the numerical model is noted and tracked[3].

Other than by comparing intrusion magnitude on the aluminum plate, which as mentioned in the introduction, isn't a direct measurement of the accuracy of delamination modeling and could be influenced by a variety of other factors (e.g. strain-rate sensitivity), one could assess the model performances by comparing the delamination shape and size, if present.

To do so, it is necessary to perform C-scans on the impacted plates; the details of the process are explained in Section 3.2.

First Layup

The first selected layup is a 6-layer glass fiber laminate. The plies are from Owens Corning, with a grammage of 440 gsm and plain weave, 600 tex both in warp and weft; each ply is 0.293 mm thick, for a total thickness of 1.758 mm, and all plies are oriented at 0/90 degrees.

[3]In the initial phases of the modeling it will be specified that a node with corresponding x-coordinate but y-coordinate=0 is tracked in the numerical model. This is done because the experimental errors that induce the shift of the impact point in the y-direction are initially not implemented, and therefore the maximum intrusion happens along the mid-section of the plate.

The criticalities of this layup are 1) a rather low thickness, which could result in premature penetration of the impactor before delaminations could absorb enough kinetic energy to play a role in the impact dynamics and 2) the fact that all layers have the same orientation, as shear-induced delamination could be prevented altogether from happening.

Therefore, one could think that delamination implementation wouldn't play much of a role in improving the match between tests and simulations for this specific layup; if that is the case, the layup represents a chance to observe the effect of the new approach on the impact dynamics outside of delamination (e.g., local stiffness reduction), by comparing it with the baseline simulative approach.

As this layup has been extensively used at the company, various impact test results are readily available. Of those, only 4 were performed with an aluminum backplate to measure maximum and plastic intrusion; the intrusion-related variables are reported in Table 3.1 (for the complete intrusion plots, see Chapter 5), while the variables detailing the impactor's position and rotations at t=0 (i.e., first contact with the plate) are reported in Table 3.2.

Among the available results, V33 appears to be a clear outlier: impact timing is different than in the other versions, and remarkably lower intrusion values are registered, probably due to the much lower pitch angle compared to the other versions; last, the impactor rolls in the opposite direction compared to the other versions. Due to these inconsistencies, V33 has therefore been excluded from this point onward.

Version	Tracked node ID	Max. intrusion [mm]	Plastic intrusion [mm]	Time of 1st impact [ms]	Time of 2nd impact [ms]
V30	100046	17	11.3	5	15.5
V31	100044	16	10	5	15
V32	100045	17.5	11.5	5	15
V33	100055	14.9	9	3	12

Table 3.1: Experimental DIC results for the Beschuss test, V30 to V33

Version	Pitch (initial) [°]	Pitch (updated) [°]	Roll [°]	Position X [mm]	Position Y [mm]
V30	$-\alpha - 4$	$-\alpha - 2.9$	-44.5	109	0
V31	$-\alpha - 1.6$	$-\alpha - 1.2$	-40.4	73	4
V32	$-\alpha - 3.8$	$-\alpha - 3.4$	-44.3	100	-3
V33	$-\alpha + 2.3$	$-\alpha + 2.2$	-48.7	65	2

Table 3.2: Experimental measurements of the impactor's position and rotations at t=0 for the Beschuss test, V30 to V33

Second Layup

The second layup is a 8-layer carbon-glass fiber laminate. The two outer plies (i.e., ply 1 and ply 8) are made of a very similar glass fibre material to the previous layup (hence the same material card will be used in simulations) and they each have a 0.2 mm thickness, while the 6 inner plies are made of carbon fibre from Toray (T300), with a 245 gsm grammage and twill weave, 200 tex both in warp and weft and a thickness per ply of 0.266 mm; this results in a total laminate thickness of 2 mm. Note that all plies are oriented at 0/90 degrees.

In this layup it is expected that the increased thickness and multiple plies orientations increase the influence of the delamination process in dissipating the impactor's kinetic energy, thus increasing the effects of the new modeling strategy on simulation results.

For this layup, only one test was performed with the aluminum backplate, hence a single set of results is available; the intrusion-related variables are reported in Table 3.3 (for the complete intrusion plots, see Chapter 5), while the variables detailing the impactor's position and rotations at t=0 (i.e., first contact with the plate) are reported in Table 3.4.

Version	Tracked node ID	Max. intrusion [mm]	Plastic intrusion [mm]	Time of 1st impact [ms]	Time of 2nd impact [ms]
V22	100037	13.9	9.2	5	17

Table 3.3: Experimental DIC results for the Beschuss test, V22

Version	Pitch (initial) [°]	Pitch (updated) [°]	Roll [°]	Position X [mm]	Position Y [mm]
V22	$-\alpha - 2.7$	$-\alpha - 2.5$	-39.1	73	2

Table 3.4: Experimental measurements of the impactor's position and rotations at t=0 for the Beschuss test, V22

3.1.3. Uncertainty Quantification of DIC Measurements

To check for the accuracy of the DIC measurements, the plastic intrusion (i.e. out-of-plane displacement w.r.t. the undeformed state) of the tracked node reported by the system is checked against the measurable residual plastic intrusion on the test plates.

This has been done by using the depth-measurement tool of a standard electronic caliper[4] and a reference plane representing the undeformed plate obtained by placing a thick straight t-shaped steel rod on the free edges of the plate (see Figure 3.5).

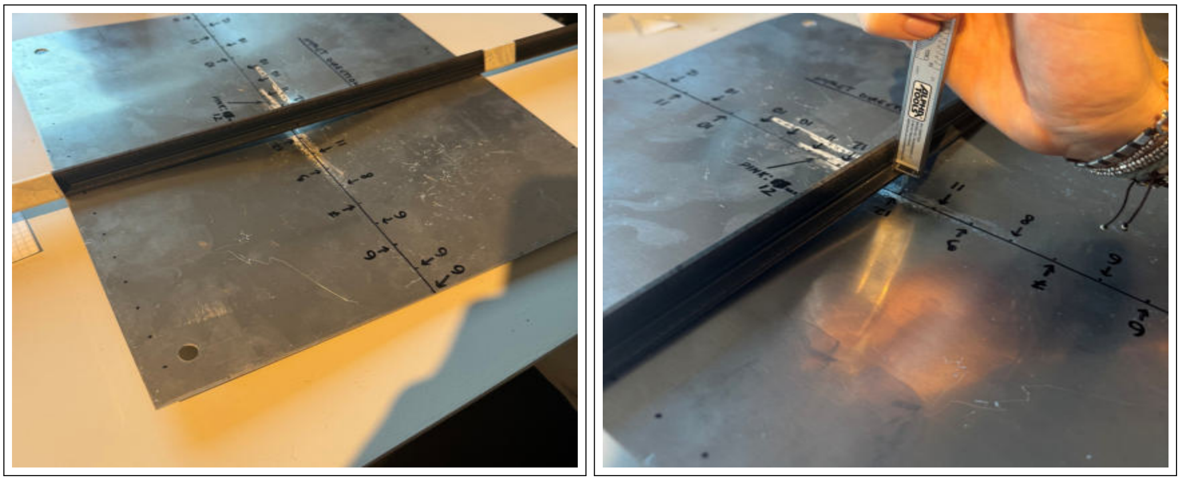

(a) Set-up **(b)** Measurement process

Figure 3.5: Experimental set-up for manual intrusion measurement

Confidence Intervals Determination

To increase accuracy, the measurement is repeated 4 times, and the average is taken; then, it would be beneficial to determine an interval of confidence for the value, so that if a discrepancy between it

[4] Sensitivity: 0.01 mm, Range: 0-150 mm

and the DIC-reported measurement falls within the interval, it can be ascribed to human measurement errors and not to issues with the DIC-system.

To do so, a standard process would be to compute the standard deviation and calculate the inverse normal cumulative distributions at the 10% and 90% probability levels, which are used to determine lower and upper bounds, but in this case the population (4 data points) is too small to obtain meaningful results.

Still, a solution has been devised while also obtaining valuable additional data: 19 equally spaced points are marked along the length-wise mid section of each plate, and 4 measurements are taken at each point, bringing the total population to 80 data-points and effectively mapping the plastic deformation of the entire plate mid-section. To apply the method previously described to this new population, each 4-measurement series has been normalized against its average to mitigate magnitude differences between the series, and the standard deviation of the whole normalized population is calculated.

Now, in addition to determining a confidence interval for the DIC-tracked point, by plotting the data-point coordinates on the x-axis and the intrusion on the y-axis, the mid-section plastic deformation profile for each plate can be obtained, and it will be used as one of the features to assess the numerical model performance (see Chapter 5).

V30 Measurements

The measurements for the V30 aluminum plate are presented in Table A.1 in Appendix A.1, while the normalized population used for the standard deviation calculation is reported for completeness in Table A.2 in Appendix A.1. The standard deviation of the normalized population is 0.012, the lower bound (P_{10}) factor is 0.984 and the upper bound (P_{90}) factor is 1.0155.

The DIC measurement of 11.3 mm (see Table 3.1) falls outside of the confidence range for the corresponding point on the plate, and differs from the measured intrusion by a factor of 1.27.

V31 Measurements

The measurements for the V31 aluminum plate are presented in Table A.3 in Appendix A.1, while the normalized population used for the standard deviation calculation is reported for completeness in Table A.4 in Appendix A.1. The standard deviation of the normalized population is 0.009, the lower bound (P_{10}) factor is 0.988 and the upper bound (P_{90}) factor is 1.012.

The DIC measurement of 10 mm (see Table 3.1) falls outside of the confidence range for the corresponding point on the plate, and differs from the measured intrusion by a factor of 1.26.

V32 Measurements

The measurements for the V32 aluminum plate are presented in Table A.5 in Appendix A.1, while the normalized population used for the standard deviation calculation is reported for completeness in Table A.6 in Appendix A.1. The standard deviation of the normalized population is 0.009, the lower bound (P_{10}) factor is 0.988 and the upper bound (P_{90}) factor is 1.012.

The DIC measurement of 11.5 mm (see Table 3.1) falls outside of the confidence range for the corresponding point on the plate, and differs from the measured intrusion by a factor of 1.24.

V22 Measurements

The measurements for the V22 aluminum plate are presented in Table A.7 in Appendix A.1, while the normalized population used for the standard deviation calculation is reported for completeness in Table A.8 in Appendix A.1. The standard deviation of the normalized population is 0.01, the lower bound (P_{10}) factor is 0.986 and the upper bound (P_{90}) factor is 1.014.

The DIC measurement of 9.2 mm (see Table 3.3) falls outside of the confidence range for the corresponding point on the plate, and differs from the measured intrusion by a factor of 1.39.

Proposed Explanations for the Intrusion Discrepancies

As the human error during the manual intrusion measurements has been excluded, two other possible explanations are provided.

The first is that the DIC system presented a systematic calibration error; this is supported by the fact that all DIC measurements of plates that were part of the same series (V30, V31, V32) and were therefore tested in the same day, differ from the manual measurements by very similar factors (1.27 for V30, 1.26 for V31, and 1.24 for V32). Unfortunately, direct verification of this hypothesis is impossible without repeating the tests, therefore the only possible solution is to scale the DIC intrusion plots by the aforementioned factors, and using them as upper experimental bounds, while the original measurements are used as lower experimental bounds, thus obtaining a band inside which the simulation results should fall to be considered good.

The second explanation is based on the plate deforming further when taken out of the measurement set-up. The DIC system measures intrusion while the aluminum plates are still clamped (see Figure 3.6a), but when the screws are loosened and the clamping force is removed, the plate could deform further, thus increasing the plastic intrusion (see Figure 3.6b). To check for this, a hole has been drilled in the plate at the DIC-tracked node position, and the plate has been "clamped" again by putting weights along its edges, making sure to reproduce the test set-up. The depth measurement tool of the electronic caliper[5] has then been put through the hole to measure intrusion in this clamped configuration, and a reduction in intrusion by around 2 mm has been registered, partially explaining the discrepancy, although to get a definitive answer, the intrusion measurements should be repeated while the plates are mounted on the real test set-up.

As the procedure just described is not so accurate that the first explanation can be totally ruled out, the "experimental bands" are still used as reference in Chapter (5), although numerical model results that more closely match the lower bound of the band (i.e. the original DIC-measured curve) are considered favourably.

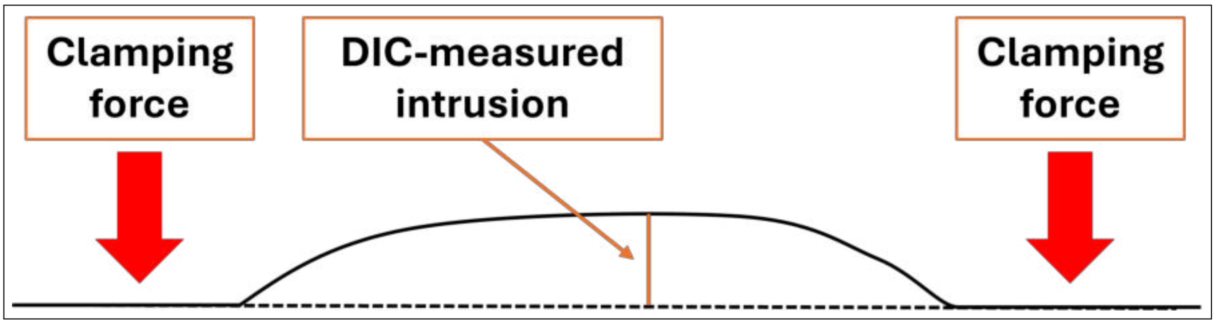

(a) Aluminum plate post-impact, still clamped to the test set-up

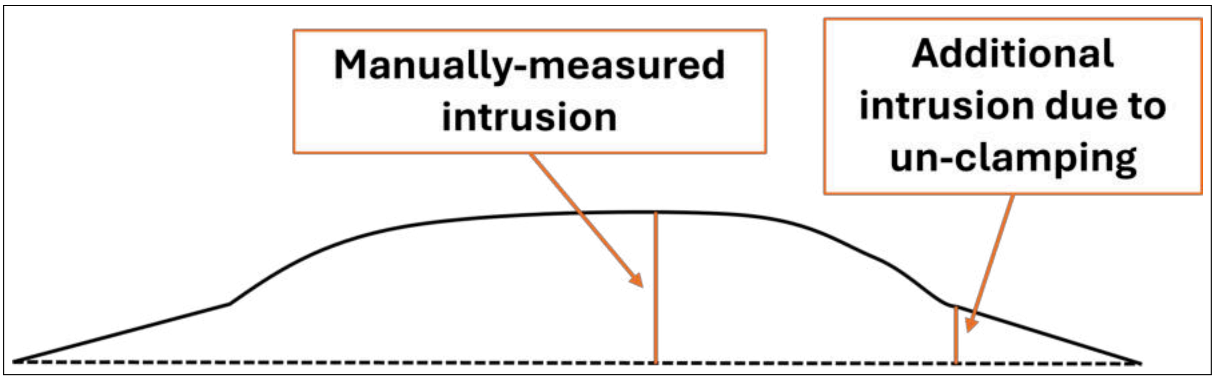

(b) Aluminum plate post-impact, after clamping force is removed

Figure 3.6: Possible explanation for the discrepancy between DIC and manual measurements on plastic intrusion

[5]Sensitivity: 0.01 mm, Range: 0-150 mm

3.2. C-Scans

The scans, performed at the DASML of the Delft University of Technology, serve the purpose of non-destructively mapping the internal damage induced by the impact events, specifically focusing on the extent of interlaminar delaminations.

However, as C-scans provide a planar projection of the damage, these results are subsequently validated and complemented by destructive optical microscopy (see Section 3.4).

3.2.1. Set-Up and Test Description

The setup, shown in Figure 3.7 is composed of the following parts: 1) a tank of water where the samples are immersed to provide a proper couplant for the ultrasonic waves; 2) adjustable fixtures to suspend the plates in the medium; 3) two probes, arranged in a through-transmission configuration; 4) a 2-axis rail system to automatically move the probes over the whole sample surface; 5) a data acquisition and processing system, to acquire the A-scans and subsequently turn them into a 2-d representation (i.e. the C-scan).

As per the test settings, the probe resolution has been set to 0.5 mm, in both Y and X direction to preserve the image aspect ratio. A 1s delay has been set after moving in x direction to wait for perturbation in water to dampen out. The scan speed in y direction has been set to 100 mm/s, as it has been deemed to be a good compromise between accuracy and reasonable scan times. Before each scan, a pre-scan is performed to ensure proper calibration.

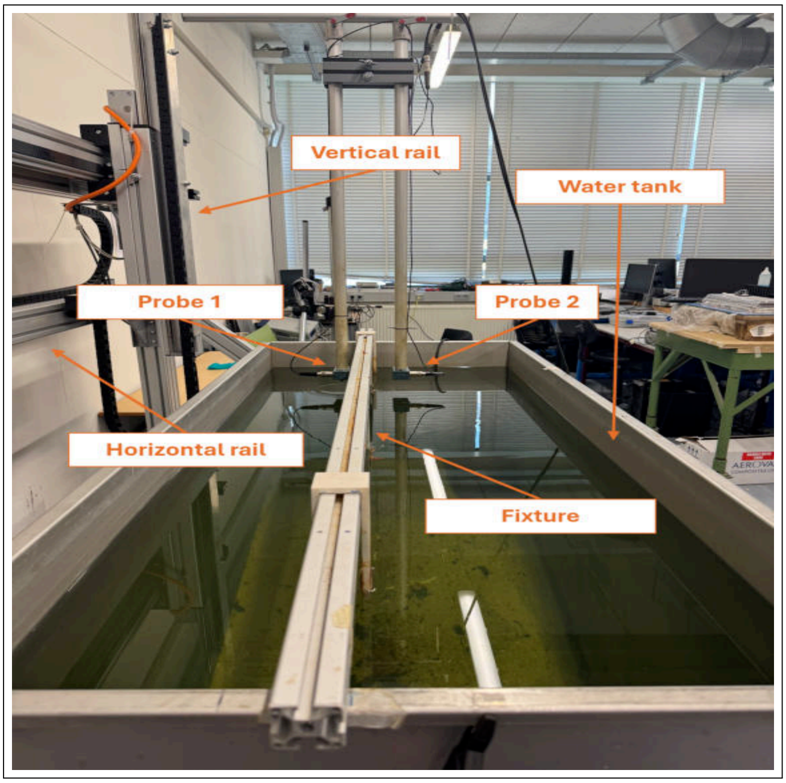

(a) Side view

Continued on next page...

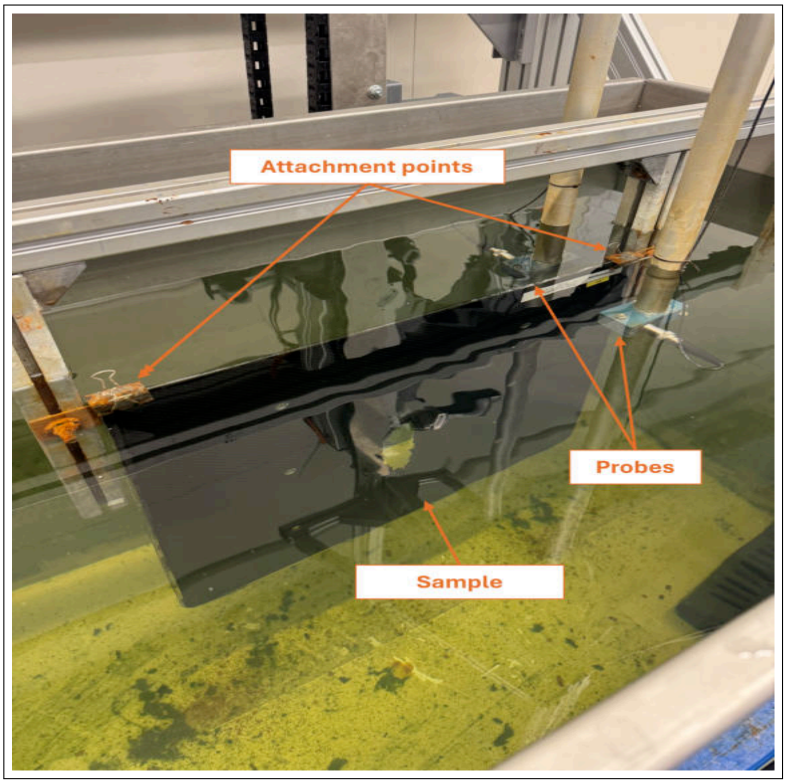

(b) Front view

Figure 3.7: Test setup for c-scans acquisition

3.2.2. Results

The C-Scan results for the test plates chosen in Section 3.1.2 are reported in Figure 3.8: black areas can indicate delaminations, clamping points (L-shaped), issues with the plate manufacturing (e.g. variable volume fraction and voids), or issues with c-scan testing due to the specimens' intrinsic properties (e.g. acoustic impedance), while light blue areas (such as the one in Figure 3.8a) indicate complete plate failure or bolt holes, as the signal passes trough with no interference.

While the V22 scan presents a clear distinction between total failure, delamination and pristine condition, the same cannot be said for the other 3 plates, which all show black areas all-over the scans; even after consultation with the laboratory personnel and re-calibration, improvements on the scan quality couldn't be obtained. This is probably due to the fact that V22 is mostly composed of carbon fibre plies, while the other plates are entirely made of glass fibre, which generally presents higher wave attenuation due to bigger fibre diameter and higher acoustic mismatch with the surrounding resin. Furthermore, the twill weave of V22 gives a much flatter surface than the plain weave used in the other versions, thus resulting in less scatter.

The different colors in the top and bottom parts of V30 (see Figure 3.8b) may also suggest manufacturing issues, such as variable volume fraction due to resin pooling, which will be addressed in Section 3.3.

As per V32, it features an additional plastic film layer 0.3 mm thick, which doesn't have significant structural properties and is therefore disregarded in the simulations-related portion of the project, but that could have had an influence in wave propagation due to possible air gaps between the film and the glass fibre ply it adheres to.

Whatever the reason for the sub-optimal scans may be, all 4 pictures allow to unequivocally identify the delamination/damage areas caused by the impact, which have a precise contour and a characteristic shape. Nevertheless, to improve visualization and comparison with simulation results, the scans have been re-elaborated and are presented in Figure 3.9, along with measurements of the major and minor axes of the delaminated areas.

As mentioned, in all tests the impactor hits the plate twice, first with its ”head” and then with its ”tail”; due to tilts and rotations, the two impacts don’t happen along the same axis, resulting in two distinct delamination ”traces” which are clearly visible in the scans. As this will be important when analyzing simulation results, the tail-induced delaminations are ”dashed” in Figure 3.9 for ease of identification.

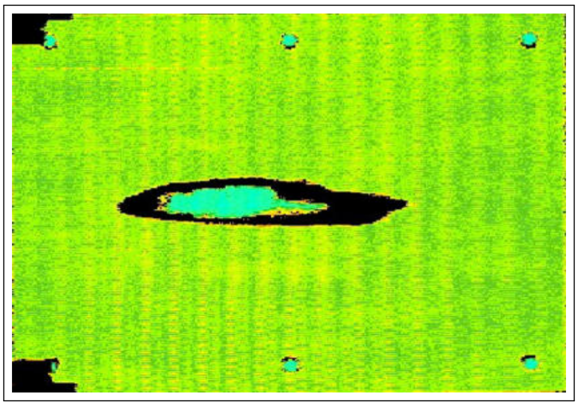

(a) V22

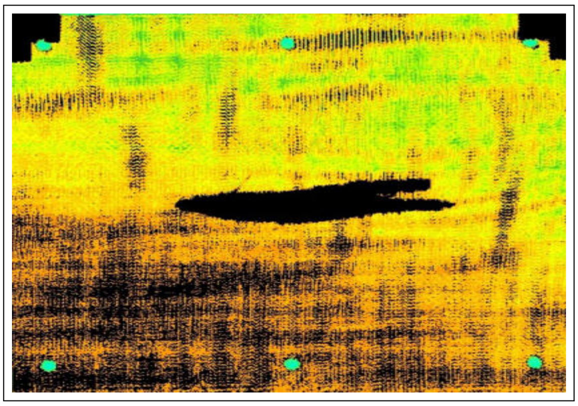

(b) V30

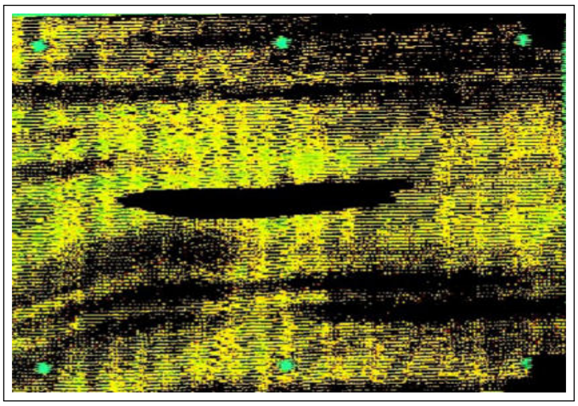

(c) V31

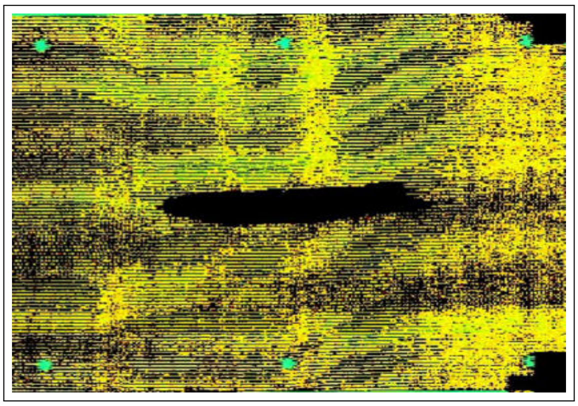

(d) V32

Figure 3.8: C-scan results of the test-plates selected for the project

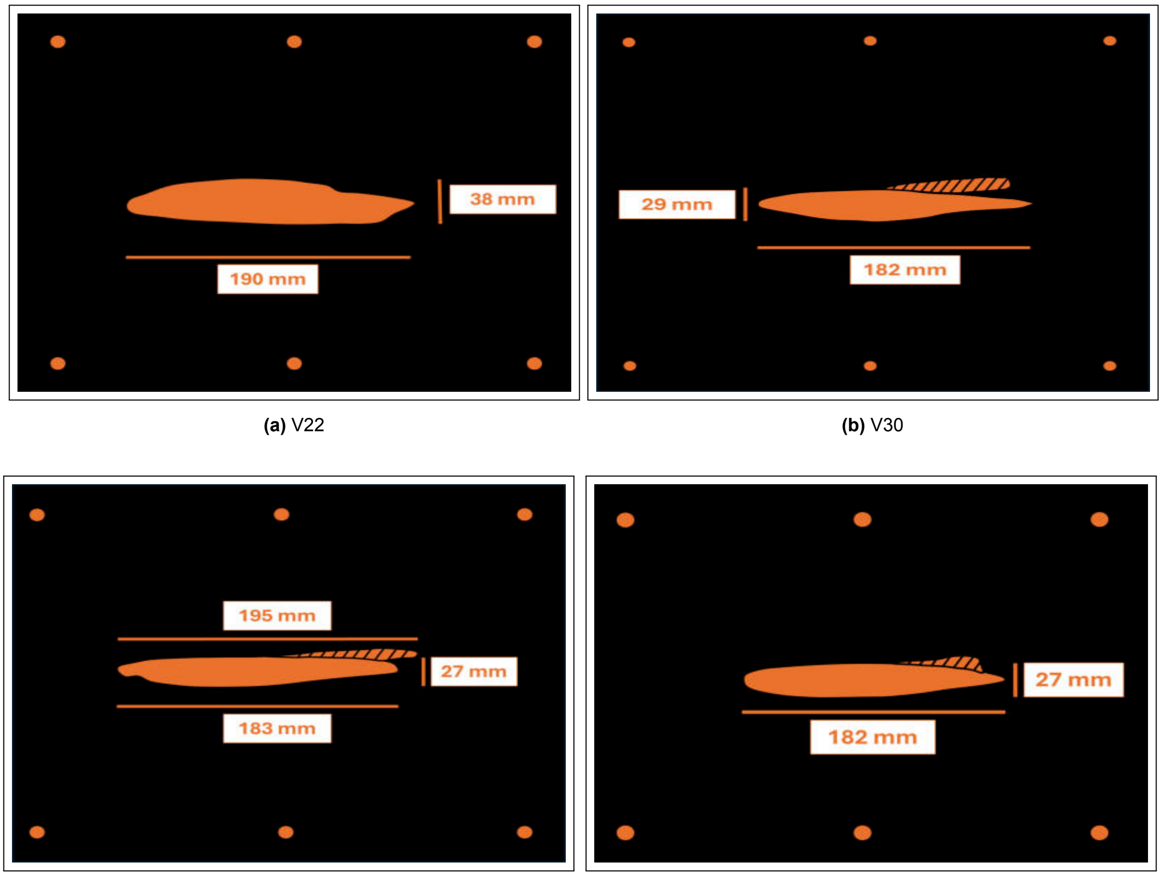

(a) V22 **(b)** V30

(c) V31 **(d)** V32

Figure 3.9: C-scan results of the test-plates selected for the project, re-elaboration. The dashed areas are delamination caused by tail impacts.

3.3. Fibre Volume Determination

In an effort to explain the poor results of the c-scans related to glass-fibre only plates, an investigation on fibre volume content is conducted. As the laminate consists of a constant number of woven layers, any deviation in the local thickness of the plates is directly attributable to fluctuations in resin content; therefore, instead of destructive characterization techniques (e.g. matrix digestion or burn off tests), thickness measurements have been used to check for resin pooling and variable fibre fraction, which have been mentioned as possible causes for signal absorption and scatter.

Each plate has been divided in 35 cells (see Figure 3.10), and thickness has been measured[6] at the center point of each one, which has been deemed to be representative of the cell it refers to. This discretization and measurement process resulted in the ”heatmap” representations in Figure 3.11. In each cell, the measured thickness is reported, and a color-coding system is adopted to assess the closeness of it to the nominal plate thickness. If the thickness falls within $\pm 8\%$ ($\approx$ half a ply) of the nominal thickness, the thickness is considered within reasonable limits (GREEN); if it falls within $\pm 16\%$ ($\approx$ one ply) of the nominal thickness, the discrepancy is considerable (YELLOW), and above/below $\pm 16\%$ the error is considered a critical defect (RED). The cells where fibre failure made measurements impossible (see Figure 3.10) are blacked out.

[6] A long-arm u-shaped caliper with 0.01 mm sensitivity and 0-25 mm range has been used to perform the measurements.

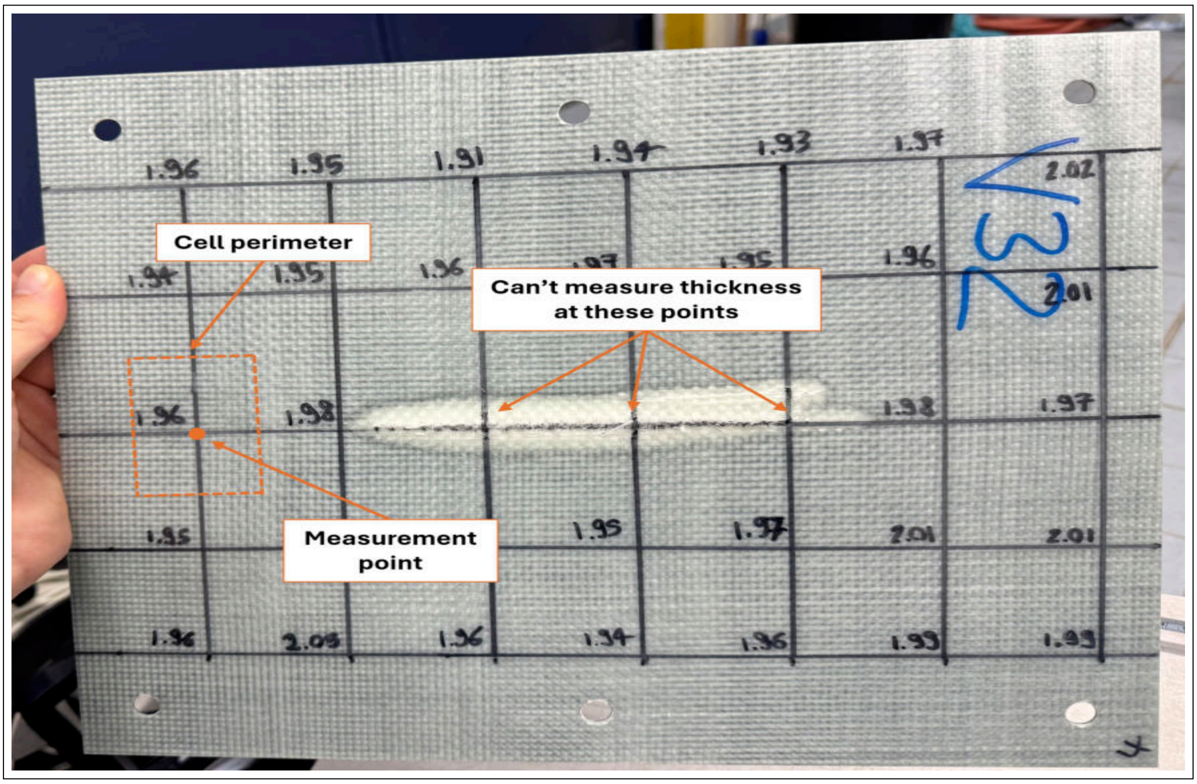

Figure 3.10: Plate discretization process for thickness measurements

Note that in V32, 0.3 mm have been subtracted from each measurement to account for the aforementioned plastic film layer.

By comparing each "heatmap" with the corresponding c-scan, it can be shown that most of the problematic features in the scans can be ascribed to thickness variations. In V30 (see Figure 3.11a), the whole bottom half of the heatmap is marked in red, while the top half is green; this corresponds well to the c-scan, where top and bottom halves have distinctly separate colors. In V31 (see Figure 3.11b), the top-center, top-right and bottom-right areas of the heatmap are yellow or red, and this coherently shows up in the c-scan, where those areas are blacked-out. In V32 (see Figure 3.11c), most of the heatmap is green, and this is reflected in the c-scan, which compared to the other 2, shows the least amount of issues, which could be ascribed to the plastic film layer (which is only present in V32, reinforcing the hypothesis) rather than to variable ply thickness.

1.71	1.66	1.64	1.68	1.68	1.65	1.62
1.82	1.77	1.74	1.7	1.68	1.67	1.64
2.09	2.05				1.79	1.7
2.53	2.44	2.4	2.31	2.19	2.07	1.93
2.84	2.76	2.64	2.54	2.44	2.38	2.06

(a) V30

Continued on next page...

1.89	1.91	1.96	1.99	2.04	2.06	2.08
1.79	1.83	1.85	1.88	1.91	1.95	1.96
1.73				1.88	1.89	1.86
1.75	1.79	1.79	1.81	1.86	1.88	1.9
1.8	1.78	1.8	1.84	1.88	1.9	1.94

(b) V31

1.66	1.65	1.61	1.64	1.63	1.67	1.72
1.64	1.65	1.66	1.67	1.65	1.66	1.71
1.66	1.68				1.68	1.67
1.65	1.73	1.65	1.65	1.67	1.71	1.71
1.66	1.75	1.66	1.64	1.66	1.69	1.69

(c) V32

Figure 3.11: Thickness measurements for V30, V31, V32 composite plates, in mm

3.4. Microscopy Examination of Impact Sites

While C-scans provide a comprehensive macroscopic overview of the damage pattern, the technique is inherently limited by its planar projection, offering little insight into the through-thickness distribution of the failure. Crucially, C-scan data alone cannot definitively distinguish between delamination and superficial damage, such as major indentations or matrix cracking, which may produce similar signal attenuation.

Therefore, optical microscopy was employed to perform a destructive cross-sectional analysis. This complementary approach serves two purposes: first, to validate that the signal loss observed in the C-scans corresponds to actual physical delaminations rather than surface artifacts; and second, to verify the extent of the damage along the y-axis (see Figure 3.4), providing a 'ground truth' for the NDT measurements.

3.4.1. Samples Preparation

To prepare the sample, the Composite plate saw "COMPCUT ACS 600" (see Figure 3.12a) from the DASML of the Delft University of Technology has been used. First, a longitudinal strip was extracted from each plate by cutting parallel to the long sides, 3 mm above and 3 mm below the geometric centerline, resulting in a 6 mm wide strip, which was then cut along the centerline to divide the damage area in 2 symmetric[7] parts, and finally segmented transversely: the first cut was performed right before the first marks of visible damage, while additional samples were obtained from the remaining strip at varying coordinates, until the last visible damage marks (see Figure 3.12b). This approach resulted in a variable number of microscopy specimens per plate, depending on the damage length and shape (see Figure 3.12c).

[7] The damage area is assumed symmetric to halve the number of analyzed samples.

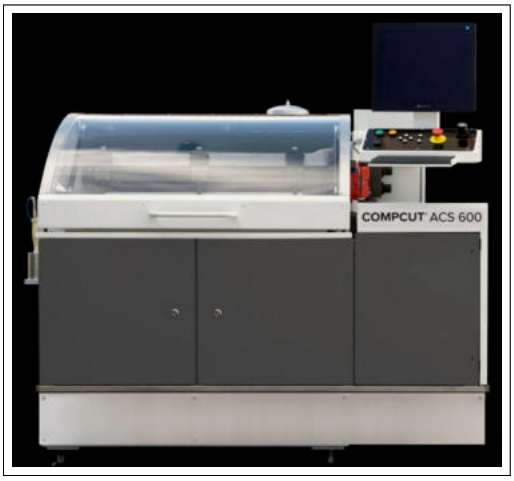

(a) Composite plate saw "COMPCUT ASC 600"

(b) Composite plate being cut, V22

(c) Composite plate after cutting, V22

Figure 3.12: Overview of the composite cutting process

The specimens were initially examined without potting to allow for the accurate measurement of the 'open' delamination width without the interference of a filling medium. To ensure stability and optical alignment, the samples were mounted on a deformable clay substrate and leveled via manual pressure to approximate a planar surface (see Figure 3.13).

(a) Leveling process

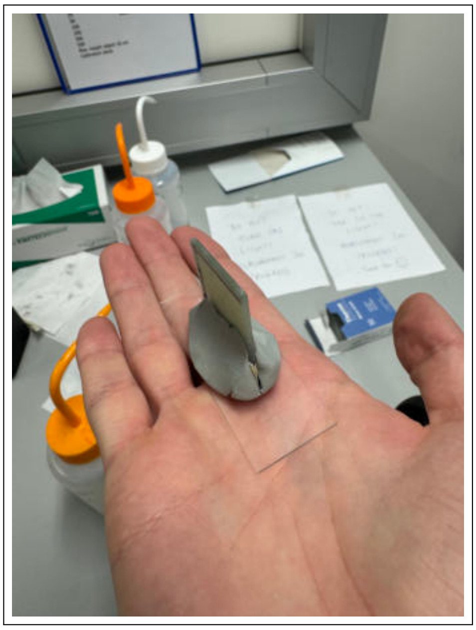

(b) Final sample (no potting)

Figure 3.13: Dry mounting of the samples

Following the initial measurements, the samples were encapsulated in a bi-component epoxy resin[8] (see Figure 3.14b) to provide structural support and edge retention. The mounts were then subjected to a standard grinding and polishing sequence[9] via the polishing machine "Struers Tegramin-20" (see Figure 3.14a) from the DASML to achieve a suitable surface finish for microscopy measurements (see Figure 3.14c). This second pass allowed for the validation of the initial measurements and a more detailed analysis of the failure morphology.

(a) Polishing machine "Struers Tegramin-20"

Continued on next page...

[8] Technovit 4071 bi-component (powder + liquid), cured at room temperature for 15 minutes

[9] Using 6 different SiC papers ranging from P180 to P4000; 150 rpm for the samples, 300 rpm for the polishing plate and water lubrication

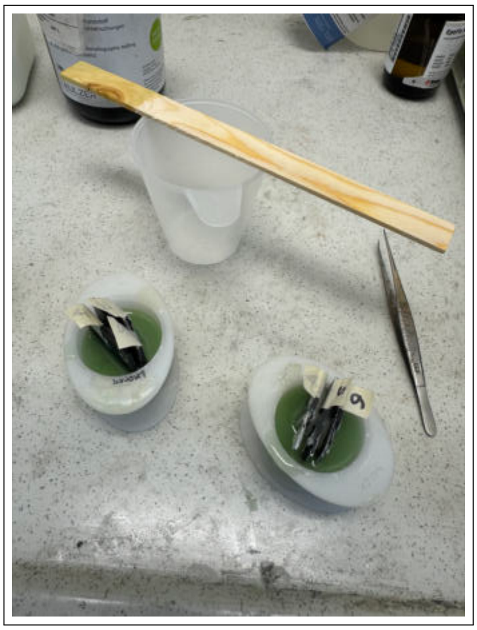

(b) Curing process

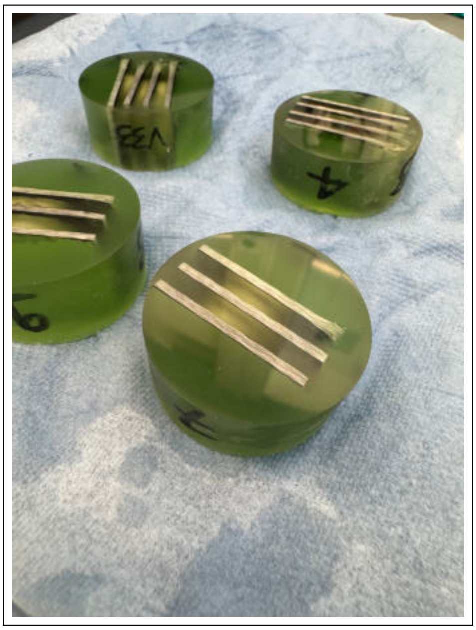

(c) Final sample (potting)

Figure 3.14: Potting of the samples

3.4.2. Microscopy Measurements

Images were acquired using the stitching microscope ”Keyence VR 5000” (see Figure 3.15a) from the DASML. Given the extensive lateral propagation of the damage relative to the field of view at 40x magnification, a raster-scanning approach was adopted. The microscope’s motorized stage and software automatically captured and stitched together adjacent tiles, generating a seamless composite image of the entire specimen cross-section (see Figure 3.15b). This technique ensured that both the macroscopic extent of the damage and the microscopic failure mechanisms were captured in a single dataset.

(a) Microscopy ”Keyence VR 5000”

Continued on next page...

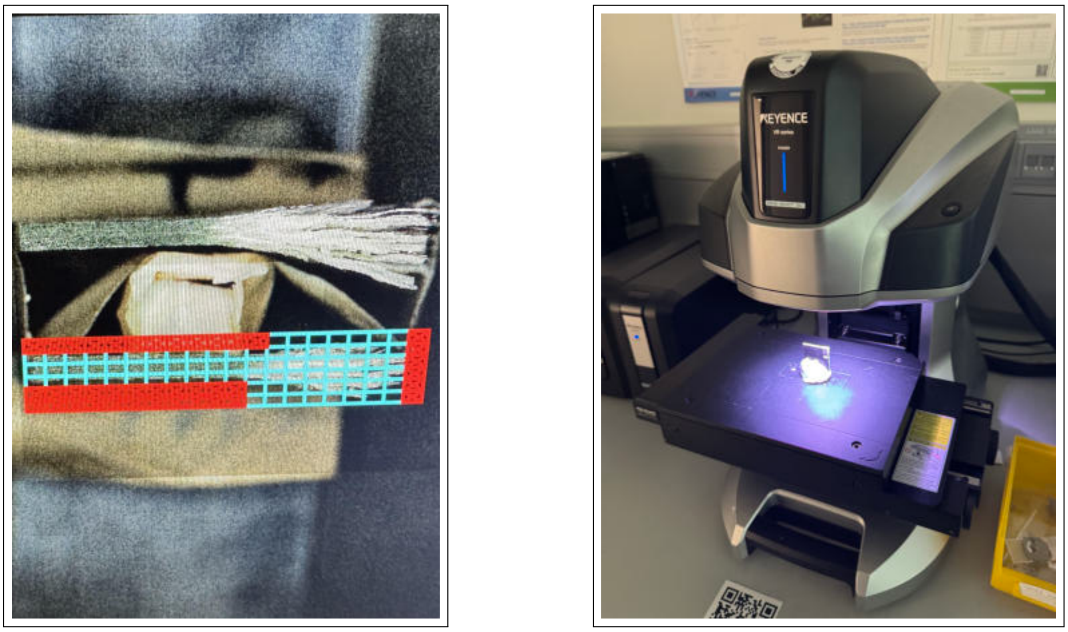

(b) Discretization of the scanning area

(c) Scanning process

Figure 3.15: Potting of the samples

3.4.3. Comparison with C-Scans

First, on each C-scan vertical lines are drawn in correspondence of the performed cuts, then delamination width is measured from the centerline on the half of the plate from where the samples examined with microscopy were taken (see Figure 3.16a).

Finally, the C-scan-derived delamination length is reported directly on the microscopy scans (green segment in Figure 3.16b), and a qualitative verification is performed, checking that delamination/damage (whiter in Figure 3.16b) extends over a length coherent with the c-scan measurement.

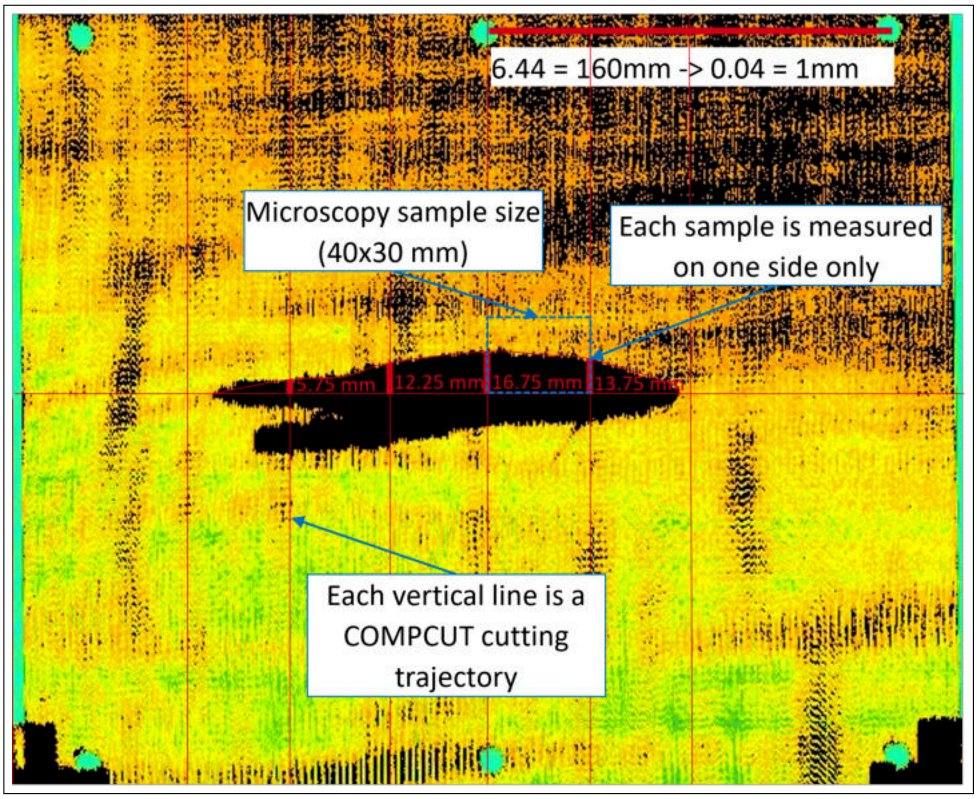

(a) Delamination width measurement at every cutting positions

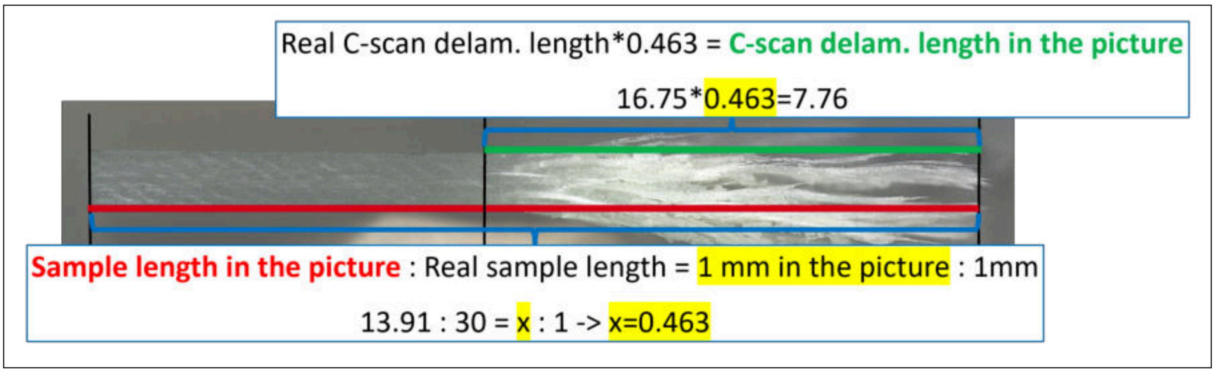

(b) Superimposition of delamination width measurement from C-scan on microscopy result

Figure 3.16: Procedure to compare C-scans with microscopy results

For brevity, only the comparison between C-scans and micrographs for V30 are included in this chapter (see Figure 3.17), as they are the most representative of the process.

The results for the remaining panels, which are similar to V30, can be found in Appendix A.2.

From the results presented, it can be seen that delaminations develop in all plies through-the-thickness, and that the lengths of the longest ones[10] are in very good agreement with the corresponding C-scan results.

[10]Longest delamination from micrography is considered, as in C-scans the shorter delaminations go undetected, being hid by the longer ones.

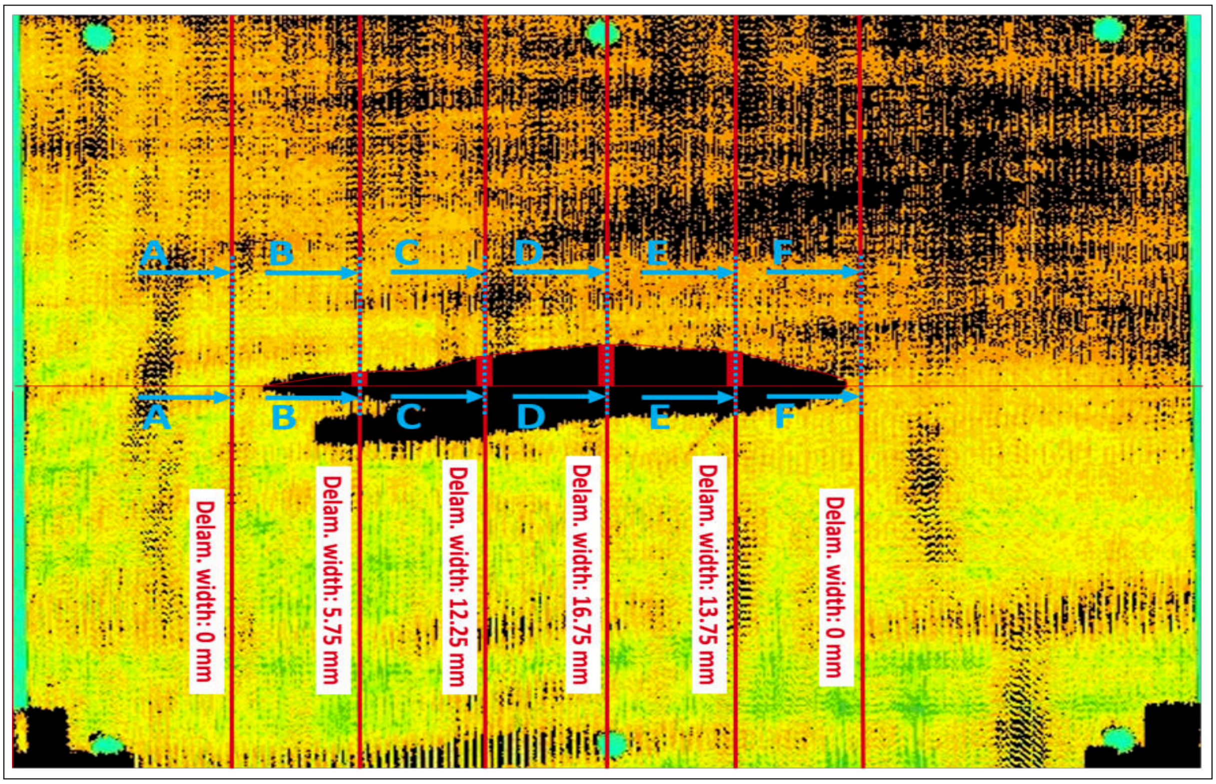

(a) Delamination width measurement at every cutting positions, V30

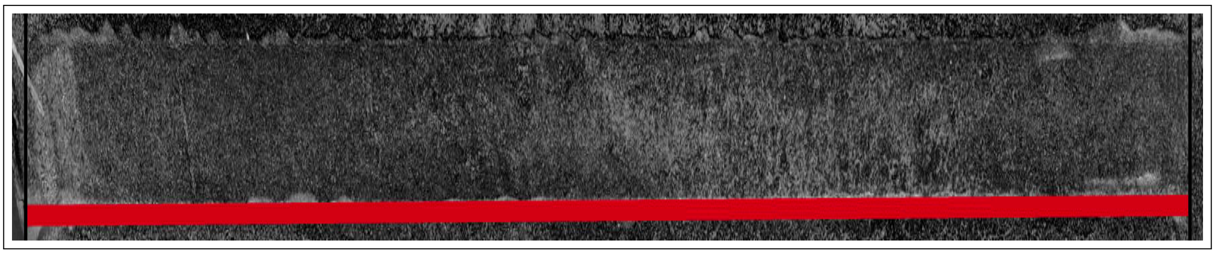

(b) Section A-A, V30

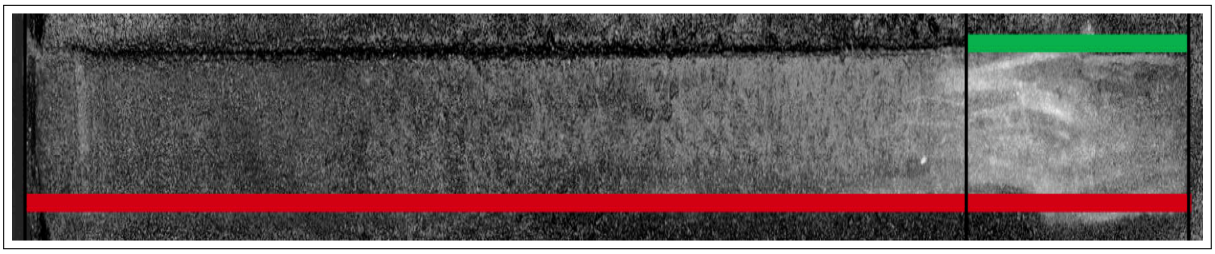

(c) Section B-B, V30

Continued on next page...

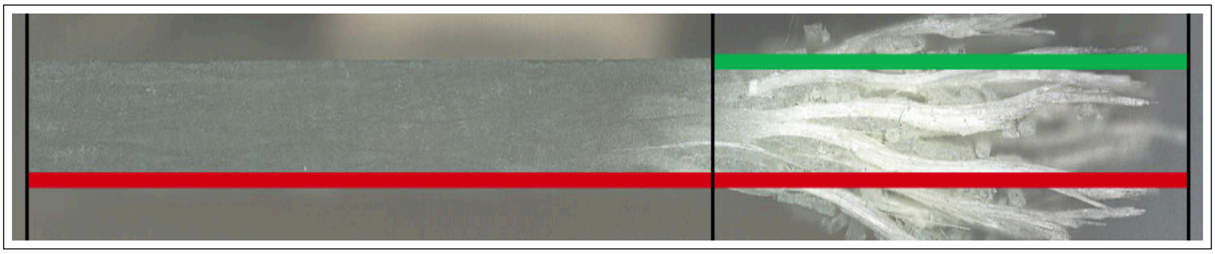

(d) Section C-C, V30

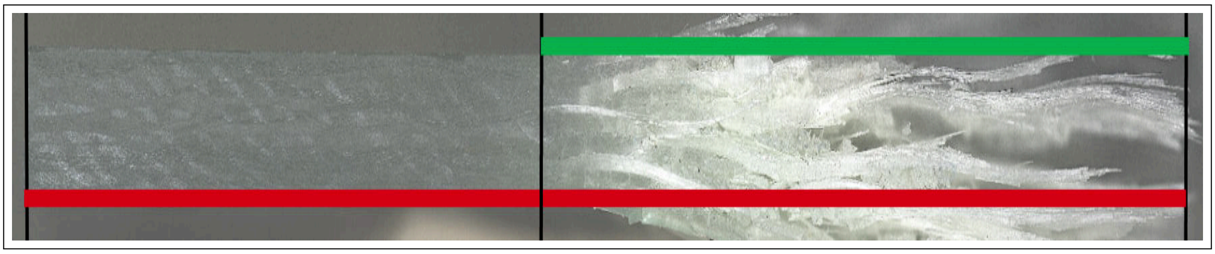

(e) Section D-D, V30

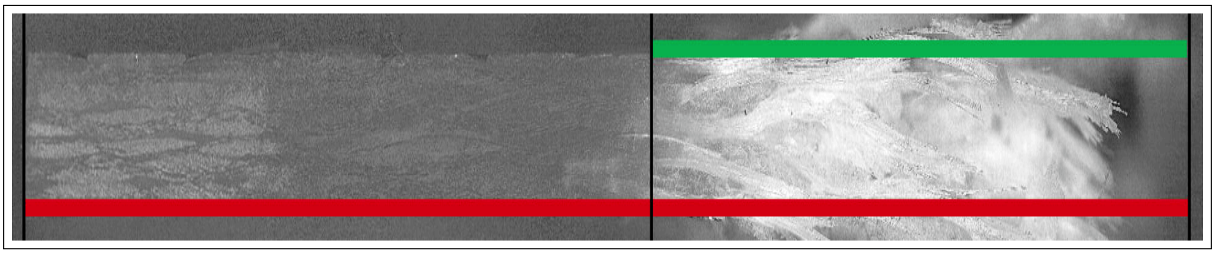

(f) Section E-E, V30

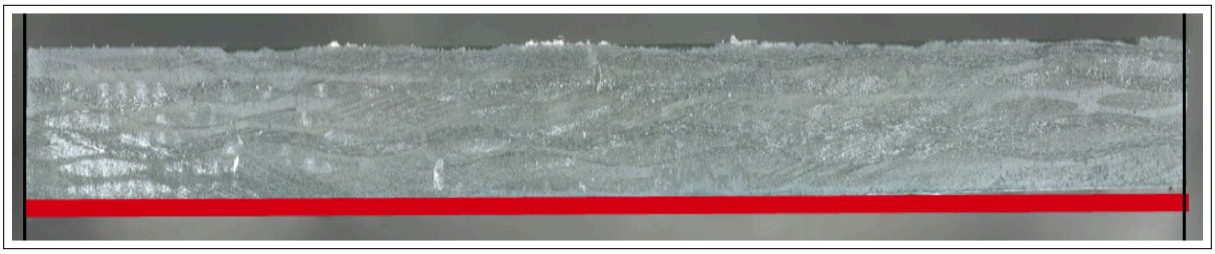

(g) Section F-F, V30

Figure 3.17: Microscopy results with C-scan measurement overlay, V30

3.5. New Aluminum Characterization

As the material card provided by the company for simulating the aluminum plates didn't exactly match the specifications of the actual test plates, a characterization campaign has been performed.

4 samples have been cut from an unused test plate, and a tensile test has been performed, resulting in the engineering strain /engineering stress curve in Figure 3.18a.

From that, a conversion to true values has been performed, using the well known equations:

$$\epsilon_{true} = ln(1 + \epsilon_{eng}) \tag{3.1}$$

$$\sigma_{true} = \sigma_{eng}(1 + \epsilon_{eng}) \tag{3.2}$$

And finally the true strain is converted to true plastic strain with:

$$\epsilon_{pl} = \epsilon_{true} - \frac{\sigma_{true}}{E} \tag{3.3}$$

Plotting the new parameters, the curve in Figure 3.18b is obtained. As the data stops at necking, an extrapolation method needs to be selected and applied, with the choice being the Swift-Voce fitting:

$$\sigma = \alpha\sigma_{swift} + (1 - \alpha)\sigma_{voce} \tag{3.4}$$

which is a weighted average (with $0 \leq \alpha \leq 1$) between the Swift and Voce hardening models.

The true stress in the Swift model is derived from the original paper from H. W. Swift [33]:

$$\sigma_{swift} = A(\epsilon_0 + \epsilon_{pl})^n \tag{3.5}$$

where A is the rate of hardening, ϵ_0 is the initial strain state in the material, and n is the decrement of the rate of hardening.

The true stress in the Voce model is derived from the original paper from E. Voce [34]:

$$\sigma_{voce} = K_0 + Q[1 - e^{-B\epsilon_{pl}}] \tag{3.6}$$

where K_0 is the yield stress, $Q = K_\infty - K_0$ (with K_∞ the saturation stress) is the total stress capacity, and $B = 1/k$ (with k rate of hardening) is a measure of the rate of hardening.

After determining the proper coefficients, the extrapolated curve is used to define a new material card, named ALU_2 (see Section 4.1.5).

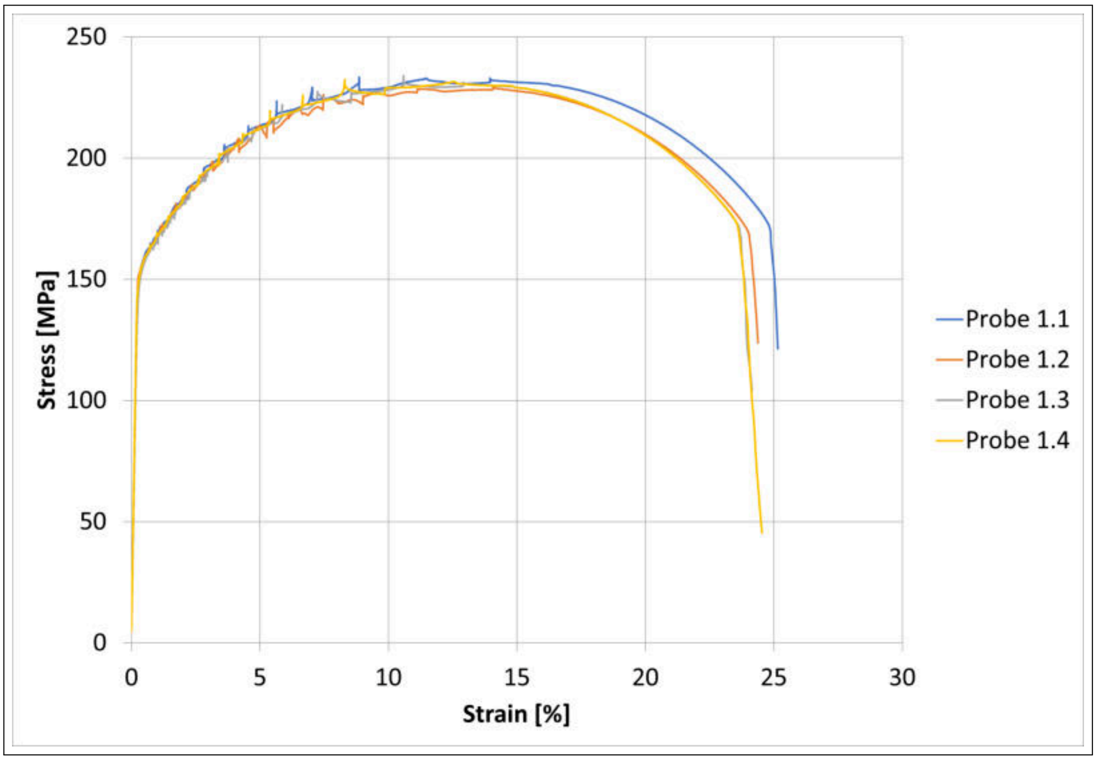

(a) Engineering curve

Continued on next page...

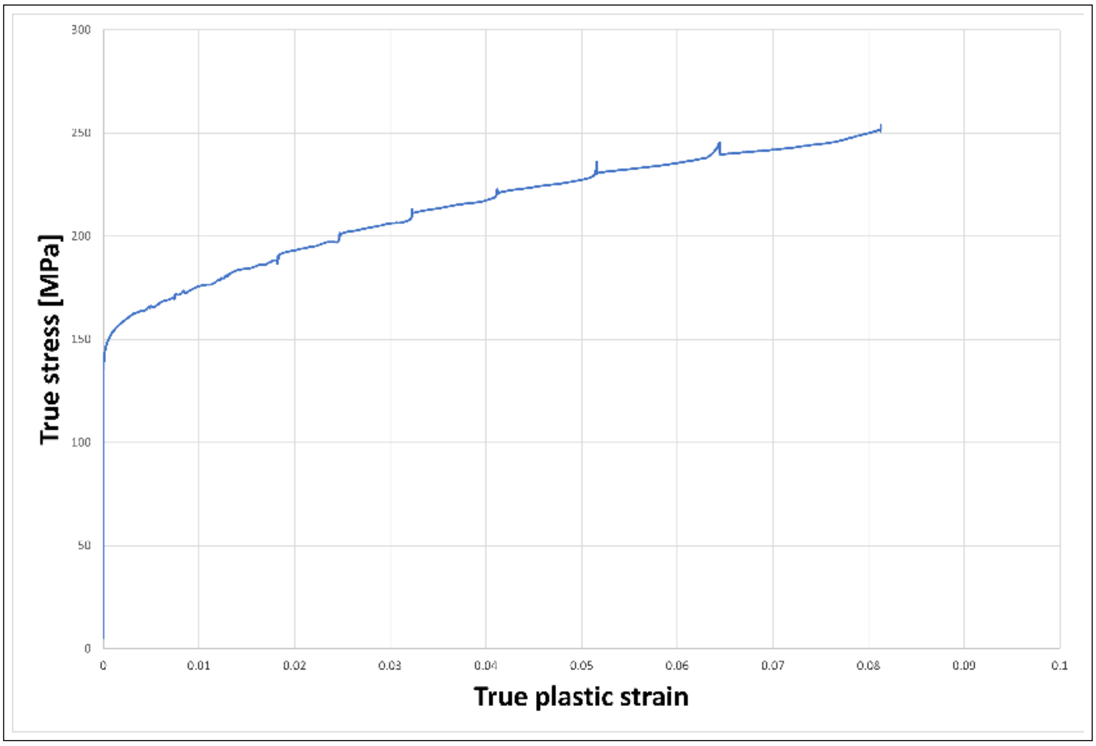

(b) True curve

Figure 3.18: Engineering and True curves for the newly characterized aluminum

4
Numerical Analysis

This chapter details the development and iterative refinement of the numerical framework used to simulate the Beschuss load-case with LS-DYNA. The simulation results for each iteration are presented in Chapter 5.

Initially, the pool of material cards used in building the models is detailed. Then, the Baseline model provided by the company is presented (see Section 4.2.2), and a simulation workflow to prepare it for comparison with the newly developed model is devised.

As the results of this first simulative block suggests the possibility to use two different material cards and mesh sizes (GLASS_2 with 2 mm mesh and GLASS_1 with 5 mm mesh) for the composite plate (see Section 5.1.13), separate workflows are proposed for each one. To streamline the execution phase, the GLASS_2 workflow is presented and simulated first, and based on the results and conclusions drawn from it (see Section 5.2.1), the GLASS_1 workflow is devised to improve on the criticalities previously encountered.

To enhance readability, all the tables detailing the input and include files settings, referenced throughout the chapter, are collected in Appendix B. To facilitate the reproducibility of the numerical results, the full source code for an example test case, comprising the main input decks (.i1) and the specific component definitions contained within the include files (.k), is reported in Appendix E.

4.1. Materials Pool

Inside the company, materials are identified through custom material IDs; **as constantly referencing IDs could be confusing, each material will hereinafter referred to with a descriptive label**; the ID/label association is presented in Table 4.1 for future reference.

Name	**ID**	**Label**
Glass fibre (calibration 1)	2781000	GLASS_1
Glass fibre (calibration 2)	1000	GLASS_2
Carbon fibre	103090	CARBON
Baseline aluminum	8310070	ALU_1
Custom aluminum	8310071	ALU_2
Custom aluminum (strain-rate)	8310075	ALU_3
Steel alloy	8930010	STEEL
Rigid material	-	RIGID

Table 4.1: Material/ID/label associations

In the following, each ID is detailed further. It should be pointed out that unless specified otherwise with the [custom][1] keyword, all the material properties described were previously determined at the company.

4.1.1. GLASS_1: Glass Fibre, Calibration 1

This card models a glass fibre woven ply, manufactured with the following combination of fabric and resin:

- **Fabric:** ”Owens Corning” TYP WR0440/150L02/250 (GOS), 440 g/m^2, woven glass fibre
- **Matrix:** ”Huntsman” Warm Curing Epoxy System Araldite LY3031 / Aradur 3032

The manufactured laminate reached a volume fraction of 59%.

The laminate has been characterized and a **ply-level** material card has been developed and calibrated, using ”MAT LAMINATED COMPOSITE FABRIC” (MAT_58) as explained in Section 2.5.2.

The card is confidential and a readable version cannot be reported, except for the parametersin Table 4.2.

ρ
1.96E-6

E_A	E_B	E_C **(not used)**
23	23	7.4

Table 4.2: Material parameters for GLASS_1

4.1.2. GLASS_2: Glass Fibre, Calibration 2

A second version of the GLASS_1 material has been developed, following a different calibration process. The card is encrypted and a readable version cannot be reported, except for the parameters in Table 4.3.

ρ
1.88E-6

E_A	E_B	E_C **(not used)**
23	23	7.4

Table 4.3: Material parameters for GLASS_2

4.1.3. CARBON: Carbon Fibre

As for the previous material, the card is encrypted and a readable version cannot be reported, except for the parameters in Table 4.4.

ρ
1.47E-6

E_A	E_B	E_C **(not used)**
56	56	-

Table 4.4: Material parameters for CARBON

4.1.4. ALU_1: Baseline Aluminum

This card models an aluminum with the following denomination: **EN 485** [= holding certification 485], **AlMg 3.5** [= Aluminum + 3.5% Magnesium], **EN AW-5154** [= Aluminum wrought (i.e. rolled/extruded), series 5000 (alloy number)], **H111** [= partially annealed and strain hardened (temper)]. ”MAT PIECE-WISE LINEAR PLASTICITY” (MAT_24) is chosen for the modeling, resulting in the material card in Table 4.5.

As the chosen material model allows for plasticity, a true plastic strain / true stress curve must be defined, and is presented in Figure 4.1. Note that even though the material model allows for strain-rate effects, this card doesn't implement them, hence a single curve is provided.

[1]As the work progressed, it was found that some of the material cards had to be changed to better reflect material behavior; these changes will be explained in more detail later.

ρ	E	ν
2.67E-6	70.5	0.33

Table 4.5: Material parameters for ALU_1

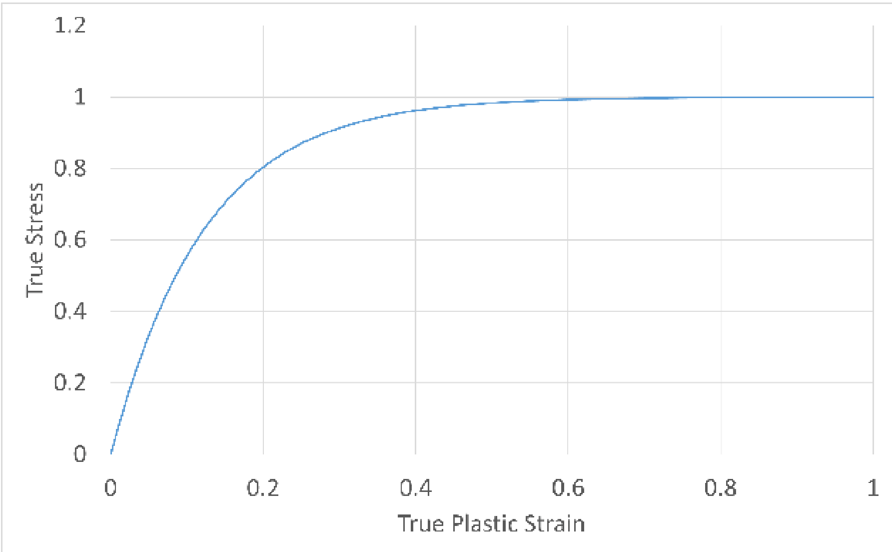

Figure 4.1: True Plastic Strain / True Stress curve for ALU_1

At the beginning of the project, this was the closest available material card to the aluminum used in the experimental tests, and the materials presented next were characterized at a later stage for additional investigations (see Section 4.3.9).

4.1.5. ALU_2 [Custom]: New Aluminum

Through test documentation, it has been determined that the aluminum used in the experimental campaign has the following denomination: **AlMg3** [= Aluminum + 3% Magnesium], **EN AW-5754** [= Aluminum wrought (i.e. rolled/extruded), series 5000 (alloy number)], **G22** [= Hardened by cold rolling, same meaning as H22].

This material has a higher strength than ALU_1, mostly due to the different hardening process it undergoes; hence, using it in the simulations would produce more accurate results, and could be one of the reasons for the overestimated intrusions, as suggested in Section 4.3.9. A material card wasn't available in the company's database, therefore by cutting various samples out of unused test plates, a characterization campaign has been set-up and performed (for a detailed explanation, see 3.5), resulting in the material card in Table 4.6, which retains a MAT_24 formulation, and true plastic strain / true stress curve in Figure 4.2.

ρ	E	ν
2.67E-6	70.5	0.33

Table 4.6: Material parameters for ALU_2

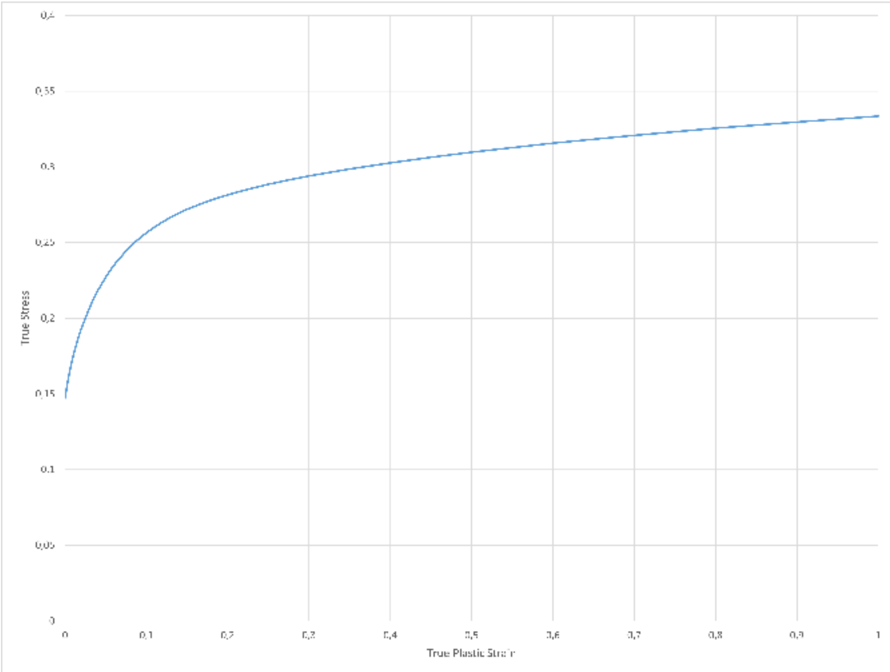

Figure 4.2: True Plastic Strain / True Stress curve for ALU_2

4.1.6. ALU_3 [Custom]: Strain Rate Dependent New Aluminum

This material card builds on top of ALU_2 by adding strain rate dependencies via a Cowper-Symonds formulation, which as mentioned can be implemented in MAT_24. Hence, stress is defined as [21]:

$$\sigma_y(\epsilon^p_{eff}, \dot{\epsilon}^p_{eff}) = \sigma_y(\epsilon^p_{eff}) \left[1 + \left(\frac{\dot{\epsilon}^p_{eff}}{C} \right)^{\frac{1}{p}} \right] \tag{4.1}$$

where C and p are determined through calibration and $\sigma_y(\epsilon^p_{eff})$ is given by the curve in Figure 4.2.

As this model is used as a proof of concept at a late stage of the project, the Cowper-Symonds constants are determined through a quick calibration process on a single set of experimental data.

4.1.7. STEEL: Steel Alloy

This material card is the company standard for steel bolts. It is again based on MAT_24, with the card in Table 4.7.

ρ	E	ν
7.85E-6	210	0.3

Table 4.7: Material parameters for STEEL

4.1.8. RIGID

This card, which corresponds to MAT_20, is a material formulation used to set-up rigid parts. In the project, it has been used for the impactor and the ”rail fixtures” that keep the assembly in place.

Within the formulation, nodal constraints can be set, therefore allowing for quick implementation of boundary conditions on the rails, resulting in the card in Table 4.8. As per the impactor, no constraints need to be set, hence giving the card in Table 4.9.

In the table:

- CMO specifies the system of reference for the constraints (CMO=1 is for global direction).

- CON1 specifies translational constraints (CON1=7 constraints all 3 directions).
- CON2 specifies rotational constraints (CON2=7 constraints all 3 directions).

Note that material properties for both parts need to be specified, even if they are rigid, for the contact algorithms to correctly compute penalty forces.

ρ	E	ν
7.85E-6	210	0.3

CMO	**CON1**	**CON2**
1	7	7

Table 4.8: Material parameters for the rail fixtures

ρ	E	ν
7.85E-6	210	0.3

CMO	**CON1**	**CON2**
0	-	-

Table 4.9: Material parameters for the impactor

4.2. Baseline Model

Before developing the delamination approach in LS-Dyna, it is necessary to build a reliable set of results for the baseline model currently in use at the company, as a benchmark. To do so, such model has been thoroughly verified and subsequently updated to reflect the choices made in Chapter 3 concerning layup definition, experimental errors and DIC results. In this section, this process will be detailed.

4.2.1. Simulations Workflow

An overview of the steps needed to obtain the ”Finalized Baseline” that will be used as a benchmark for the delamination modeling is provided in Figure 4.3.

First, a ”Starting Baseline” is defined by using the glass fibre plate chosen for the project in Section 3.1.2 [step 0]; then, a Simpson integration rule through-the-thickness is defined for it, to ensure a fairer comparison with the new model, which as mentioned in Section 2.5.4 will require Simpson integration to properly compute bending stiffness [step 1]. Subsequently, the impactor size is updated to fix a mismatch with the one used in experimental tests [step 2], a ”Version Specific Baseline” is defined by introducing experimental errors in impact position and angle from a specific test among the available ones (presented in Section 3.1.2) [step 3], the global friction scaling factor is updated to improve on the match with experimental results [step 4], and a comparison between different bolt pre-loads is performed by assessing its influence in the final intrusion and global deformation shape [step 5]. As a final step, besides the standard material card GLASS_1 for the glass fibre, a new calibrated card (GLASS_2) for the same material is introduced, and the combined influence of 3 total is assessed: material card (GLASS_1, GLASS_2), protection plate mesh size (5 mm, 2 mm) and minimum allowed time-step ($5E-4$ ms, $5E-6$ ms) [step 6].

In the following, each step is detailed further. **Always keep in mind that each step builds on top of the modifications and updates of the previous ones, unless specified otherwise**.

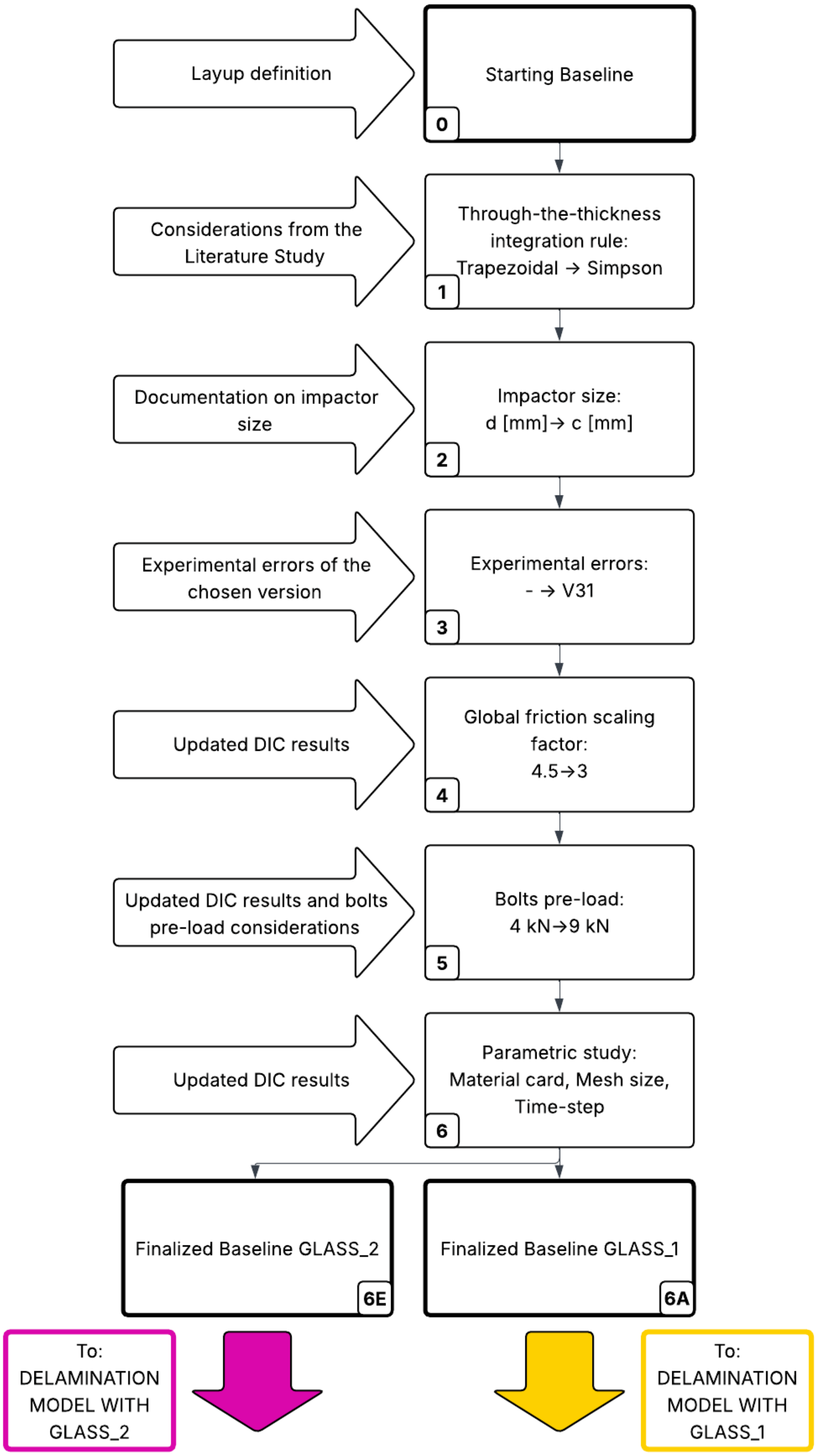

Figure 4.3: Simulations workflow for the Baseline Model. The large arrows represents links from/to different sections.

4.2.2. Step 0: Starting Baseline

The baseline model has been developed to mimic the experimental set-up detailed in Section 2.1. An initial version of the model has been provided by the company, and it has then been reconstructed and updated to satisfy the project requirements.

As mentioned in Section 2.4.3, the simulation input file (.i1) can be split into multiple sub-files, hereinafter called includes (.k), through the *INCLUDE card. This feature has been leveraged to prepare a single input file for all simulations, where different versions for the various components are invoked depending on the intended set-up. Of course, there are multiple cases where the contents of specific includes need to be translated or rotated (e.g. variable plate thickness, variable impact angle and impact position); to this end, the *PARAMETER card (also mentioned in Section 2.4.3) has been used to set up includes transformations depending on the requirements. This file architecture helped enormously in reducing both pre-processing time and chances for errors, thanks to a standardized approach where changing a few lines of code can result in different simulation conditions.

The main components of the model will be now discussed.

Input File

Although the assembly components are handled by the includes, the input file is still responsible for setting the main simulation parameters, which are reported in Table B.1, where: **a)** The name ”B0” stands for ”Baseline, step 0”. **b)** ”TERMTIME” specifies the total duration of the simulation. **c)** ”DT2MS” specifies the minimum allowed time-step. The negative sign in front of it is used to allow for mass scaling (see Section 2.4.2) if the time step tries to go below it. **d)** The ”impact angle” is specified w.r.t. the protection plate, hence a $-\alpha^\circ$ angle is the intended impact condition (see Figure 3.1). **e)** The ”impact position” is specified w.r.t. the plate center, positive towards the plate’s front end (from where the projectile comes). **f)** The ”friction SF” is a scaling factor applied to the global contact defined between all parts, and scales the standard values of f_{static}=0.15 and $f_{dynamic}$=0.08.

Controls Include

The Controls include file governs the global numerical framework of the explicit analysis. This deck contains the *CONTROL keyword family, which defines critical solution parameters including the time-step stability criteria (via *CONTROL_TIMESTEP), hourglass energy suppression algorithms, and the simulation termination time.

Database Output Include

The Database Output include file manages the Input/Output (I/O) frequency for post-processing. It specifies the write intervals for binary plot files (d3plot) required for geometric visualization, as well as ASCII history files (e.g., glstat, matsum, rcforc) used to monitor global energy balances, part-specific momentum, and contact interface forces.

Contacts Include

In the original model provided by the company, 3 contact definitions were defined within the input file:

- An AUTOMATIC_SINGLE_SURFACE contact (”soft-constraint” formulation), responsible of handling the interactions between all parts of the model, except for the bolt assemblies. For it, friction coefficients of f_s=0.15 and f_d=0.08 were defined for all pairs, with the possibility of scaling them through the SF parameter discussed previously.
- An AUTOMATIC_GENERAL contact, responsible of handling the interaction between the bolt shank and the holes edges; this is standard practice in FEA simulations.
- A TIED_NODES_TO_SURFACE_OFFSET contact, responsible of the tie between the screws and the fixtures.

In foresight of the delamination modeling implementation, which will require to set-up individual contacts between each pair of plies, a separate contact include is set-up between the protection plate (slave) and all the other components of the assembly (master). This is done because if the plies were left as part of the AUTOMATIC_SINGLE_SURFACE contact, they would have had 2 competing contacts handling their mutual interactions once the delamination contacts were set-up, causing numerical instability. Delaying this modification to a later time would introduce a discrepancy in contact handling between the benchmark and the new model, making it harder to assess the merits of the delamination modeling. The added contact is therefore:

- An AUTOMATIC_SURFACE_TO_SURFACE contact (called ”plate_to_everything_contact”) with standard ”penalty” formulation, handling the interaction between the protection plate and the rest of the model. The SF parameter still handles friction scaling.

Gravity Include

To apply gravity to the model, a *LOAD_BODY card is used. Basically, both coordinate systems are accelerated in the positive C-direction (see Figure 3.4) with $a = 9.81m/s^2$, thus giving inertial loads of opposite sign acting on the model [18]. Note that to vary the impact angle to assess different scenarios, the impactor is never rotated, as it is the rest of the set-up rotating around the Y-axis (see Figure 3.4); therefore, the direction of the acceleration doesn't need to be changed.

Bolt Include

An overview of the bolt include components is provided in Figure 4.4, while its main parameters are reported in Table B.2.

The bolts are modeled with a beam connected through rigid beams to a screw head and a screw end. The end is tied to the fixtures, while the head is in contact with the rest of the model and has an oversized dimension to simulate the presence of a washer. At the beginning of the simulation, during a step called dynamic relaxation, a compressive force whose load curve is shown in Figure 4.5 is applied to the beam, which compresses and ends up pushing the screw head into the plates, applying a contact force that keeps them in place and thus mimicking the effect of applying a pre-load to the screws.

In an ideal set-up, the friction caused by the pressure of the screw heads keep the plates in place, but in real scenarios slipping can happen, loading the screws in shear. In simulations, this results in a beam to shell edge contact, which is notoriously hard to handle for contact algorithms; to solve the issue, beams hereinafter referred to as ”contact beams” are placed around the holes in the shell, and a special contact is set-up between the screw beam and the contact beams.

At the company, these beams are usually placed all-around the holes, to account for all possible contact scenarios, but this practice has a significant disadvantage: when contact is initiated on one side of the hole, the beams transfer the loads to the other side, loading it in tension. This behaviour, which doesn't happen in real scenarios, alters the load distribution around the hole and can produce unrealistic results, hence a simple solution has been adopted: after some preliminary runs to determine the areas of the holes which contact the screws during impact, all the contact beams in tension have been removed, resulting in the configuration for the protection plate holes labeled ”compression-only contact beams” in Figure 4.4b. A full all-around configuration has been kept for the aluminum plate and spacers, for which no significant screw/hole contacts and deformations are expected.

Note that a single model exists for all bolts; after being invoked 6 times in the input file, each bolt is translated and rotated in place based on the specified parameters.

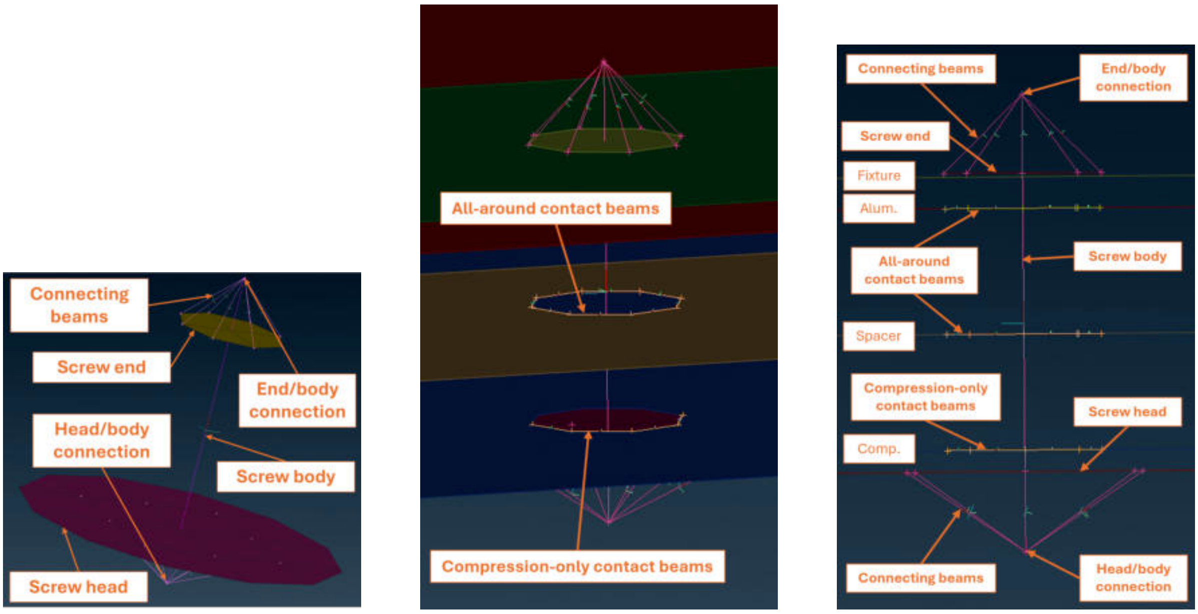

(a) Bolt include.

(b) Comparison between all-around and compression-only contact beams.

(c) Bolt include in relation to the entire set-up.

Figure 4.4: Bolts assembly from the LS-Dyna model.

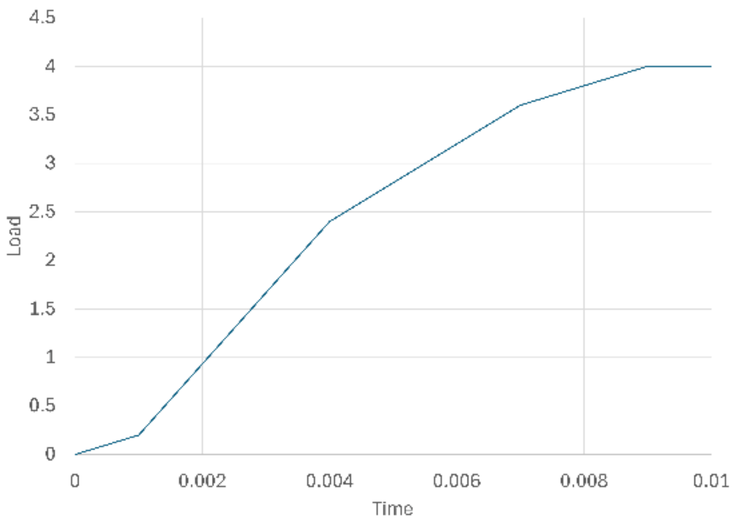

Figure 4.5: Pre-load of the screws to 4kN

Protection Plate Include

An overview of the protection plate include is provided in Figure 4.6, while its main parameters are reported in Table B.3. By leveraging the *PART_COMPOSITE card as discussed in Section 2.5.2, the whole layup, defined in Section 3.1.2, is represented by a single shell.

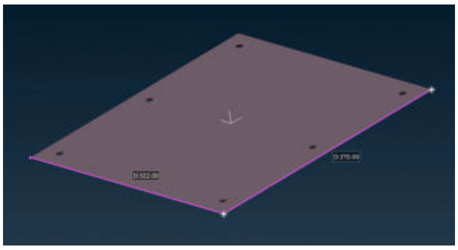

Figure 4.6: Protection plate include from the LS-Dyna model.

Aluminum Plate Include

An overview of the aluminum plate include is provided in Figure 4.7, while its main parameters are reported in Table B.4. The plate is modeled via a single shell.

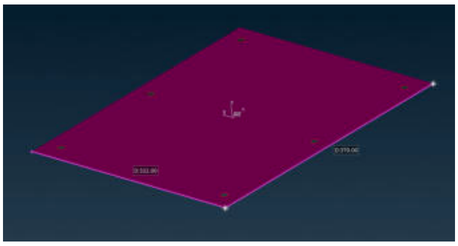

Figure 4.7: Aluminum plate include from the LS-Dyna model.

Spacer Include

An overview of the spacer include is provided in Figure 4.8, while its main parameters are reported in Table B.5. The spacer is modeled via a single shell.

Being a non-symmetric part, the spacer model needs to be mirrored to be used in both sides of the plates. This can be done easily directly in the input file after invoking the include; hence, a single spacer model is required.

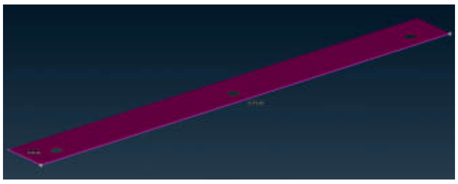

Figure 4.8: Spacer include from the LS-Dyna model.

Impactor Include

An overview of the impactor include is provided in Figure 4.9, while its main parameters are reported in Table B.6. The projectile is modeled via a shell, hence it doesn't have the mass of the real component. To obviate to this, the mass of the shell elements is computed, and nodal masses are evenly added on the shell surface to match the mass m of the real impactor.

Regarding trajectory and velocity, initial velocities are applied to the impactor nodes in positive-A direction (see Figure 3.4), via a variable *PARAMETER called VEL, which can be modified from the input file. Note that to vary the impact angle to assess different scenarios, the impactor is never rotated, as it is the rest of the set-up rotating around the Y-axis (see Figure 3.4); therefore, the direction of the initial velocity doesn't need to be changed. As per the impactor position at t=0, it is placed right at the impact point, as the specified VEL is the intended velocity at contact time.

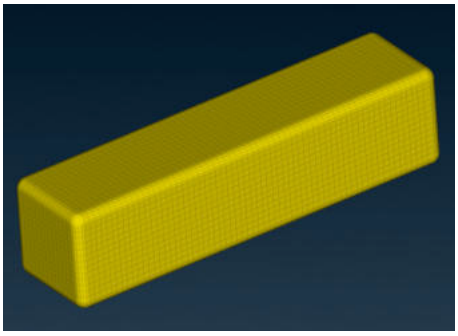

Figure 4.9: Impactor include from the LS-Dyna model.

Fixture Include

An overview of the fixture include is provided in Figure 4.10, while its main parameters are reported in Table B.7. The fixture is modeled via a single shell.

As two fixtures are needed, the same copy/translation process used for the screws is adopted, hence a single fixture model is required.

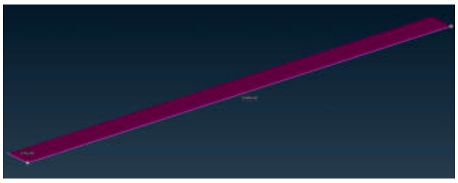

Figure 4.10: Fixture include from the LS-Dyna model.

4.2.3. Step 1: Switch of Through-the-Thickness Integration Rule

First, the input file name is updated as shown in Table B.8.

Then, the integration rule is changed from ”trapezoidal” to ”Simpson”. As mentioned, the delamination implementation will require 3 through-the-thickness integration points per ply in order to effectively compute ply-level bending stiffness, since all plies will be modeled individually. As more integration points will generally produce more accurate results, the switch to ”Simpson” has to be performed already at this stage, otherwise the comparison between the benchmark and the delamination-capable model would be unfair, as it would be hard to isolate the effect of delaminations alone. Hence, the protection plate include is substituted with the one detailed in Table B.9. The increase in computational time due to this modification should be negligible, but will be evaluated in Chapter 5 for confirmation.

4.2.4. Step 2: Correction of Impactor Size

First, the input file name is updated as shown in Table B.10.

During the documentation phase for the project, a document detailing the impactor characteristics has been found. Interestingly, the reported length was c mm (option A), while the model used in simulations is d mm (option B). This difference, if confirmed, is significant and enough to alter impact dynamics due to geometrical and mass distribution effects, therefore a check has been performed via a simple calculation: as the impactor's base dimensions ($a \times b$ mm), mass (m kg), and material (steel) are known and the same for both options A and B, length can be computed to match the material's density, and the correct option can therefore be determined. The results prove that the impactor is in fact c mm long, and therefore that the current model needs to be updated with the include in Table B.11.

Note that the added mass needs to be updated to account for the new nodes in the model, and this change is reflected in the table, with a variation of -0.07 kg.

4.2.5. Step 3: Introduction of Experimental Errors

A big source of discrepancy between tests and simulations is represented by the experimental errors registered during testing, mostly concerning impact angle and position, which deviated from the intended values. Among the available versions (see 3.1.2), V31 has been chosen to illustrate the present step-by-step workflow. Hence, the input file has been updated to reflect this, as shown in Table B.12.

4.2.6. Step 4: Change of Global Friction Scaling Factor

The friction scaling factor of 4.5 was applied in previous studies on the Beschuss load case to improve on the experimental/simulations match of the intrusion peaks of the plate; since the mismatch was probably caused, among other reasons, by a wrongly sized impactor (fixed in Step 2), the standard scaling factor of 3 has been re-introduced by modifying the input file (see Table B.13), and a comparison between the two cases is performed in Chapter 5.

4.2.7. Step 5: Comparison of Bolts Pre-Load

First, the input file name is updated as shown in Table B.14.

As mentioned, the pre-load on the bolts isn't specified in any test standard or related documentation. Being M6, a maximum force of around 8-10 kN is usually applied, but for this specific application it could result in the thin glass-fibre plate being crushed; therefore, a reduction to around 4 kN was performed in the provided model.

Still, it could be that in the experimental tests a different pre-load was applied; to check for this, the higher bound case of 9 kN pre-load is simulated, by substituting the standard bolt include with the one in Table B.15, with the only difference being that the curve in Figure 4.5 has been scaled up to match the new pre-load.

In Chapter 5, it will be shown that the 9 kN pre-load results in more accurate deformation shapes and intrusion values, hence it will be used in the following steps.

4.2.8. Step 6: Parametric Study on Glass Fibre Material Card, Protection Plate Mesh Size and Minimum Allowed Time-Step

As mentioned, besides the standard material card for glass fibre, a second card with a different calibration is available. Testing both of them in baseline conditions could be very useful in determining their differences and choosing which one to use for the following steps.

Specifically, their predictive capabilities at different mesh sizes will be compared.

Additionally, the effect of minimum allowed time-step reduction on the simulation accuracy of the mesh-refined models will be analyzed.

Then, 2 material cards, 2 mesh-sizes and 2 minimum allowed time-steps will be analyzed, resulting in 6 different models, which are summarized in Table 4.10 and explained in greater detail in the following.

Step	Material ID	Mesh size [mm]	Minimum ts [ms]
6A	GLASS_1	5	5E-4
6B	GLASS_1	2	5E-4
6C	GLASS_1	2	5E-6
6D	GLASS_2	5	5E-4
6E	GLASS_2	2	5E-4
6F	GLASS_2	2	5E-6

Table 4.10: Summary of the explored combinations, step 6

Step 6A: GLASS_1, Mesh 5 mm, Min. Timestep 5E-4 ms

First, the input file name is updated as shown in Table B.16. This model is effectively the same as Step 5, since the bolt pre-load of 9kN is ultimately chosen; hence, the protection plate include is not modified (see Table B.17)

Step 6B: GLASS_1, Mesh 2 mm, Min. Timestep 5E-4 ms
First, the input file name is updated as shown in Table B.18. In this model, compared to Step 6A, the mesh size of the protection plate is reduced from 5mm to 2mm (see Table B.19).

Step 6C: GLASS_1, Mesh 2 mm, Min. Timestep 5E-6 ms
First, the input file name is updated, and the minimum allowed time-step is reduced from 5E-4 ms (6A) to 5E-6 ms, as shown in Table B.20. Then, compared to 6A, the mesh size of the protection plate is reduced from 5 mm to 2 mm (see Table B.21).

Step 6D: GLASS_2, Mesh 5 mm, Min. Timestep 5E-4 ms
First, the input file name is updated as shown in Table B.22. In this model, compare to Step 6A, the material card is changed from GLASS_1 to GLASS_2 (see Table B.23).

Step 6E: GLASS_2, Mesh 2 mm, Min. Timestep 5E-4 ms
First, the input file name is updated as shown in Table B.24. In this model, compare to Step 6A, the material card is changed from GLASS_1 to GLASS_2, and the mesh size is reduced from 5mm to 2mm (see Table B.25).

Step 6F: GLASS_2, Mesh 2 mm, Min. Timestep 5E-6 ms
First, the input file name is updated and the minimum allowed time-step is reduced from 5E-4 ms (6A) to 5E-6 ms, as shown in Table B.26. Then, compared to Step 6A, the material card is changed from GLASS_1 to GLASS_2, the mesh size is reduced from 5mm to 2mm (see Table B.27).

4.3. Delamination Model with GLASS_2

In Section 5.1.13, it has been decided to implement the delamination model with both GLASS_2 and GLASS_1. In this section, the GLASS_2-related simulations will be detailed.

4.3.1. Simulations Workflow

An overview of the steps taken in the implementation of the delamination model and subsequent verifications is provided in Figure 4.11.

First, the chosen benchmark baseline [step 6E] is updated with a new protection plate model (ONEWAY contact formulation between the plies) to allow for delamination implementation [step 7], then the delamination parameters are set and the delamination pattern is analyzed [step 8], and finally a TWOWAY contact formulation with reduced minimum timestep is adopted to solve numerical issues of the model [step 9]. A DoE[2] is set up to verify the chosen strength parameters [step 10], and the finalized model is obtained. The generality of the model is then tested against different impact conditions [step 11] and layups [step 12].

Along the regular simulations workflow, additional simulations to answer specific questions are performed. Those are highlighted in orange in Figure 4.11, and will be explained after the regular ones.

In the following, each step of the regular workflow is detailed further. **Always keep in mind that each step builds on top of the modifications and updates of the previous ones, unless specified otherwise.**

[2] Design of Experiments

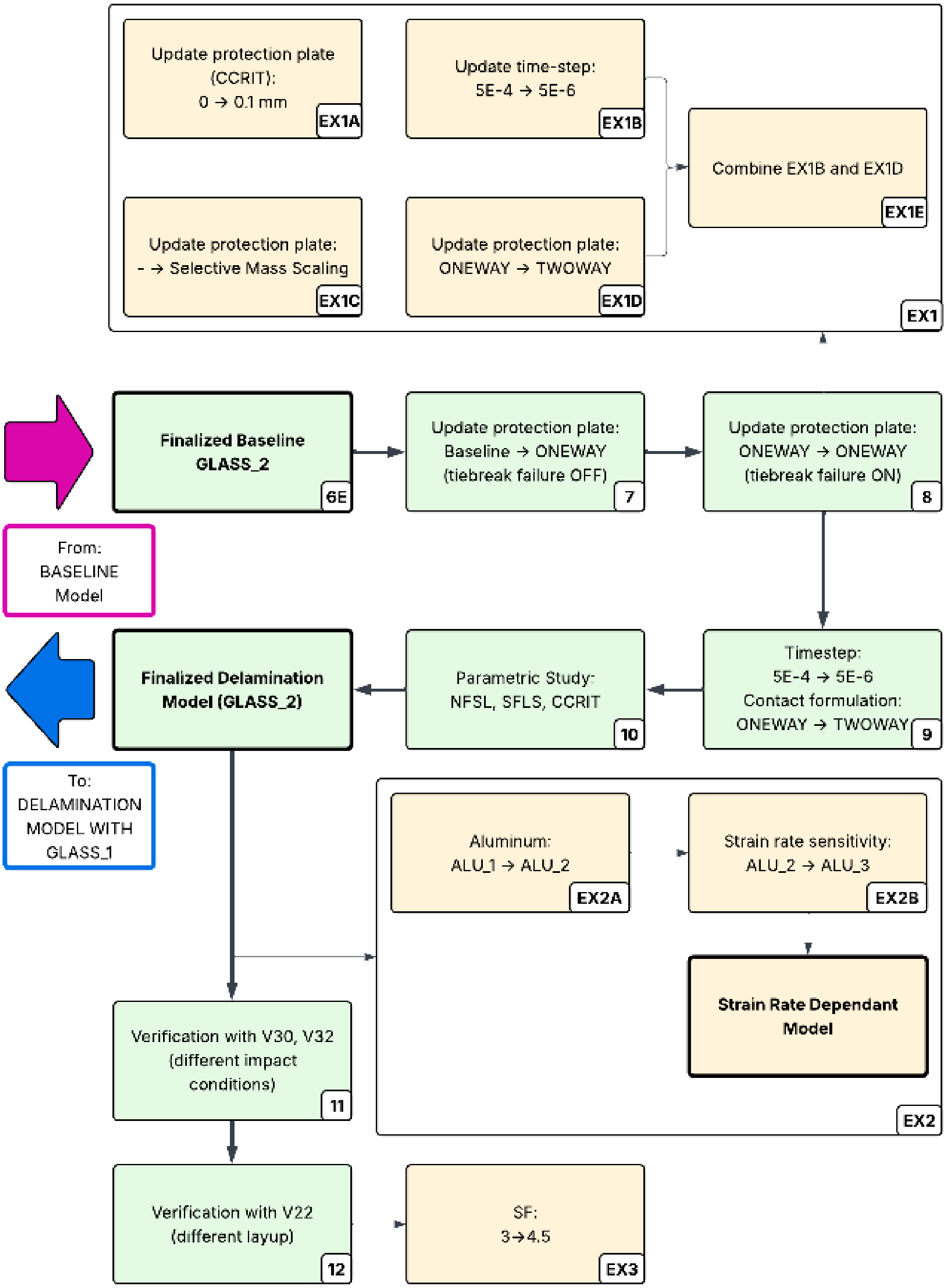

Figure 4.11: Simulations workflow for the Delamination Model with GLASS_2. The large arrows represents links from/to different sections.

4.3.2. Step 7: Equivalent New Model

First, the input file name is updated as shown in Table B.28.

The baseline model has been previously updated to be able to easily integrate delamination capabilities at a later stage; therefore, to create the new model, it is sufficient to substitute the baseline protection plate. The new protection plate, which is shown in Figure 4.12 and whose features are summarized in Table B.29, is modeled according to the concepts expressed in Chapter 2; therefore, the plies are held together via TIEBREAK contacts with OPTION 8. The contacts are defined within the plate's include file, completing all needed data.

Note that 5 contact definitions are required, one per ply pair; the only difference between them are the plies they refer to.

For a detailed explanation of the model build-up, refer to Appendix E.

In the current step, no strength values are set for the contacts, which therefore act as penalty-based ties, not allowing any delamination. This intermediate step serves to create a model equivalent to the baseline it refers to, which should therefore behave in the same way. This equivalency is checked for, and in case of discrepancies, explanations are provided.

Also note that no inter-ply friction is defined. This is done because without layup-specific results, extensive calibration would be required to identify the correct coefficients; furthermore the expected delamination areas are quite small, hence the expected energy dissipation is limited. Nevertheless, recognizing the potential of this phenomenon in influencing the final results, a simple implementation will be explored when developing a new simulations workflow with GLASS_1, where reasonable guesses will be provided for the inter-ply friction coefficients.

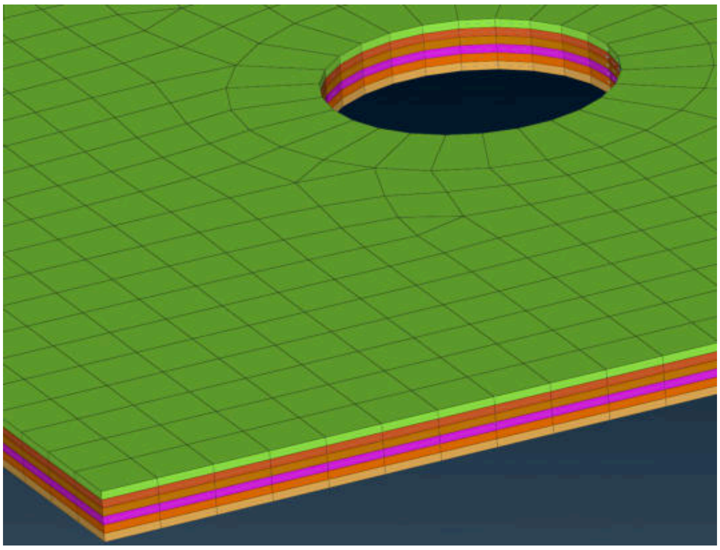

Figure 4.12: Detail of the new protection plate, from the LS-Dyna model

4.3.3. Step 8: Delaminating New Model

First, the input file name is updated as shown in Table B.30.

In this step, the protection plate is updated (see Table B.31) with strength values for the tiebreak contacts, enabling delamination. The damage patterns on it will be analyzed and compared with C-SCAN results, to determine predictive capabilities (see Section C.2.2).

As CCRIT is not defined in this stage, delamination won't absorb any additional energy, as contacts break via a purely strength-based criterion; therefore, a slightly higher intrusion is expected than in the baseline model, due to the loss of stiffness produced by delaminations.

4.3.4. Step 9: Two-way Contact Formulation with Reduced Timestep

Solution EX1E is chosen to solve the numerical issues encountered in step 8 (see Section C.2.2), resulting in the input file in Table B.32 and in the protection plate in Table B.33.

4.3.5. Step 10: Design of Experiment Study on Contact Parameters

The contact parameters of the tiebreak contacts (NFLS, SFLS, CCRIT), which were defined in Chapter 2, are calibrated via a DoE study; in this case, minor calibration is expected as mesh size is matching the physical cohesive zone length of composites (see Section 2.5.7).

For each parameter, a low (L), medium (M) and high (H) value are defined (see Table 4.11), and all combinations are tested in a full factorial study, resulting in $3^3 = 27$ combinations. The full factorial option is chosen as reduced-order methods would be incapable of capturing the strong non-linearities and parametric interaction effects typical of ballistic impacts.

The low (L) values for the strengths are chosen to be almost negligible, to highlight whether delamination is shear- or normal-failure dominated; the medium (M) values are the ones used in the previous steps; the high (H) values are preliminary chosen as upper bounds for the study, and will be re-evaluated in case delamination patterns suggest the need for it.

After the model was finalized, discrepancies with the experimental results are addressed, and additional hypotheses are formulated; based on those, an alternative model update based on strain rate sensitivity of the aluminum plate, which was already mentioned in Chapter 1 as a possible cause for the simulation/test mismatch, is explored (see Section 4.3.9).

	L	**M**	**H**
NFLS [GPa]	0.005	0.05	0.1
SFLS [GPa]	0.005	0.02	0.05
CCRIT [mm]	0	0.02	0.1

Table 4.11: Low (L), Medium (M) and High (H) settings for DoE study on tiebreak contact parameters

4.3.6. Step 11: Verification with Different Impact Conditions

By modifying the impact angle and position from the input file, the remaining available experimental tests described in Chapter 3 are simulated, and their respective input files reported in Table B.34. This is done to test the generality of the approach in different impact conditions.

4.3.7. Step 12: Verification with a Different Layup

By modifying both the impact conditions and the protection plate include, an experimental test with a different layup (see Chapter 3) is simulated, to test the generality of the approach with different material cards and layup configurations. The updated input file is presented in Table B.35, while the new protection plate features are summarized in Table B.36. In this version, the spacing between the protection and the aluminum plate is reduced from 13 mm to 10 mm, thus requiring a different spacer model (see Table B.37), which, after being imported in the .i1 file, is mirrored to be used on both sides of the assembly, like it was done for the baseline model.

4.3.8. EX1: Solutions to Numerical Errors

In this series of simulations, possible solutions to the numerical errors observed in step 8 (see Section C.2.2) are explored. **Note that each solution is obtained updating the one proposed in step 8 (see Figure 4.11).**

EX1A: CCRIT-Induced Damping

First, the input file name is updated as shown in Table B.38.

This solution is based on the idea that instantaneous failure of the tiebreak can release the energy stored in the contact spring in a step-like manner, causing numerical instabilities. By setting an arbitrary small value for the critical separation distance CCRIT, this release happens with a ramp-down behaviour, possibly preventing ringing. To test this concept, the protection plate is substituted with the one in Table B.39, where CCRIT=0.1 mm.

EX1B: Minimum Timestep Reduction

Another possible source of error is the minimum timestep limit set to a value too high; to test for this, a reduction by a factor 100 is performed (see Table B.40).

EX1C: Selective Mass-Scaling

First, the input file name is updated as shown in Table B.41.

Selective mass scaling is a different kind of mass scaling that can be applied to selected elements instead than on the whole model; while normal scaling simply adds mass to critical elements, selective scaling modifies their mass matrices to filter out high-frequency vibrations while preserving the low-frequency (i.e., rigid body modes) response.

In this step, selective scaling is applied to the composite plate, i.e. to a SET comprising all plies, by specifying the SET ID in the IMSCL field in the *CONTROL_TIMESTEP card [18].

EX1D: Two-Way Contact Formulation

First, the input file name is updated as shown in Table B.42.

In Appendix E.1, two different contact formulations are presented for the tiebreak, with the ONEWAY formulation being used until now. With its different contact handling, the TWOWAY formulation could be more robust and prevent numerical issues. To test for this, the protection plate is substituted with the one in Table B.43, where a TWOWAY formulation is adopted.

EX1E: Combination of EX1B and EX1D

Reduced minimum timestep and TWOWAY contact formulation are combined to achieve contact stability; the input file is presented in Table B.44.

4.3.9. EX2: Update of the Aluminum Material Model

In this series of simulations, alternative material cards for the aluminum plate are introduced and evaluated, taking the finalized model from step 10 as a starting point. This is done since, as previously discussed, the material card provided by the company didn't accurately represent the aluminum plate used in experimental tests, and a combination of different strain/stress curves and strain rate sensitivities could be a key factor to explain the test/simulation discrepancy.

EX2A: Switch to the Newly Characterized Aluminum (ALU_2)

First, the input file name is updated as shown in Table B.45.

The true plastic strain / true stress curves presented in Section 4.1 for ALU_1 and ALU_2 are compared in Figure 4.13, with a zoom on the 0-5% region. From the plot, it can be seen that the new aluminum is stronger until $\approx 5\%$ plastic strain.

The area of the aluminum plate in the step 10 model where plastic strain is $< 5\%$, highlighted in Figure 4.14, is significant, and it suggests that updating the aluminum material model could result in a reduction of the intrusion even though the curve worsens for plastic strains $> 5\%$. To check for this, the aluminum plate include is updated as shown in Table B.46.

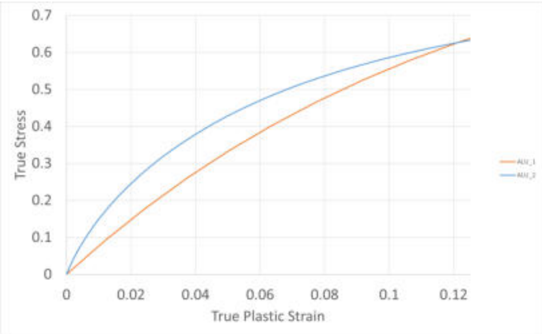

Figure 4.13: True Plastic Strain / True Stress curves, comparison between ALU_1 and ALU_2

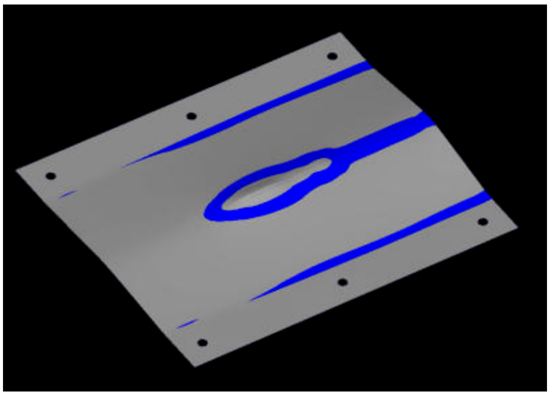

Figure 4.14: In blue, the area with plastic strain between 1% and 5%, where the new aluminum performs better; results from the finalized model

EX2B: Switch to the Strain-Rate Sensitive Aluminum (ALU_3)
First, the input file name is updated as shown in Table B.47.

Strain rate sensitivity is implemented for ALU_2 using the Cowper-Symonds model, resulting in the ALU_3 card, which is then applied to the aluminum plate include (see Table B.48). The constants for the model have been selected through trial and error until a satisfactory match with the experimental results has been achieved. Naturally, this trial and error process can be only justified if the fitted coefficients, while falling within plausible ranges, can be shown to apply to a wide variety of test conditions and layups, thus both plausibility and generality will be checked in Chapter 5.

4.3.10. EX3: Improving on the CARBON Layup Results

As it will be shown in Section C.2.7, the test/simulation match of the intrusion plot for the V22 layup (step 12) is unsatisfactory. Therefore, the global friction coefficient is increased from 3 to 4.5 (see Table B.49) in an attempt to improve on the simulation results. This is done because of the higher number of plies of the V22 plate that could have resulted in a higher drag for the impactor during the tearing, which is suggested by the deeper and more visible scratches on the aluminum backplate, and by the increased contact time between plate and impactor, compared to the other versions (see Tables 3.1 and 3.3).

4.4. Delamination Model with GLASS_1

Based on the conclusions drawn from the previous simulation results (see Section 5.2.1), a new simulation workflow has been designed, and will be executed directly with the GLASS_1 material card, as a coarser mesh will be used to reduce computational time and align to the company's crash simulations standards, and GLASS_2 doesn't respond well to mesh coarsening (see Section 5.1.13).

4.4.1. Simulations Workflow

An overview of the steps taken in the implementation of the new delamination model and subsequent verifications is provided in Figure 4.15.

First, the chosen benchmark baseline [step 6A] is updated according to the final settings of the previous workflow, with the only difference being that GLASS_1 is used in place of GLASS_2 [step F1], then a switch back to a ONEWAY formulation is performed to solve numerical issues [step F2], and finally a re-calibration is performed on the contact strength parameters to adapt to the new mesh size[3] [step F3].

Then, a new, more accurate material model for the aluminum plate, already discussed in Section 4.3.9, is implemented (although strain rate sensitivity is ignored, due to the conclusions drawn in Section 5.2.1) [step F4], inter-ply friction is introduced to produce a more realistic behaviour of the delaminated plies

[3]As anticipated in Chapter 2.5.7, the strength parameters depend on the mesh size.

[step F5], and reinforcing beams all-around the plate holes are re-introduced to stabilize the contacts, while verifying whether their influence on the impact dynamics is negligible [step F6].

To conclude, an analysis of the test footage is performed to introduce accurate initial shifts, tilts and rotation of the impactor in the simulation, as they have been deemed critical to improve on the test-simulation match [steps F8 and F9].

In the following, each step is detailed further. **Always keep in mind that each step builds on top of the modifications and updates of the previous ones, unless specified otherwise.**

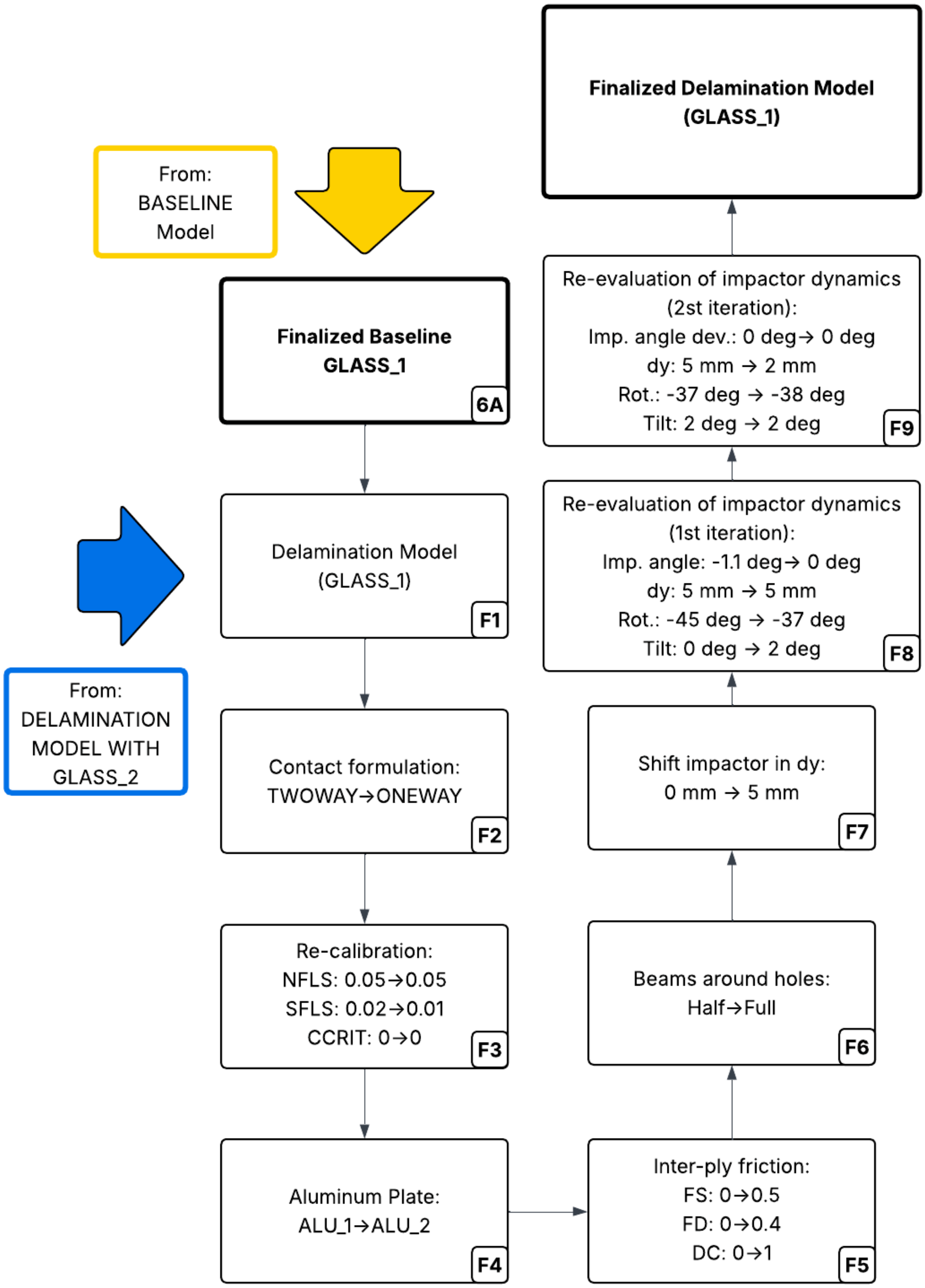

Figure 4.15: Simulations workflow for the Delamination Model with GLASS_1. The large arrows represents links from/to different sections.

4.4.2. Step F1: Delaminating New Model

The starting point for the new workflow is a model analogous to the final one from the previous simulations workflow (see Section 4.3.4), where the protection plate has been updated with a coarser mesh and a different material card (see Table B.51). The input file is presented in Table B.50.

4.4.3. Step F2: One-way Contact Formulation with Reduced Timestep

After the TWOWAY formulation resulted in numerical issues with the new combination of material card and mesh size (see Section 5.3.1), a switch to the ONEWAY formulation is performed (see Table B.53).

4.4.4. Step F3: Recalibration of Contact Parameters

In this step the contact strengths are re-calibrated to account for the coarser mesh size, which is not comparable to the physical cohesive zone length of composites anymore (see Section 2.5.7), with the combinations in Table 4.12 being tested. Note that CCRIT is kept 0 for every combination due to the considerations made in Section 5.2.1. The rationale behind each combination is the following: after realizing that re-calibration was necessary, both strength parameters have been gradually reduced until the delamination pattern started to match the experimental results again; then, NFLS has been increased to its original value to confirm its irrelevance in the failure dynamics (i.e., to confirm that delamination is shear-driven).

The input file is presented in Table B.54.

Combination	**NFLS** [GPa]	**SFLS** [GPa]	**CCRIT** [mm]
1	0.05	0.02	0
2	0.0375	0.015	0
3	0.025	0.01	0
4	0.05	0.01	0

Table 4.12: Combinations tested in the tiebreak contact re-calibration process, step F3

4.4.5. Step F4: Update of the Aluminum Material Model

In this step the aluminum plate include is updated with the ALU_2 material card (see Table B.46). Since strain rate sensitivity implementation increases the material characterization effort, and doesn't seem to provide any substantial intrusion reduction when realistic Cowper-Symonds parameters are used, it hasn't been implemented in the current workflow. The input file is presented in Table B.55.

4.4.6. Step F5: Introduction of Inter-Ply Friction

Inter-ply friction is determined to be critical to improve the behaviour of the protection plate (see Section 5.2.1), therefore in this step it has been introduced by updating the plate's include (see Table B.57). The input file is presented in Table B.56.

For the values of the coefficients, reasonable values for a rough interface are chosen: 0.5 for the static coefficient FS, and 0.4 for the dynamic coefficient FD. To ensure a smooth transition from static to dynamic friction, a value of 1 is chosen for the decay factor DC[4].

4.4.7. Step F6: Re-evaluation of Reinforcing Beams Around Plate Holes

First, the input file name is updated as shown in Table B.58.

In the previous workflow, the reinforcing beams around the plate holes that were in tension have been removed, as they could have resulted in non-realistic load distributions. In an effort to solve numerical issues around the holes, the beams have been re-introduced all-around because of their contact-stabilizing capabilities, and the effect of the beams in tension on the impact global response is evaluated.

[4]The decay factor is a parameter in LS-Dyna which acts as a mathematical control for the exponential decay from the Static Friction Coefficient (FS) to the Dynamic Friction Coefficient (FD) as the relative velocity between contacting parts increases.

4.4.8. Step F7: Change of the Impactor Initial Position in the Y-Direction

In this step, the y-coordinate of the impact position is shifted in the positive direction (see Figure 4.16) by 5 mm; this shift has been measured and reported during the experimental campaign, but up to this point it has been considered to be negligible. Now, in an effort to explain the residual test/simulation discrepancies, it has been introduced (see Table B.59).

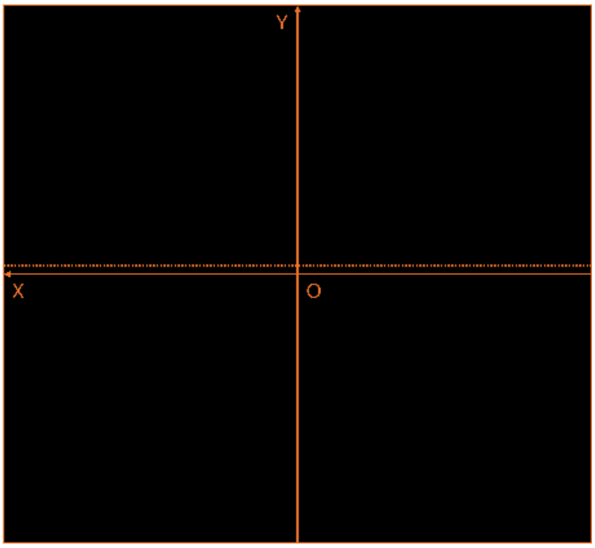

Figure 4.16: The plate is represented in black, in scale 1:2. The dashed line represents the new ”line of action” of the impactor, shifted by 5 mm in the positive y direction

4.4.9. Step F8: Re-Evaluation of Impactor Dynamics (1st Iteration)

As the shift performed in step 7 has a detrimental effect on the intrusion (see Section 5.3.7), the impact footage is re-evaluated to highlight impactor parameters that were not measured during the experimental tests. By examining Figure 4.17, which shows the V31 impact test at the moment of the first contact between the impactor and the plate, it can be seen that the impactor rotated around its axis; a rotation of 4.6° was in fact reported in the test results.

What is missing in the report of the experimental tests, but can be inferred from footage analysis, is that the impactor exhibits a tilt (i.e., yaw) misalignment (rotation around point A in the positive-c direction) relative to its trajectory. Consequently, the tail of the impactor is positioned to the right of the ’head’ at the moment of initial contact. This additional rigid body rotation explains the specific damage morphology observed in Figure 4.18, where the secondary ’tail’ impact generates an intrusion mark laterally offset from the primary head impact.

As it wouldn’t be feasible to precisely measure the combination of rotation and tilt without repeating the tests with added cameras, initial guesses are obtained from the available footage.

Since tilt wasn’t contemplated as a possible experimental error in the initial input file, a new transformation has been defined in the form of a rotation around the c-axis and centered on point A. The updated input file, with the final guesses for impact angle, dy shift (from the previous step), rotation around the impactor axis, and tilt around the c-axis, is reported in Table B.60. Note that the impact angle has been updated, too, as the footage showed a flat impact (i.e., $-\alpha°$) in contrast with the reported -$-\alpha - 1°$; in any case, as a $\pm 1°$ error is expected, the update in impact angle falls within the allowed range.

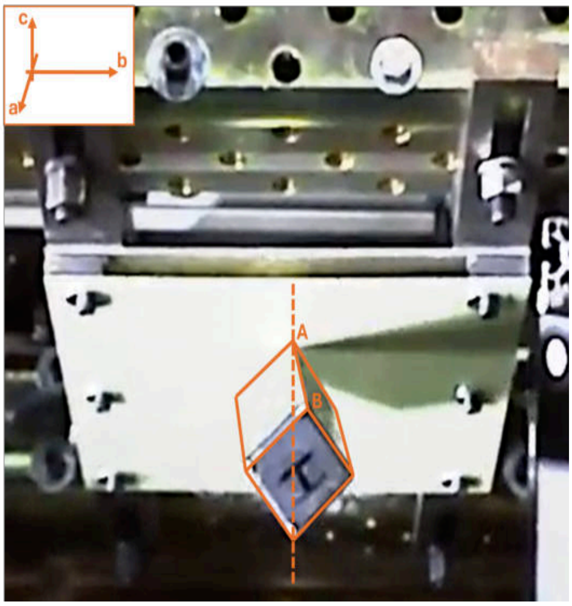

Figure 4.17: Impact test footage, at the time of the first contact between plate and impactor, V31. "Head" and "tail" are labeled A and B, respectively

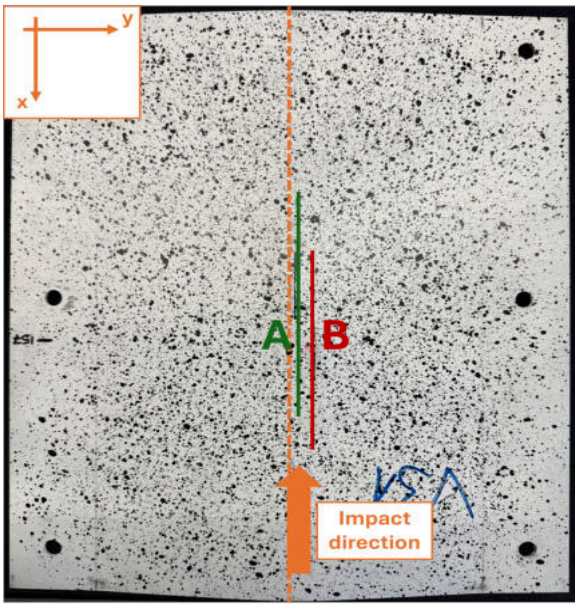

Figure 4.18: Head (A) and tail (B) impact marks on the aluminum backplate, V31

4.4.10. Step F9: Re-Evaluation of Impactor Dynamics (2nd Iteration)

After analyzing the simulation results from the previous steps, it has been determined that the measured shift in the y-direction of the impactor (introduced in step F7) was in fact caused by the impactor rotation around its axis (introduced in step F8) due to geometric coupling. This effectively resulted in twice the shift in the y-direction, with the impactor hitting the plate at y=170 mm instead of y=165 mm. In the current step, the translation has been tweaked while integrating rotation and tilt to obtain the correct impact position, resulting in the input file shown in Table B.61.

5

Results and Discussion

In this chapter, the results of the simulations set up in Chapter 4 are presented and discussed. First, the Baseline workflow (see Figure 4.3) results are analyzed, followed by the GLASS_2 workflow (see Figure 4.11) and the GLASS_1[1] workflow (see Figure 4.15). At the end of each section, a summary with final considerations is provided, based on which the following simulations workflow is defined.

In each section, results are presented in a step-by-step fashion, so that comparisons can be made with preceding or related simulation steps to highlight differences and improvements within and between workflows.

To assess a simulation step, 5 features will be considered: **1)** Runtime (wall-clock). Note that all simulations are performed using LS-DYNA MPP R12 with 16 parallel processes (cores) on a Linux HPC[2] cluster node. **2)** Plastic deformation profile of the aluminum plate, taken at the mid-section length-wise (see Figure 5.1). Keep in mind that as discussed in Section 3.1.3, the experimental curves used for comparison can be treated as an indication of the deformation shape, but magnitude comparisons should be performed with caution, as they have been measured after un-clamping of the plates, possibly resulting in increased intrusions. **3)** Position of the maximum intrusion node on the aluminum plate, hereinafter referred to as ”green node”[3]. **4)** Intrusion over time for the node tracked by the DIC system on the aluminum plate, hereinafter referred to as ”orange node” [4]. For the Baseline and GLASS_2 workflows, the x-coordinate of the orange node is taken from the DIC measurements, but the y-coordinate is set to 0 (i.e., plate’s mid-section), since the small positive shift recorded in tests in the y-direction of the impact point, which in turn shifts the y-coordinate of the orange node, has only been introduced in the GLASS_1 workflow[5]. Note that to enhance readability, all the intrusion plots referenced throughout the chapter are collected in Appendix C. **5)** Damage pattern on the protection plate. Since the Baseline model do not simulate delamination, which primarily drives damage propagation in the transverse direction (width), a direct comparison of damage width with the C-scans will be only performed for the GLASS_2 and GLASS_1 models. However, as delamination exerts a reduced influence on the longitudinal extent of the damage, the damage length measured via the C-scans remains a reliable metric for validating the Baseline model numerical predictions.

Note that in all pictures throughout the chapter, the impactor comes from the right side and moves towards the left.

The chosen markers are summarized in Table 5.1 for future reference. While the runtime is useful to assess efficiency and determine the most computationally expensive choices, the other features allow to assess predictive accuracy by comparing them to the experimental results.

[1] For reference, the association between each material and its descriptive label was summarized in Table 4.1.

[2] High Performance Computing

[3] The node ID is variable, as the position of the maximum intrusion node changes based on simulation parameters.

[4] This node ID is fixed, as its coordinates come from measurements on the test plate.

[5] This is because the influence of the shift in the y-direction of the impact point on the simulation outcome has been initially deemed negligible due to its small magnitude.

Marker	Notes
Runtime	Wall-clock
Plast. def. alu. plate	at mid-sec. (see Fig. 5.1)
Position green node	green node = max. intrusion point on alu. plate
Intrusion/t orange node	orange node = DIC-tracked point on alu. plate
Dmg. pattern comp. plate	Qualitative assessment

Table 5.1: Summary of the markers to assess the match between experimental results and simulations.

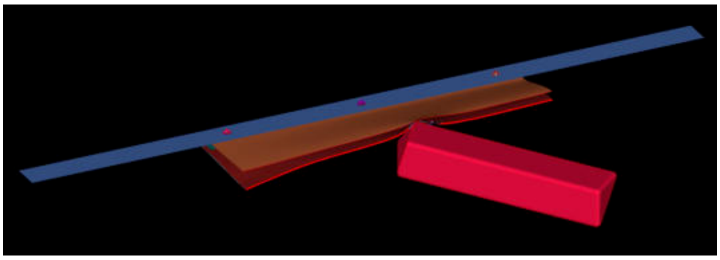

Figure 5.1: Cross-section view to check for the deformation profile of the aluminum plate.

5.1. Baseline Model

As explained in Section 4.2.5, V31 experimental errors on impact angle and position are the ones introduced in the model, hence the V31 deformation and damage patterns, reported in Figures 5.2a and 5.3a and determined through the methods described in Chapter 3, are the target to match in simulations.

5.1.1. Step 0: Starting Baseline

Runtime

The total run time for this model is 318 s (wall-clock).

Plastic Deformation Profile and Position of the Maximum Intrusion Node (Aluminum Plate)

The deformation profile at the end of the simulation, along with the position of the maximum intrusion node and the position of the node tracked by the DIC system in experimental tests, are shown in Figure 5.2b. Compared to the experimentally derived profile (Figure 5.2a), the main intrusion area is shifted considerably to the left; this is trivially explained by the central impact position, as experimental errors are introduced from step 3 only. Furthermore, the shift causes the left side of the plate to show little to no intrusion, confirming a complete mismatch with the experimental results.

Intrusion Over Time (Aluminum Plate)

The intrusion over time for the orange node, compared with the v31 ”experimental band” determined in Chapter 3, is reported in Figure C.1. The curve is shown for completeness, but as explained, not having introduced experimental errors makes these results inconsequential.

Damage Pattern (Protection Plate)

The damage pattern on the protection plate at the end of the simulation is presented in Figure 5.3b. As for the other features, there is a significant mismatch with the experimental data (see Figure 5.3a), due to the different impact angle and position, hence no insightful observations can be made.

5.1.2. Step 1: Switch of Through-The-Thickness Integration Rule

Runtime

The total run time for this model is 547 s (wall clock). This is a considerable increase (+72%) compared to the previous step, and it is due to the increase in the through the thickness integration points. Still, compared to the subsequent steps, it can be considered to be negligible in practical terms.

Plastic Deformation Profile and Position of the mMaximum Intrusion Node (Aluminum Plate)

The deformation profile at the end of the simulation, along with the position of the maximum intrusion node and the position of the node tracked by the DIC system in experimental tests, are shown in Figure 5.2c. Compared to the the previous step, the profile remains substantially the same, although the coordinate of the maximum intrusion node shifts slightly (15 mm) to the left.

Intrusion Over Time (Aluminum Plate)

As in the previous step, the intrusion plot is reported for completeness in Figure C.2. Although the comparison between step 1 and the v31 experimental band is again inconsequential, the comparison between step 0 and step 1 shows how the switch to the Simpson integration rule has a limited influence on the simulation accuracy for the specific load case. This is supported by the the LS-Dyna Keyword Manual [18], which deems the trapezoidal integration sufficient for most applications, but it must be noted that the switch to Simpson has the primary goal of aligning the baseline model with the delamination model, which can't compute single-ply stiffness without 3 integration points per ply.

Damage Pattern (Protection Plate)

The damage pattern on the protection plate at the end of the simulation is presented in Figure 5.3c. Like for the previous step, no insightful observations can be made.

5.1.3. Step 2: Correction of Impactor Size

Runtime

The total run time for this model is 527 s (wall clock). This is comparable to the previous step.

Plastic Deformation Profile and Position of the Maximum Intrusion Node (Aluminum Plate)

The deformation profile at the end of the simulation, along with the position of the maximum intrusion node and the position of the node tracked by the DIC system in experimental tests, are shown in Figure 5.2d. As was happening in the previous two steps, the intrusion area is shifted to the left, but this time, due to the longer impactor, the dynamics of the impact are modified: the impactor's "tail" hits the plate at around 150 mm, prolonging the intrusion area to the left, until around 200 mm. This has the added effect of distributing the impact over a larger length, resulting in a slightly smaller intrusion at the green node[6].

Intrusion Over Time (Aluminum Plate)

As in the previous step, the intrusion plot is reported for completeness in Figure C.3. Once again, comparing the simulations with the experimental curves is inconsequential, but in this case the comparison between step 1 and step 2 shows how changing the impactor size has little influence on the deformation of the orange node. This is probably due to the node coordinate being far from both the head and tail impact sites; if the switch had been performed after introducing the experimental errors, which shift the impact sites closer to the orange node, the difference between the steps would have been more pronounced.

Damage Pattern (Protection Plate)

The damage pattern on the protection plate at the end of the simulation is presented in Figure 5.3d. Like for the previous step, no insightful observations can be made.

5.1.4. Step 3: Introduction of Experimental Errors

Runtime

The total run time for this model is 589 s (wall clock). This is comparable to the previous step.

Plastic Deformation Profile and Position of the Maximum Intrusion Node (Aluminum Plate)

The deformation profile at the end of the simulation, along with the position of the maximum intrusion node and the position of the node tracked by the DIC system in experimental tests, are shown in Figure 5.2e. Compared to the experimentally derived profile (Figure 5.2a), this is a much better match than the previous simulations, as introducing the experimental errors changes the impact dynamics dramatically.

[6]Node of maximum intrusion.

In particular, the shift to the right of the impact position brings the main intrusion area and the green node much closer to their experimental counterparts. Still, there are some notable differences: the intrusion at 0 mm is comparable to the one at 370 mm, while in the experimental results the intrusion lowers slightly after the green node, but it maintains a rather high magnitude until the plate's end at 370 mm. This is probably due to the high scaling factor on the global friction, which creates a more localized intrusion; if so, the next step should improve on the match.

Intrusion Over Time (Aluminum Plate)

The intrusion over time for the orange node is reported in Figure C.4. Compared to the previous step, the curve gets closer to the experimental band in magnitude terms, but it completely loses its previous trend: the first peak (head impact) is much more pronounced than the second one (tail impact), showing how most of the impactor's energy is dissipated during the first contact. This is probably due to the high global friction scaling factor, which increases the initial contact time, and if that's the case, reducing it in the following step should restore the curve's shape.

Damage Pattern (Protection Plate)

The damage pattern on the protection plate at the end of the simulation is presented in Figure 5.3e. The damage has a teardrop shape, similar to the experimental result in Figure 5.3a, but it must be noted that the C-SCAN is highlighting the tear + delamination combination, with no possibility of distinguishing between the two, while in Section 3.4 the extent of each type of damage is determined, revealing a much narrower tear.

The considerable width of the simulation result, which cannot come from delamination as the baseline model is incapable of showing it, is due to the high friction scaling, which causes the impactor to lose too much energy during the head contact with the aluminum plate, coming back down slowly and tearing through the composite with its whole frontal area. If correct, the shape would become narrower again once the scaling factor is reduced.

An additional discrepancy is reported regarding the distance between the end of the tear and the plate's front end, which is too short.

5.1.5. Step 4: Change of Global Friction Scaling Factor

Runtime

The total run time for this model is 590 s (wall clock). This is comparable to the previous step.

Plastic Deformation Profile and Position of the Maximum Intrusion Node (Aluminum Plate)

The deformation profile at the end of the simulation, along with the position of the maximum intrusion node and the position of the node tracked by the DIC system in experimental tests, are shown in Figure 5.2f. Compared to the experimentally derived profile (Figure 5.2a), the match is quite good, and an improvement over the previous step as now the intrusion plateaus after the green node, confirming that reducing the scaling factor on global friction can accentuate the global bending response of the plate.

Interestingly, the green and orange nodes coincide, meaning that the simulation predicts the highest intrusion at the node tracked by the DIC system; this contrasts with the picture painted by the experimental results, where the green node is shifted to the left.

Intrusion Over Time (Aluminum Plate)

The intrusion over time for the orange node is reported in Figure C.5. As theorized in the previous paragraphs, lowering the global friction scaling factor restores the correct curve shape, with a lower first peak induced by the head impact, followed by a higher peak due to the tail impact.

This is in line with the fact, mentioned in 4.2.6, that the higher scaling was introduced to improve on the time-wise match of the peaks, which was thought to be caused by wrongly defined friction values. It is now apparent that the mismatch was in the major part due to a wrongly sized impactor, which has been fixed. Therefore, the global friction scaling factor can be again set to its standard value of 3.

Now that the bigger picture is accurate enough, it is possible to focus on a more specific discrepancy, which lies in the plastic portions of the curve. Even though the peaks are getting closer to the experimental band, the plastic deformations post-impact aren't. There are two possible reasons for this:

1. The bolt pre-load is too high, resulting in perfect clamping, while in tests the plates can slip slightly, allowing for more deformation without getting into plastic behaviour. While there is evidence in the video footage of this happening to a minor extent, it is highly unlikely for it to explain the discrepancy shown in the plots. To test for this, the pre-load is lowered from 4 kN to 2 kN to allow for more slipping and a test run has been performed, resulting in similar plastic behaviour (see Figure C.6), and thus disproving this theory. Furthermore, slipping was definitely not an intended behaviour during tests, and a 4 kN pre-load with large washers can be considered a lower bound.
2. The aluminum used in tests has different properties than the one used in simulations. The hypothesis comes from the fact that while the magnitude-wise match on the peaks can depend on the impact dynamics and on how specific components (e.g. the protection plate) are modeled, once that is achieved the plastic deformation will only depend on the aluminum plate properties.

Since the mismatch between the aluminum material card and the real material properties has been proven during the documentation phase for the project, material characterization for a more accurate (and strain rate dependent) aluminum has been performed (see Section 3.5) as an additional research outside of the main scope of the thesis. The new material card will be explored further in the relevant section (see C.2.9), but until then the mismatch in plastic intrusion magnitude won't be addressed further.

Damage Pattern (Protection Plate)

The damage pattern on the protection plate at the end of the simulation is presented in Figure 5.3f. The reduction in the tear width confirms the scaling factor hypothesis made at the previous step, and now both the tear's shape and dimensions are comparable to the experimental results, and the same can be said for the distance from the plate's front edge.

5.1.6. Step 5: Comparison of Bolts Pre-Load

Runtime

The total run time for this model is 545 s (wall clock). This is comparable to the previous step.

Plastic Deformation Profile and Position of the Maximum Intrusion Node (Aluminum Plate)

The deformation profile at the end of the simulation, along with the position of the maximum intrusion node and the position of the node tracked by the DIC system in experimental tests, are shown in Figure 5.2g. Compared to the previous step, the curve retains its positive features, but this time the green and orange nodes are not coincident anymore, with the green node now matching the position of the experimental one. Concerning the deformation profile, then, a 9 kN pre-load seems to improve on the model's accuracy.

Intrusion Over Time (Aluminum Plate)

The intrusion over time for the orange node is reported in Figure C.7. Compared to the previous step, it retains a realistic shape, but results in lower peaks, closer to the experimental band. As the peaks' magnitude reduction in the real tests could be caused by a multitude of factors, this plot alone is not enough to prove that a higher 9 kN pre-load is representative of the experimental situation.

Damage Pattern (Protection Plate)

The damage pattern on the protection plate at the end of the simulation is presented in Figure 5.3g. Compared to the previous model, the pattern is very similar, but the tear's length is slightly higher, now precisely matching the experimental result. This is again an indicator that the 9 kN bolts pre-load could be a realistic modeling choice, but can't be considered a definitive proof.

5.1.7. Step 6A: GLASS_1, Mesh 5 mm, Min. Timestep 5E-4 ms

Step 6A is effectively the same as Step 5, hence no additional considerations are needed.

5.1.8. Step 6B: GLASS_1, Mesh 2 mm, Min. Timestep 5E-4 ms

Runtime

The total run time for this model is 2987 s (wall clock). This is a significant increase (5.5 times higher) compared to the previous step, but it is expected due to the considerable mesh refinement (-60% mesh size) performed.

Plastic Deformation Profile and Position of the Maximum Intrusion Node (Aluminum Plate)

The deformation profile at the end of the simulation, along with the position of the maximum intrusion node and the position of the node tracked by the DIC system in experimental tests, are shown in Figure 5.2h. Compared to the previous step, no significant differences are reported, other than a more pronounced intrusion due to the tail impact, probably due to the difference in the protection plate's response.

Intrusion Over Time (Aluminum Plate)

The intrusion over time for the orange node is reported in Figure C.8. Compared to the previous step, no substantial differences are observable, other than a slight increase in the first peak, with a consequent increase of the post-impact plasticity.

Damage Pattern (Protection Plate)

The damage pattern on the protection plate at the end of the simulation is presented in Figure 5.3h. This is the definitive proof that this version shouldn't be used as the project's benchmark, as the tear, which extends all the way to the plate's front, is completely unrealistic and different from the experimental result.

The reason behind this most probably lies in the characterization process for material cards at the company. In crash simulations with very big models, meshes under 3 mm are considered to be unpractical, hence all the cards are calibrated for 3 to 5 mm mesh sizes. When refining the meshes, simulation results can be quite unpredictable and the card often requires additional calibrations. In this case, a 2 mm element size is incompatible with GLASS_1.

5.1.9. Step 6C: GLASS_1, Mesh 2 mm, Min. Timestep 5E-6 ms

Runtime

The total run time for this model is 5285 s (wall clock). This is 1.8 times higher than in the previous step, due to the minimum allowed timestep being reduced by a factor of 100.

Plastic Deformation Profile and Position of the Maximum Intrusion Node (Aluminum Plate)

The deformation profile at the end of the simulation, along with the position of the maximum intrusion node and the position of the node tracked by the DIC system in experimental tests, are shown in Figure 5.2i. Compared to the previous step, no significant differences are reported, highlighting that minimum allowed time-step reduction doesn't produce noticeable benefits.

Intrusion Over Time (Aluminum Plate)

The intrusion over time for the orange node is reported in Figure C.9. Compared to the previous step, the curve is almost exactly the same, confirming the conclusions derived from the observations on the plastic deformation profile.

Damage Pattern (Protection Plate)

The damage pattern on the protection plate at the end of the simulation is presented in Figure 5.3i. The same considerations made for the previous step apply.

5.1.10. Step 6D: GLASS_2, Mesh 5 mm, Min. Timestep 5E-4 ms

Runtime

The total run time for this model is 577 s (wall clock). This is comparable with the runtime of Step 5, highlighting how the GLASS_2 material carries a similar computational weight to the GLASS_1.

Plastic Deformation Profile and Position of the Maximum Intrusion Node (Aluminum Plate)

The deformation profile at the end of the simulation, along with the position of the maximum intrusion node and the position of the node tracked by the DIC system in experimental tests, are shown in Figure 5.2j. Compared to the experimentally derived profile (Figure 5.2a), the match is generally good. Notably, the green node is located at the plate's edge, at 370 mm. Although this doesn't happen in the experimental profile, the differences in intrusion between the area around the 200 mm coordinate and the plate's end is small (around 2 mm in the real test), hence very small differences in intrusion can cause a shift in the green node position.

Intrusion Over Time (Aluminum Plate)

The intrusion over time for the orange node is reported in Figure C.10. Compared to the corresponding step with GLASS_1, the new material card causes a slight reduction in the second peak's magnitude, and a time-wise shift to the left of the same peak by around 2 ms. This is probably due to the unique behaviour of the protection plate in this step, which will be explained while discussing its damage pattern.

Damage Pattern (Protection Plate)

The damage pattern on the protection plate at the end of the simulation is presented in Figure 5.3j. The plate appears to be completely undamaged, therefore it is clearly incapable to accurately model the impact event.

5.1.11. Step 6E: GLASS_2, Mesh 2 mm, Min. Timestep 5E-4 ms

Runtime

The total run time for this model is 2928 s (wall clock). This increase follows a similar pattern as the one highlighted for step 5 to step 6B, as it also happens due to the applied mesh refinement.

Plastic Deformation Profile and Position of the Maximum Intrusion Node (Aluminum Plate)

The deformation profile at the end of the simulation, along with the position of the maximum intrusion node and the position of the node tracked by the DIC system in experimental tests, are shown in Figure 5.2k. Compared to the previous step, mesh refinement brings the green node back towards the center of the plate, while the other features remain unvaried.

Intrusion Over Time (Aluminum Plate)

The intrusion over time for the orange node is reported in Figure C.11. Compared to the previous step, the second peak shifts again to the right, matching steps 5 (i.e. 6A), 6B and 6C time-wise; his confirms the hypothesis that the shift at the previous step was caused by the protection plate's behaviour.

Magnitude-wise, a substantial reduction in the intrusion at the second peak is observed, with the simulation now matching the lower experimental bound (i.e. the DIC measurement, see Section 3.1.3).

Damage Pattern (Protection Plate)

The damage pattern on the protection plate at the end of the simulation is presented in Figure 5.3k. Mesh refinement in this case appears to benefit the model's performance, showing a tear size and distance from the plate's front edge compatible with the experimental result, although on the shorter side. This is acceptable as delamination implementation will likely lengthen the damage area.

5.1.12. Step 6F: GLASS_2, Mesh 2 mm, Min. Timestep 5E-6 ms

Runtime

The total run time for this model is 5071 s (wall clock). This increase follows a similar pattern as the one highlighted for step 6B to 6C, as it also happens due to the minimum allowed timestep reduction.

Plastic Deformation Profile and Position of the Maximum Intrusion Node (Aluminum Plate)

The deformation profile at the end of the simulation, along with the position of the maximum intrusion node and the position of the node tracked by the DIC system in experimental tests, are shown in Figure 5.2l. Compared to the previous step, no significant differences are reported, highlighting that minimum allowed time-step reduction doesn't produce noticeable benefits, like in step 6C.

Intrusion Over Time (Aluminum Plate)

The intrusion over time for the orange node is reported in Figure C.12. Compared to the previous step, the curve is almost exactly the same, confirming the conclusions derived from the observations on the plastic deformation profile.

Damage Pattern (Protection Plate)

The damage pattern on the protection plate at the end of the simulation is presented in Figure 5.3l. The same considerations from the previous step apply here; additionally, it can be observed how minimum time-step reduction doesn't significantly influence the pattern's characteristics.

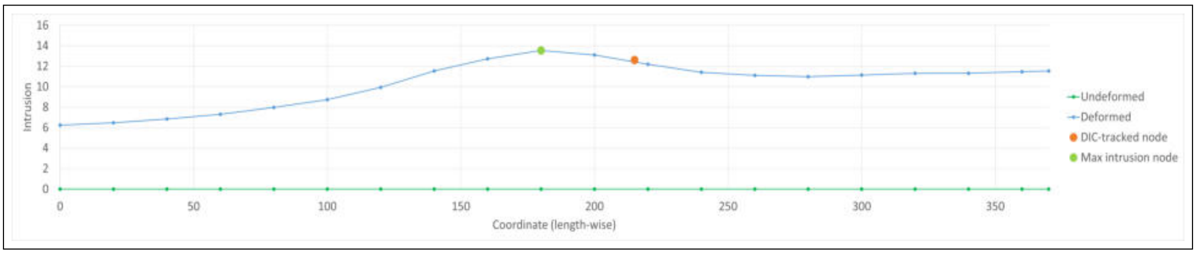

(a) Experimental

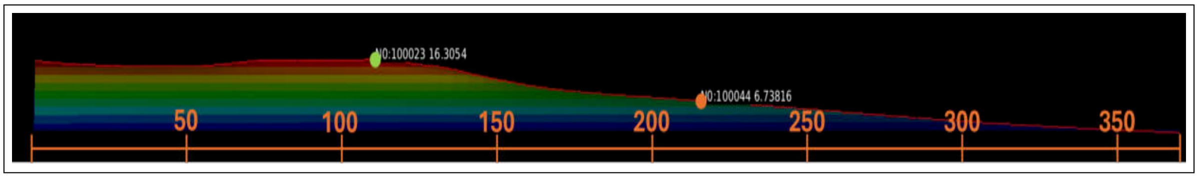

(b) Step 0

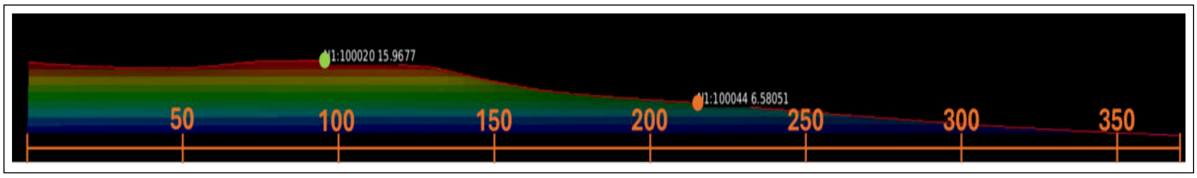

(c) Step 1

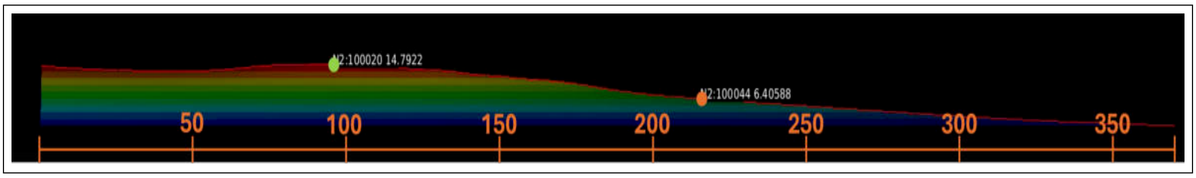

(d) Step 2

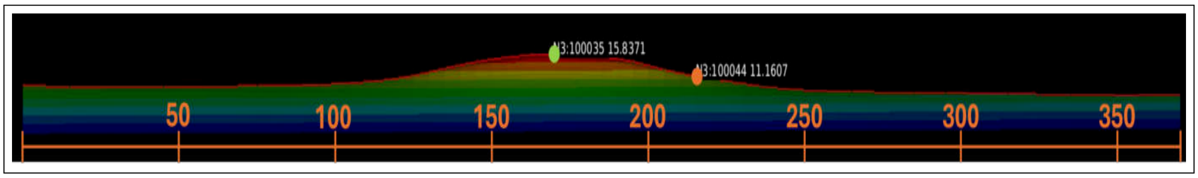

(e) Step 3

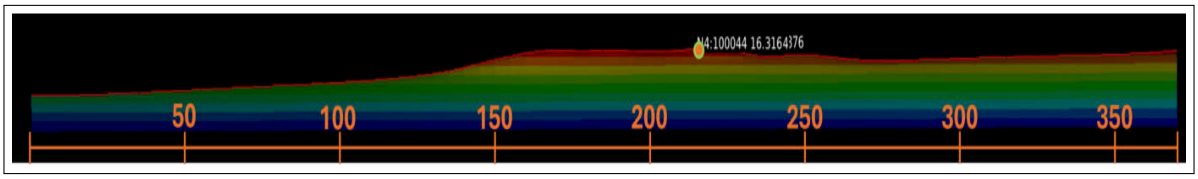

(f) Step 4

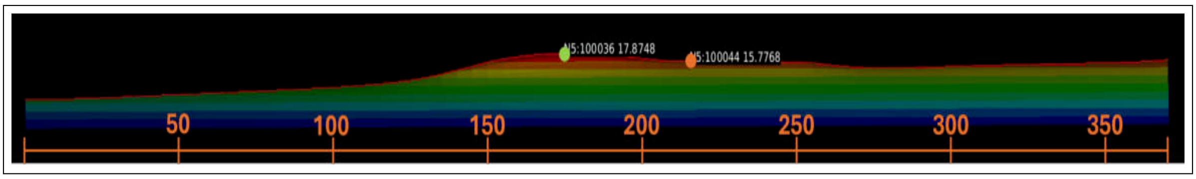

(g) Step 5

Continued on next page...

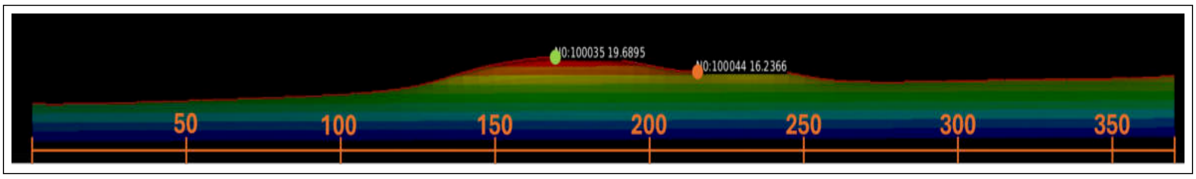

(h) Step 6B

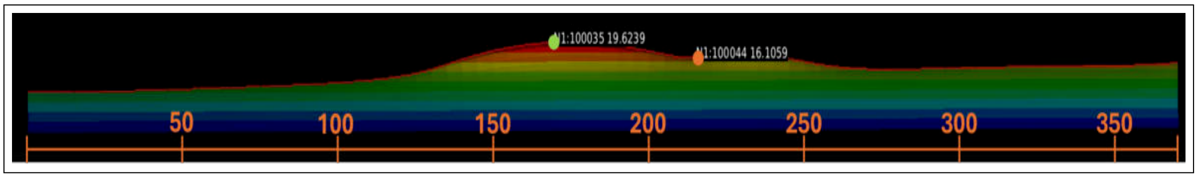

(i) Step 6C

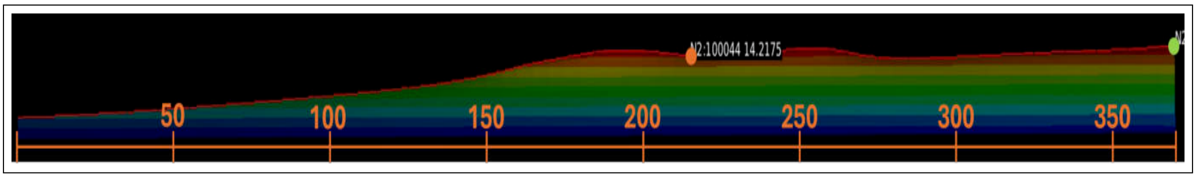

(j) Step 6D

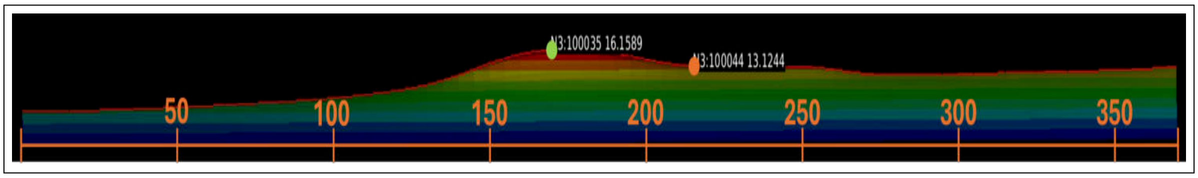

(k) Step 6E

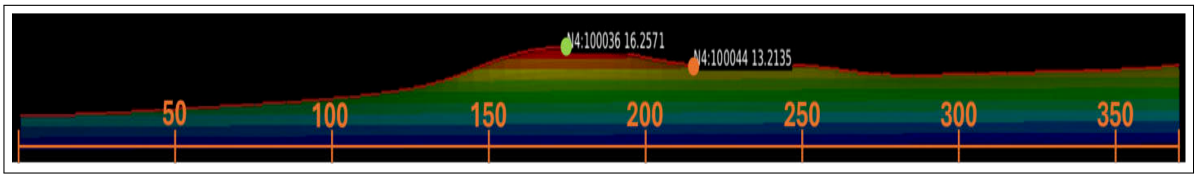

(l) Step 6F

Figure 5.2: Comparison of profile deformation: Experimental vs. Simulation, steps 0 to 6F.

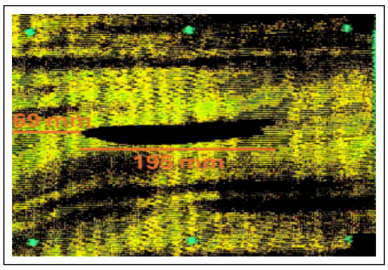

(a) Experimental

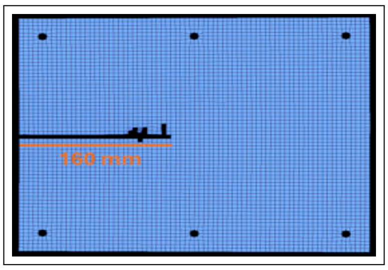

(b) Step 0

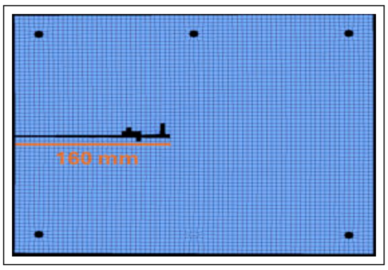

(c) Step 1

Continued on next page...

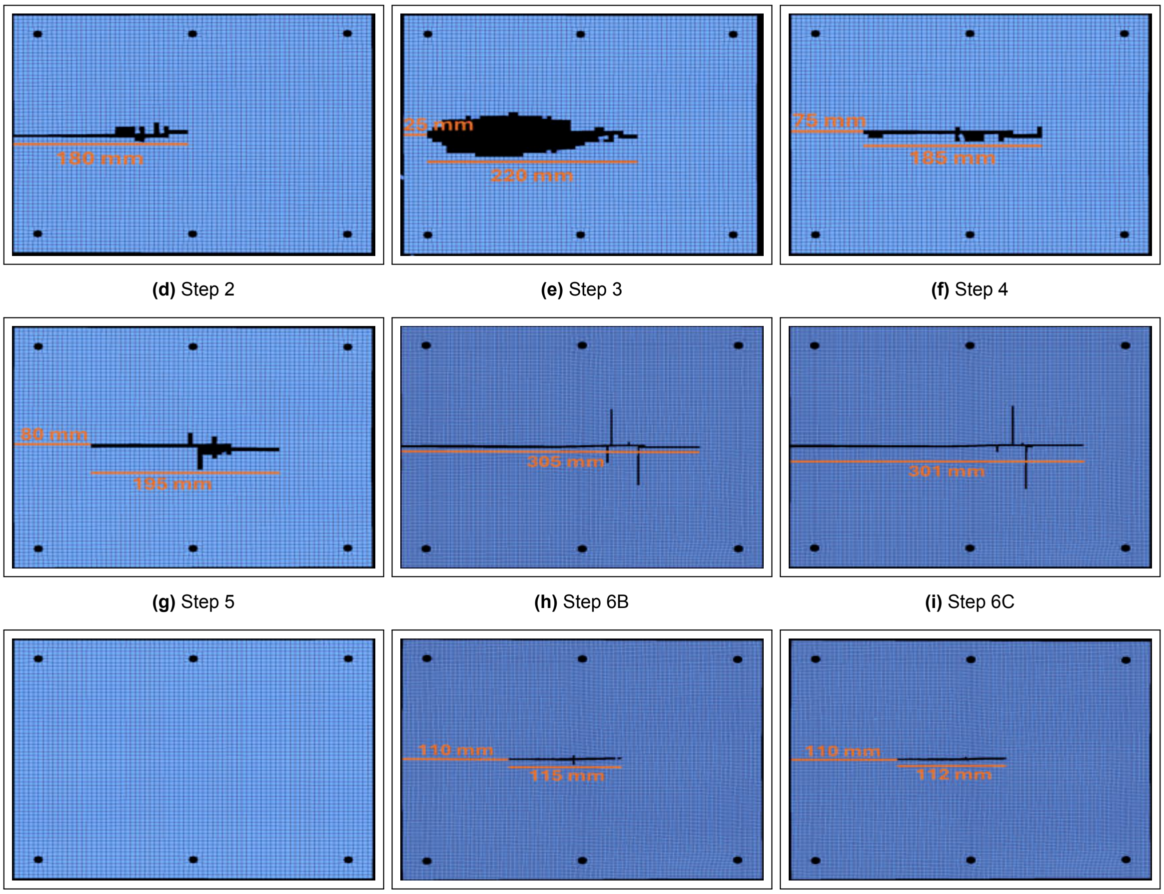

(d) Step 2 **(e)** Step 3 **(f)** Step 4

(g) Step 5 **(h)** Step 6B **(i)** Step 6C

(j) Step 6D **(k)** Step 6E **(l)** Step 6F

Figure 5.3: Comparison of damage patterns: Experimental result (C-SCAN of V31) vs. Simulation, steps 0 to 6F.

5.1.13. Summary and Final Considerations

To summarize the results from the baseline simulations workflow, Table 5.2 has been compiled, adopting the same "traffic light" approach proposed in the previous chapters; this allows to get an overview of all the markers (see Table 5.1) for each step, assessing them together for more meaningful conclusions.

First, steps 0 to 2 appear incapable of accurately capturing the impact dynamics; this was expected, as they don't model experimental errors, but they are valuable when compared between each other, as they highlight the effects of integration rule switching and update of the impactor model.

Step 3 starts to produce meaningful results, as experimental errors are introduced but it is with the reduction of the global friction scaling at step 4 that the plastic deformation profile, one of the most important markers for simulation accuracy, starts to match experimental results.

Step 5 (6A in the following parametric study) further improves the match by increasing the bolts pre-load, and all markers show a good match with experimental results. Still, it must be noted that preferring it over the 4 kN pre-load of the previous step is mostly due to the improvement on the green node position, which although a telling indicator, could be a false flag given the multitude of influencing parameters involved in its determination; as proceeding with both pre-loads would result in doubling the project's time to completion, a choice has to be made based on the available data, which favours the 9 kN pre-load.

Then, the parametric study (see Section 4.2.8) is performed. Mesh refinement in step 6B worsens the results, turning the damage pattern on the protection plate into a completely unrealistic tear, and the subsequent minimum timestep reduction in step 6C doesn't produce any meaningful improvement.

The material ID switch from step 6A to 6D produces acceptable results for all markers except the damage pattern, as the simulation fails to capture any damage on it. In this case, mesh refinement in step 6E seems to improve on the results, with all markers showing a good match with the experimental results. Then, timestep reduction in step 6F doesn't seem to produce any meaningful change in the results, although it dramatically increases the runtime.

Given all these considerations, both steps 6A (GLASS_1, 5 mm mesh size) and 6E (GLASS_2, 2 mm mesh size) represent good candidates as benchmark baseline models for the project. They show slightly different behaviour intrusion-wise, with the peak intrusion of the orange node being lower (-13.4%) for 6E (16.1 mm) than for 6A (18.6 mm), but they share a comparable general intrusion shape time-wise, and a similar deformation profile.

Picking both models for delamination implementation represents an interesting choice, as it allows to work at different mesh sizes, understanding how mesh dependent certain parameters can be.

Furthermore, two strong cases can be made for each model:

- **6A:** bigger element size gives faster simulations and ease of integration in existing models in use at the company; furthermore, between the two material IDs, GLASS_1 is the most widely used and recognized, while the GLASS_2 is more experimental and calibrated for specific high-speed applications.
- **6E:** finer mesh allows for more accurate delamination shapes, easier to compare with C-SCANS; furthermore, the lower intrusion values provide an already improved baseline model, thus the expected reduction produced by delamination modeling (in case CCRIT is implemented) doesn't need to be as dramatic as for GLASS_1. This would probably be more in line with the expected energy absorption capabilities of localized delaminations.

In light of these considerations, GLASS_2 will be analyzed first, as a calibration process against C-SCAN results is expected to be necessary to fine-tune the strength values presented in Section 2.5.7, and a finer mesh (to which GLASS_1 reacts poorly, as seen in Section 5.1.8) will be useful in precisely determining the delaminated area's shape and dimensions.

Then, the finalized delamination model parameters determined for GLASS_2 will be used to replicate the implementation for GLASS_1, thus testing both mesh and material model sensitivity of the new approach.

Step	Runtime	Plastic Def. Profile	Green Node Pos.	Orange Node Intr.	Damage Pattern
0	GOOD	BAD	BAD	BAD	BAD
1	GOOD	BAD	BAD	BAD	BAD
2	GOOD	BAD	BAD	BAD	BAD
3	GOOD	MID	GOOD	MID	MID
4	GOOD	GOOD	MID	MID	GOOD
5 (6A)	GOOD	GOOD	GOOD	GOOD	GOOD
6B	MID	GOOD	GOOD	GOOD	RED
6C	RED	GOOD	GOOD	GOOD	BAD
6D	GOOD	GOOD	MID	GOOD	BAD
6E	MID	GOOD	GOOD	GOOD	GOOD
6F	BAD	GOOD	GOOD	GOOD	GOOD

Table 5.2: Comparison between between Baseline model's behaviours at different steps.

5.2. Delamination Model with GLASS_2

The GLASS_2 workflow is an intermediate step in this project:

it marks the first implementation of the delamination model, where LS-Dyna-specific modeling choices are made and evaluated, and it deals with the verification of the proposed contact parameter values through a structured Design of Experiments (DoE) study, arguing for a full strength-based approach by demonstrating the limited influence of fracture energy dissipation on intrusion reduction. Furthermore, it verifies the generality of the implementation by modeling different impact scenarios and layups. Finally, it deals with other significant implementations that might have relevance in improving the test/simulation match, such as an updated material card for the aluminum blank, and material-specific coefficients of friction.

From the physical and modeling insights generated by the GLASS_2 workflow, a new workflow (GLASS_1) is designed (see Figure 4.15) and executed, providing the final results for the project.

Due to its intermediate nature between the baseline and final models, and since many of the simulation steps will be re-proposed in an improved format in the GLASS_1 workflow, the results for the GLASS_2 workflow are only reported in summary format in the following sub-section, along with final considerations. For a complete discussion in a step-by-step format, see Appendix C.2.

5.2.1. Summary and Final Considerations

After analyzing all the GLASS_2-related simulation results, conclusions can be drawn.

First, the good match achieved with the C-Scans (see Section C.2.3) shows how the developed model is able to capture the delamination shape with good accuracy, which is retained when impact conditions (see Sections C.2.5 and C.2.6) and laminate sequence (see Section C.2.7) are changed, proving the framework generality in this regard.

On the negative side, the reduced mesh size and the two-way contact formulation raise the computational effort and simulation time considerably. Furthermore, the reduced mesh size made it necessary to use the GLASS_2 card, as GLASS_1 didn't perform well with a refined mesh (see Section 5.1.8); although it allows to use literature values directly for contact parameters (see Section C.2.4), proving the hypothesis proposed in Section 2.5.7, this is sub-optimal, as between the two calibrations, GLASS_1 is the most accurate modeling of the material, and the most widely used within the company.

As per the effect of delamination modeling on the intrusion plot, a slight increase of the intrusion magnitude has been observed in both the main (see Section C.2.2) and validation (see Sections C.2.5, C.2.6 and C.2.7) models, due to the obvious reduction in stiffness of the area surrounding the tear in the composite plate, caused by plies separation. Note that no inter-ply friction has been introduced between the plies; this can be problematic as after the head impact causes delamination and separates the plies, the tail impact applies pressure to the "flaps" at the sides of the tear: if no inter-ply friction is defined, each ply's flap slides freely on the ones above and below, offering minimal resistance to the impactor. When inter-ply friction is defined instead, there is resistance to the relative sliding, and under pressure the flaps behave like a single body, offering more resistance to the tail impact, and reducing the second peak's magnitude.

Concerning the energy absorption due to delamination, the C-Scan results show an area too small to cause enough dissipation to significantly reduce the impactor's kinetic energy post-impact and improve on the test/simulation match (see Section C.2.4 for a simplified calculation supporting the argument), thus proving that not implementing a fracture dynamics approach has been the correct choice, as keeping CCRIT=0 won't affect the model accuracy while significantly decreasing the material characterization effort.

Moving to the aluminum plate, the newly characterized material card (ALU_2) has shown a reduction in intrusion and a more realistic deformation shape (see Section C.2.9), although it is not enough to match the experimentally measured intrusion plots; for that, the strain-rate sensitive aluminum material card (ALU_3) needs to be introduced, but extremely high, and thus unrealistic, Cowper-Symonds coefficients are necessary to achieve a satisfactory match (see Section C.2.10). Since the strain-rate sensitivity of aluminum is usually low, it is clear that this phenomenon cannot explain the intrusion discrepancy.

Since neither delamination implementation nor changing the aluminum material card can completely fix the test/simulation mismatch, one or multiple other causes need to be determined. By systematically analyzing the model's assumptions, the one most likely responsible for the mismatch is the selected set of experimental errors introduced in the simulation. In Section 4.4.9, along with the experimental errors implemented until now, the impactor has been reported to rotate slightly along its longitudinal axis, while also tilting along the plane parallel to the floor. The first rotation has been measured by the experimental set-up, while the magnitude of the tilt is unknown. Furthermore, the impact point has been reported to be 5 mm to the side of the composite plate's major symmetry axis (i.e., there is a 5 mm translation in the y-direction). These additional errors haven't been implemented until now because they have been deemed not relevant (rotation and y-translation) or because no experimental data was available (tilt); moreover, their implementation would have considerably increased the complexity of the impactor dynamics, while the focus of the project resided in determining the influence of delamination modeling on the test/simulation match. At this stage though, after the delamination influence and behaviour have been clarified, a procedure can be defined to determine these errors and implement them in the simulation.

In light of these considerations, an updated simulations plan can be drafted following the recommendations proposed in Table 5.3, resulting in the workflow proposed in Section 4.4. The results of these simulations will be analyzed in the next section.

Observation	Recommendation
High simulation time	Increase mesh size, check for delamination shape accuracy
GLASS_2 was necessary due to mesh size refinement, but it has less generality than GLASS_1	Switch to GLASS_1
Energy absorbed by delamination isn't critical for the test/simulation match	Keep CCRIT=0
No inter-ply friction was defined between the plies, although it might play a role in the impact dynamics	Introduce inter-ply friction and determine its influence
The new aluminum material card (ALU_2) shows an improvement in the test/simulation match	Use ALU_2 in the new simulations
Strain rate sensitivity (ALU_3) can explain the test/simulations mismatch only when unrealistic Cowper-Symonds coefficients are used	Do not use ALU_3, as it would introduce additional parameters, that if kept within realistic ranges don't significantly improve on the test/simulation match
The simplification of the impactor dynamics might play a big role in the test/simulation mismatch	Impactor y-position, rotation and tilt should be introduced

Table 5.3: Recommendations based on GLASS_2 Model results

5.3. Delamination Model with GLASS_1

V31 test results are the target reference, and the same markers presented in the previous sections (see Table 5.1) are considered to assess the model's performance, but since the workflow also integrates additional impactor shift and tilts to more accurately represent the impact dynamics, the full C-SCAN results, comprising the portion of delamination caused by the tail impact (see Figure C.13), are used as experimental target. Furthermore, the intrusion plots now all refer to the exact node that was tracked by the DIC-system (i.e., slightly shifted in the positive y-direction compared to the plate's mid-section), while as explained, in the previous workflow they referred to a node with the same x-coordinate but y-coordinate equal to 0 (i.e., lying on the plate's mid-section). Note that in the intrusion plot, only the lower bound of the experimental band (i.e., the DIC-measured intrusion) is reported.

5.3.1. F1: Delaminating New Model

Runtime

The total runtime for this model is 1116 s (wall clock). Although both reduced timestep and two-way contact formulation are in use, the coarser mesh size results in a percentage variation of the simulation time of -90.2% compared to the equivalent model from the previous workflow (step 9).

Plastic Deformation Profile and Position of the Maximum Intrusion Node (Aluminum Plate)

The deformation profile at the end of the simulation, along with the position of the maximum intrusion node and the position of the node tracked by the DIC system in experimental tests, are shown in Figure 5.4b. Compared to the experimental curve, the tail impact extends the intrusion area between the 200 mm and 250 mm marks.

Intrusion Over Time (Aluminum Plate)

The intrusion over time for the orange node is reported in Figure C.42. Although a good time-wise match of the peaks can be observed, both the peak and plastic intrusions are considerably far from the experimental plot (see Table 5.4 for percentage variations); this can partially be ascribed to the numerical issues happening around the screw holes, resulting in plate slipping and non-physical behaviour.

Damage Pattern (Protection Plate)

The damage pattern on the protection plate at the end of the simulation is presented in Figure 5.5a. Extensive element failure and delamination around all plate holes signal that re-evaluation of the contact parameters for the protection plate and/or holes is needed.

5.3.2. F2: One-Way Contact Formulation with Reduced Timestep

Runtime

The total runtime for this model is 885 s (wall clock). The switch to a one-way formulation produced a considerable decrease in the run-time, with a relative change of -20% w.r.t. the previous step.

Plastic Deformation Profile and Position of the Maximum Intrusion Node (Aluminum Plate)

The deformation profile at the end of the simulation, along with the position of the maximum intrusion node and the position of the node tracked by the DIC system in experimental tests, are shown in Figure 5.4c. As in the previous step, the intrusion area extends in the 200-250 mm segment.

Intrusion Over Time (Aluminum Plate)

The intrusion over time for the orange node is reported in Figure C.43. The switch to a one-way contact formulation, which solved the numerical issues encountered in the previous steps, results in a decrease of intrusion magnitude for both peaks and for the plastic intrusion after the first peak, while the final plastic intrusion remains approximately the same.

Damage Pattern (Protection Plate)

The damage pattern on the protection plate at the end of the simulation is presented in Figure 5.5b. Although the numerical issues of the previous step are solved, the plate doesn't show any sign of delamination; this happens as a coarser mesh might require strength parameter re-calibration, confirming the hypothesis proposed in Section 2.5.7.

5.3.3. F3: Recalibration of Contact Parameters

Runtime

The total runtime for this model is 796 s (wall clock), which is comparable to the previous step.

Plastic Deformation Profile and Position of the Maximum Intrusion Node (Aluminum Plate)

The deformation profile at the end of the simulation, along with the position of the maximum intrusion node and the position of the node tracked by the DIC system in experimental tests, are shown in Figure 5.4d. The general shape is compatible with the one observed in the previous step.

Intrusion Over Time (Aluminum Plate)

The intrusion over time for the orange node is reported in Figure C.44. The re-calibration of contact parameters to allow for delamination with a coarser mesh results in a ”plowing” motion of the impactor, already encountered in Section C.2.11. As it will be shown shortly, this motion produces a large tear in the plate, dissipating more energy and reducing the intrusion compared to the previous step, even though the expected result would have been no plowing and a slight increase in the intrusion due to the reduction in bending stiffness caused by the delamination and the absence of energy dissipation (as CCRIT=0).

Damage Pattern (Protection Plate)

The damage pattern on the protection plate at the end of the simulation is presented in Figure 5.5c. Although the plate now shows delamination, its pattern doesn’t match the experimentally measured one, due to extensive element failure caused by the ”plowing” motion previously detailed.

5.3.4. F4: Update of the Aluminum Material Model

Runtime

The total runtime for this model is 846 s (wall clock), which is comparable to the previous step.

Plastic Deformation Profile and Position of the Maximum Intrusion Node (Aluminum Plate)

The deformation profile at the end of the simulation, along with the position of the maximum intrusion node and the position of the node tracked by the DIC system in experimental tests, are shown in Figure 5.4e. Compared to the previous steps, the current model produces a decrease in the 200-250 mm segment intrusion, highlighting how the updated aluminum material card helps improving the test/simulation match.

Intrusion Over Time (Aluminum Plate)

The intrusion over time for the orange node is reported in Figure C.45. As expected, the new aluminum material card results in a decrease of intrusion, but it must be noted that the beneficial ”plowing” effect of the previous step is still present and will be addressed in the next step.

Damage Pattern (Protection Plate)

The damage pattern on the protection plate at the end of the simulation is presented in Figure 5.5d. The pattern is substantially the same as in the previous step, as the ”plowing” dynamic persists.

5.3.5. F5: Introduction of Inter-Ply Friction

Runtime

The total runtime for this model is 1188 s (wall clock), which is a relative increase of +40% compared to the previous step, which is due to the newly introduced inter-ply friction.

Plastic Deformation Profile and Position of the Maximum Intrusion Node (Aluminum Plate)

The deformation profile at the end of the simulation, along with the position of the maximum intrusion node and the position of the node tracked by the DIC system in experimental tests, are shown in Figure 5.4f. Introduction of inter-ply friction doesn’t seem to significantly alter the profile, compared to the previous step.

Intrusion Over Time (Aluminum Plate)

The intrusion over time for the orange node is reported in Figure C.46. Compared to the previous step, the introduction of inter-ply friction helped solving the ”plowing” effect, due to higher resistance of the delaminated flaps to the impactor motion, which is pushed down earlier after the first impact, resulting in a smaller tear, as it will be shown later, and a smaller first peak; this in turn will naturally give a higher second peak, as the impactor retains more of its kinetic energy. This is beneficial as it helps improving the match for both peaks (see Table 5.4 for percentage variations).

Damage Pattern (Protection Plate)

The damage pattern on the protection plate at the end of the simulation is presented in Figure 5.5e. Due to the mechanism previously detailed, the ”plowing” issue is solved, and a smaller tear, compatible with the experimental results, is now present. On the negative side, anomalous failures are now present again around the holes: this can probably be ascribed to the complex screw-hole contact coupled with a coarser mesh than in the previous workflow, and might require introduction of reinforcing beams all-around the holes. Although not perfectly accurate, as it could alter the loading path of the beams in compression, this solution should have a small influence on the final results and plate dynamics while dramatically helping to solve the persisting issue. To check for this hypothesis, the reinforcing contact beams will be re-introduced all-around the holes in the next step, and their influence on the simulation results will be thoroughly examined.

5.3.6. F6: Re-Evaluation of Reinforcing Beams Around Plate Holes

Runtime

The total runtime for this model is 1121 s (wall clock), which is comparable to the previous step.

Plastic Deformation Profile and Position of the Maximum Intrusion Node (Aluminum Plate)

The deformation profile at the end of the simulation, along with the position of the maximum intrusion node and the position of the node tracked by the DIC system in experimental tests, are shown in Figure 5.4g. Compared to the previous step, the profile shape remains substantially the same.

Intrusion Over Time (Aluminum Plate)

The intrusion over time for the orange node is reported in Figure C.47. As the previous step presented failures around 3 holes due to numerical issues, more slipping of the plate was allowed, resulting in more elastic deformation and less plastic intrusion. Although it helped matching the experimental curve, this had to be corrected and with the re-introduction of the reinforcing beams, the final plastic intrusion is again increased, getting further from the target (see Table 5.4 for percentage variations). It must be noted that since the numerical errors happened quite late in the simulation, only the last portion of the intrusion plot (after t=15 ms) presents significant differences with the previous step, showing how the introduction of the reinforcing beams all-around the holes doesn't compromise the meaningfulness of the results.

Damage Pattern (Protection Plate)

The damage pattern on the protection plate at the end of the simulation is presented in Figure 5.5f. A good match is achieved, although the tail-induced delamination is missing, as the impactor rotations required to obtain it are still missing and will be introduced in the next steps.

5.3.7. F7: Change of the Impactor Initial Position in the Y-Direction

Runtime

The total runtime for this model is 837 s (wall clock). This is shorter than the previous step, and it could be probably explained by more favorable impact conditions that reduced the amount of plastic intrusion, in favor of a computationally less expensive elastic deformation.

Plastic Deformation Profile and Position of the Maximum Intrusion Node (Aluminum Plate)

The deformation profile at the end of the simulation, along with the position of the maximum intrusion node and the position of the node tracked by the DIC system in experimental tests, are shown in Figure 5.4h. Shifting the impact in the y-direction makes it so that a slight bump can be seen in the 150-200 mm segment. This is the intrusion caused by the head impact, which is not localized on the mid-section cut anymore. As the data used to build the experimental profile is gathered at the mid-section, though, the bump can be disregarded. As per the general shape of the profile, it is quite similar to the previous step, although an expected small reduction of plastic intrusion can be observed.

Intrusion Over Time (Aluminum Plate)

The intrusion over time for the orange node is reported in Figure C.48. Even though the impact direction is now aligned with the tracked node, a slight reduction in the second peak and final plastic intrusion can be observed (see Table 5.4 for percentage variations), showing how even a small variation in the y-coordinate of the impactor (see Figure 4.16) produces measurable changes in the intrusion.

Notably, this step marks a small worsening of the match for both peaks; this is because, as it was argued in Section 4.4.10, the y-direction shift of the impact position introduced in this step was in fact a secondary effect of the impactor rotation and tilt (due to geometric coupling) applied in Step F9, therefore its standalone introduction doesn't match the actual impact dynamics and has a detrimental effect on the results.

Damage Pattern (Protection Plate)

The damage pattern on the protection plate at the end of the simulation is presented in Figure 5.5g. The delamination area is now bigger, worsening the match with the experimental pattern. This can be explained by the fact that the shift in the y-direction of the impactor introduced in the current step was caused by a geometric coupling with the impactor rotation, hence the current set-up, missing the rotation, isn't fully representative of the real impact dynamics.

5.3.8. F8: Re-Evaluation of Impact Dynamics (1st Iteration)

Runtime

The total runtime for this model is 859 s (wall clock), which is comparable to the previous step.

Plastic Deformation Profile and Position of the Maximum Intrusion Node (Aluminum Plate)

The deformation profile at the end of the simulation, along with the position of the maximum intrusion node and the position of the node tracked by the DIC system in experimental tests, are shown in Figure 5.4i. Among all the profiles analyzed until now, the best match with experimental results is achieved, although the bumps not localized on the mid-section appear to be too prominent compared to what can be seen on the test specimen. This issue will be addressed in the next step.

Intrusion Over Time (Aluminum Plate)

The intrusion over time for the orange node is reported in Figure C.49. The improvement of the match across all the simulation time-span is considerable, highlighting the critical role played by accurate modeling of all impactor parameters. The most apparent remaining discrepancies are in the second peak, which is too low compared to the experimental results, and in the final plastic intrusion, which is instead too high (see Table 5.4 for percentage variations). This can be explained by the fact that, as explained in Section 4.4.10, the y-coordinate of the impact in the simulation is 170 mm instead of the experimentally measured 165 mm, thus shifting the maximum intrusion node farther from the tracked one and reducing the measured intrusion magnitude. This hypothesis is supported by the previously made observation that a large bump was present in the background (i.e., at a different y-coordinate) of the measured mid-section profile.

Damage Pattern (Protection Plate)

The damage pattern on the protection plate at the end of the simulation is presented in Figure 5.5h. A considerable improvement from the previous step can be observed in the general shape of the delamination, although it appears to be shifted in the positive y direction compared to the experimental envelope; this is consistent with the previous observations, and will be addressed in the next step.

5.3.9. F9: Re-Evaluation of Impact Dynamics (2nd Iteration)

Runtime

The total runtime for this model is comparable to the previous step.

Plastic Deformation Profile and Position of the Maximum Intrusion Node (Aluminum Plate)

The deformation profile at the end of the simulation, along with the position of the maximum intrusion node and the position of the node tracked by the DIC system in experimental tests, are shown in Figure 5.4j. There is a really good match with the experimental curve, and the bumps not localized on the mid-section are not as pronounced as in the previous step, showing how the second iteration on the re-evaluation of the impact dynamics produced an improved test/simulation match.

Intrusion Over Time (Aluminum Plate)

The intrusion over time for the orange node is reported in Figure C.50. The corrections made in the current step improve on the match of the second peak and on the final plastic intrusion, as expected. The match with the experimental results is now extremely good at all critical points (see Table 5.4 for percentage variations), and the current step results can be considered a satisfying end-point for the project.

Damage Pattern (Protection Plate)

The damage pattern on the protection plate at the end of the simulation is presented in Figure 5.5i. Excellent agreement can be observed in the delamination shape, position and length; furthermore, the effect of the tail impact, whose direction is highlighted in the picture, is correctly represented, resulting in a slightly curved delamination shape.

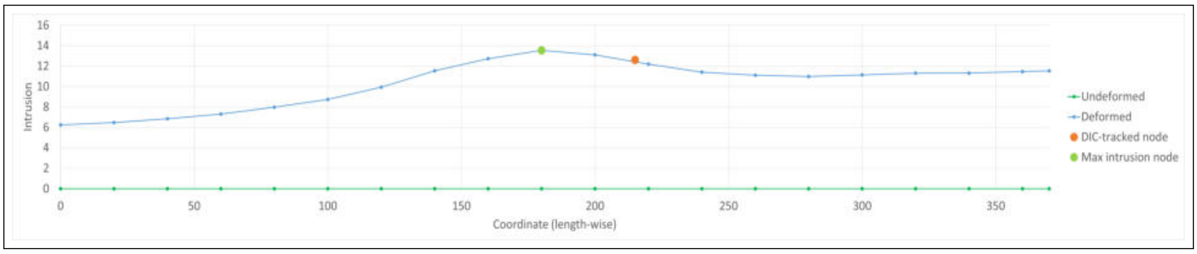

(a) Experimental (V31)

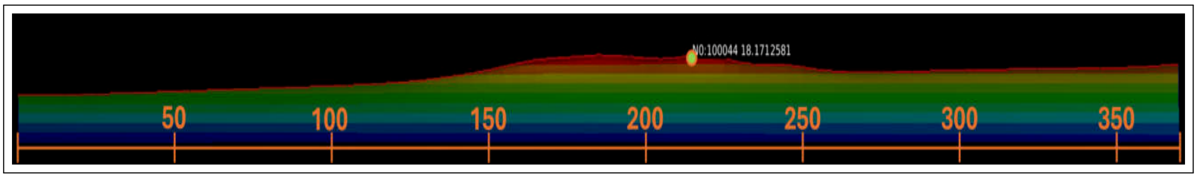

(b) Step F1: Delaminating New Model

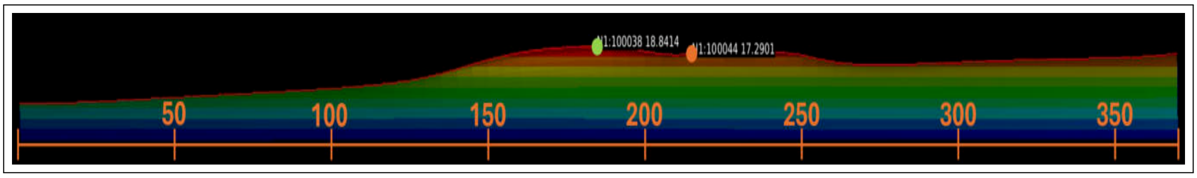

(c) Step F2: One-way contact formulation with reduced timestep

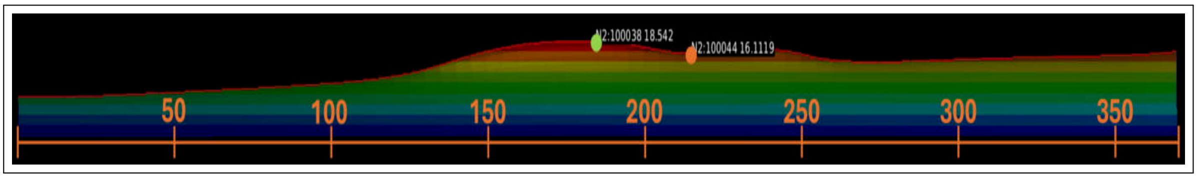

(d) Step F3: Recalibration of contact parameters

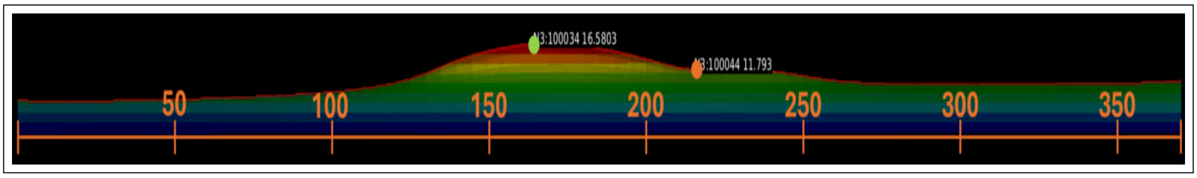

(e) Step F4: Update of the aluminum material model

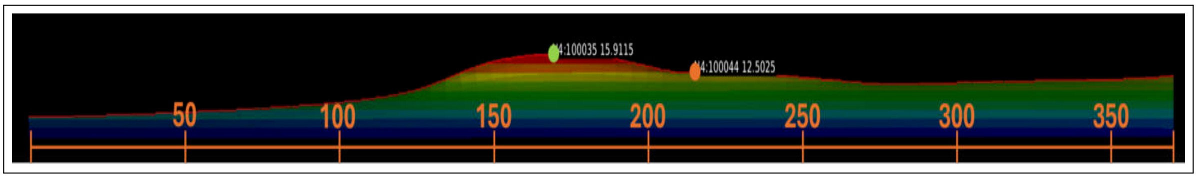

(f) Step F5: Introduction of inter-ply friction

Continued on next page...

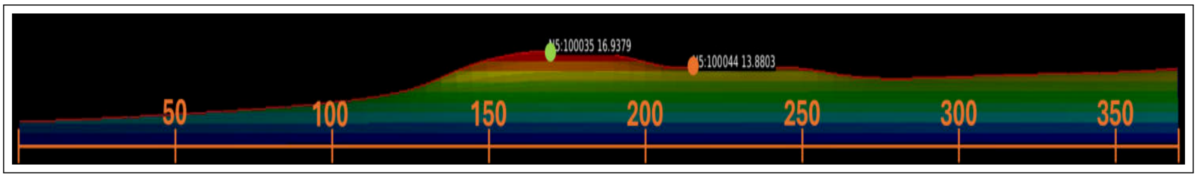

(g) Step F6: Re-evaluation of reinforcing beams around plate holes

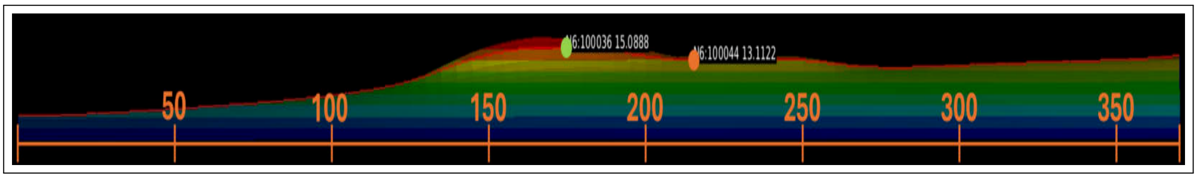

(h) Step F7: Change of the impactor initial position in the y-direction

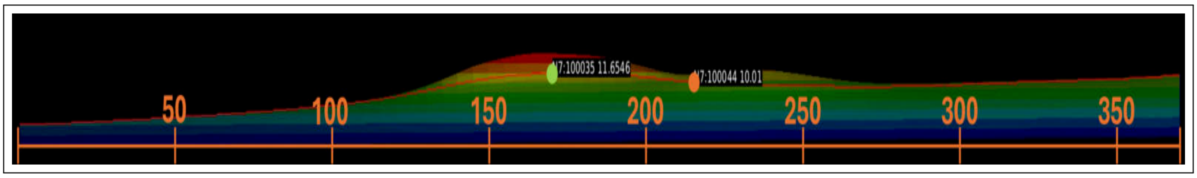

(i) Step F8: Re-evaluation of impactor dynamics (1st iteration)

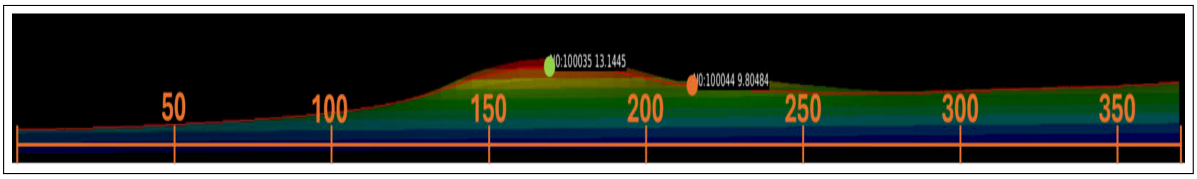

(j) Step F9: Re-evaluation of impactor dynamics (2nd iteration)

Figure 5.4: Comparison of profile deformation: Experimental (V31) vs. Simulation, steps F1 to F9.

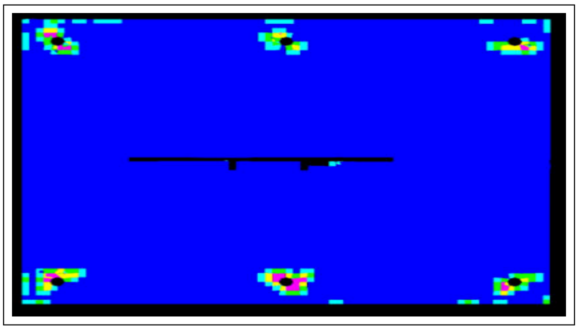

(a) Step F1 (only the first impacted ply is shown)

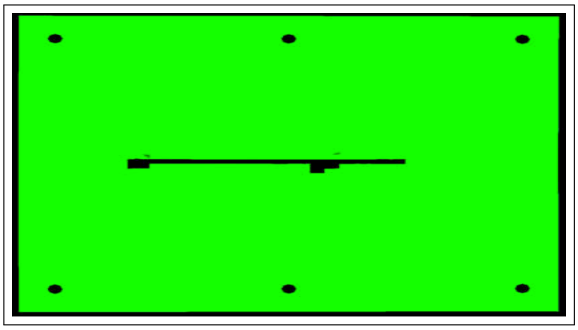

(b) Step F2 (only the first impacted ply is shown)

Continued on next page...

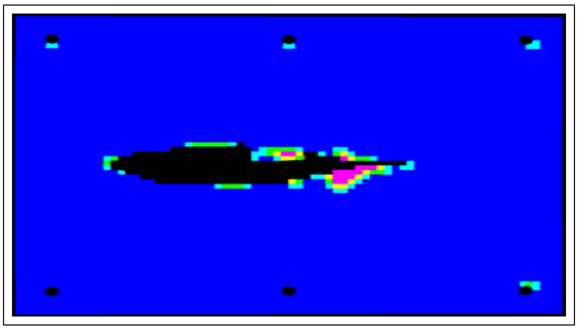

(c) Step F3 (only the first impacted ply is shown)

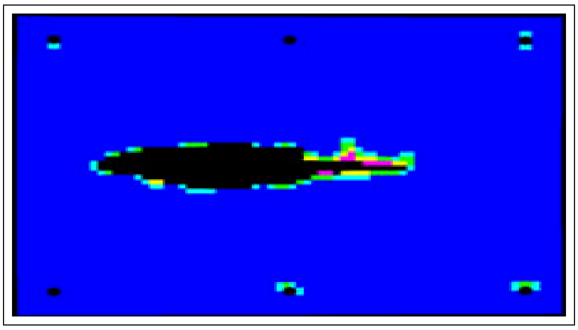

(d) Step F4 (only the first impacted ply is shown)

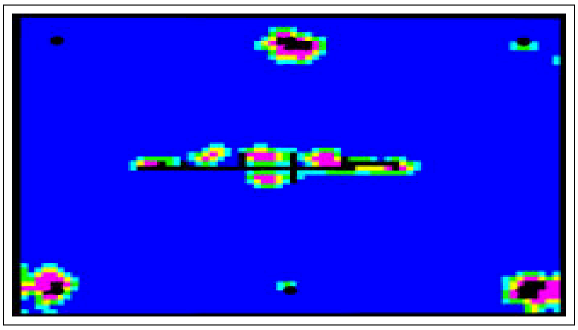

(e) Step F5 (only the first impacted ply is shown)

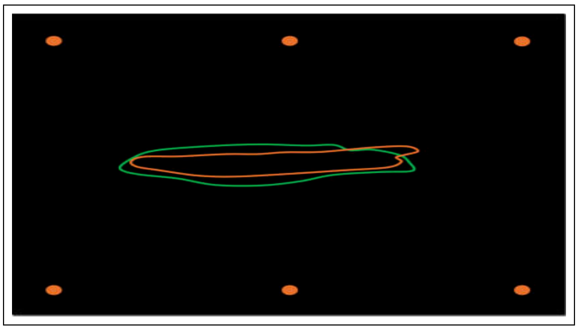

(f) Step F6

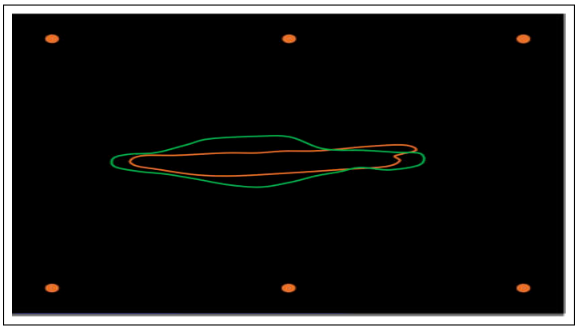

(g) Step F7

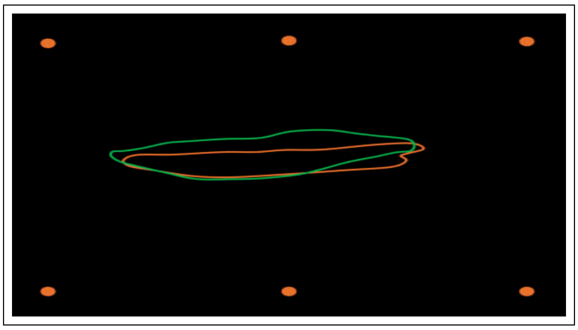

(h) Step F8

Continued on next page...

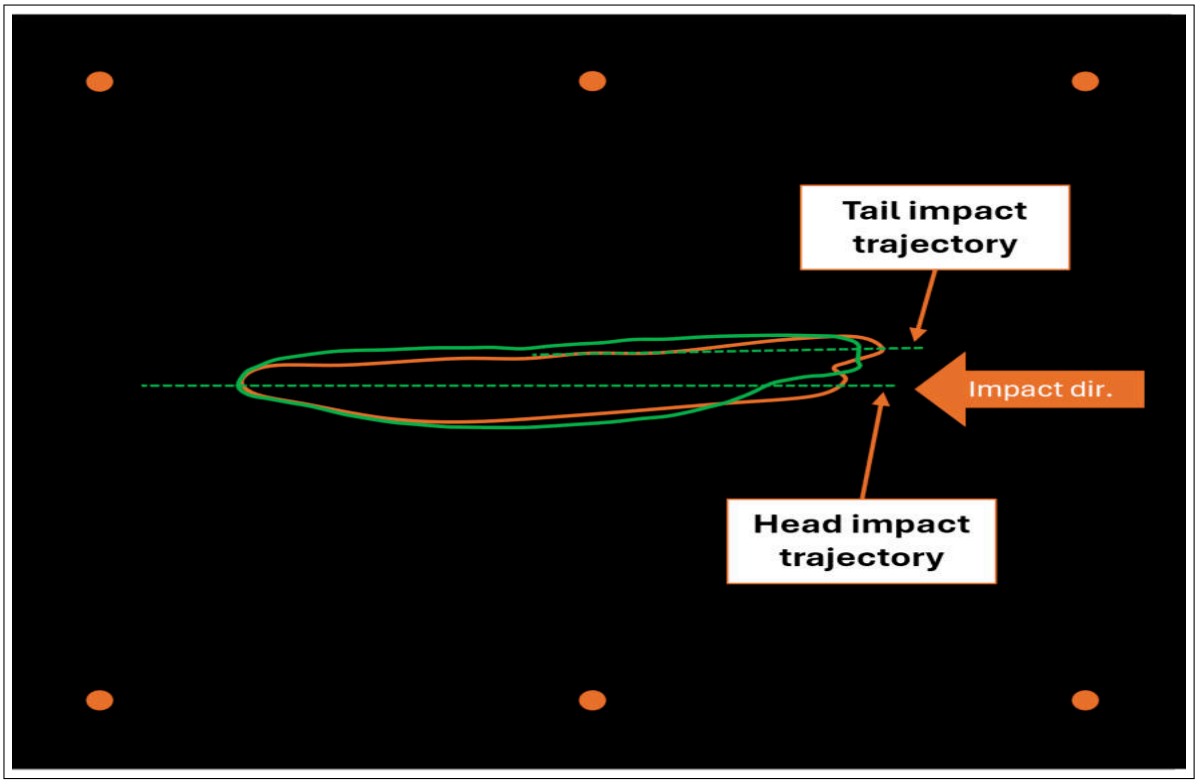

(i) Step F9

Figure 5.5: Comparison of damage patterns: Experimental results (orange envelope) vs. Simulations (green envelope), steps F1 to F9.

5.3.10. Summary and Final Considerations

To conclude this section, a comparison between the intrusion plots of all simulation results at specific critical points is performed to summarize the step by step improvements (see Table 5.4). To demonstrate the significance of the newly introduced impactor dynamics, test footage is compared with simulation results at various time-steps (see Figure 5.6). This comparison evaluates the model both with and without the new dynamics. Last, the aluminum plates post impact are reported for both F6 and F9, along with the real test plate (see Figure 5.7), and it can be seen how the final version (i.e., F9) is much closer to the test specimen, with non-aligned head and tail intrusions.

Intrusion Comparison at Critical Points

Step	Peak 1	Plastic 1	Peak 2	Plastic 2
F1	+45.7	+89.5	+32.3	+61
F2	+23.8	+71.1	+16.5	+56
F3	+25.7	+82.5	+10.75	+47
F4	+16.2	+41.6	-9.5	+7
F5	+7.6	+28.2	+2.5	+11

Continued on next page...

Step	Peak 1	Plastic 1	Peak 2	Plastic 2
F6	+8.6	+30.7	+1.3	+22
F7	+12.4	+37.5	+8.2	+33
F8	-1.9	+4.7	-7.6	+11
F9	-2.9	+0.4	-2.5	+5

Table 5.4: Percentage variation of intrusion w.r.t. experimental results at critical points, steps F1 to F9. Color coding: GREEN between $\pm 5\%$, YELLOW between $\pm 20\%$, RED otherwise.

Frame by Frame Impact Dynamics Comparison

The point of view in the simulation environment has been positioned in a way that mimics the real camera used in tests.

The difference between the F6 and F8 model is apparent at all time-steps: at t_0, the top-left face of the impactor is more visible than the top-right one in both F8 and V31, while in F6 both faces are equally exposed to the camera; at t_3 the impactor undergoes a rotation that precedes the tail impact which will therefore be more blunt than what would have happened with a direct corner impact, and it is correctly captured by F8; at t_4 the bending of the plate is not perfectly centered like in F6, but rather shifted to the left, like it happens in F8; at t_5 the tail impact is completed, with the impactor rotated by slightly less than $45°$ w.r.t. its original position, and one corner still deep in the composite plate, and both features have been correctly captured by F8; at t_6 the impactor is about to lose contact with the plate, and it is almost completely flat against it, like it can be seen in F8; at t_7 the impactor came to a stop and started falling down due to gravity after completing a rotation of slightly more than $45°$ w.r.t. its initial position, and this is correctly captured by F8.

These observation make it clear that all initial rotations and shifts of the impactor need to be accurately captured, measured and introduced in simulations in order to achieve satisfying results, as they can dramatically alter the results.

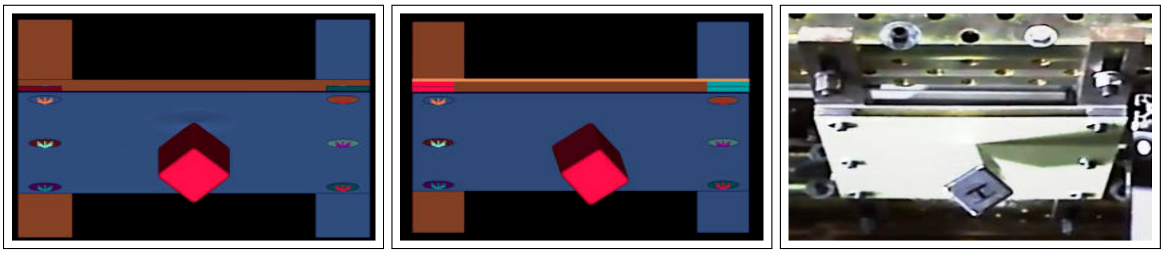

(a) F6 (t_0) **(b)** F8 (t_0) **(c)** V31 (t_0)

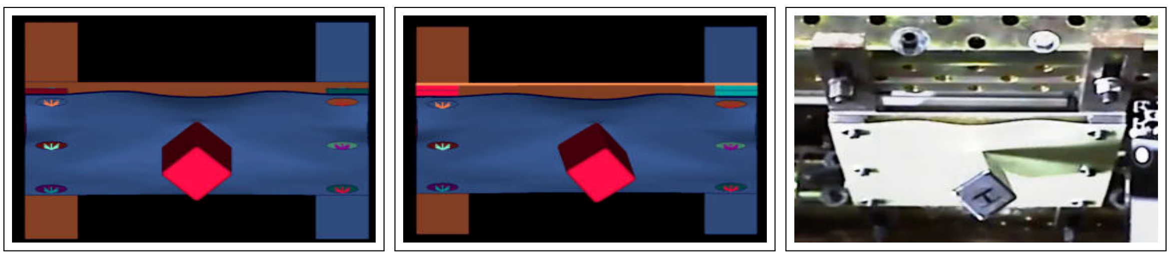

(d) F6 (t_1) **(e)** F8 (t_1) **(f)** V31 (t_1)

Continued on next page...

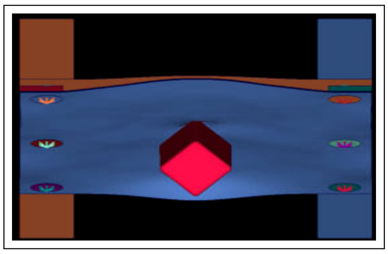
(g) F6 (t_2)

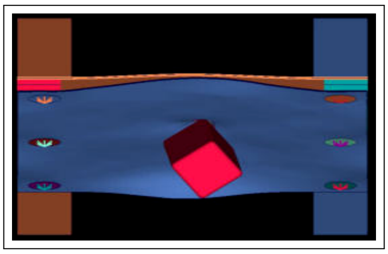
(h) F8 (t_2)

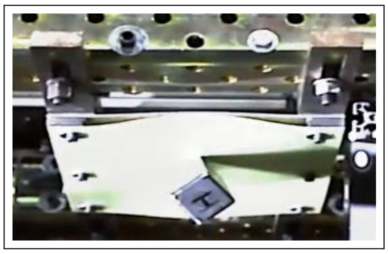
(i) V31 (t_2)

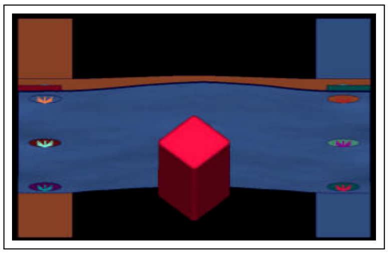
(j) F6 (t_3)

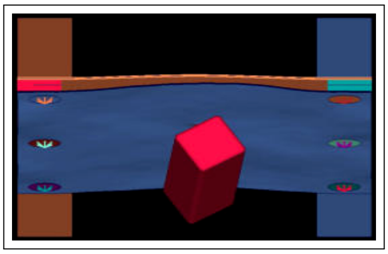
(k) F8 (t_3)

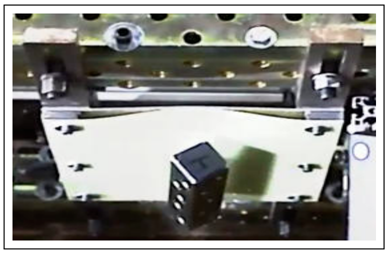
(l) V31 (t_3)

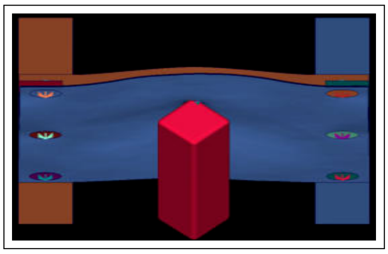
(m) F6 (t_4)

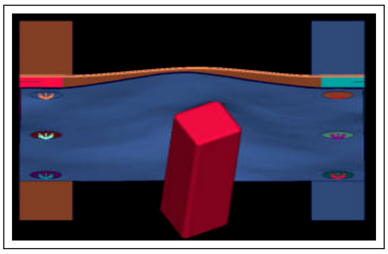
(n) F8 (t_4)

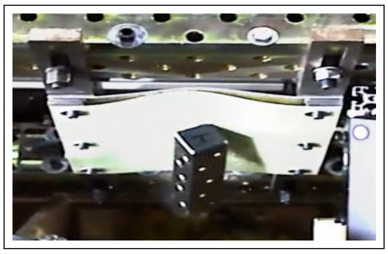
(o) V31 (t_4)

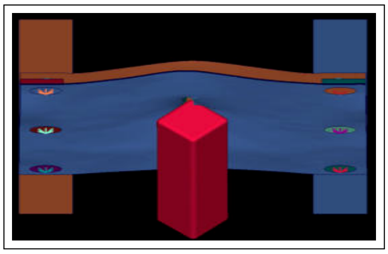
(p) F6 (t_5)

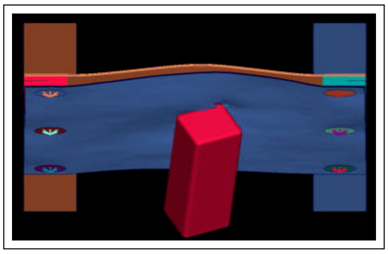
(q) F8 (t_5)

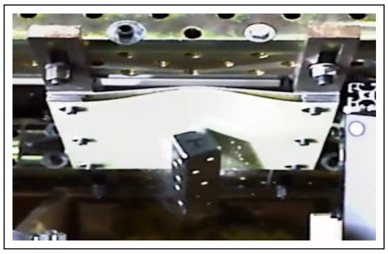
(r) V31 (t_5)

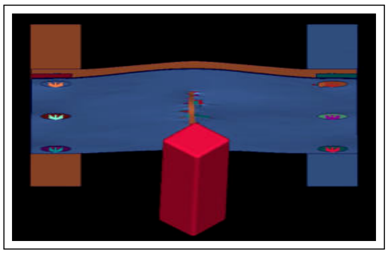
(s) F6 (t_6)

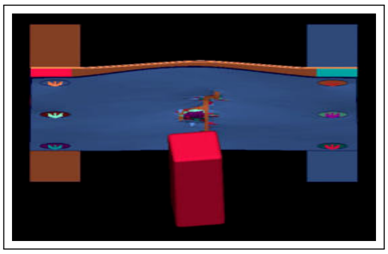
(t) F8 (t_6)

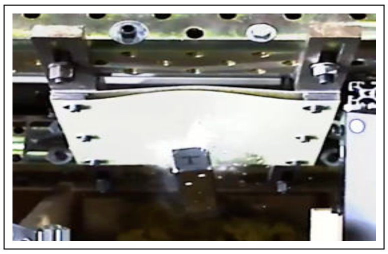
(u) V31 (t_6)

Continued on next page...

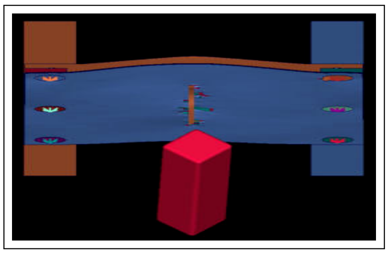

(v) F6 (t_7)

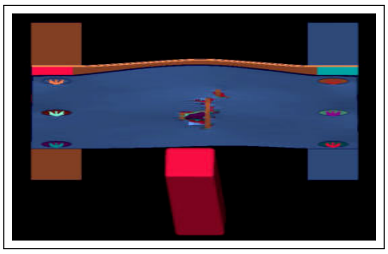

(w) F8 (t_7)

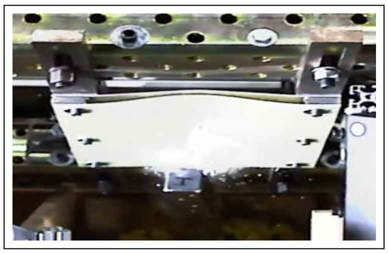

(x) V31 (t_7)

Figure 5.6: Frame by frame comparison of impact dynamics against V31 test footage, F6 vs F8.

Aluminum Plates Post-Impact

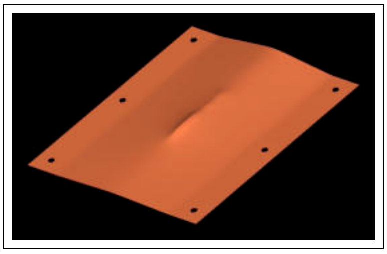

(a) F6

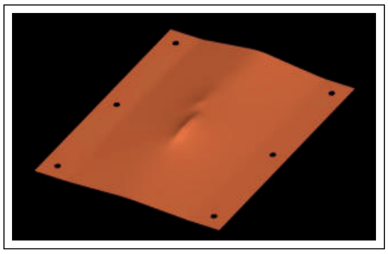

(b) F9

(c) V31

Figure 5.7: Aluminum plates post-impact comparison against V31 test specimen, F6 vs F9

6 Conclusions and Recommendations

This final chapter synthesizes the research outcomes concerning the predictive modeling of high-speed oblique impacts on composite laminates. The discussion begins with an Overview of the research objectives, revisiting the primary challenge of simulating complex contact dynamics and shear-driven delamination within an industrial vehicle safety context.

Subsequently, a Summary of Findings details the hierarchy of physical parameters identified as governing the structural response. This section emphasizes the critical interplay between delamination-induced structural softening, inter-ply friction, and the ”tail impact” kinematics derived from the forensic reconstruction of the event.

The Contributions section then outlines the novelty of the work, specifically the definition of a robust modeling framework and the validation of a computationally efficient discretized shell methodology capable of capturing complex damage morphologies without extensive fracture energy characterization.

Following this, the Limitations of the proposed approach are critically assessed, addressing boundaries related to the material constitutive assumptions and the available experimental data range.

Finally, Recommendations are provided to guide future experimental campaigns and simulation developments. This section extends beyond modeling improvements to propose New Design Possibilities, utilizing the validated framework to explore alternative laminate architectures and damage-tolerant configurations aimed at optimizing the protective performance of the under-ride system.

6.1. Overview

The main goal of this thesis is simulating high-speed oblique impacts on composite laminates, a complex load-case governed by the coupling of shear-driven delamination, inertial effects and contact dynamics. A robust methodology suitable for industrial applications is developed, starting from the baseline model provided by the company which used a monolithic shell formulation incapable of capturing delamination.

Given the project scope, defined in Chapter 1, the research shows that accurate intrusion prediction in the ”Beschuss” load-case doesn’t require computationally expensive and characterization intensive state-of-the-art models (e.g., MAT 162). In fact, a ”discretized” approach combining shell elements and tiebreak contacts proved to be the optimal solution, offering a combination of computational efficiency and satisfactory predictive accuracy.

Furthermore, the investigation identified that predictive fidelity depends on the interplay of two main factors, which are the delamination-induced mechanisms (specifically, stiffness reduction and friction between delaminated plies) and the impactor kinematics. While a monolithic formulation resulted in excessive bending stiffness, the inaccurate representation of the impactor rotation and tilt generated non-representative loading paths.

Consequently, this thesis defines a new simulation framework that couples a simplified strength-based delamination model with high-fidelity boundary conditions to obtain satisfactory predictive accuracy both in terms of deformation magnitude and damage size, without the need to characterize complex fracture energy parameters (e.g., G_{Ic}, G_{IIc}).

6.2. Summary of Findings

This research resulted in many significant insights into high-speed oblique impact modeling on composite plates, determining the required physical parameters to achieve predictive accuracy. The findings are categorized below in three key areas: the validation of the modeling architecture, the physics of the inter-laminar failure, and the critical role of impact dynamics and boundary conditions.

At the end, a multi-metric validation of the project results is presented.

6.2.1. Validation of the Modeling Architecture

The investigation establishes that industrial-grade accuracy in the simulation of high-speed impacts on composite laminates can be achieved via a discretized shell-based approach coupled with tiebreak contacts, without requiring advanced and computationally expensive solid-element based frameworks.

Validity of the Strength-Based Criterion

A critical finding was that the energy dissipated by delamination in high-speed impacts is negligible, accounting for approximately 3% of the impactor's total kinetic energy (see Section C.2.4). This validates the decision of using a purely strength-based failure criterion (CCRIT=0), showing how it can adequately capture the structural response of the plate without the need for complex fracture mechanics parameters.

Structural Softening

Although the fracture energy is negligible, a comparison between the baseline monolithic model and the new implementation confirms how delamination reduces the composite plate's bending stiffness, critically influencing the global structural response.

This is especially noticeable in the tail impact phase, where the impactor's tail contacts the delaminated area, encountering less resistance and allowing for a deeper intrusion profile that the monolithic model couldn't reproduce.

Mesh Sensitivity and Characteristic Length

As theorized in Chapter 2, a correlation exists between mesh size and contact strength parameters (NFLS, SFLS), which is ascribed to a potential discrepancy between the numerical discretization performed during meshing and the physical length of the material's cohesive zone.

In FEA, stresses are averaged over each element's area, therefore meshes too coarse can smear stress concentrations, failing to trigger delamination at the expected (literature based) values: conversely, aligning the mesh size closer to the material's cohesive zone length creates a more realistic force balance, thus only requiring minimal calibration to attain predictive accuracy.

Material Characterization and Strain Rate Sensitivity

The standard material card for aluminum (AlMg3.5) used in the baseline simulation to model the backplate (i.e., the payload) has proven to be unrepresentative of the real material in the context of high-speed impacts. A characterization campaign has been performed on the actual backplates, resulting in a new card (AlMg3 G22) which possesses higher strength than its generic counterpart in part of the strain range of interest for the project, possibly resulting in a deformation reduction.

Furthermore, while the investigated concept of strain rate sensitivity for the aluminum plate has been proved to be theoretically valid, its application within reasonable ranges (from literature) doesn't produce significant effects, and unrealistic Cowper-Symonds coefficients are required to be the primary driver for test/simulation matching.

6.2.2. Physics of Inter-Laminar Failure

Through the iterative modeling approach adopted for the research, specific insights were obtained regarding the physical drivers of damage.

Shear-Dominated Failure

The Design of Experiments (DoE) confirmed that delamination in the project load-case is almost entirely shear-driven, as variations in the inter-laminar shear strength parameter (SFLS) significantly altered its shape and size. Conversely, the model proved to be insensitive to variations to the inter-laminar normal strength parameter (NFLS), which is consistent with the compressive nature of the impact which suppresses Mode I delamination. These findings validate the use of literature-based parameters as the main calibration parameter.

Inter-Ply Friction and the "Plowing" Effect

Inter-ply friction has been identified as a critical mechanism in governing the post-failure behaviour of the impactor. Simulations lacking this friction resulted in an unrealistic ”plowing” effect, where the impactor tore through the laminate with its front face (instead of a single corner), creating damage patterns significantly larger than those observed in C-scans. The introduction of inter-ply friction (FS[1]=0.5, FD[2]=0.4) was found to be the necessary mechanism to stabilize the ”flaps” of the delaminated plies, as it forced the laminate to behave as a coherent body by resisting sliding between its delaminated layers, thus offering higher resistance to the impactor and preventing ”plowing”.

Influence of Global Friction

Global friction coefficient between the impactor and the plates has been found to regulate the energy distribution between the two impact events (head and tail impact). While a standard scaling factor (SF=3) on the friction coefficients (FS=0.15, FD=0.08) was adequate for capturing the behaviour of both steel-glass and steel-aluminum interfaces, validation on a hybrid glass/carbon layup showed how the scaling has to be increased (SF=4.5) to match the energy distribution of the experimental test, suggesting that surface friction and projectile drag are governed by laminate topology and ply count.

6.2.3. Impact Dynamics and Boundary Conditions

The most significant finding of the thesis is that the discrepancy between the initial simulations and experimental results was driven by the coupling of delamination-induced reduction in structural stiffness with unmodeled physical boundary conditions.

The "Tail Impact" Kinematics

The research identified that the discrepancy in damage morphology between test and simulations was caused by poor representation of the impactor’s secondary kinematics. The simulations proved that the specific curved shape of the delamination observed in the C-scans is caused by the impactor’s rotation and tilt, as models that didn’t account for those specific rotational dynamics produced linear damage patterns that disagreed with the NDT data.

Correction of the Deformation Mode

Precise modeling of these impact dynamics was found to be the main driver in correcting the position of the maximum intrusion point, which in earlier iterations was incorrectly shifted in the x- or y-direction. The final update successfully aligned the peak deformation with the experimental measurements, once again proving the validity of the newly measured impactor dynamics.

Bolt Pre-load and Constraints

The investigation revealed that the clamping force has a measurable influence on the global deformation profile. Increasing the modeled bolt pre-load from 4 kN to 9 kN improved the correlation with the experimental data, suggesting that boundary conditions in experimental tests provided higher clamping force than initially documented, and that their accurate representation is necessary for increased predictive accuracy.

[1] Static friction coefficient
[2] Dynamic friction coefficient

6.2.4. Multi-Metric Validation

The interplay between the physical parameters identified in the previous sections was validated through a step-by-step implementation. By isolating the effects of numerical stability, material characterization, and boundary conditions, the research demonstrated that high-fidelity prediction is achievable only when these factors are coupled.

Convergence of Intrusion Metrics (Aluminum Plate)

Table 5.4 provides the quantitative evidence for this convergence, highlighting the convergence of the intrusion measurements on the aluminum plate. The initial implementation of the delamination model (Step F1, see Section 5.3.1), while superior to the monolithic baseline in accounting for stiffness reduction due to local damage, resulted in a significant over-prediction of the first (+45.7%) and second (+32.3%) intrusion peaks and plastic deformations (+89.5% and +61%, respectively) compared to the experimental data.

The transition to a stable contact formulation (Step F2, see Section 5.3.2) helped solving some numerical issues around the plates' holes, and the re-calibration of the tiebreak contact parameters (Step F3, see Section 5.3.3), along with the update of the aluminum constitutive model (Step F4, see Section 5.3.4) reduced the peaks' errors to +16.2% and -9.5%, respectively, establishing a reliable numerical baseline.

The introduction of inter-ply friction (Step F5, see Section 5.3.5) marked a critical turning point, reducing the errors to +7.6% and +2.5%. This proves the finding that frictional resistance between delaminated flaps is a governing mechanism in both energy dissipation and distribution between the peaks.

After some iterations (Step F7 and F8, see Sections 5.3.7 and 5.3.8, respectively), the final integration of the corrected impactor kinematics in (Step F9, see Section 5.3.9) reduced the errors in the peaks to -2.9% and -2.5%, and the final plastic deformation errors to +0.4% and +5%. This result confirms that the remaining discrepancy was due to poor kinematic assumptions rather than to constitutive issues.

To summarize the thesis results, a comparison between the baseline (Step 6A, see Section 4.2.8) and final (Step F9, see Section 4.4.10) model is presented in Figure 6.1, with the error on maximum intrusion (i.e., 2nd peak) going from +17.7% to -2.53%. For additional information on the fairness of the comparison, see Appendix D.

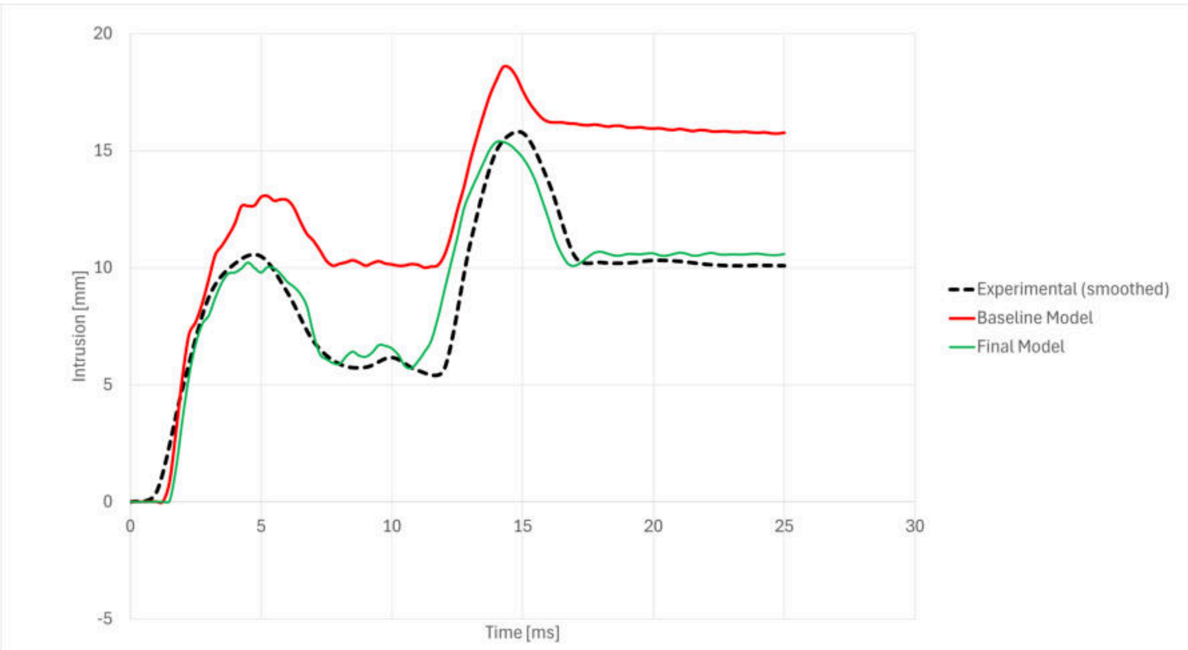

Figure 6.1: Intrusion over time, Smoothed Experimental Curve VS Baseline Model VS Final Model

Damage Pattern Correlation (Composite Plate)

The quantitative accuracy is mirrored by the qualitative match with the C-scans[3] performed on the composite plates, which confirm the validity of the adopted strength-based delamination criterion.

While the baseline model was completely incapable of realistically modeling the damage (see Figure 6.2a), the finalized model reproduces the specific geometry of the damage observed in C-scans (see Figure 6.2b): as shown, the simulation accurately represents both the length of the shear-driven delamination and the curvature induced by the impactor's tail rotation, confirming that the chosen methodology captures the physical failure mechanisms without the need for fracture energy parameters.

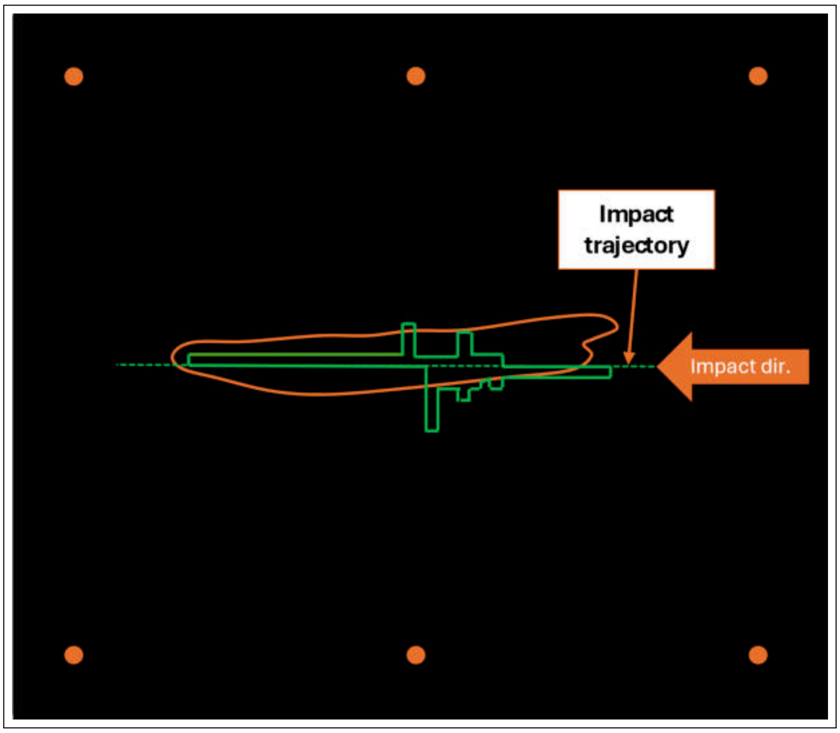

(a) Baseline Model

Continued on next page...

[3]C-scan (NDT) results are a reliable benchmark as they have been verified through microscopy observations on section-cuts of the plates, see Section 3.4

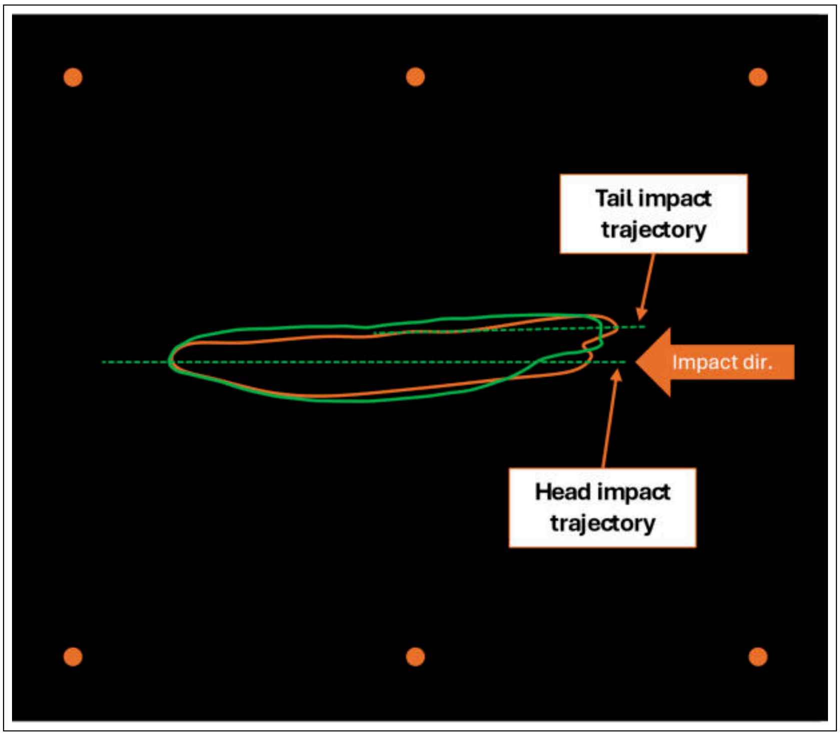

(b) Final Model

Figure 6.2: Comparison of damage patterns: Experimental results (orange envelope) vs. Simulations (green envelope), Baseline Model VS Final Model

Damage Pattern Correlation (Aluminum Plate)

As per the damage pattern on the aluminum plates, visual inspection of the aluminum backplates revealed that the permanent indentations caused by the ”head” and ”tail” strikes are not aligned, instead exhibiting a distinct lateral offset relative to the plate’s longitudinal axis (See Figure 6.3c). While in the Baseline Model the plate’s deformation is aligned along its centerline (see Figure 6.3a), the Final Model demonstrates good fidelity in reproducing the lateral shift of the impact footprint (see Figure 6.3b).

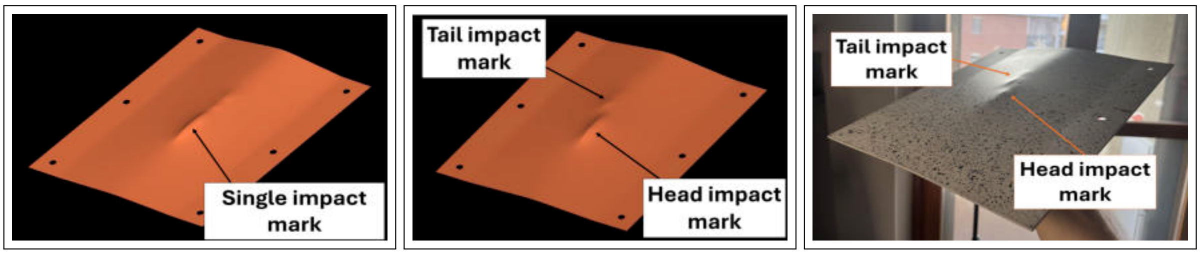

(a) Baseline Model **(b)** Final Model **(c)** Experimental

Figure 6.3: Aluminum plates post-impact comparison against test specimen, Baseline Model vs Final Model

Kinematic Validation

Beyond the more traditional metrics, the simulation was validated through a rigorous frame-by-frame comparison with high-speed video footage of the experimental test (see Figure 5.6).

The match between the new model at all time-frames throughout the footage (and the mismatch with the baseline model) demonstrates that the rotation and tilt parameters introduced are not merely calibration variables tuned to force a fit with the intrusion curves, but are accurate representations of the actual dynamics governing the test, thus validating the proposed forensic reconstruction methodology.

For a complete frame-by-frame discussion, see Section 5.3.10.

6.3. Contributions

This thesis contributes to the field of composite impact modeling by bridging the gap between high-fidelity academic theories and the efficiency constraints of industrial vehicle safety analysis; specific contributions are detailed in the following paragraphs.

6.3.1. Development and Validation of a Discretized Shell Methodology

The research demonstrated that computationally expensive solid-element models (e.g., MAT 162) are not a prerequisite for predicting intrusion with industry-level accuracy in high-speed oblique impacts; in fact, it establishes a solution capable of capturing delamination by means of a discretized approach based on standard shell elements connected by tiebreak contacts, retaining the computational efficiency and ease of integration in bigger models typical of monolithic approaches.

6.3.2. Simulation of a Novel Safety-Critical Load-case

Many literature sources use complex state-of-the-art models to obtain high-fidelity results, but they often demonstrate their approaches on highly specific load-cases, with simple impactor geometries (e.g., hemisphere), impact scenarios (e.g., 90 degrees) and boundary conditions (e.g., simply supported); when one of multiple of these conditions are changed, these approaches require extensive phenomenological calibration to retain predictive accuracy.

The approach developed in this project, instead, can match the experimental results of a complex load-case in the literature (hit at the impactor's corner, α° impact, realistic bolted connection to the fixtures, see Figures 3.1 and 3.2), paramount for safety in a variety of fields and not previously seen in the literature, with little to no required calibration.

6.3.3. Development of a Tunable Fidelity Framework

The thesis provides a flexible simulation architecture where complexity can be scaled based on the load case requirements. By demonstrating that the critical failure distance CCRIT can be set to zero for high-speed impacts without accuracy loss (due to negligible fracture energy absorption), the methodology offers a tunable workflow that allows to choose between ease of calibration (strength-based) and higher physical fidelity (energy-based) depending on the specific load-case.

6.3.4. Identification of the Interplay Between Delamination Modeling, Friction and Impact Dynamics

The research goes beyond the new framework implementation, investigating the mutual influence of different aspects of the impact event; specifically, the paramount importance of accurate inter-ply friction and impact dynamics representation for both damage magnitude and morphology has been highlighted, demonstrating how the modeling effort should shift from material calibration to kinematic precision.

6.3.5. Determination of a "Forensic Approach" to Modeling

Through a rigorous forensic analysis of experimental results and high-speed videography, previously unmeasured kinematics variables were introduced into the simulation environment.

To bridge the gap between the baseline model and the physical reality, a characterization campaign was performed (C-scans, microscopy, fibre volume determination, geometric measurements). The expanded database obtained through this additional testing facilitated a systematic analysis on the influence of various simulation parameters on the test/simulation match.

This allowed to isolate and correct discrepancies in the baseline model through an iterative simulation process, and ensured that every modification to the numerical model was substantiated by physical evidence or phenomenological proof, establishing a robust framework for future modeling efforts.

6.3.6. Material Characterization Effort

By identify that standard library materials are insufficient for high-fidelity modeling, the research produced a new material card via a characterization campaign that prioritized static strain-stress curve definition over strain-rate sensitivity measurements, which have been deemed non-critical for the project's load case.

6.4. Limitations

While the research successfully improved the predictive accuracy of the baseline model through various implementations, several limitations regarding the experimental results and the numerical simplifications must be acknowledged. These constraints establish the boundaries within which the current validation holds true.

6.4.1. Assumptions Regarding Laminate Uniformity

As detailed in Section 3.3, thickness measurements revealed significant resin pooling and variable fibre volume fractions, which correlated directly with the signal attenuation and noise observed in the ultrasonic C-scans.

Although these inconsistencies don't directly affect the measurement of the delamination area, they were not mapped into the finite element model, which utilized a constant nominal thickness for the protection plate. Consequently, the simulation represents an idealized structural response that cannot account for the local stiffness variations and stress concentrations induced by resin-rich zones in the physical plate, as modeling the stochastic distribution of manufacturing defects is computationally prohibitive for industrial applications.

6.4.2. Kinematic Reverse-Engineering

A significant limitation of the study was the lack of high-fidelity experimental telemetry regarding the impactor's secondary kinematics. The values for tilt were completely derived through a forensic frame-by-frame analysis of high-speed video footage rather than direct measurement, while both the "pitch" and "roll" values had to be reviewed and corrected. While the simulation results confirm a reproduction of the physical damage trace, the solution relies on a "reverse-engineering" approach; consequently, the kinematic definition is limited to this specific test.

Furthermore, the Digital Image Correlation (DIC) tracking was limited to a specific pre-defined node which, due to the complex motion of the impactor, was not always coincident with the point of absolute maximum intrusion. This introduced an extra layer of complexity in the test/simulation match, as the coordinates of the exact point to be tracked in the simulations had to be measured from test footage without any references but the speckle patterns on the aluminum plate (see Section 3.1.2).

6.4.3. Mesh Dependency of the Failure Criterion

The decision to use a stress-based tiebreak formulation prioritizes computational efficiency but introduces a mesh dependency. Because the failure criterion relies on stresses averaged over the element area, the calibrated strength limits (SFLS[4], NFLS[5]) are valid only for the specific mesh density (2 mm) used in the final model. Unlike fracture-energy-based models which can theoretically be regularized to be mesh-independent, the current methodology requires a re-calibration of the stress limits if the element size is significantly altered.

6.4.4. Tribological Simplification

The modeling of friction was simplified through the use of a global scaling factor (SF) applied to standard static/dynamic coefficients, rather than characterizing specific tribological pairs (e.g., Steel-Aluminum, Steel-Glass, Steel-Epoxy). While the scaling factor (SF=3) proved sufficient for the glass-fibre model, the necessity to increase this factor (SF=4.5) for the carbon-hybrid validation case (V22) indicates that

[4] Parameter representing Inter-laminar Shear Strength.
[5] Parameter representing Inter-laminar Normal Strength.

the current friction model groups various physical aspects (surface roughness, fiber tearing, debris accumulation) into a single scalar parameter; limiting the model's ability to predict energy dissipation without prior calibration based on the specific laminate's properties.

6.4.5. Limited alternative load-cases validation

The GLASS_1 workflow (see Section 4.4), which integrates inter-ply friction and secondary kinematics, was designed during the final stages of the project to implement the insights (see Section 5.2.1) generated by analyzing the GLASS_2 workflow (see Section 4.3), which was initially meant to be the final numerical model in the project.

Therefore, according to the initial research planning, validation with different test versions and laminates was performed within the GLASS_2 workflow (see Sections 4.3.6 and 4.3.7), and the same was not possible for GLASS_1 due to time constraints, as forensic studies on high-speed footage and experimental results are individual for each test version.

Still, it must be noted that although intermediate, the validation results showed good agreement w.r.t. the experimental results in the delamination shape and size, suggesting robustness in the delamination modeling capabilities of the developed framework.

Furthermore, as no curve fitting has been performed, the approach virtually retains generality, even though a rigorous simulation campaign has to be performed to verify this claim (see Section 6.5.2).

6.5. Recommendations

Based on the simulation results, the forensic analysis of the modeling discrepancies and the identified limitations of the current testing protocol, the following recommendations are proposed to enhance both the predictive fidelity of the model and the structural performance of the protection system.

6.5.1. Enhancements to Experimental Protocol

One of the biggest challenges of the project was the uncertainty on boundary conditions and projectile kinematics. Future test campaigns should implement the following recommendations to facilitate accurate replication in simulations.

Advanced Kinematic Tracking

The test set-up should be updated with additional sensors to record all the projectile rotations (pitch, roll, yaw) before impact. The best candidates for such a task are high-speed stereo-vision cameras, or inertial measurement units. These additions would remove the need to manually extract the required parameters from test footage.

Launch System Upgrade

The variability in the impactor motion between tests is attributed to the current ”cart+spring” launch mechanism (see Section 3.1.1). A different choice, such a pressure cannon system, would me more suitable, providing a cleaner, more controlled flight path and ensuring higher repeatability.

Quantification of Pre-load

As the simulation showed high sensitivity to the clamping force (see Section 5.1.6), future tests should use torque-controlled tightening to precisely define the bolt load, which should then be reported in the experimental test reports so that it can be mapped into the *INITIAL_AXIS_FORCE_BEAM card in LS-Dyna.

DIC Target Optimization

The current Digital Image Correlation (DIC) set-up tracks a pre-defined node that does not always coincide with the maximum intrusion point. In the future, full-field strain analysis should be used to identify the coordinates of the maximum intrusion node on a case-by-case basis, so that it can be precisely tracked in simulations, ensuring a 1:1 comparison and more meaningful results.

Alternatively, if a different node has to be tracked for any reasons, its coordinates on the plate should still be explicitly stated in the experimental test reports, so that no additional forensic work is required to set-up the simulations.

6.5.2. Numerical Method Refinements

To further increase the robustness of the new simulation workflow, the following numerical improvements are suggested.

Tribological Characterization

The global friction was controlled by a single scaling factor (SF), which has been found to be a critical parameter to calibrate the model. To remove this limitation, it is recommended to perform specific friction characterization tests (e.g., pin-on-disk) to determine the exact coefficients between all material pairs.

Mesh Regularization at Connections

Numerical instabilities were observed around bolt holes, leading to non-physical element failures. As this was most probably caused by triangular elements in the mesh that concentrated the stress and lead to premature failure, special treatment around holes (e.g., washer patterns) is recommended to regularize the mesh.

Strain Rate Dependency

While the investigation in Section C.2.10 excluded that strain rate effects can be the main driver of intrusion discrepancy (as unrealistic Cowper-Symonds coefficients were necessary to get a match), rate dependency probably plays a role in the fine-tuning of the plate's plastic response. Future work should utilize rate-dependent strain-stress tables for the aluminum to ensure maximum accuracy.

More critically, the current composite material model utilizes quasi-static strength values for the glass-fibre plies. Literature suggests that GFRP[6] present significant strain-rate sensitivity [35], particularly in matrix-dominated failure modes (transverse compression and in-plane shear) and at the high strain rates characteristic of the project's load-case.

Since the chosen methodology utilizes tiebreak contacts to represent the matrix, the visco-elastic behavior of the resin cannot be modeled explicitly; instead, it must be represented at the lamina level. Therefore, it is recommended to replace quasi-static characterization with SHPB[7]. This would allow for the definition of rate-dependent curves within the shell material formulation, potentially improving the prediction of the shear-driven damage propagation.

Additional validation campaign

As mentioned in Section 6.4.5, different load-case (impact position and angles) and laminate (hybrid glass-carbon) validation of the simulative approach developed in this thesis has been performed on intermediate results only.

As a fundamental procedure to confirm the model's generality (even though available data suggest it), a structured multi-case and multi-material validation is recommended. For a comprehensive evaluation, it is advised to determine a wide range of impact speeds (low speed to check for BVID), as well as to change plies material, number and orientation (to check for delamination branching). Furthermore, models with no expected delamination should be prepared, to further assess tie-break contact stability.

6.5.3. Design Optimization Opportunities

Now that the simulation workflow validity is established, the developed model can be used to explore design improvements for the under-ride protection system (UFS). The following design features are proposed for virtual testing.

Hybrid Layup Architectures

As the current results highlighted how both glass and carbon layups undergo tearing in the initial phases of the impact, a hybrid configuration is proposed, where an outer layer of aramid (e.g., Kevlar) or S2-Glass provides superior toughness and abrasion resistance to limit the "plowing" effect, while internal glass or carbon layers provide bending stiffness.

[6] Glass Fibre Reinforced Polymers
[7] Split Hopkinson Pressure Bar

Conversely, as the simulation results indicated that ”plowing” (while undesirable for structural integrity) acts as a significant energy sink that reduces global intrusion, an alternative design strategy could exploit this mechanism by utilizing a sacrificial outer architecture. A thick, lower-shear strength outer laminate (e.g., Glass) could be designed to intentionally fail and tear under the projectile’s ”head impact”, dissipating kinetic energy through fracture and friction. This sacrificial layer would be coupled with a high-stiffness laminate (e.g., Carbon) to act as a backstop. This ”Soft-wall” approach could potentially reduce the peak intrusion more effectively than a purely rigid solution.

Sandwich Structures

Since global bending significantly contributes to intrusion, increasing the area moment of inertia is one of the most efficient ways to reduce deformation. A foam core (e.g., Rohacell or aluminum foam) inserted between thin composite skins could significantly increase bending stiffness without adding mass, with the added benefit of dissipating energy through core crushing rather than back-plate intrusion.

Combining this proposal with the plowing-exploiting one previously defined, a multi-stage energy absorption system is proposed, with an outer E-Glass/Epoxy face sheet to favor projectile ”plowing” and frictional dissipation, bonded to a crushable foam core (modeled with e.g., MAT_063) to facilitate deceleration and increase bending stiffness. This assembly should be backed by a carbon fiber sub-laminate. This configuration exploits the high-friction ”plowing” mechanism identified in this study to lower the impactor’s kinetic energy before the load is transferred to the stiff carbon backstop, minimizing intrusion through a ”Catch-and-Crush” mechanism rather than pure deflection.

Ply Orientation Optimization

The current configuration uses a 0/90 fabric configuration, mainly for ease of manufacturing. While it also offers high stiffness in the 1- and 2-direction, it might be sub-optimal in oblique impacts with off-axis cutting vectors. Therefore, an optimization study should be performed to evaluate multi-directional layups that maximize performance while also promoting delamination branching to increase energy dissipation.

6.5.4. Environmental and Operational Safety Considerations

While considering the usage of the protection plate in the UFS, the validation scope must expand beyond the ”dry and static” mechanical response to account for environmental degradation and thermal risks typical of battery applications.

Simulation of Hygrothermal Aging

The current validation utilizes ”pristine” material properties. However, the vehicle undercarriage can be subjected to wet environments, and moisture can reduce the SFLS[8], a parameter to which the simulation is highly sensitive.

Therefore, a ”Degraded State” validation should be performed, where the contact strength parameters in the model are reduced by factors established in the literature (e.g., 20-30% reduction). This will determine whether the protection plate maintains intrusion resistance after years of service life or the addition of a moisture-resistant external layer is required.

Coupled Thermal-Mechanical Analysis

The thesis identified that friction and plowing are the primary energy dissipation mechanisms. In a real scenario, this frictional work is converted into heat, which could have an influence on the plate response.

Hence, future simulations should utilize LS-Dyna’s coupled thermal-structural capabilities to calculate the temperature increase at the contact interface during the impact event, verifying it doesn’t exceed the Glass Transition Temperature (T_g) of the epoxy matrix.

Battery Crush and Short Circuit Modeling

To move from a structure-specific analysis to a comprehensive safety assessment, the aluminum back-plate in the simulation should be replaced by a representative battery cell model.

[8]This reduction in the Inter-laminar Shear Strength (SFLS) can be caused by matrix swelling, plasticization, and a weakening of the fiber-matrix interface bond

This allows the simulation to determine whether the predicted intrusion deforms the battery pack enough to trigger an internal short circuit or exothermal reaction, providing a true ”Pass/Fail” safety criterion.

BVID Detectability Thresholds

The protection plate operational strategy relies on ”replacement upon damage,” but this fails in case of BVID[9] as in composite structures significant sub-surface delamination can exist with minimal external indentation.

To address this issue, the validated model could be used to establish a ”Damage Visibility Correlation”: by running simulations at lower energy levels (e.g., stone chips impact), it is possible to correlate the predicted plastic deformation of the shell with the predicted tiebreak failure area, thus defining the minimum visible dent size required to justify a maintenance check, ensuring that plates with compromised stiffness are not left in service.

Alternatively, a conservative damage tolerance philosophy could be adopted. Assuming that BVID may remain undetected by standard visual inspections, the protection system is sized to guarantee sufficient residual strength and protective capacity even in the presence of pre-existing delamination.

[9] Barely Visible Impact Damage

References

[1] M. Albayrak, M. O. Kaman, and I. Bozkurt, "Determination of LS-DYNA MAT162 material input parameters for low velocity impact analysis of layered composites," in *Conference Proceedings, Paris France February 17-18*, 2022.

[2] D. Ma, R. Scazzosi, and A. Manes, "Modeling approaches for ballistic simulations of composite materials: Analytical model vs. finite element method," *Composites Science and Technology*, vol. 248, p. 110 461, 2024. DOI: 10.1016/j.compscitech.2024.110461.

[3] M. Ilyas, "Modélisation de l'endommagement de composites stratifiés carbone époxy sous impact / damage modelling of carbon epoxy laminated composites submitted to impact loading," Ph.D. dissertation, Institut Supérieur de l'Aéronautique et de l'Espace (ISAE), Université de Toulouse, Jul. 2010.

[4] C.-F. Yen, "Ballistic impact modeling of composite materials," in *7th International LS-DYNA Users Conference*, 2002, pp. 6.15–6.26.

[5] M. Albayrak, A. M. Asan, M. O. Kaman, and İ. Bozkurt, "Experimental and numerical determination of interlayer shear strength of glass fiber-reinforced epoxy composites," *Journal of Structural Engineering & Applied Mechanics*, vol. 5, no. 4, pp. 289–299, 2022. DOI: 10.31462/jseam.2022.04289299.

[6] L. J. Deka, S. D. Bartus, and U. K. Vaidya, "Damage evolution and energy absorption of FRP plates subjected to ballistic impact using a numerical model," in *9th International LS-DYNA Users Conference*, 2006, pp. 4.49–4.60.

[7] M. Rahman et al., "Effect of NH2-MWCNTs on crosslink density of epoxy matrix and ILSS properties of e-glass/epoxy composites," *Composite Structures*, vol. 95, pp. 213–221, 2013. DOI: 10.1016/j.compstruct.2012.07.019.

[8] S. Pati, P. Satapathy, M. Sahu, U. Mohanty, and S. Beura, "Estimation of ILSS of seawater-immersed GFRP composites, a statistical approach," *Materials Today: Proceedings*, 2024. DOI: 10.1016/j.matpr.2024.02.034.

[9] C. Kassapoglou, *Modeling the Effect of Damage in Composite Structures: Simplified Approaches* (Aerospace Series). Chichester, West Sussex, United Kingdom: John Wiley & Sons Ltd, 2015, ISBN: 9781119013211.

[10] W. Cui, T. Liu, J. Len, and R. Ruo, "Interlaminar tensile strength (ILTS) measurement of woven glass/polyester laminates using four-point curved beam specimen," *Composites Part A: Applied Science and Manufacturing*, vol. 27, no. 11, pp. 1097–1105, 1996. DOI: 10.1016/1359-835X(96)00071-1.

[11] LS-DYNA Aerospace Working Group (AWG), "Modeling guidelines document," Livermore Software Technology Corporation (LSTC), Tech. Rep., May 2024.

[12] I. Jerez Sotoca, "Final work: Impact damage modelling on composite structures," Academic Promoter: Jean-Philippe Ponthot, M.S. thesis, Université de Liège, 2023.

[13] M. M. Ansari and A. Chakrabarti, "Influence of projectile nose shape and incidence angle on the ballistic perforation of laminated glass fiber composite plate," *Composites Science and Technology*, vol. 142, pp. 107–116, 2017. DOI: 10.1016/j.compscitech.2016.12.033.

[14] Wikipedia contributors. "Explicit and implicit methods," Wikipedia, The Free Encyclopedia, Accessed: Oct. 2025. [Online]. Available: https://en.wikipedia.org/wiki/Explicit_and_implicit_methods.

[15] ANSYS, Inc. "Implicit and explicit time integration," Ansys Innovation Space, Accessed: Oct. 2025. [Online]. Available: https://innovationspace.ansys.com/courses/courses/time_integration/lessons/implicit-and-explicit-time-integration-methods-lesson-2/.

[16] ANSYS, Inc. “Discussion of time-step size,” Ansys Innovation Space, Accessed: Oct. 2025. [Online]. Available: https://innovationspace.ansys.com/courses/courses/time_integration/lessons/discussion-of-time-step-size-lesson-3/.

[17] Wikipedia contributors. “LS-DYNA,” Wikipedia, The Free Encyclopedia, Accessed: Oct. 2025. [Online]. Available: https://en.wikipedia.org/wiki/LS-DYNA.

[18] *ANSYS LS-DYNA keyword user’s manual, volume I*, Version master@1914b557e, ANSYS, Inc., Oct. 2025.

[19] BETA CAE Systems. “ANSA pre-processor,” BETA CAE Website, Accessed: Oct. 2025. [Online]. Available: https://www.beta-cae.com/ansa.htm.

[20] S. Muflahi, G. Mohamed, and S. Hallett, “Investigation of delamination modeling capabilities for thin composite structures in LS-DYNA,” in *13th International LS-DYNA Users Conference*, 2014, pp. 1.1–1.14.

[21] *ANSYS LS-DYNA keyword user’s manual, volume II: Material models*, Version master@5825cf602, ANSYS, Inc., Oct. 2025.

[22] *LS-DYNA theory manual*, Version master@e24ec890e, ANSYS, Inc., Aug. 2025.

[23] DYNAmore GmbH. “Shell formulations,” LS-DYNA Support Website, Accessed: Nov. 2025. [Online]. Available: https://www.dynasupport.com/howtos/element/shell-formulations.

[24] B. Z. Haque and J. W. G. Jr., “Rate dependent progressive composite damage modeling using MAT162 in LS-DYNA,” in *13th International LS-DYNA Users Conference*, 2014, pp. 1.1–1.15.

[25] M. Loikkanen, G. Praveen, and D. Powell, “Simulation of ballistic impact on composite panels,” in *10th International LS-DYNA Users Conference*, 2008, pp. 9.1–9.12.

[26] J. Karlsson and M. Fagerström, “Edge-to-edge cohesive shell elements in LS-DYNA,” in *10th European LS-DYNA Conference*, 2015.

[27] C. G. Dávila and P. P. Camanho, “Decohesion elements using two and three-parameter mixed-mode criteria,” in *Proceedings of the American Helicopter Society Conference*, Williamsburg, VA, Oct. 2001.

[28] ASTM International, *ASTM D2344/D2344M-22: Standard Test Method for Short-Beam Strength of Polymer Matrix Composite Materials and Their Laminates*, Book of Standards Volume 15.03, West Conshohocken, PA, 2022. DOI: 10.1520/D2344_D2344M-22. [Online]. Available: https://www.astm.org/d2344_d2344m-22.html.

[29] ASTM International, *ASTM C297-94(1999): Standard Test Method for Flatwise Tensile Strength of Sandwich Constructions*, Book of Standards Volume 15.03. Reapproved 1999., West Conshohocken, PA, 1999. DOI: 10.1520/C0297-94R99. [Online]. Available: https://www.astm.org/c0297-94r99.html.

[30] D. Ranz, J. Cuartero, A. Miravete, and R. Miralbes, “Experimental research into interlaminar tensile strength of carbon/epoxy laminated curved beams,” *Composite Structures*, vol. 164, pp. 189–197, 2017. DOI: 10.1016/j.compstruct.2016.12.010.

[31] A. Kaddour, M. Hinton, P. Smith, and S. Li, “Mechanical properties and details of composite laminates for the test cases used in the third world-wide failure exercise,” *Journal of Composite Materials*, vol. 47, no. 20-21, pp. 2427–2442, 2013. DOI: 10.1177/0021998313499477.

[32] A. Gaurav and K. Singh, “ILSS improvement of quasi-isotropic glass fiber reinforced epoxy laminate enhanced with arc discharged multi-walled carbon nanotubes,” in *Materials Today: Proceedings 5*, 2018, pp. 8638–8644.

[33] H. W. Swift, “Plastic instability under plane stress,” *Journal of the Mechanics and Physics of Solids*, vol. 1, pp. 1–18, 1952.

[34] E. Voce, “The relationship between stress and strain for homogeneous deformation,” *Journal of the Institute of Metals*, vol. 74, pp. 537–562, 1948.

[35] G. C. Jacob, J. M. Starbuck, J. F. Fellers, S. Simunovic, and R. G. Boeman, “Strain rate effects on the mechanical properties of polymer composite materials,” *Journal of Applied Polymer Science*, vol. 94, no. 1, pp. 296–301, 2004. DOI: 10.1002/app.20901.

A

Supplement to the "Experimental Methodology" Chapter

A.1. Uncertainty Quantification of C-Scan Measurements

A.1.1. V30

ID	M1 [mm]	M2 [mm]	M3 [mm]	M4 [mm]	AVG [mm]	Lower Bound (P_{10})	Upper Bound (P_{90})
1	4.5	4.4	4.5	4.4	4.5	4.4	4.5
2	4.9	4.9	4.6	4.6	4.8	4.7	4.8
3	5.3	5.3	5.1	5.1	5.2	5.1	5.3
4	5.9	6	5.7	5.7	5.8	5.7	5.9
5	6.5	6.4	6.4	6.4	6.4	6.3	6.5
6	7.3	7.1	7.1	7.2	7.2	7.1	7.3
7	8.2	8.2	8.1	8.1	8.2	8.0	8.3
8	9.5	9.5	9.6	9.5	9.5	9.4	9.7
9	11.3	11.2	11	11.1	11.2	11.0	11.3
10	13	12.8	13	13.2	13.0	12.8	13.2
11	14.2	14.2	14.3	14.4	14.3	14.1	14.5
12	14.3	14.5	14.2	14.3	14.3	14.1	14.5
13	13.7	13.8	13.6	13.8	13.7	13.5	13.9
14	12.8	12.9	12.8	12.9	12.9	12.7	13.0
15	12.6	12.3	12.4	12.3	12.4	12.2	12.6
16	12.3	12.5	12.4	12.5	12.4	12.2	12.6
17	12.6	12.8	12.8	12.6	12.7	12.5	12.9
18	13	13.2	13	12.9	13.0	12.8	13.2
19	13.3	13.5	13.2	13.3	13.3	13.1	13.5
DIC-tracked	14.4	14.4	14.3	14.3	14.4	14.1	14.6

Table A.1: Intrusion measurements on the aluminum test-plate, V30

ID	M1N	M2N	M3N	M4N
1	1.011	0.989	1.011	0.989
2	1.032	1.032	0.968	0.968
3	1.019	1.019	0.981	0.981
4	1.013	1.030	0.979	0.979
5	1.012	0.996	0.996	0.996
6	1.017	0.990	0.990	1.003
7	1.006	1.006	0.994	0.994
8	0.997	0.997	1.008	0.997
9	1.013	1.004	0.987	0.996
10	1.000	0.985	1.000	1.015
11	0.995	0.995	1.002	1.009
12	0.998	1.012	0.991	0.998
13	0.998	1.005	0.991	1.005
14	0.996	1.004	0.996	1.004
15	1.016	0.992	1.000	0.992
16	0.990	1.006	0.998	1.006
17	0.992	1.008	1.008	0.992
18	0.998	1.013	0.998	0.990
19	0.998	1.013	0.991	0.998
DIC-tracked	1.003	1.003	0.997	0.997

Table A.2: Normalized measurements for standard deviation calculation, V30

A.1.2. V31

ID	M1 [mm]	M2 [mm]	M3 [mm]	M4 [mm]	AVG [mm]	Lower Bound (P_{10}) [mm]	Upper Bound (P_{90}) [mm]
1	6.3	6.3	6.1	6.3	6.3	6.2	6.3
2	6.8	6.5	6.4	6.3	6.5	6.4	6.6
3	6.9	6.8	6.9	6.8	6.9	6.8	6.9
4	7.4	7.3	7.3	7.2	7.3	7.2	7.4
5	8.0	7.9	8.2	7.9	8.0	7.9	8.1
6	8.7	8.8	8.8	8.7	8.7	8.6	8.8
7	9.8	10.0	9.9	10.0	9.9	9.8	10.1
8	11.6	11.5	11.7	11.5	11.5	11.4	11.7
9	12.8	12.8	12.8	12.6	12.7	12.6	12.9
10	13.6	13.5	13.6	13.5	13.5	13.4	13.7
11	13.2	13.1	13.1	13.1	13.1	13.0	13.3
12	12.2	12.2	12.2	12.3	12.2	12.1	12.3
13	11.5	11.4	11.4	11.4	11.4	11.3	11.6
14	11.2	11.1	11.1	11.1	11.1	11.0	11.2
15	11.0	11.0	11.0	11.0	11.0	10.9	11.1
16	11.2	11.2	11.1	11.1	11.1	11.0	11.3
17	11.4	11.3	11.3	11.3	11.3	11.2	11.4
18	11.4	11.3	11.3	11.3	11.3	11.2	11.5
19	11.5	11.5	11.5	11.5	11.5	11.3	11.6
DIC-tracked	12.7	12.6	12.6	12.6	12.6	12.5	12.8

Table A.3: Intrusion measurements on the aluminum test-plate, V31

ID	M1N	M2N	M3N	M4N
1	1.010	1.008	0.971	1.011
2	1.046	0.997	0.980	0.978
3	1.007	0.996	0.999	0.998
4	1.010	1.001	0.998	0.991
5	0.998	0.984	1.028	0.990
6	0.992	1.009	1.003	0.996
7	0.988	1.009	0.996	1.006
8	1.001	0.995	1.013	0.992
9	1.003	1.003	1.003	0.991
10	1.003	0.999	1.001	0.997
11	1.004	1.000	1.000	0.996
12	0.997	0.997	1.000	1.005
13	1.006	0.997	1.000	0.997
14	1.003	0.998	0.999	1.000
15	0.999	1.000	1.000	1.001
16	1.000	1.001	1.000	0.999
17	1.006	1.001	0.999	0.994
18	1.004	1.000	1.001	0.996
19	1.000	1.001	0.998	1.001
DIC-tracked	1.009	0.997	0.997	0.998

Table A.4: Normalized measurements for standard deviation calculation, V31

A.1.3. V32

ID	M1 [mm]	M2 [mm]	M3 [mm]	M4 [mm]	AVG [mm]	Lower Bound (P_{10}) [mm]	Upper Bound (P_{90}) [mm]
1	5.1	5.0	5.0	5.1	5.1	5.0	5.1
2	5.4	5.3	5.2	5.5	5.3	5.3	5.4
3	6.0	5.8	5.8	6.0	5.9	5.8	5.9
4	6.7	6.7	6.5	6.7	6.7	6.6	6.7
5	7.1	7.0	7.0	7.1	7.0	7.0	7.1
6	7.9	8.0	7.9	7.9	7.9	7.8	8.0
7	8.8	8.7	8.8	8.6	8.7	8.6	8.8
8	9.9	9.8	9.9	9.9	9.9	9.8	10.0
9	11.2	11.3	11.2	11.3	11.3	11.1	11.4
10	12.5	12.6	12.6	12.6	12.6	12.4	12.7
11	13.8	13.9	13.9	13.9	13.9	13.7	14.0
12	14.3	14.3	14.3	14.4	14.3	14.1	14.5
13	13.7	13.7	13.7	13.7	13.7	13.5	13.8
14	12.5	12.5	12.6	12.7	12.6	12.4	12.7
15	12.2	12.2	12.2	12.2	12.2	12.1	12.3
16	12.4	12.4	12.5	12.4	12.4	12.3	12.6
17	12.7	12.8	12.7	12.8	12.8	12.6	12.9
18	12.9	12.9	13.0	12.9	12.9	12.8	13.1
19	13.5	13.7	13.5	13.5	13.5	13.4	13.7
DIC-tracked	14.3	14.3	14.3	14.4	14.3	14.1	14.5

Table A.5: Intrusion measurements on the aluminum test-plate, V32

ID	M1N	M2N	M3N	M4N
1	1.015	0.982	0.994	1.009
2	1.011	0.992	0.970	1.026
3	1.018	0.977	0.984	1.020
4	1.012	0.998	0.980	1.010
5	1.009	0.991	0.994	1.006
6	0.997	1.010	0.996	0.997
7	1.012	0.990	1.011	0.988
8	0.997	0.993	1.004	1.006
9	0.991	1.004	0.998	1.007
10	0.998	1.000	1.001	1.002
11	0.996	0.998	1.003	1.003
12	0.997	1.001	0.997	1.005
13	1.002	1.001	0.999	0.999
14	0.995	0.996	1.002	1.006
15	1.002	0.999	1.000	0.999
16	0.998	0.999	1.003	1.000
17	0.995	1.004	0.999	1.002
18	0.998	0.999	1.002	1.000
19	0.996	1.011	0.994	0.999
DIC-tracked	0.997	1.001	0.997	1.005

Table A.6: Normalized measurements for standard deviation calculation, V32

A.1.4. V22

ID	M1 [mm]	M2 [mm]	M3 [mm]	M4 [mm]	AVG [mm]	Lower Bound (P_{10}) [mm]	Upper Bound (P_{90}) [mm]
1	4.6	4.6	4.7	4.6	4.6	4.5	4.7
2	4.9	4.8	4.7	4.8	4.8	4.7	4.8
3	5.1	5.4	5.2	5.0	5.2	5.1	5.3
4	5.3	5.5	5.4	5.6	5.4	5.4	5.5
5	6.0	5.8	5.9	6.1	6.0	5.9	6.0
6	6.7	6.6	6.7	6.7	6.7	6.6	6.8
7	7.9	7.9	7.9	8.0	7.9	7.8	8.0
8	10.4	10.2	10.3	10.3	10.3	10.2	10.4
9	12.6	12.5	12.5	12.5	12.5	12.3	12.7
10	13.0	12.7	12.7	12.9	12.8	12.7	13.0
11	11.9	11.8	11.8	11.9	11.9	11.7	12.0
12	9.9	9.8	9.8	9.7	9.8	9.7	10.0
13	8.0	8.0	8.0	7.9	8.0	7.9	8.1
14	6.4	6.4	6.4	6.4	6.4	6.3	6.5
15	5.7	5.7	5.7	5.7	5.7	5.6	5.7
16	5.2	5.2	5.4	5.2	5.2	5.2	5.3
17	4.8	5.0	4.9	4.9	4.9	4.8	4.9
18	4.7	4.6	4.5	4.6	4.6	4.5	4.6
19	4.5	4.5	4.5	4.4	4.5	4.4	4.5
DIC-tracked	13.0	12.7	12.7	12.9	12.8	12.7	13.0

Table A.7: Intrusion measurements on the aluminum test-plate, V22

ID	M1N	M2N	M3N	M4N
1	0.998	0.998	1.011	0.992
2	1.015	0.994	0.990	1.002
3	0.990	1.038	1.001	0.971
4	0.980	1.008	0.991	1.021
5	1.011	0.981	0.991	1.016
6	0.997	0.995	1.010	0.998
7	0.996	1.001	0.997	1.006
8	1.012	0.991	0.995	1.002
9	1.008	1.000	0.996	0.996
10	1.014	0.990	0.992	1.004
11	1.006	0.992	0.996	1.007
12	1.009	1.001	0.999	0.991
13	1.002	0.998	1.005	0.995
14	0.997	0.997	1.002	1.004
15	1.002	1.004	0.996	0.998
16	0.993	0.991	1.022	0.993
17	0.978	1.017	1.011	0.994
18	1.019	1.006	0.978	0.997
19	0.998	1.003	1.012	0.987
DIC-tracked	1.014	0.990	0.992	1.004

Table A.8: Normalized measurements for standard deviation calculation, V22

A.2. Microscopy Verification of C-Scan Results

A.2.1. V31

The microscopy results for V31 with C-scan measurements overlays are presented in Figure A.1. Delaminations develop in all plies through-the-thickness and the lengths of the longest ones are comparable to the corresponding C-scans results.

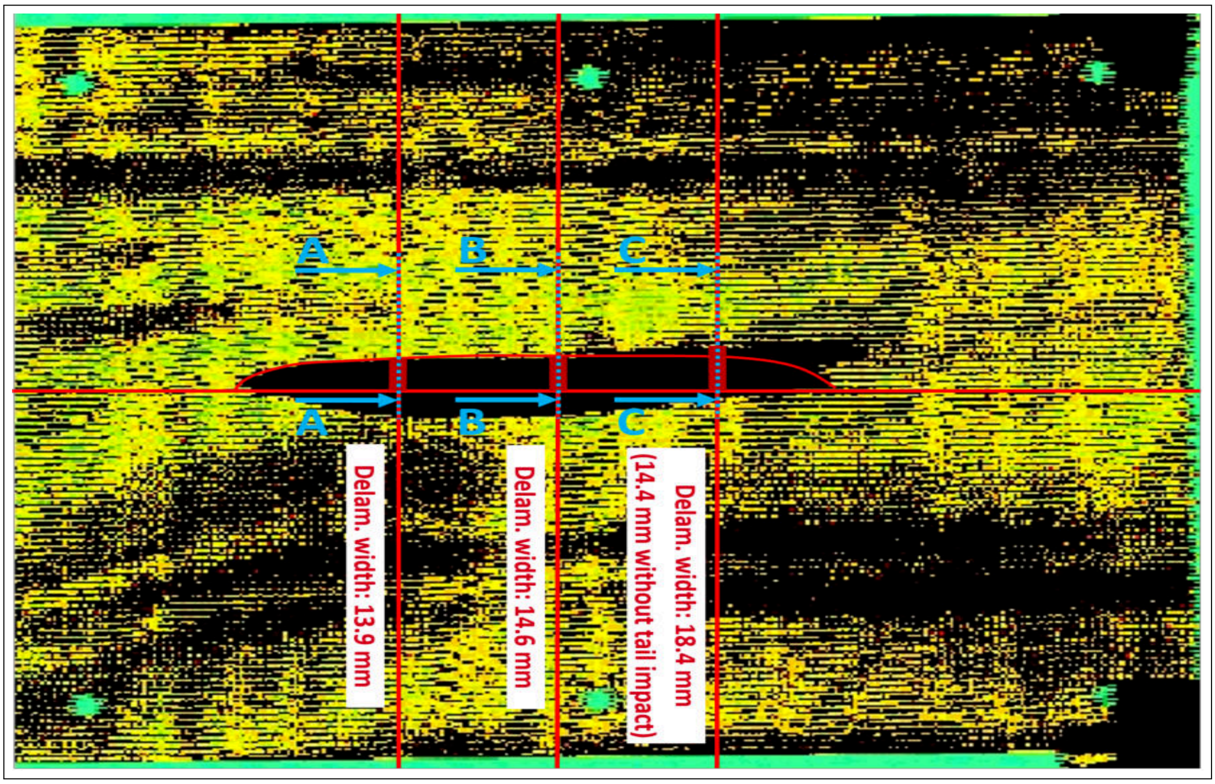

(a) Delamination width measurement at every cutting positions, V31

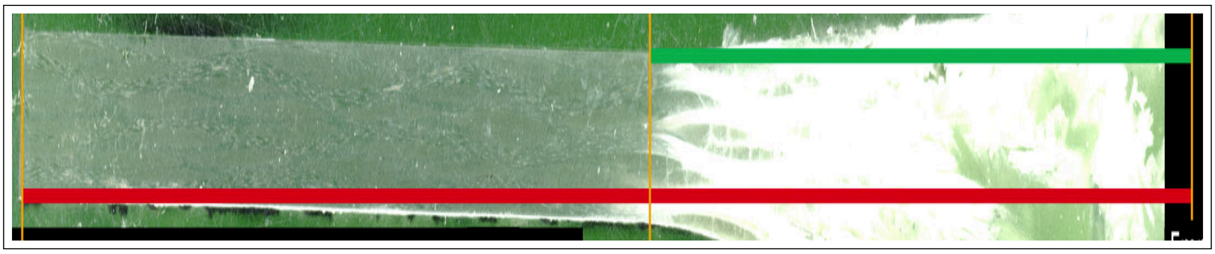

(b) Section A-A, V31

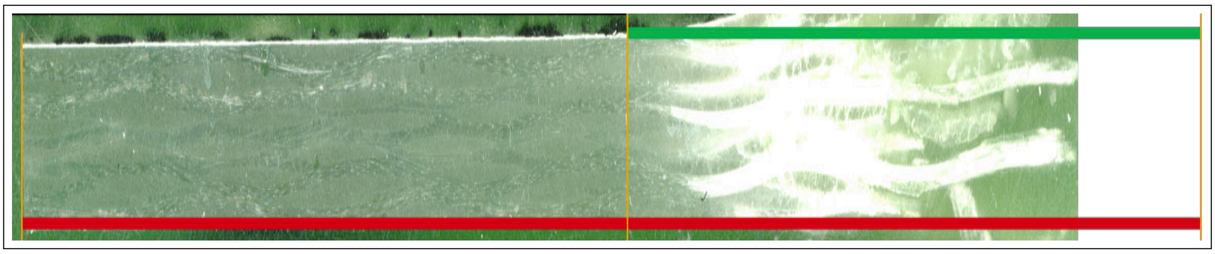

(c) Section B-B, V31

Continued on next page...

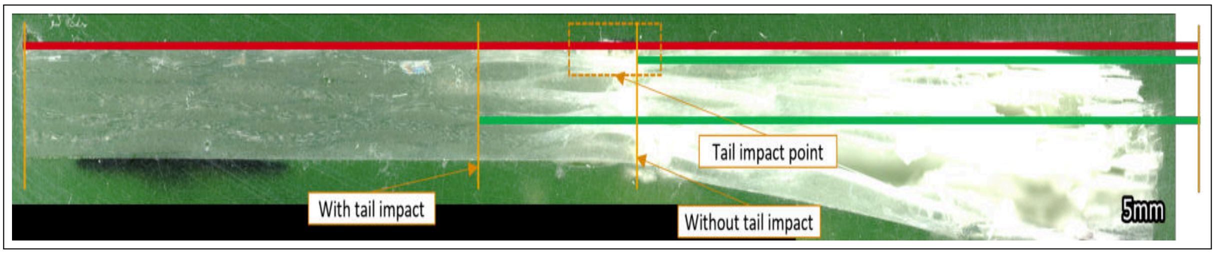

(d) Section C-C, V31

Figure A.1: Microscopy results with C-scan measurement overlay, V31

A.2.2. V32

The microscopy results for V32 with C-scan measurements overlays are presented in Figure A.2. Delaminations develop in all plies through-the-thickness and the lengths of the longest ones are comparable to the corresponding C-scans results.

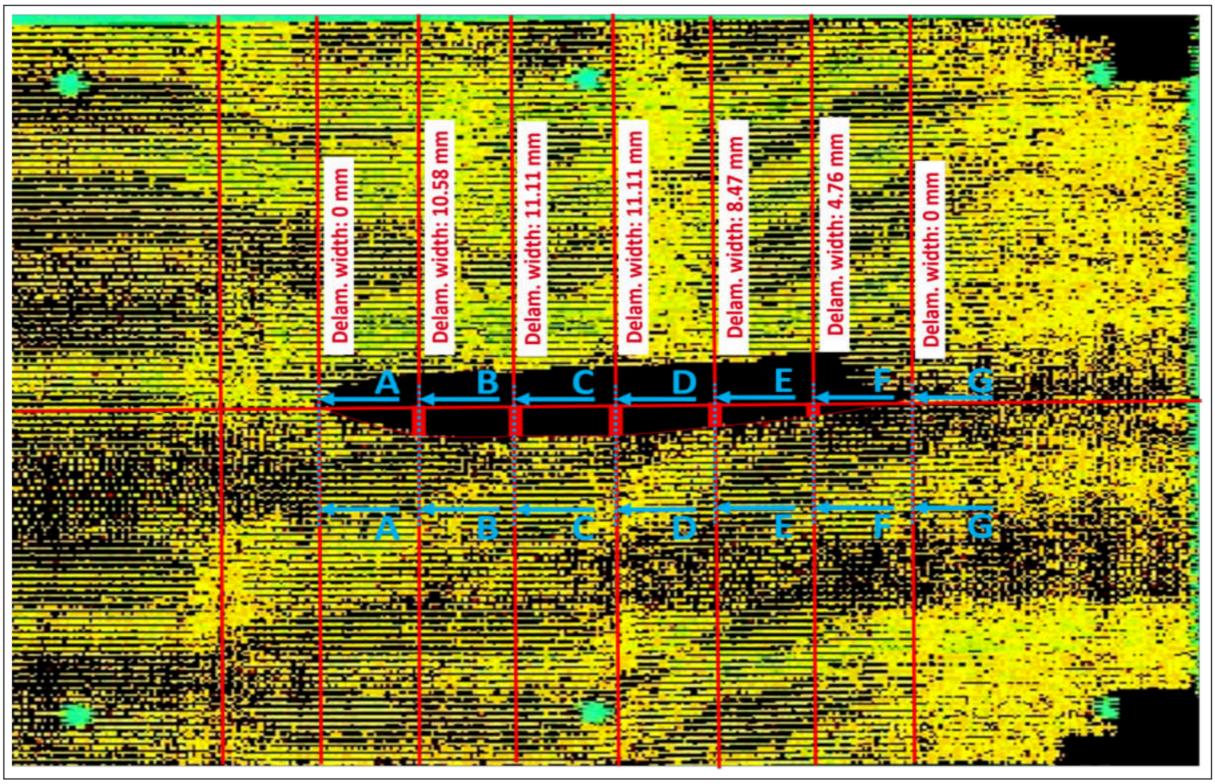

(a) Delamination width measurement at every cutting positions, V32

Continued on next page...

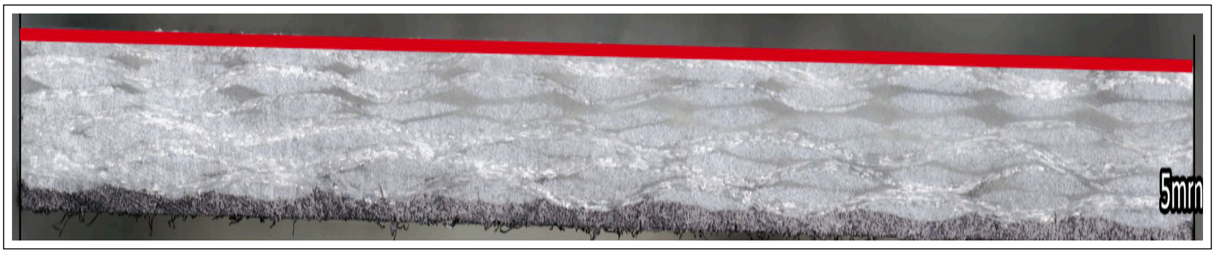

(b) Section A-A, V32

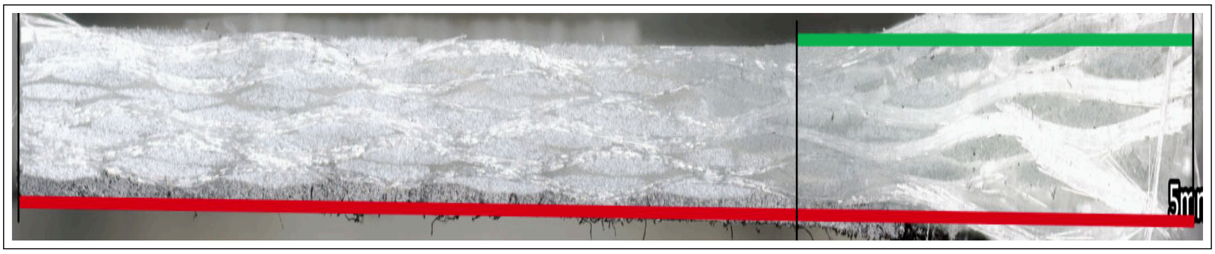

(c) Section B-B, V32

(d) Section C-C, V32

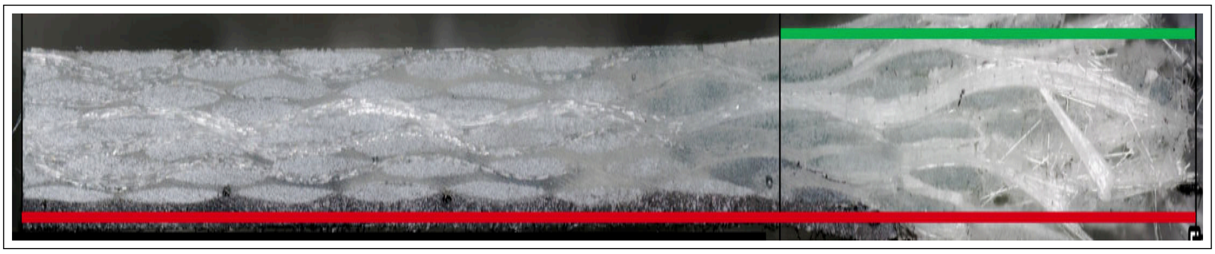

(e) Section D-D, V32

(f) Section E-E, V32

Continued on next page...

(g) Section F-F, V32

(h) Section G-G, V32

Figure A.2: Microscopy results with C-scan measurement overlay, V32

A.2.3. V22

The microscopy results for V22 with C-scan measurements overlays are presented in Figure A.3. Delaminations develop in all plies through-the-thickness and the lengths of the longest ones are comparable to the corresponding C-scans results.

Note that as V22 is highly damaged and it is hard to mentally visualize the original sample width, for each measurement an undamaged sample is placed next to the tested sample for reference.

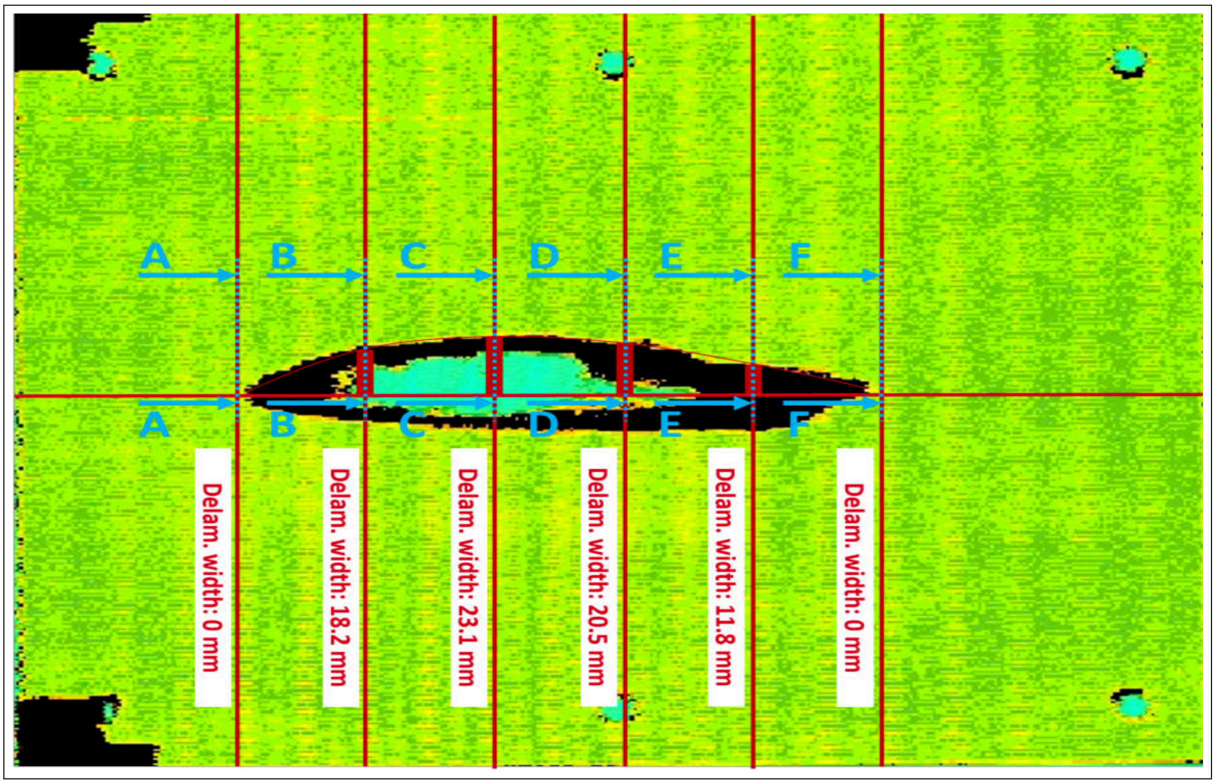

(a) Delamination width measurement at every cutting positions, V22

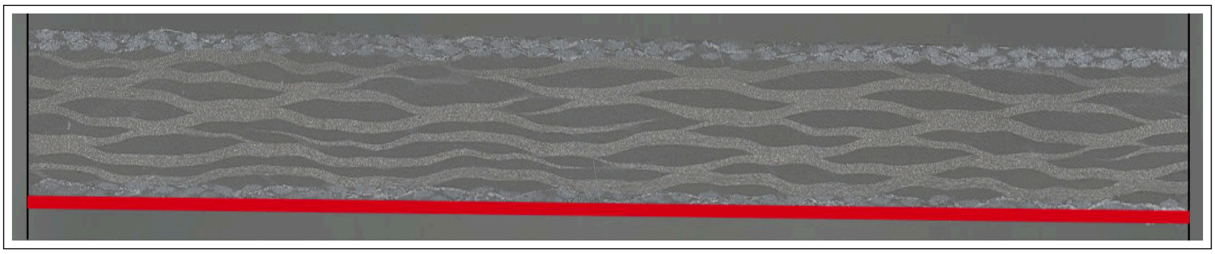

(b) Section A-A, V22

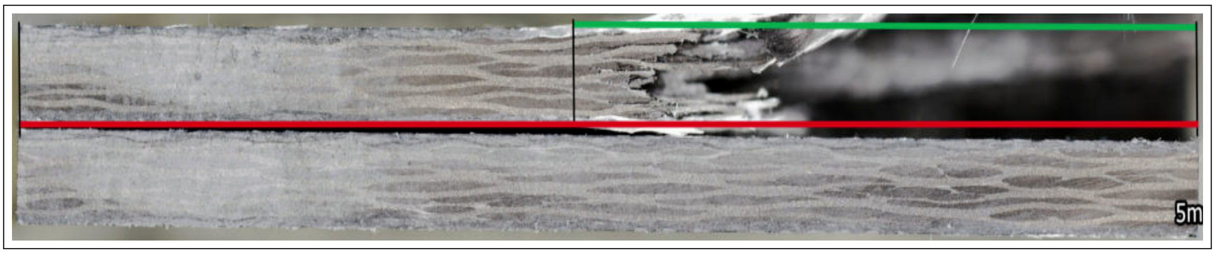

(c) Section B-B, V22

Continued on next page...

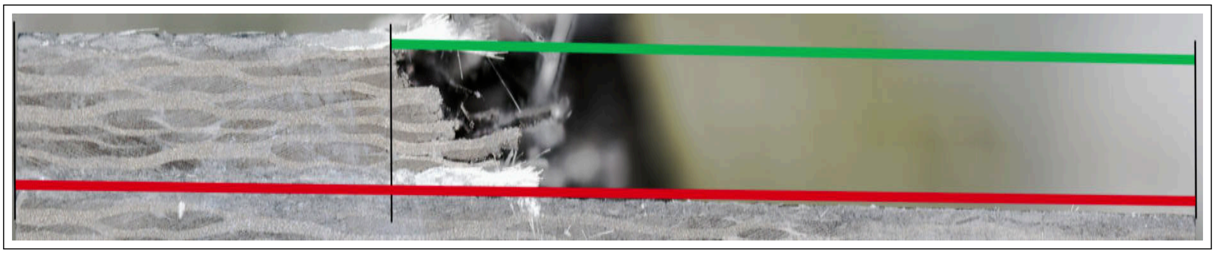

(d) Section C-C, V22

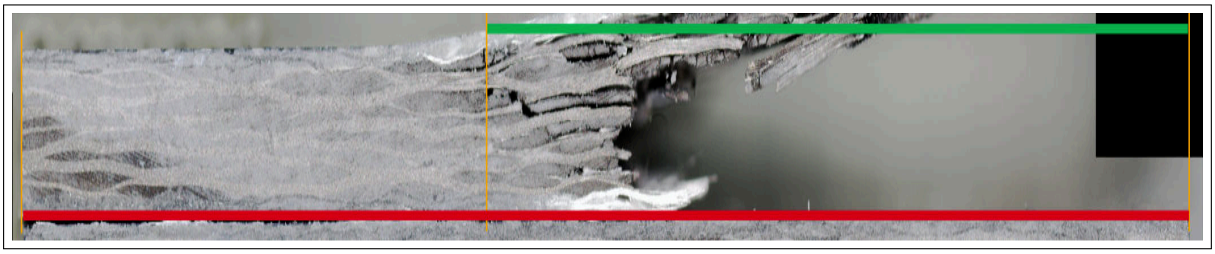

(e) Section D-D, V22

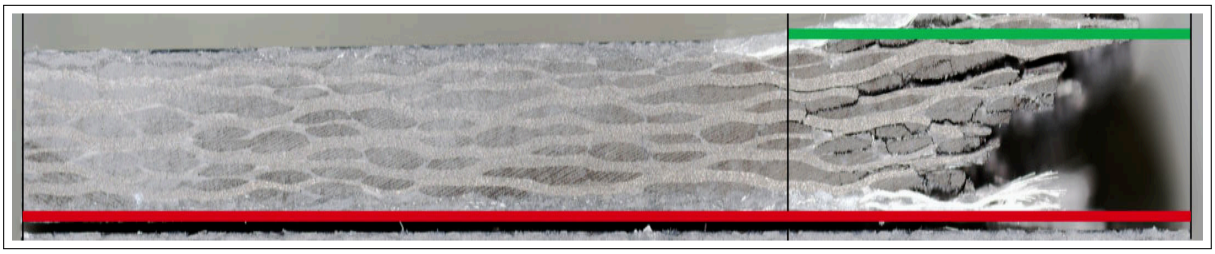

(f) Section E-E, V22

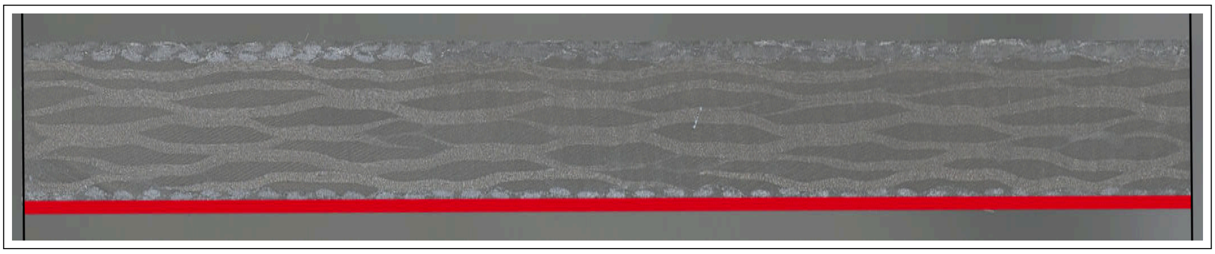

(g) Section F-F, V22

Figure A.3: Microscopy results with C-scan measurement overlay, V22

B

Supplement to the "Numerical Analysis" Chapter

B.1. Baseline Model

B.1.1. Step 0

Name	Value
File Name	B0.i1
TERMTIME	25 ms
DT2MS	-5E-4 ms
Impact Angle	$-\alpha°$
Impact Position	0 mm
Friction SF	4.5

Table B.1: Input file parameters, Step 0

Name	Value
File Name	screw_4kN.key
Type	M6
Mesh size screw head	7mm
Diameter screw head	30mm
Mesh size screw end	5mm
Material ID	STEEL
Pre-load	4kN

Table B.2: Bolt include parameters, Step 0

Name	Value
File Name	final_baseline_2781000_5mm_trap.key
Length	370mm
Width	322mm
Thickness	1.758mm
Mesh size	5mm
Integration rule	Trapezoidal
Material ID	GLASS_1

Table B.3: Protection plate include parameters, Step 0

Name	Value
File Name	aluminum_plate.key
Length	370mm
Width	322mm
Thickness	3mm
Mesh size	5mm
Material ID	ALU_1

Table B.4: Aluminum plate include parameters, Step 0

Name	Value
File Name	spacer_13mm.key
Length	370mm
Width	40mm
Thickness	13mm
Mesh size	5mm
Material ID	ALU_1

Table B.5: Spacer include parameters, Step 0

Name	Value
File Name	projectile_A.key
Length	d mm
Base	$a \times b$mm
Mesh size	3mm
Material ID	RIGID
Initial velocity	v [m/s]
Mass	m [Kg]

Table B.6: Impactor include parameters, Step 0

Name	Value
File Name	rail_fixture.key
Length	800mm
Width	50mm
Thickness	1mm
Mesh size	5mm
Material ID	RIGID

Table B.7: Fixture include parameters, Step 0

B.1.2. Step 1

Name	Value
File Name	B1.i1
TERMTIME	25 ms
DT2MS	-5E-4 ms
Impact Angle	$-\alpha°$
Impact Position	0 mm
Friction SF	4.5

Table B.8: Input file parameters, Step 1

Name	Value
File Name	final_baseline_2781000_5mm.key
Length	370mm
Width	322mm
Thickness	1.758mm
Mesh size	5mm
Integration rule	Simpson
Material ID	GLASS_1

Table B.9: Protection plate include parameters, Step 1

B.1.3. Step 2

Name	Value
File Name	B2.i1
TERMTIME	25 ms
DT2MS	-5E-4 ms
Impact Angle	$-\alpha°$
Impact Position	0 mm
Friction SF	4.5

Table B.10: Input file parameters, Step 2

Name	Value
File Name	projectile_B.key
Length	c mm
Base	$a \times b$mm
Mesh size	3mm
Material ID	RIGID
Initial velocity	v m/s
Mass	m Kg

Table B.11: Impactor include parameters, Step 2

B.1.4. Step 3

Name	Value
File Name	B3.i1
TERMTIME	25 ms
DT2MS	-5E-4 ms
Impact Angle	$(-\alpha - 1.155)°$
Impact Position	73 mm
Friction SF	4.5

Table B.12: Input file parameters, Step 3

B.1.5. Step 4

Name	Value
File Name	B4.i1
TERMTIME	25 ms
DT2MS	-5E-4 ms
Impact Angle	$(-\alpha - 1.155)°$
Impact Position	73 mm
Friction SF	3

Table B.13: Input file parameters, Step 4

B.1.6. Step 5

Name	Value
File Name	B5.i1
TERMTIME	25 ms
DT2MS	-5E-4 ms
Impact Angle	$(-\alpha - 1.155)^\circ$
Impact Position	73 mm
Friction SF	3

Table B.14: Input file parameters, Step 5

Name	Value
File Name	screw_9kN.key
Type	M6
Mesh size screw head	7mm
Diameter screw head	30mm
Mesh size screw end	5mm
Material ID	STEEL
Pre-load	9kN

Table B.15: Bolt include parameters, Step 5

B.1.7. Step 6A

Name	Value
File Name	B6A.i1
TERMTIME	25 ms
DT2MS	-5E-4 ms
Impact Angle	$(-\alpha - 1.155)^\circ$
Impact Position	73 mm
Friction SF	3

Table B.16: Input file parameters, Step 6A

Name	Value
File Name	final_baseline_2781000_5mm.key
Length	370mm
Width	322mm
Thickness	1.758mm
Mesh size	5mm
Integration rule	Simpson
Material ID	GLASS_1

Table B.17: Protection plate include parameters, Step 6A

B.1.8. Step 6B

Name	Value
File Name	B6B.i1
TERMTIME	25 ms
DT2MS	-5E-4 ms
Impact Angle	$(-\alpha - 1.155)^\circ$
Impact Position	73 mm
Friction SF	3

Table B.18: Input file parameters, Step 6B

Name	Value
File Name	final_baseline_2781000_2mm.key
Length	370mm
Width	322mm
Thickness	1.758mm
Mesh size	2mm
Integration rule	Simpson
Material ID	GLASS_1

Table B.19: Protection plate include parameters, Step 6B

B.1.9. Step 6C

Name	Value
File Name	B6C.i1
TERMTIME	25 ms
DT2MS	-5E-6 ms
Impact Angle	$(-\alpha - 1.155)^\circ$
Impact Position	73 mm
Friction SF	3

Table B.20: Input file parameters, Step 6C

Name	Value
File Name	final_baseline_2781000_2mm.key
Length	370 mm
Width	322 mm
Thickness	1.758 mm
Mesh size	2 mm
Integration rule	Simpson
Material ID	GLASS_1

Table B.21: Protection plate include parameters, Step 6C

B.1.10. Step 6D

Name	Value
File Name	B6D.i1
TERMTIME	25 ms
DT2MS	-5E-4 ms
Impact Angle	$(-\alpha - 1.155)^\circ$
Impact Position	73 mm
Friction SF	3

Table B.22: Input file parameters, Step 6D

Name	Value
File Name	final_baseline_1000_5mm.key
Length	370 mm
Width	322 mm
Thickness	1.758 mm
Mesh size	5 mm
Integration rule	Simpson
Material ID	GLASS_1

Table B.23: Protection plate include parameters, Step 6D

B.1.11. Step 6E

Name	Value
File Name	B6E.i1
TERMTIME	25 ms
DT2MS	-5E-4 ms
Impact Angle	$(-\alpha - 1.155)^\circ$
Impact Position	73 mm
Friction SF	3

Table B.24: Input file parameters, Step 6E

Name	Value
File Name	final_baseline_1000_2mm.key
Length	370 mm
Width	322 mm
Thickness	1.758 mm
Mesh size	2 mm
Integration rule	Simpson
Material ID	GLASS_1

Table B.25: Protection plate include parameters, Step 6E

B.1.12. Step 6F

Name	Value
File Name	B6F.i1
TERMTIME	25 ms
DT2MS	-5E-6 ms
Impact Angle	$(-\alpha - 1.155)^{\circ}$
Impact Position	73 mm
Friction SF	3

Table B.26: Input file parameters, Step 6F

Name	Value
File Name	final_baseline_1000_2mm.key
Length	370 mm
Width	322 mm
Thickness	1.758 mm
Mesh size	2 mm
Integration rule	Simpson
Material ID	GLASS_1

Table B.27: Protection plate include file parameters, Step 6F

B.2. Delamination Model with GLASS_2

B.2.1. Step 7

Name	Value
File Name	v31_oneway_nofail.i1
TERMTIME	25 ms
DT2MS	-5E-4 ms
Impact Angle	$(-\alpha - 1.155)^{\circ}$
Impact Position	73 mm
Friction SF	3

Table B.28: Input file parameters, Step 7

Name	Value
File Name	schutzplatte_g_oneway_nofail.key
Length	370 mm
Width	322 mm
Thickness	1.758 mm
Mesh size	2 mm
Integration rule	Simpson
Material ID	GLASS_2
Contact Option	8 (ONEWAY)
NFLS	-
SFLS	-
CCRIT	0 mm
FS	-
FD	-

Table B.29: Protection plate include parameters, Step 7

B.2.2. Step 8

Name	Value
File Name	v31_oneway.i1
TERMTIME	25 ms
DT2MS	-5E-4 ms
Impact Angle	$(-\alpha - 1.155)^\circ$
Impact Position	73 mm
Friction SF	3

Table B.30: Input file parameters, Step 8

Name	Value
File Name	schutzplatte_g_oneway.key
Length	370 mm
Width	322 mm
Thickness	1.758 mm
Mesh size	2 mm
Integration rule	Simpson
Material ID	GLASS_2
Contact Option	8 (ONEWAY)
NFLS	0.05 GPa
SFLS	0.02 GPa
CCRIT	0 mm
FS	-
FD	-

Table B.31: Protection plate include parameters, Step 8

B.2.3. Step 9

Name	Value
File Name	v31_twoway_ts6.i1
TERMTIME	25 ms
DT2MS	-5E-6 ms
Impact Angle	$(-\alpha - 1.155)^\circ$
Impact Position	73 mm
Friction SF	3

Table B.32: Input file parameters, Step 9

Name	Value
File Name	schutzplatte_g_twoway.key
Length	370 mm
Width	322 mm
Thickness	1.758 mm
Mesh size	2 mm
Integration rule	Simpson
Material ID	GLASS_2
Contact Option	8 (TWOWAY)
NFLS	0.05 GPa
SFLS	0.02 GPa
CCRIT	0 mm
FS	-
FD	-

Table B.33: Protection plate include parameters, Step 9

B.2.4. Step 11

Name	Value
File Name	v30_twoway_ts6.i1
TERMTIME	25 ms
DT2MS	-5E-6 ms
Impact Angle	$(-\alpha - 2.943)^\circ$
Impact Position	109 mm
Friction SF	3

(a) Input file parameters V30

Name	Value
File Name	v32_twoway_ts6.i1
TERMTIME	25 ms
DT2MS	-5E-6 ms
Impact Angle	$(-\alpha - 3.415)^\circ$
Impact Position	100 mm
Friction SF	3

(b) Input file parameters V32

Table B.34: Input file parameters for V30 and V32, Step 11

B.2.5. Step 12

Name	Value
File Name	v22_twoway_ts6.i1
TERMTIME	25 ms
DT2MS	-5E-6 ms
Impact Angle	$(-\alpha - 2.534)^\circ$
Impact Position	73 mm
Friction SF	3

Table B.35: Input file parameters, Step 12

Name	Value
File Name	schutzplatte_cg_twoway.key
Length	370 mm
Width	322 mm
Thickness	2 mm
Mesh size	2 mm
Integration rule	Simpson
Material ID	GLASS_2, CARBON
Contact Option	8 (TWOWAY)
NFLS	0.05 GPa
SFLS	0.02 GPa
CCRIT	0 mm
FS	-
FD	-

Table B.36: Protection plate include parameters, Step 12

Name	Value
File Name	spacer_10mm.key
Length	370mm
Width	40mm
Thickness	10mm
Mesh size	5mm
Material ID	ALU_1

Table B.37: Spacer include parameters, Step 12

B.2.6. EX1A

Name	Value
File Name	v31_EX1A.i1
TERMTIME	25 ms
DT2MS	-5E-4 ms
Impact Angle	$(-\alpha - 1.155)^{\circ}$
Impact Position	73 mm
Friction SF	3

Table B.38: Input file parameters, Step EX1A

Name	Value
File Name	schutzplatte_g_oneway_lowccrit.key
Length	370 mm
Width	322 mm
Thickness	1.758 mm
Mesh size	2 mm
Integration rule	Simpson
Material ID	GLASS_2
Contact Option	8 (ONEWAY)
NFLS	0.05 GPa
SFLS	0.02 GPa
CCRIT	0.1 mm
FS	-
FD	-

Table B.39: Protection plate include parameters, Step EX1A

B.2.7. EX1B

Name	Value
File Name	v31_EX1B.i1
TERMTIME	25 ms
DT2MS	-5E-6 ms
Impact Angle	$(-\alpha - 1.155)^{\circ}$
Impact Position	73 mm
Friction SF	3

Table B.40: Input file parameters, Step EX1B

B.2.8. EX1C

Name	Value
File Name	v31_EX1C.i1
TERMTIME	25 ms
DT2MS	-5E-4 ms
Impact Angle	$(-\alpha - 1.155)^{\circ}$
Impact Position	73 mm
Friction SF	3

Table B.41: Input file parameters, Step EX1C

B.2.9. EX1D

Name	Value
File Name	v31_EX1D.i1
TERMTIME	25 ms
DT2MS	-5E-4 ms
Impact Angle	$(-\alpha - 1.155)^\circ$
Impact Position	73 mm
Friction SF	3

Table B.42: Input file parameters, Step EX1D

Name	Value
File Name	schutzplatte_g_twoway.key
Length	370 mm
Width	322 mm
Thickness	1.758 mm
Mesh size	2 mm
Integration rule	Simpson
Material ID	GLASS_2
Contact Option	8 (TWOWAY)
NFLS	0.05 GPa
SFLS	0.02 GPa
CCRIT	0 mm
FS	-
FD	-

Table B.43: Protection plate include parameters, Step EX1D

B.2.10. EX1E

Name	Value
File Name	v31_EX1E.i1
TERMTIME	25 ms
DT2MS	-5E-6 ms
Impact Angle	$(-\alpha - 1.155)^\circ$
Impact Position	73 mm
Friction SF	3

Table B.44: Input file parameters, Step EX1E

B.2.11. EX2A

Name	Value
File Name	v31_EX2A.i1
TERMTIME	25 ms
DT2MS	-5E-4 ms
Impact Angle	$(-\alpha - 1.155)^\circ$
Impact Position	73 mm
Friction SF	3

Table B.45: Input file parameters, Step EX2A

Name	Value
File Name	aluminum_plate_v2.key
Length	370mm
Width	322mm
Thickness	3mm
Mesh size	5mm
Material ID	ALU_2

Table B.46: Aluminum plate include parameters, EX2A

B.2.12. EX2B

Name	Value
File Name	v31_EX2B.i1
TERMTIME	25 ms
DT2MS	-5E-4 ms
Impact Angle	$(-\alpha - 1.155)^{\circ}$
Impact Position	73 mm
Friction SF	3

Table B.47: Input file parameters, Step EX2B

Name	Value
File Name	aluminum_plate_sr.key
Length	370mm
Width	322mm
Thickness	3mm
Mesh size	5mm
Material ID	ALU_3

Table B.48: Aluminum plate include parameters, EX2B

B.2.13. EX3

Name	Value
File Name	v22_EX3.i1
TERMTIME	25 ms
DT2MS	-5E-6 ms
Impact Angle	$(-\alpha - 2.534)^{\circ}$
Impact Position	73 mm
Friction SF	4.5

Table B.49: Input file parameters, Step EX3

B.3. Delamination Model with GLASS_1

B.3.1. Step F1

Name	Value
File Name	v31_F1.i1
TERMTIME	25 ms
DT2MS	-5E-6 ms
Impact Angle	$(-\alpha - 1.155)^{\circ}$
Impact Position	73 mm
Friction SF	3

Table B.50: Input file parameters, Step F1

Name	Value
File Name	schutzplatte_F1.key
Length	370 mm
Width	322 mm
Thickness	1.758 mm
Mesh size	5 mm
Integration rule	Simpson
Material ID	GLASS_1
Contact Option	8 (TWOWAY)
NFLS	0.05 GPa
SFLS	0.02 GPa
CCRIT	0 mm
FS	-
FD	-

Table B.51: Protection plate include parameters, Step F1

B.3.2. Step F2

Name	Value
File Name	v31_F2.i1
TERMTIME	25 ms
DT2MS	-5E-6 ms
Impact Angle	$(-\alpha - 1.155)^{\circ}$
Impact Position	73 mm
Friction SF	3

Table B.52: Input file parameters, Step F2

Name	Value
File Name	schutzplatte_F2.key
Length	370 mm
Width	322 mm
Thickness	1.758 mm
Mesh size	5 mm
Integration rule	Simpson
Material ID	GLASS_1
Contact Option	8 (ONEWAY)
NFLS	0.05 GPa
SFLS	0.02 GPa
CCRIT	0 mm
FS	-
FD	-

Table B.53: Protection plate include parameters, Step F2

B.3.3. Step F3

Name	Value
File Name	v31_F3.i1
TERMTIME	25 ms
DT2MS	-5E-6 ms
Impact Angle	$(-\alpha - 1.155)^{\circ}$
Impact Position	73 mm
Friction SF	3

Table B.54: Input file parameters, Step F3

B.3.4. Step F4

Name	Value
File Name	v31_F4.i1
TERMTIME	25 ms
DT2MS	-5E-6 ms
Impact Angle	$(-\alpha - 1.155)^{\circ}$
Impact Position	73 mm
Friction SF	3

Table B.55: Input file parameters, Step F4

B.3.5. Step F5

Name	Value
File Name	v31_F5.i1
TERMTIME	25 ms
DT2MS	-5E-6 ms
Impact Angle	$(-\alpha - 1.155)^{\circ}$
Impact Position	73 mm
Friction SF	3

Table B.56: Input file parameters, Step F5

Name	Value
File Name	schutzplatte_F5.key
Length	370 mm
Width	322 mm
Thickness	1.758 mm
Mesh size	5 mm
Integration rule	Simpson
Material ID	GLASS_1
Contact Option	8 (ONEWAY)
NFLS	0.05 GPa
SFLS	0.02 GPa
CCRIT	0 mm
FS	0.5
FD	0.4
DC	1

Table B.57: Protection plate include parameters, Step F5

B.3.6. Step F6

Name	Value
File Name	v31_F6.i1
TERMTIME	25 ms
DT2MS	-5E-6 ms
Impact Angle	$(-\alpha - 1.155)^{\circ}$
Impact Position	73 mm
Friction SF	3

Table B.58: Input file parameters, Step F6

B.3.7. Step F7

Name	Value
File Name	v31_F7.i1
TERMTIME	25 ms
DT2MS	-5E-6 ms
Impact Angle	$(-\alpha - 1.155)^\circ$
Impact Position (dx)	73 mm
Impact Position (dy)	5 mm
Friction SF	3

Table B.59: Input file parameters, Step F7

B.3.8. Step F8

Name	Value
File Name	v31_F8.i1
TERMTIME	25 ms
DT2MS	-5E-6 ms
Impact Angle	$-\alpha^\circ$
Impact Position (dx)	73 mm
Impact Position (dy)	5 mm
Rotation	-37°[a]
Tilt	2°
Friction SF	3

Table B.60: Input file parameters, Step F8

[a]The model is imported flat, hence the standard rotation is -45°, and updating the angle to -37° results in a clock-wise rotation

B.3.9. Step F9

Name	Value
File Name	v31_F8.i1
TERMTIME	25 ms
DT2MS	-5E-6 ms
Impact Angle	$-\alpha°$
Impact Position (dx)	73 mm
Impact Position (dy)	2 mm
Rotation	$-38°$
Tilt	$2°$
Friction SF	3

Table B.61: Input file parameters, Step F9

C

Supplement to the "Results and Discussion" Chapter

C.1. Baseline Model

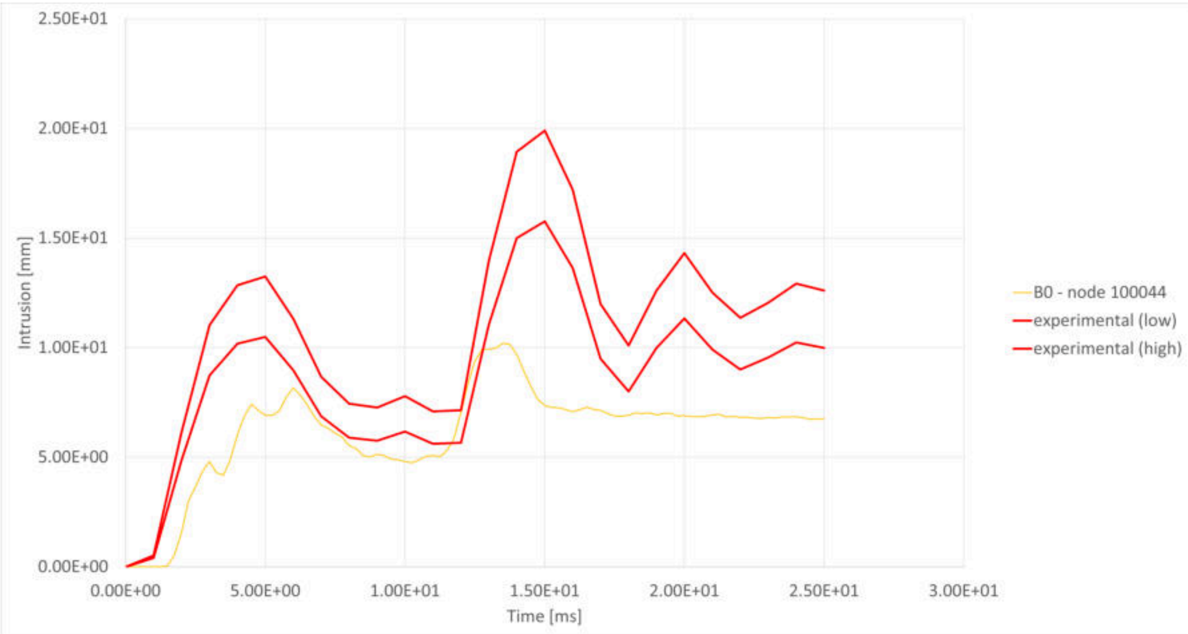

Figure C.1: Intrusion over time for orange node, compared to v31 experimental band, step 0

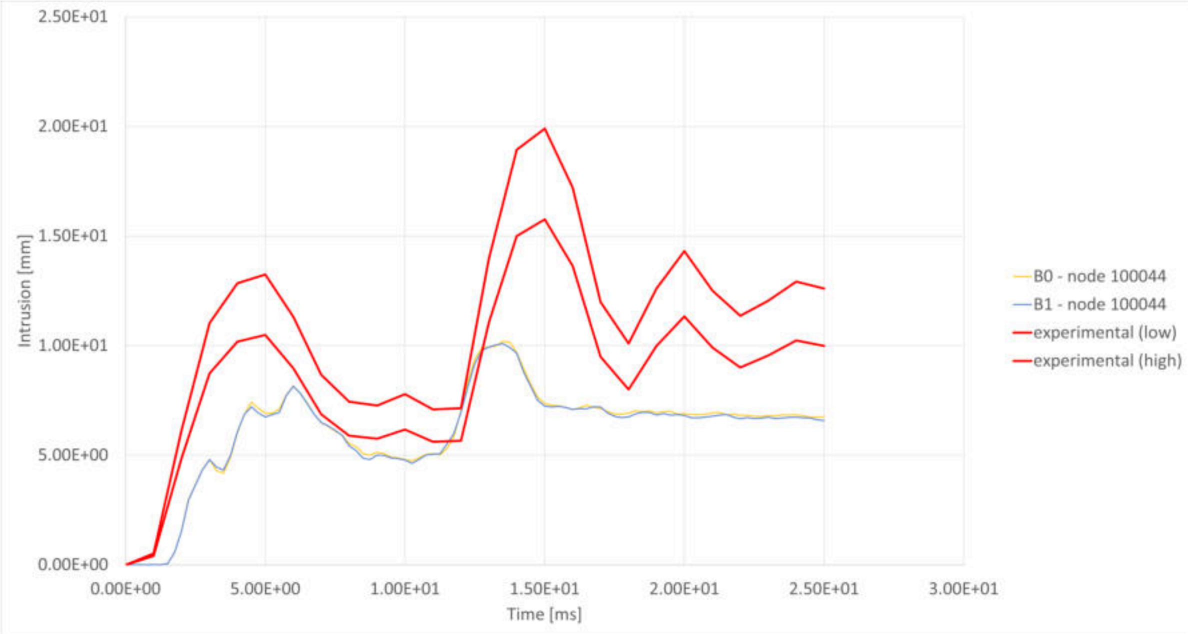

Figure C.2: Intrusion over time for orange node, compared to the v31 experimental band and to the step 0 curve, step 1

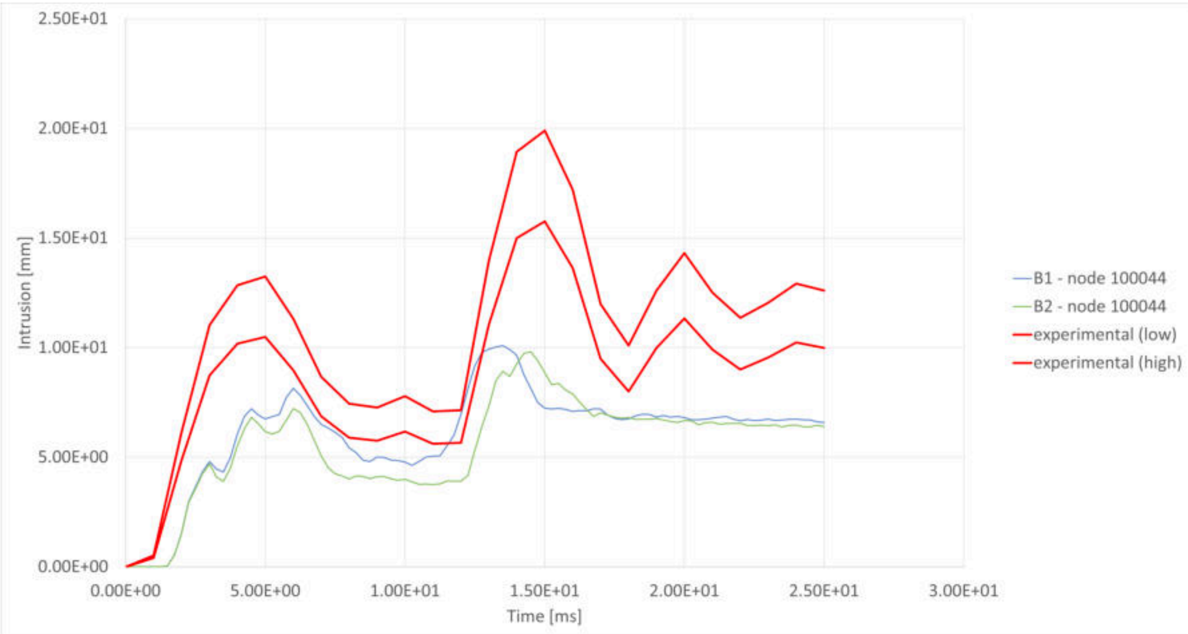

Figure C.3: Intrusion over time for orange node, compared to v31 experimental band and to the step 1 curve, step 2

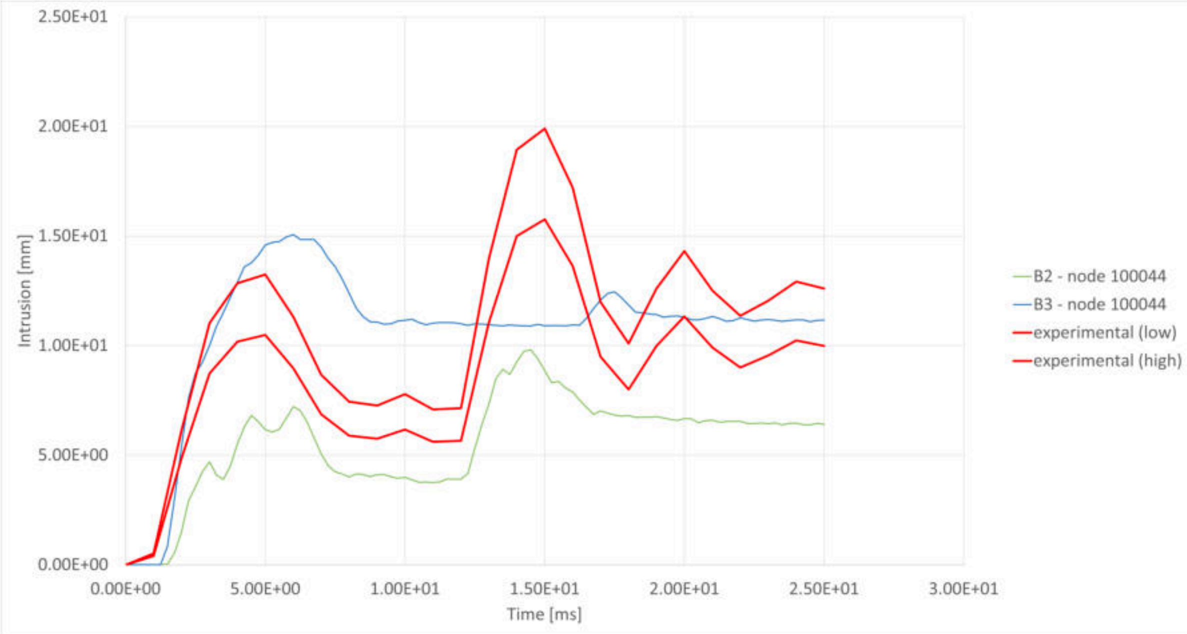

Figure C.4: Intrusion over time for orange node, compared to v31 experimental band and to the step 2 curve, step 3

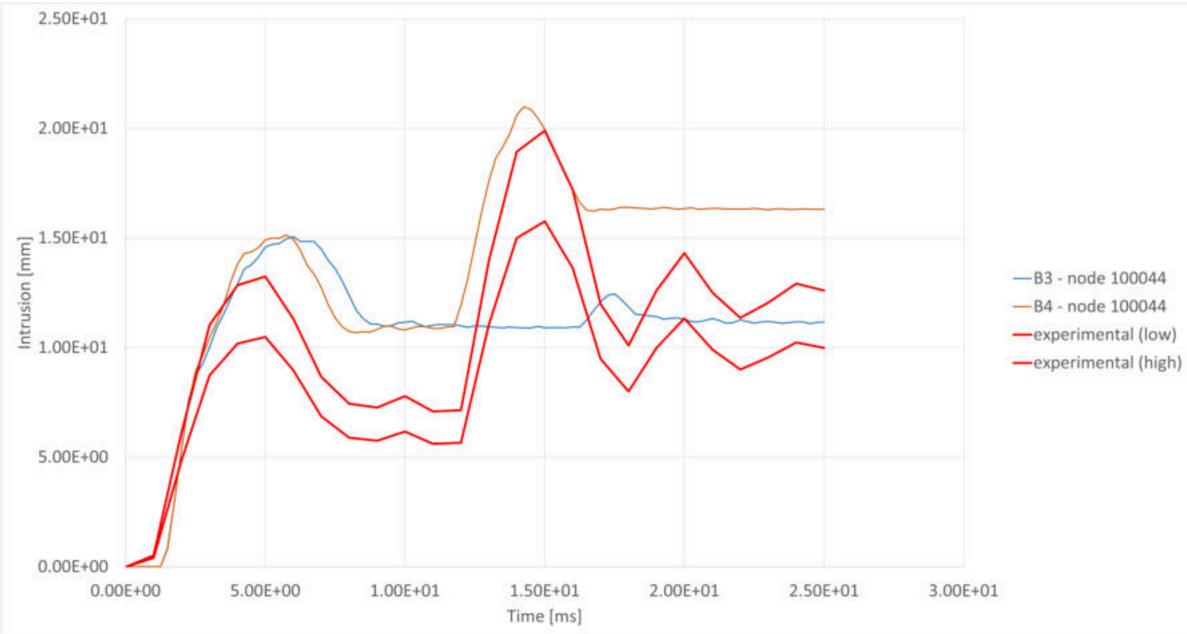

Figure C.5: Intrusion over time for orange node, compared to v31 experimental band and to the step 3 curve, step 4

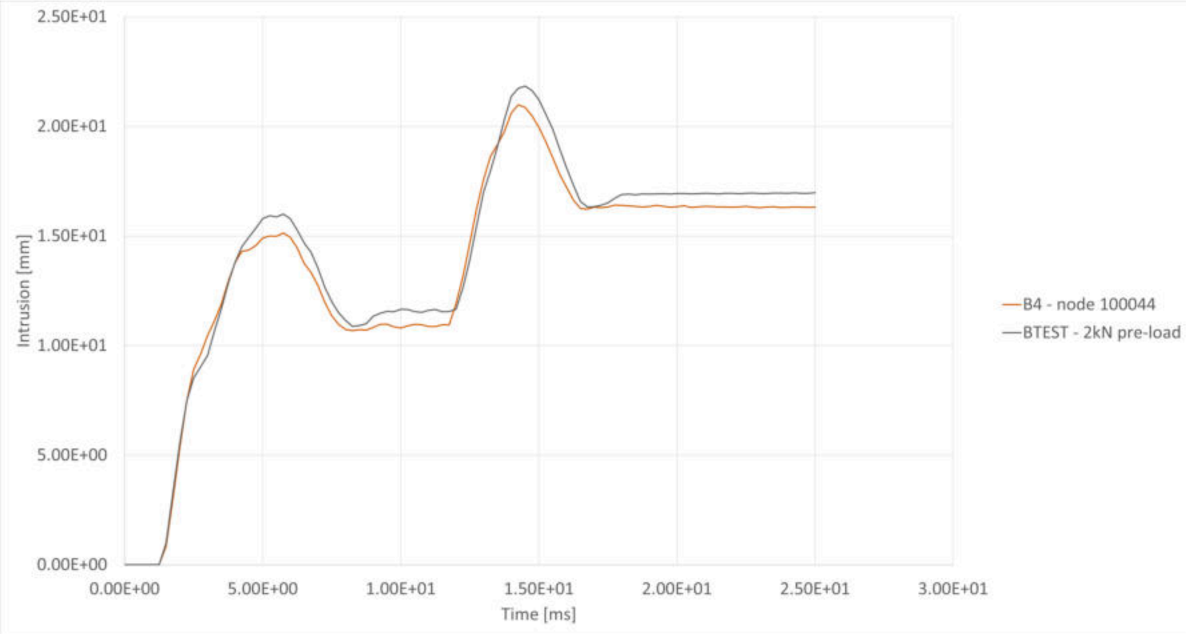

Figure C.6: Intrusion over time for orange node, effect of further pre-load reduction on plastic intrusion, step 4

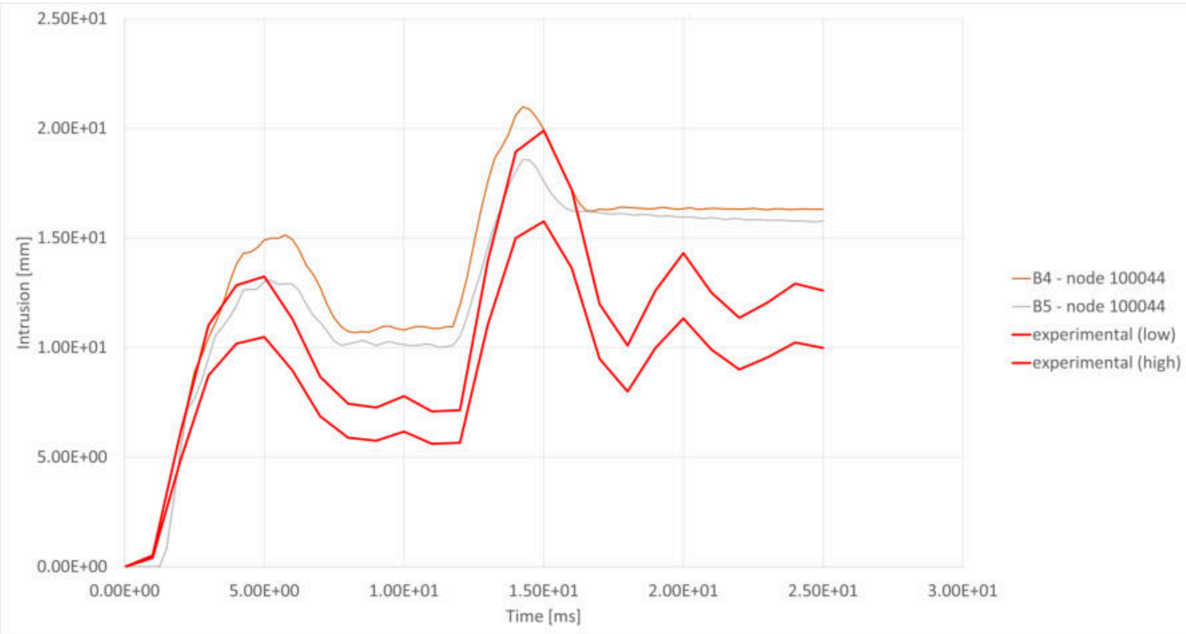

Figure C.7: Intrusion over time for orange node, compared to v31 experimental band and to the step 4 curve, step 5

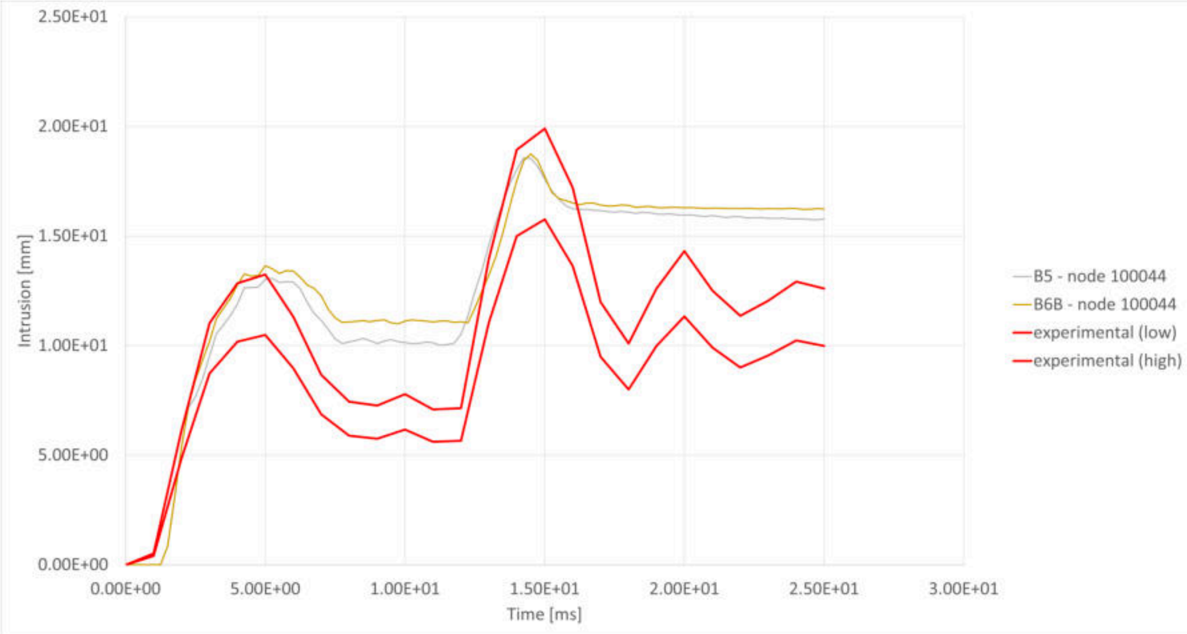

Figure C.8: Intrusion over time for orange node, compared to v31 experimental band and to the step 5 (i.e. 6A) curve, step 6B

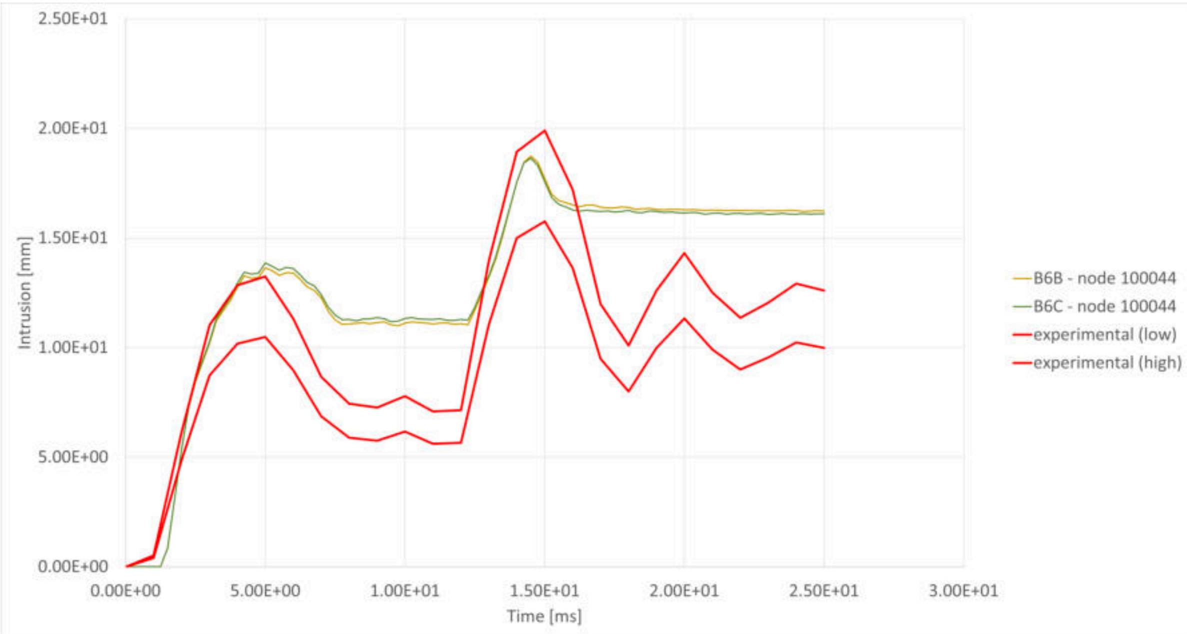

Figure C.9: Intrusion over time for orange node, compared to v31 experimental band and to the step 6B curve, step 6C

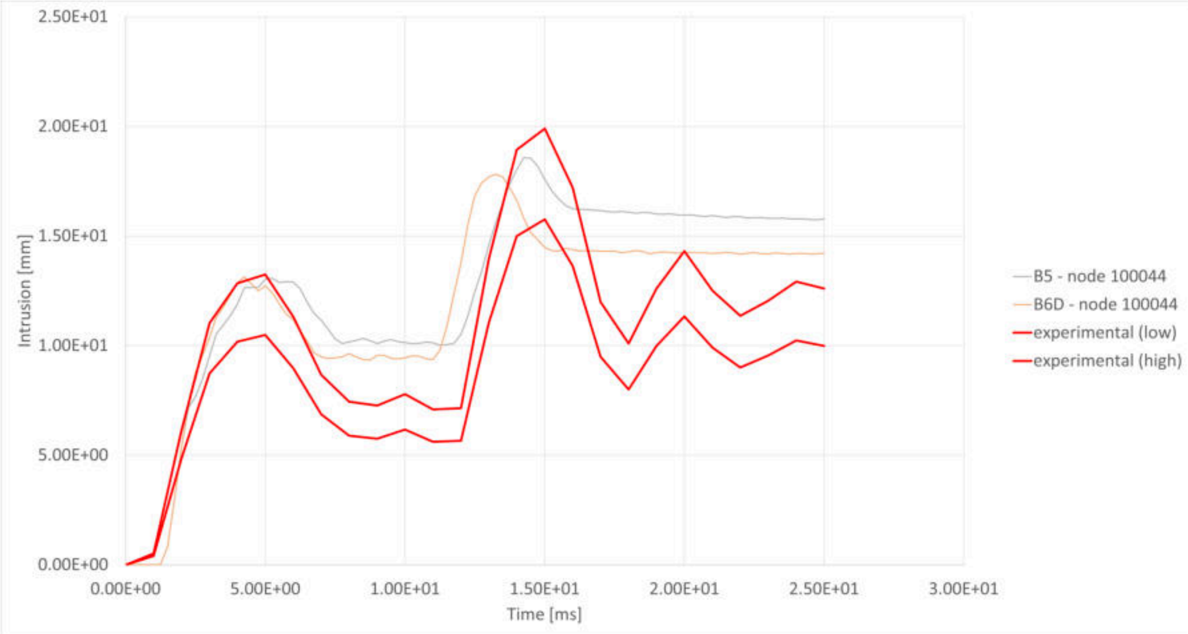

Figure C.10: Intrusion over time for orange node, compared to v31 experimental band and to the step 5 (i.e. 6A) curve, step 6D

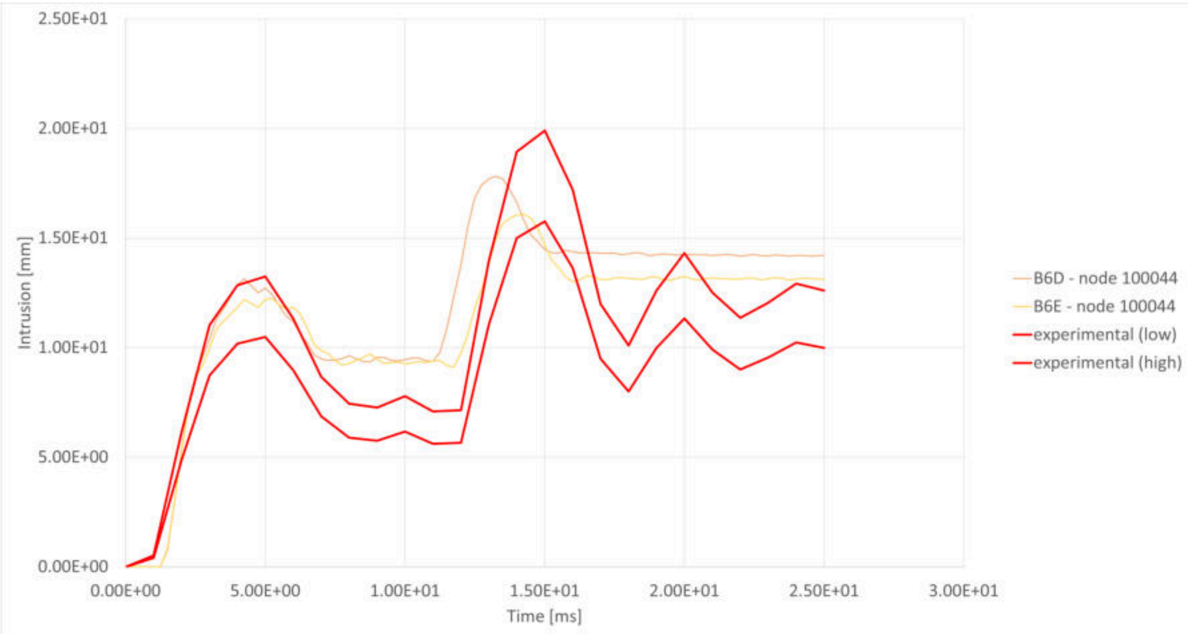

Figure C.11: Intrusion over time for orange node, compared to v31 experimental band and to the step 6D curve, step 6E

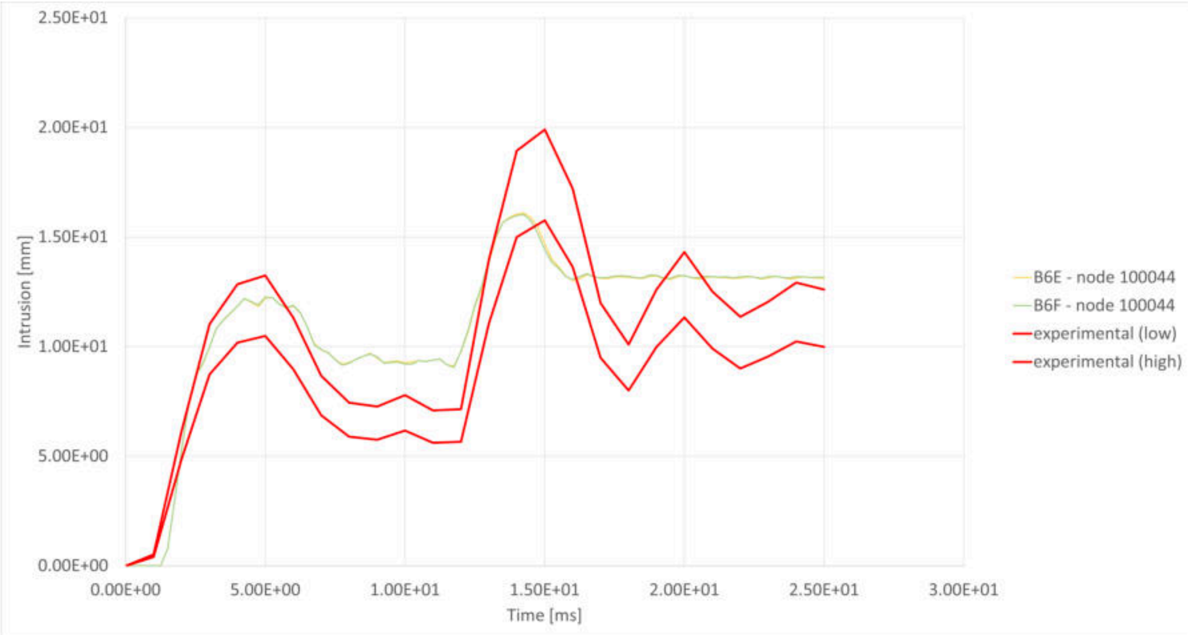

Figure C.12: Intrusion over time for orange node, compared to v31 experimental band and to the step 6E curve, step 6F

C.2. Delamination Model with GLASS_2

Until new test versions are introduced in steps 11 and 12, V31 remains the target reference, and the same markers considered in the previous section (see Table 5.1) are used to assess the model's performance, the only difference being that for the damage pattern the whole delamination area is now considered and compared to the C-SCAN results.

Note that since the impact dynamics have been simplified with the impactor's head and tail hitting along the same line (i.e., the plate's mid-section), the delaminations created by the tail impacts, which are dashed in Figure C.13, have been disregarded when comparing C-SCAN and simulation damage patterns.

For the same reason, the orange node is still localized on the mid-section, like in the previous workflow, even though in tests the tail impact shifts it slightly in the positive y-direction.

As per the baseline benchmark, as concluded in Section 5.1.13, the model of step 6E (GLASS_2, mesh 2 mm, minimum timestep 5E-4) is chosen.

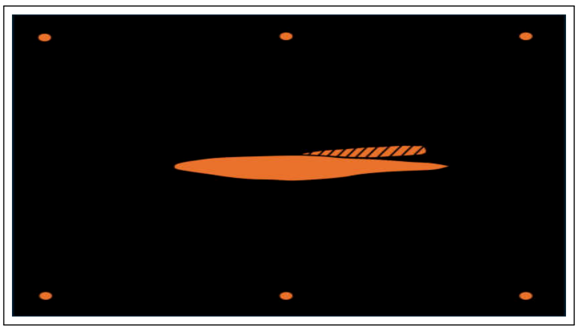

(a) V30

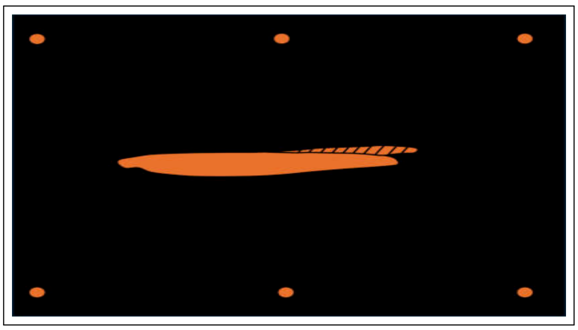

(b) V31

Continued on next page...

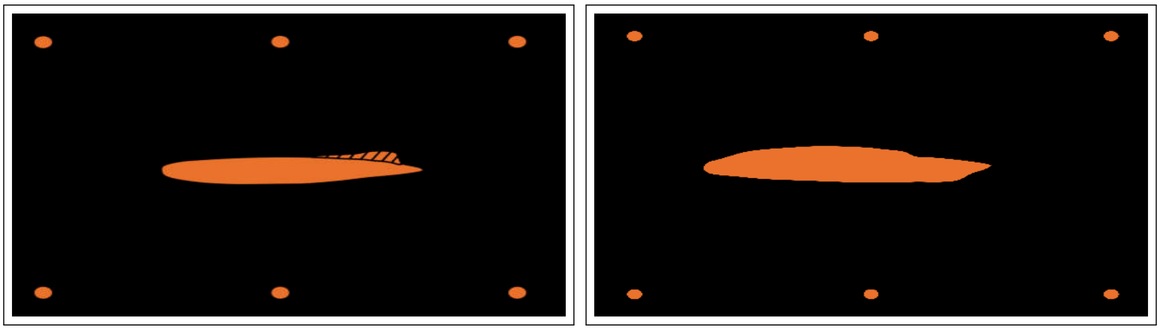

(c) V32 (d) V22

Figure C.13: C-SCANS delamination results; the delaminations caused by the tail impact are dashed.

C.2.1. Step 7: Equivalent New Model

Runtime

The total runtime for this model is 3994 s (wall clock); compared to the 6E baseline benchmark, there is a 36% increase, explained by the increase in the number of unique elements due to the individual ply modeling.

Plastic Deformation Profile and Position of the Maximum Intrusion Node (Aluminum Plate)

The deformation profile at the end of the simulation, along with the position of the maximum intrusion node and the position of the node tracked by the DIC system in experimental tests, are shown in Figure C.25b. As for this step delamination is inhibited, the profile looks similar to the baseline benchmark (6E, see Figure 5.2k), confirming the equivalence of the 2 models.

Intrusion Over Time (Aluminum Plate)

The intrusion over time for the orange node is reported in Figure C.14. Compared to the benchmark baseline, the curves are comparable, with the new model showing slightly higher magnitude (+9%) for the first peak.

The explanation for this discrepancy probably resides in the individual modeling of the plies. In the baseline solution, the plies are part of a single shell, thus incapable of any relative motion, but in the delamination model, they are tied with contact springs which need to deform slightly to generate contact forces, increasing compliance.

Moreover, the individual deletion of failed layers instantly reduces the section thickness of the layup, while in the monolithic solution the thickness is maintained until all integration points through-the-thickness fail, thus artificially retaining higher structural inertia during the impact.

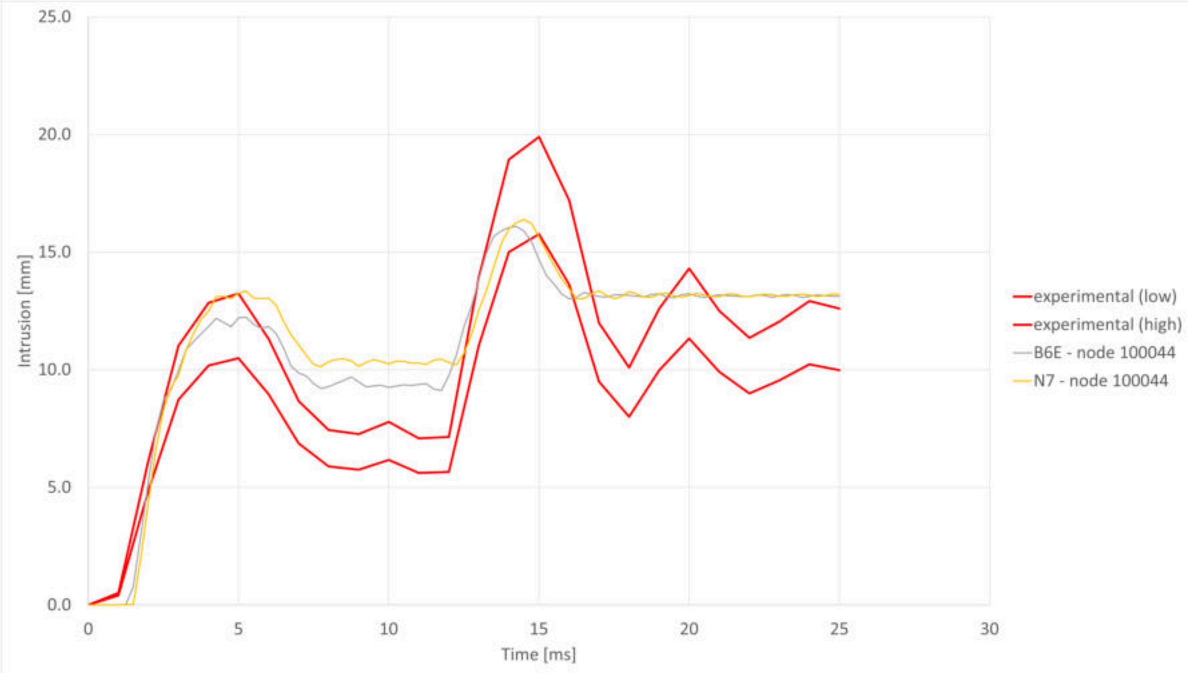

Figure C.14: Intrusion over time for orange node, compared to v31 experimental band and to the step 6E curve, step 7

Damage Pattern (Protection Plate)

The damage pattern on the protection plate at the end of the simulation is presented in Figure C.15. It can be seen how the model doesn't show any delamination, as expected since tiebreak failure has been de-activated in the current step.

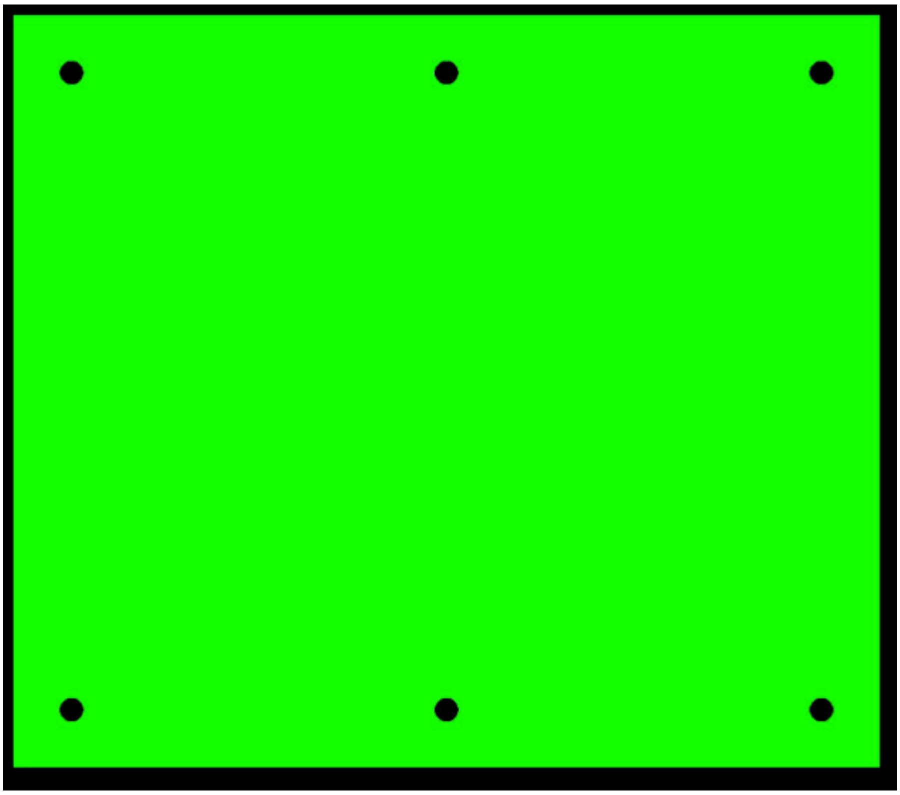

Figure C.15: Damage pattern, step 7

C.2.2. Step 8: Delaminating New Model

Runtime

The total runtime for this model is 4046 s (wall clock); this is substantially the same as in the previous step, highlighting how the increase in computational time from the baseline was mostly due to the increase in elements' number rather than to the tiebreak contact itself, which once activated in the current step proved to be rather inexpensive

Plastic Deformation Profile and Position of the Maximum Intrusion Node (Aluminum Plate)

The deformation profile at the end of the simulation, along with the position of the maximum intrusion node and the position of the node tracked by the DIC system in experimental tests, are shown in Figure C.25c. Compared to the previous step, the profile retains its shape, but the plastic intrusion magnitude increases slightly. This was expected and can be explained by the reduction in the protection plate's stiffness due to delamination.

Intrusion Over Time (Aluminum Plate)

The intrusion over time for the orange node is reported in Figure C.16. Compared to the previous step, the first peak's intrusion doesn't change, while the second peak is slightly higher.

The equivalence of the first peaks can be explained as although in the current step delamination is developing around the tear, CCRIT=0[1] prevents energy absorption.

Then, when the impactor rotates and the tail hits the composite, in the non-delaminated model (step 7) it has to go through a monolithic area, while in the delaminated one it encounters de-coupled plies which have reduced bending stiffness compared to their monolithic equivalent, resulting in less momentum dissipation and thus deeper intrusion in the aluminum plate (i.e. a higher second peak).

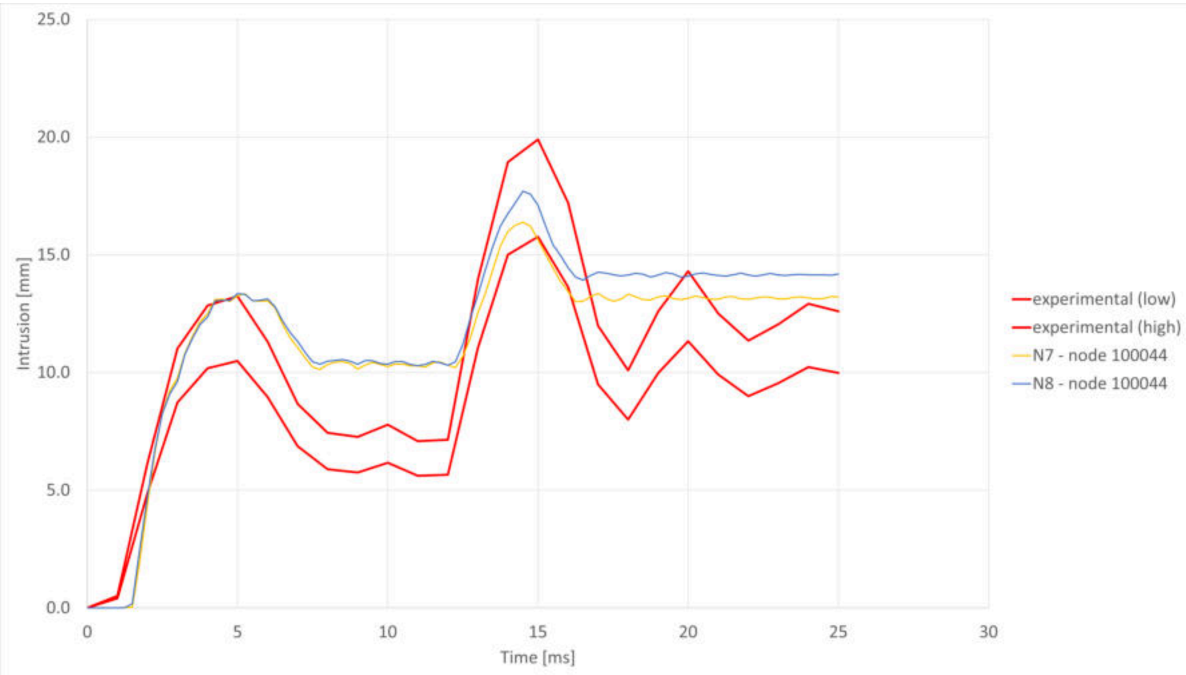

Figure C.16: Intrusion over time for orange node, compared to v31 experimental band and to the step 7 curve, step 8

Damage Pattern (Protection Plate)

The damage pattern on the protection plate at the end of the simulation is presented in Figure C.17[2].

[1]As explained in Chapter 2, CCRIT represents the critical distance at which the interface failure is complete, and setting it to 0 results in no energy dissipation due to istantaneous contact failure.

[2]To obtain a single pattern for the whole laminate instead than a single picture per each ply (so that a direct comparison can be made with the C-SCAN results), a screenshot is taken of all 5 interfaces, a certain degree of transparency is applied to each one, and they are then superimposed aligning the plate holes.

One of the holes shows delamination all around it, which is non-physical and due to numerical errors, possibly caused by the chosen one-way contact formulation and by the failure of triangular elements in the mesh. Notably, the delaminated area shows significant inter-penetration between the plies (see Figure C.18). Since the interested area is between screw heads and fixtures, it could result in slipping, altering the impact dynamics.

Furthermore, the plate edges and corners show signs of delamination too, which is again non-physical. Solutions to this issue are explored in Section 4.3.8.

Despite all these considerations, the delamination pattern of the impact region can still be analyzed for meaningful conclusions, and it is reported in Figure C.29a. One side of the impact area isn't fully delaminating, resulting in a mismatch with the C-SCAN envelope; furthermore, the right side of the simulation envelope doesn't follow the general shape of the C-SCAN, being larger and extending more to the right.

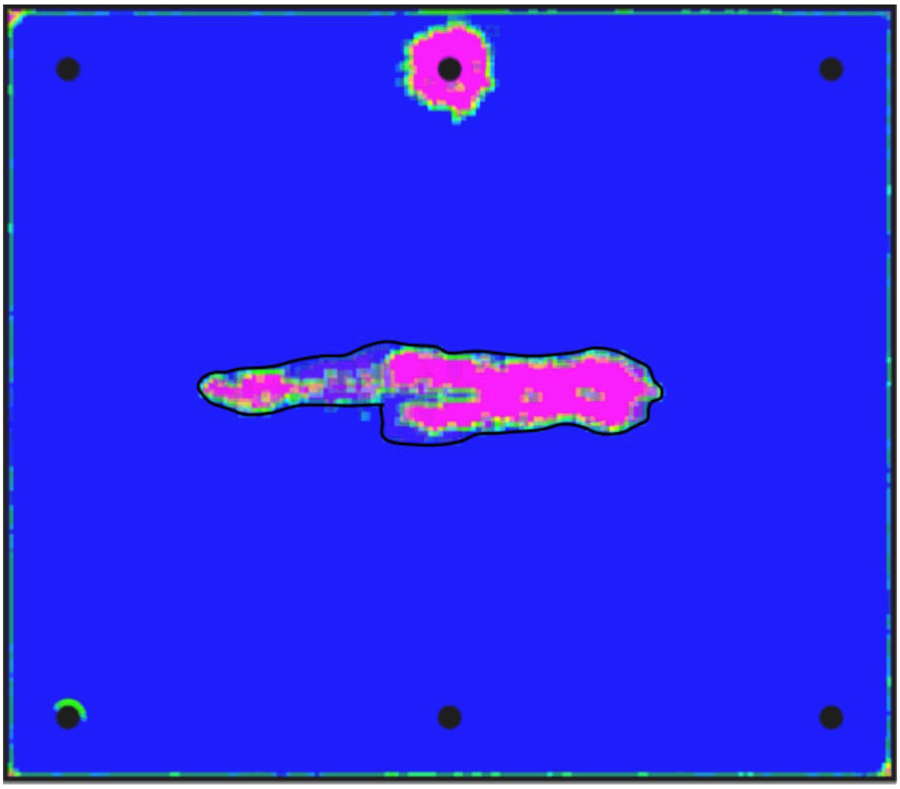

Figure C.17: Delamination pattern, step 8. Note that the tear is present but not shown in the picture.

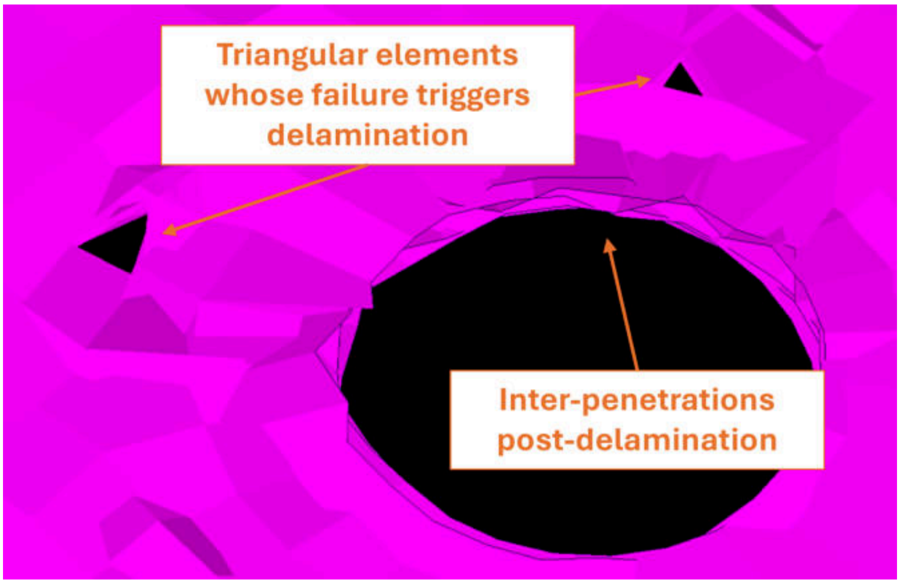

Figure C.18: Plies losing contact stability after failure, step 8.

C.2.3. Step 9: Two-Way Contact Formulation with Reduced Timestep

Runtime

The total runtime for this model is 11391 s (wall clock). This is a significant increase (x2.8) w.r.t. the previous step, and is due to the minimum timestep reduction, as the runtime is similar to the one-way formulation with reduced timestep, proving that the switch to the two-way contact formulation doesn't significantly increase computational time.

Plastic Deformation Profile and Position of the Maximum Intrusion Node (Aluminum Plate)

The deformation profile at the end of the simulation, along with the position of the maximum intrusion node and the position of the node tracked by the DIC system in experimental tests, are shown in Figure C.25d. As will be argued shortly, the switch to a two-way contact formulation produces a more realistic (and extended) delaminated area, further decreasing the protective capabilities of the composite plate, and resulting in a slight increase in plastic intrusion compared to the previous step.

Intrusion Over Time (Aluminum Plate)

The intrusion over time for the orange node is reported in Figure C.19. The two-way formulation behaves similarly to its one-way counterpart from the previous step for the first peak, but it shows higher intrusion for the second one. Again, this is due to the bigger and more uniform delamination zone observed with the two-way formulation, which further reduces the resistance encountered during the tail's impact. As both curves lie within the experimental band, intrusion cannot be used to assess whether the two-way formulation is better than the one-way one.

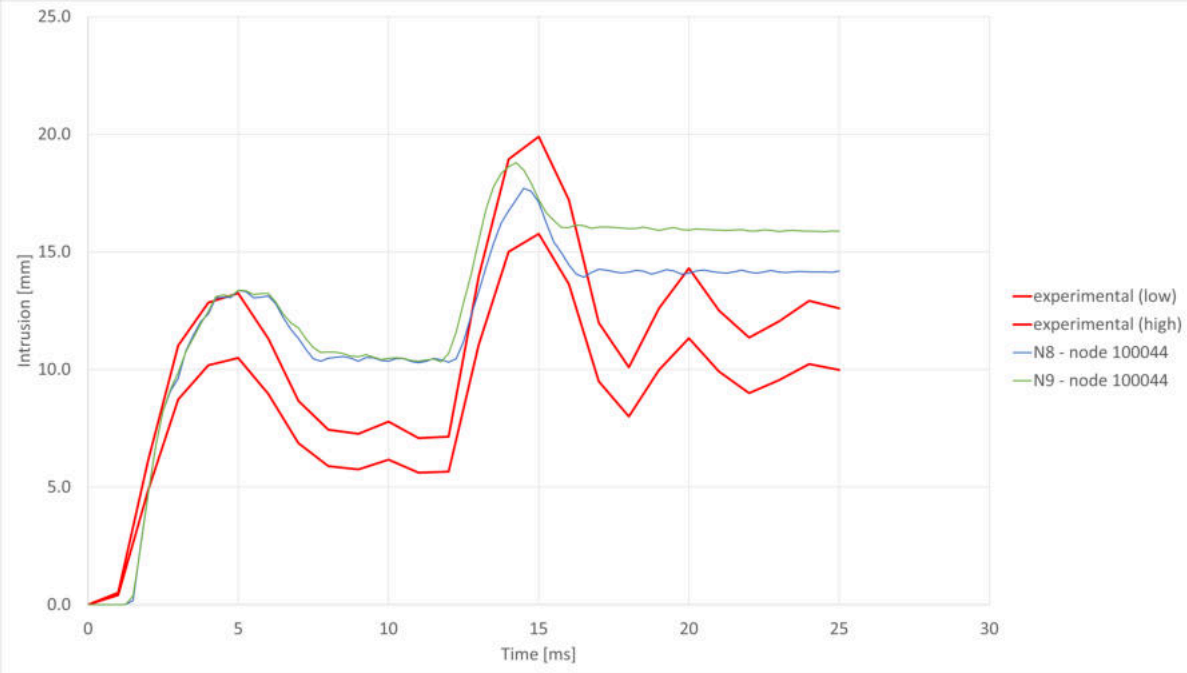

Figure C.19: Intrusion over time for orange node, compared to v31 experimental band and to the step 8 curve, step 9

Damage Pattern (Protection Plate)

The damage pattern on the protection plate at the end of the simulation is presented in Figure C.20[3].

The chosen solution to solve the numerical errors of step 8 still presents non-physical delamination around the hole due to failure of triangular elements, and one could argue that the problem gets even worse as it extends to other holes, too. However, opposed to the previous step: [a] the plies in the delaminated area retain contact stability after failure with no inter-penetrations (see Figure C.21), thus preventing slipping, [b] the delamination at the edges/corners of the plates (which couldn't be ascribed to a specific cause like it could be done with the triangular elements) is now solved, and [c] the match with experimental results of the delamination pattern is improved (see Figure C.29b).

Usually, one-way formulations are advised when working with composites, but the better match with the experimental delamination pattern, plus a more robust post-failure behaviour around the holes, make the two-way contact the preferred choice.

[3]To obtain a single pattern for the whole laminate instead than a single picture per each ply (so that a direct comparison can be made with the C-SCAN results), a screenshot is taken of all 5 interfaces, a certain degree of transparency is applied to each one, and they are then superimposed aligning the plate holes.

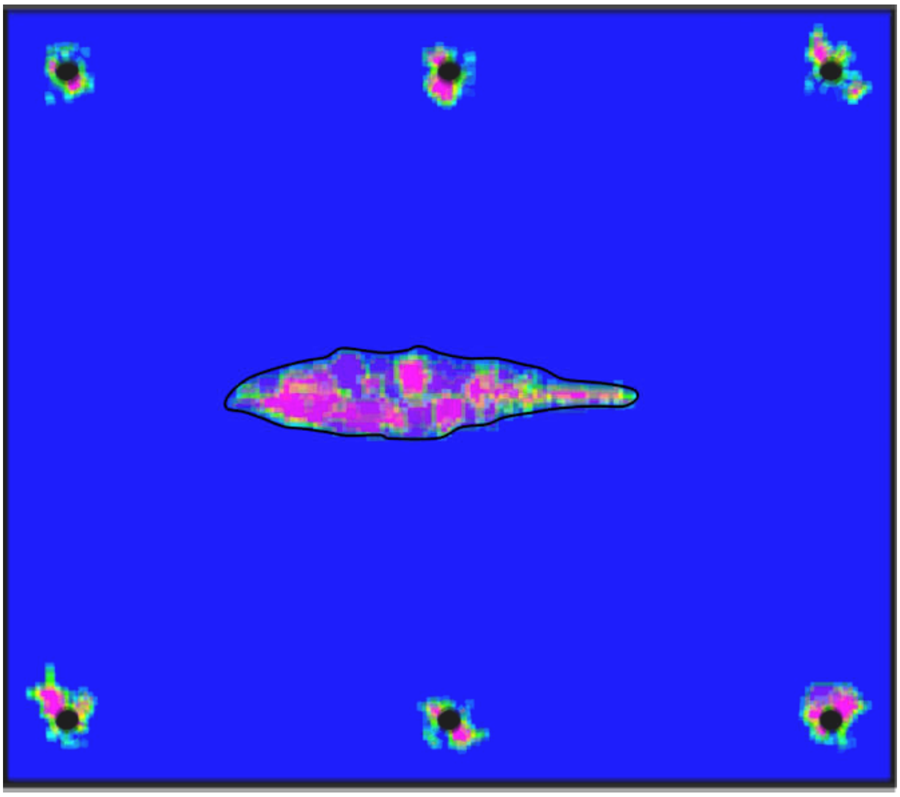

Figure C.20: Delamination pattern, step 9. Note that the tear is present but not shown in the picture.

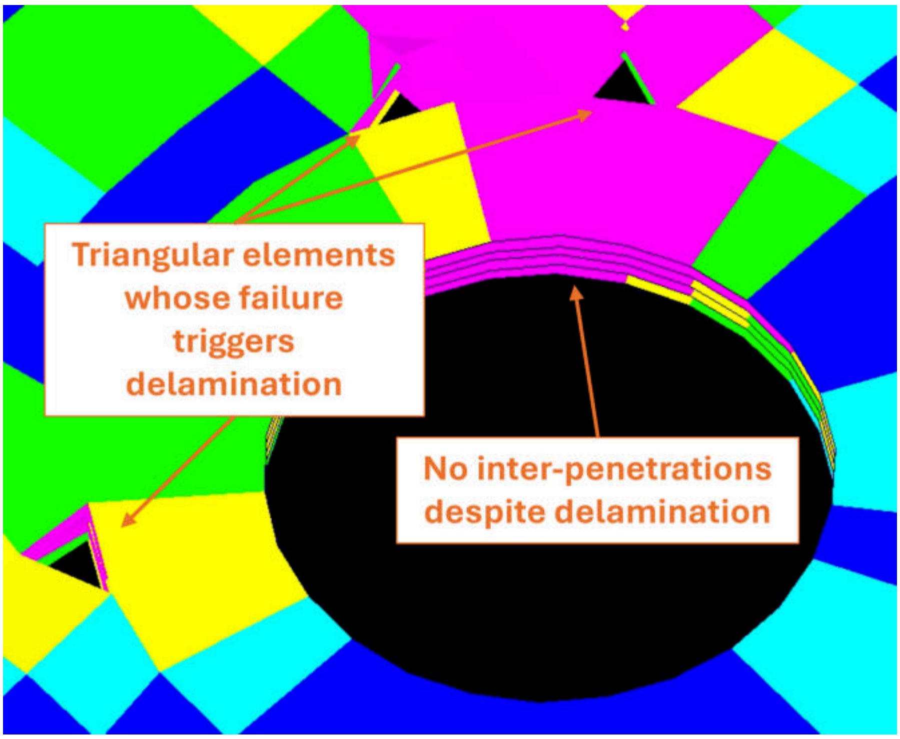

Figure C.21: Plies retaining contact stability after failure, step 9.

C.2.4. Step 10: Design of Experiment Study on Contact Parameters

The results from the DoE performed to fine-tune the contact parameters are shown in Table C.1. For each combination, a brief qualitative description of the delamination pattern is provided.

The low NFLS ans SFLS settings, used in any combination, result in non-physical damage patterns; this is expected as the low settings are chosen as ”control parameters”.

SFLS only results in physical and realistic damage and delamination patterns when at its mid setting (which is in the range predicted by the literature review in Chapter 2), with NFLS either mid (literature range) or high, but the opposite is not true. This highlights the delamination dependency on the shear strength of the contact and its insensitivity to changes in normal strength; this is an expected result for the chosen load case, where failure has to be shear-driven and no significant tensile stresses are present, and confirms the improved physics based characteristics of the model. Due to these considerations, the literature supported ([8] [32] [7]) SFLS=0.02 is confirmed; this is significant as it strengthens the hypothesis, presented in Section 2.5.7, that a mesh size matching the physical cohesive zone length allows for the direct application of unscaled literature strength values; as per the tensile strength, NFLS=0.05 is chosen as it is again supported by literature ([10] [30] [31]), and the delamination patterns have proven to be rather insensitive to its value (additional tests have been performed with NFLS=[0.02, 0.03] and have led to similar conclusions).

As per CCRIT, it doesn’t seem to substantially influence the damage pattern or energy absorption, highlighting how in this load-case, delamination-driven energy absorption is negligible, and not capable of reducing the intrusion values to the experimentally measured ones.

A simple calculation can be set up as proof of concept: the impactor has a mass m and an initial velocity of v; this results in an initial kinetic energy of:

$$E_k = \frac{1}{2}mv^2 \tag{C.1}$$

Assuming a very generous high-performance toughness value of $G_{IIc} = 2000J/m^2$, and a delamination area per ply equal to the most delaminated ply of e.g. step 9 ($\approx 180 \times 30mm$), with 6 plies (i.e., 5 interfaces), the energy absorbed by the fracture would be:

$$E_{fracture} = n_{interfaces} \times A_{delamination} \times G_{IIc} \tag{C.2}$$

Plugging in the numbers, it would equal to $\approx 3.2\%$ of the impactor energy, hence not enough to justify 4-5 mm drops in plate intrusion.

For this reason, CCRIT can be set to 0 for the specific class of layups and load-case related to the project, but its influence needs to be re-evaluated in case of layups with more plies or bigger delamination patterns.

No further tuning of the parameters has been performed, as the chosen values result in a sufficiently accurate damage pattern for the scope of this project, as it was predicted in Section 2.5.7.

#	NFLS	SFLS	CCRIT	Physical?
1	0.005	0.005	0	NO, all plies separate
2	0.005	0.005	0.02	NO, all plies separate
3	0.005	0.005	0.1	NO, shearing in middle
4	0.005	0.02	0	NO, shear mid, edge & corner sep
5	0.005	0.02	0.02	NO, shear mid & slight edge sep
6	0.005	0.02	0.1	NO, shear mid & slight edge sep
7	0.005	0.05	0	NO, shear mid & slight edge sep
8	0.005	0.05	0.02	NO, shear mid & slight edge sep
9	0.005	0.05	0.1	NO, all plies separate
10	0.05	0.005	0	NO, all plies separate
11	0.05	0.005	0.02	NO, all plies separate
12	0.05	0.005	0.1	NO, all plies separate
13	0.05	0.02	0	YES
14	0.05	0.02	0.02	YES
15	0.05	0.02	0.1	YES
16	0.05	0.05	0	NO, no delam, straight cut
17	0.05	0.05	0.02	NO, no delam, straight cut
18	0.05	0.05	0.1	NO, no delam, straight cut
19	0.1	0.005	0	NO, all plies separate
20	0.1	0.005	0.02	NO, all plies separate
21	0.1	0.005	0.1	NO, all plies separate
22	0.1	0.02	0	YES
23	0.1	0.02	0.02	YES
24	0.1	0.02	0.1	YES
25	0.1	0.05	0	NO, no delam, straight cut
26	0.1	0.05	0.02	NO, no delam, straight cut
27	0.1	0.05	0.1	NO, no delam, straight cut

Table C.1: DoE results for NFLS, SFLS, and CCRIT

C.2.5. Step 11A: Different Impact Conditions (V30)

Runtime

The total runtime for this model is 11155 s (wall clock). This is comparable to the previous step, as the only difference in the model is represented by the impact conditions.

Plastic Deformation Profile and Position of the Maximum Intrusion Node (Aluminum Plate)

The deformation profile at the end of the simulation, along with the position of the maximum intrusion node and the position of the node tracked by the DIC system in experimental tests, are shown in Figure C.26b. Compared to the experimentally derived profile in Figure C.26a, the green node shifts to the right, sitting on top of a secondary intrusion at around 250 mm, absent in the experimental curve. The explanation for this resides in the impact dynamics of V30; as the impact progresses, the impactor tilts on a plane parallel to the protection plate, resulting in a tail impact along a different line than the mid-section, which therefore cannot be shown in the experimental curve, which is measured at the mid-section. The simulation, although including experimental errors on impact angle and position, cannot re-create this shift due to absence of records on the tilt angle, thus resulting in a tail impact aligned with the initial one along the mid-section, creating the added bump in Figure C.26b. As per the rest of the profile, the shape is retained.

Intrusion Over Time (Aluminum Plate)

The intrusion over time for the orange node is reported in Figure C.22. The peaks show a good time-wise alignment with the experimental results, and the second peak is close in magnitude to the upper experimental bound, but the first peak's intrusion is much higher. This issue has already been observed when running baseline simulations, and cannot therefore be ascribed to the delamination implementation.

As V30 has a steeper impact angle than V31, the higher perpendicular component of the impact force results in a higher intrusion; this happens in the experimental curves, where the peaks of V30 are higher than the ones of V31, but in the simulations this increase in intrusion is much more pronounced; this could be due to the inaccurate behaviour of one between the protection plate and the aluminum plate.

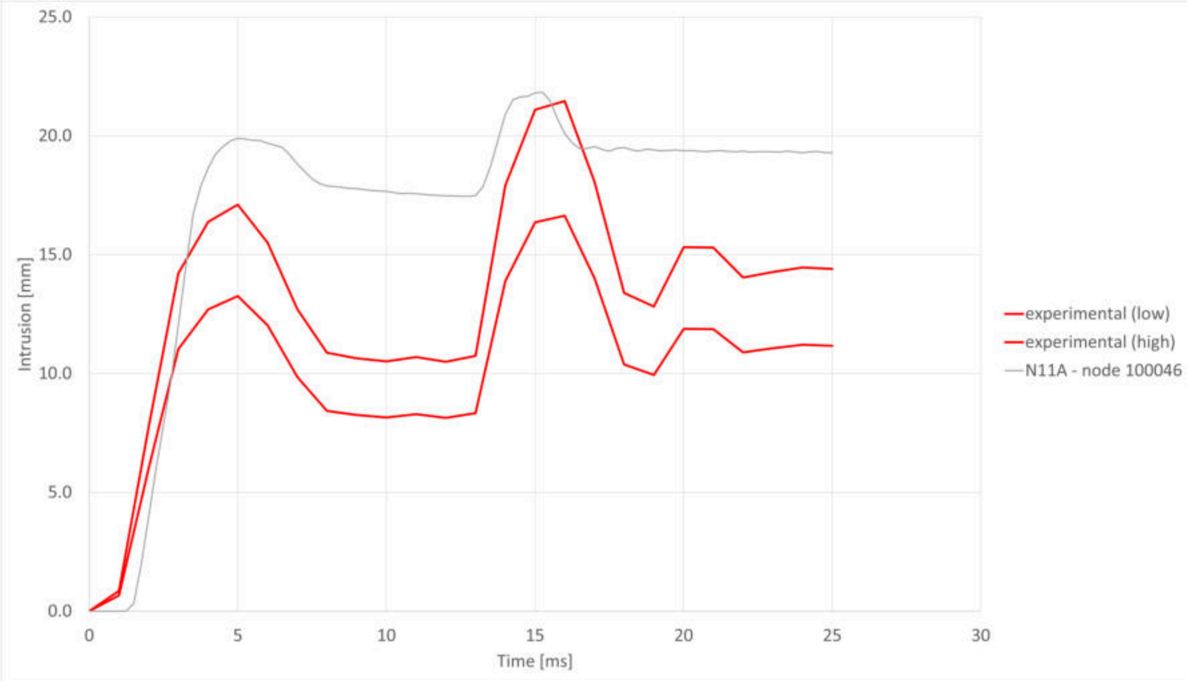

Figure C.22: Intrusion over time for orange node, compared to v30 experimental band, step 11A

Damage Pattern (Protection Plate)

The damage pattern on the protection plate at the end of the simulation is presented in Figure C.29c, and it shows a good match with the experimental envelope. This contrasts with the discrepancy in the intrusion plot, prompting the idea that the reason for the discrepancy may lie in the aluminum plate rather than in the composite one. This possibility will be investigated in Section C.2.9.

C.2.6. Step 11B: Different Impact Conditions (V32)

Runtime

The total runtime for this model is 11376 s (wall clock). This is comparable to the previous step, as the only difference in the model is represented by the impact conditions.

Plastic Deformation Profile and Position of the Maximum Intrusion Node (Aluminum Plate)

The deformation profile at the end of the simulation, along with the position of the maximum intrusion node and the position of the node tracked by the DIC system in experimental tests, are shown in Figure C.27b. Compared to the experimentally derived profile in Figure C.27a, the green node shifts to the right edge of the plate. This isn't particularly concerning, as the right edge shows a comparable intrusion magnitude to the expected position of the green node (difference of $|0.7|mm$) close to the orange one, and the same pattern can be observed in the experimental curve. As in V30, the shifted tail impact in the experiments results in a longer intrusion area, only for the simulation.

Intrusion Over Time (Aluminum Plate)

The intrusion over time for the orange node is reported in Figure C.23. As before, a discrepancy in magnitude can be observed for the first peak; again, V32 has a steeper impact angle than V31, and the same pattern of the previous step shows up, with the culprit being one between the protection and the aluminum plate.

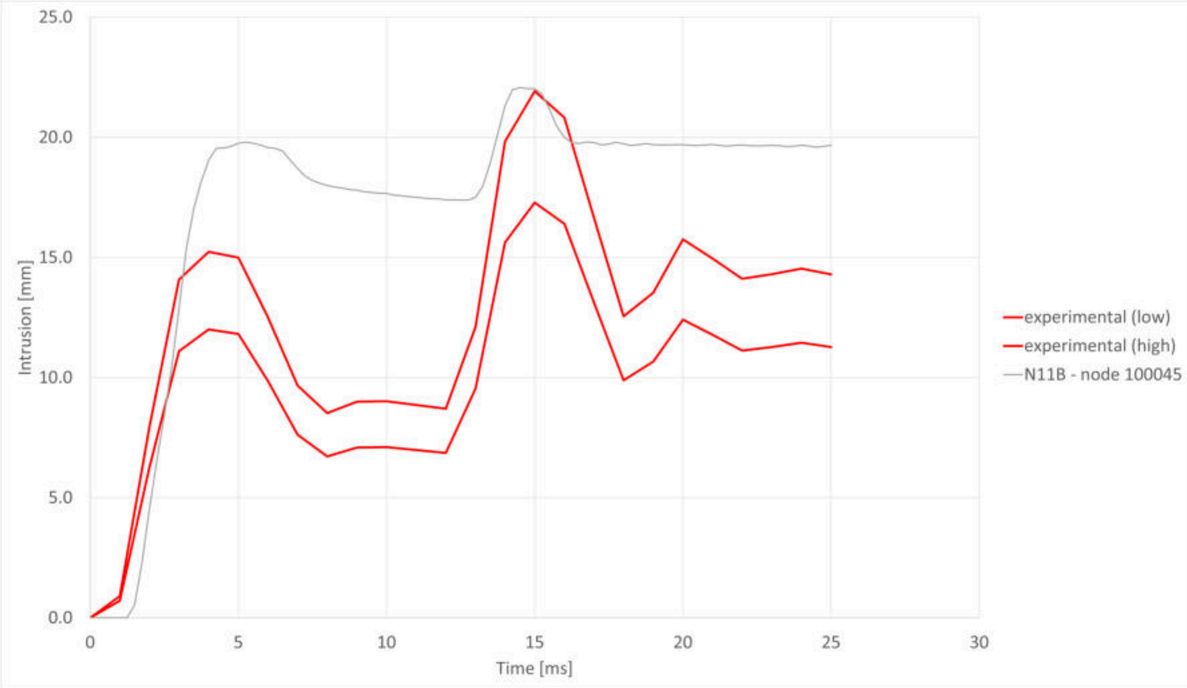

Figure C.23: Intrusion over time for orange node, compared to v32 experimental band, step 11B

Damage Pattern (Protection Plate)

The damage pattern on the protection plate at the end of the simulation is presented in Figure C.29d. Here, like in the previous step, a good match with the experimental envelope is observed, leading to the same conclusions as before on the possible influence of the aluminum plate modeling on the results.

C.2.7. Step 12: Different Layup (V22)

Runtime

The total runtime for this model is 20890 s (wall clock). This is significantly higher than the previous steps, as the layup has more plies, hence both more elements and interfaces.

Plastic Deformation Profile and Position of the Maximum Intrusion Node (Aluminum Plate)

The deformation profile at the end of the simulation, along with the position of the maximum intrusion node and the position of the node tracked by the DIC system in experimental tests, are shown in Figure C.28b. Compared to the experimentally derived profile in Figure C.28a, the match is quite poor; in the simulation, there is a higher intrusion at the right edge than at the left one, while in the test they are comparable; furthermore, a very prominent secondary intrusion area shows up in the simulation at around 225 mm, resulting in a shift to the right of the green node, which should instead be closer to the orange. In V22, no considerable tilt of the impactor can be inferred from examining the aluminum plate, thus the explanation used in the previous step doesn't apply. Still, deeper dents and scratches can be seen on it; this, combined with the different layup sequence and higher number of plies, suggest that applying a different scaling factor to the friction coefficient could improve on the results. This idea will be reinforced by the considerations that follow.

Intrusion Over Time (Aluminum Plate)

The intrusion over time for the orange node is reported in Figure C.24. In this case, the match is quite poor intrusion-wise for both peaks, and time-wise for the second one. During preliminary studies, it has been observed that increasing the scaling factor on friction reduces the magnitude of the second peak and shifts it to the right, which is exactly what is needed to improve on the match with experimental results and it is supported by previous considerations; a version of this model with scaled up friction will be constructed and analyzed in Section C.2.11.

As per the magnitude of the whole curve, the same argument as in the previous steps can be made, prompting an investigation on the aluminum plate modeling.

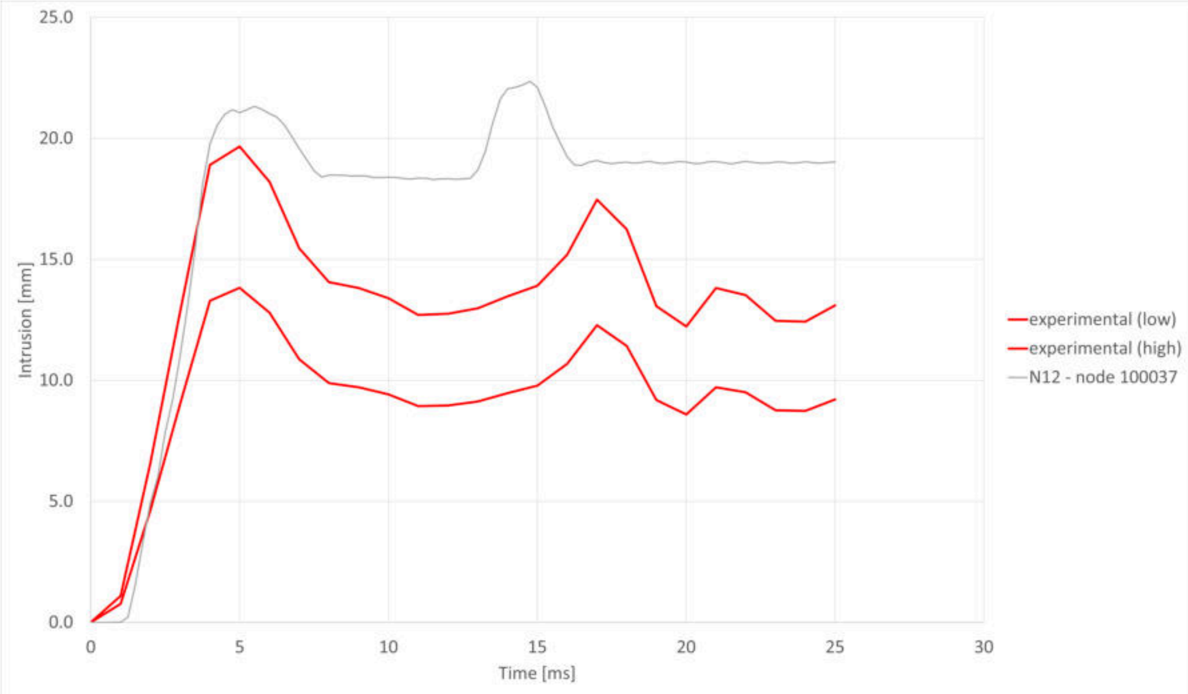

Figure C.24: Intrusion over time for orange node, compared to v22 experimental band, step 12

Damage Pattern (Protection Plate)

The damage pattern on the protection plate at the end of the simulation is presented in Figure C.29e. Again, like in the two versions before, the match with the experimental envelope is good, confirming that the discrepancy isn't caused by inaccurate modeling of the protection plate. In this version, the slight mismatch at the delamination front tip is absent, and almost a perfect match is registered instead; since V22 was the only tested version where a different material card than GLASS_2 was prominent in the layup, this could suggest that the slight mismatch could be ascribed to the use of GLASS_2 instead of the standard GLASS_1. This idea will be explored when analyzing the results of the updated simulations workflow in Section 5.3.

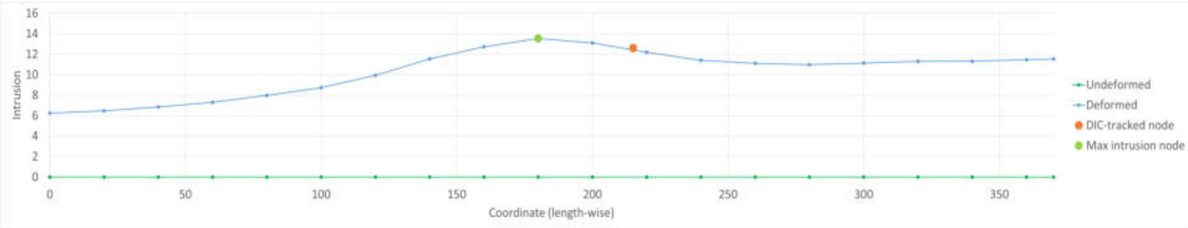

(a) Experimental (V31)

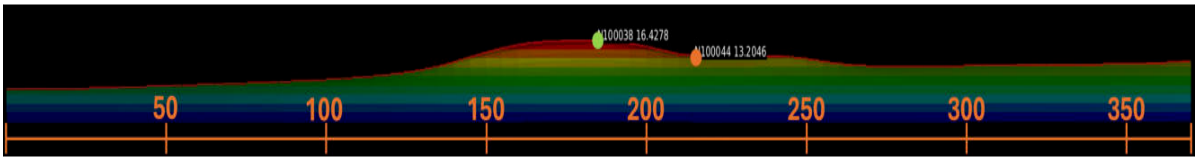

(b) Step 7

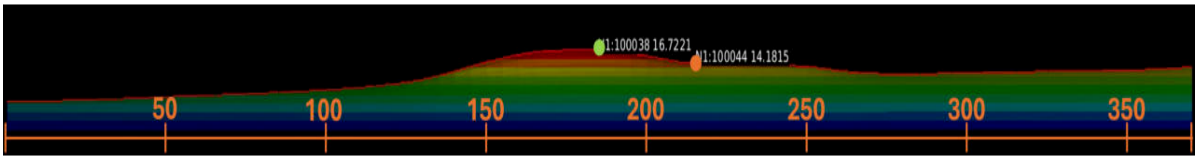

(c) Step 8

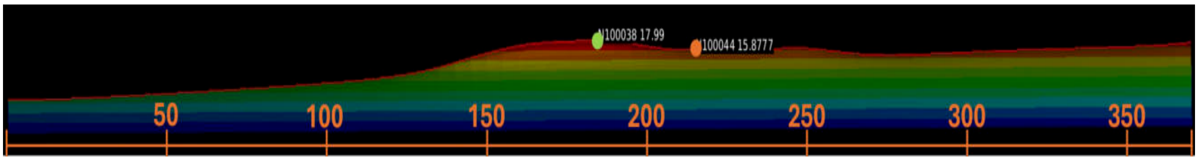

(d) Step 9

Figure C.25: Comparison of profile deformation: Experimental (V31) vs. Simulation, steps 7 to 9.

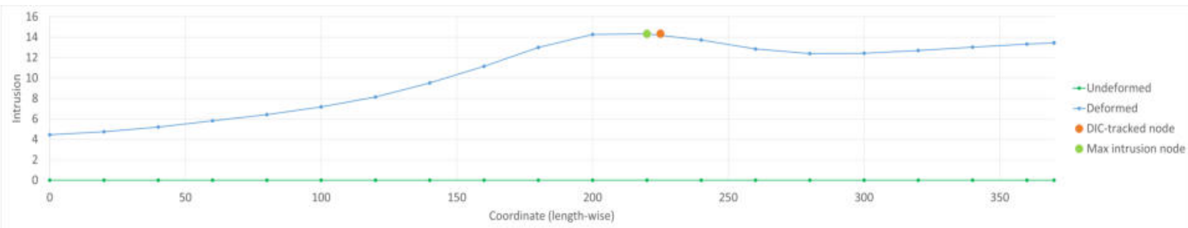

(a) Experimental (V30)

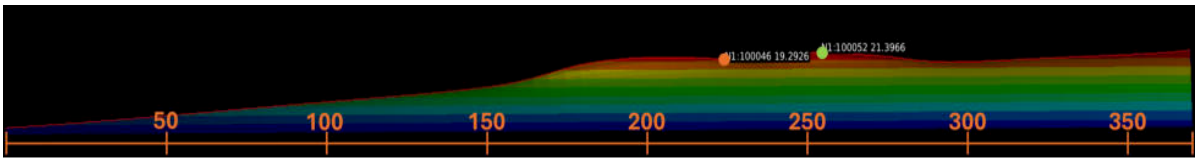

(b) Step 11A

Figure C.26: Comparison of profile deformation: Experimental (V30) vs. Simulation, step 11A.

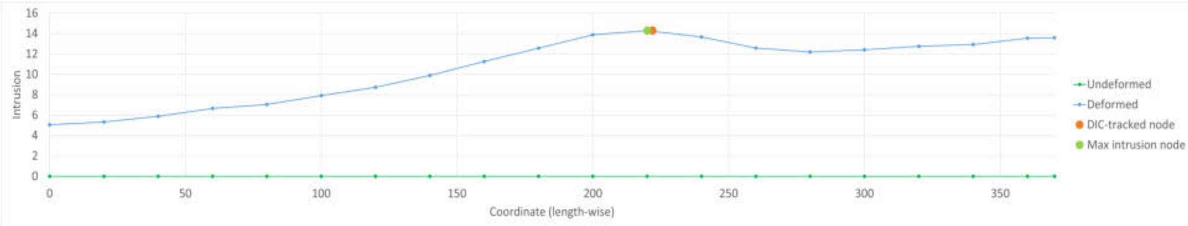

(a) Experimental (V32)

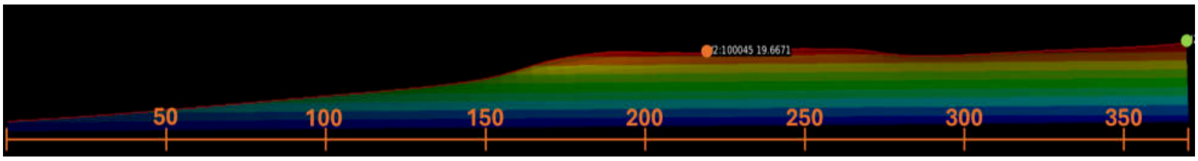

(b) Step 11B

Figure C.27: Comparison of profile deformation: Experimental (V32) vs. Simulation, step 11B.

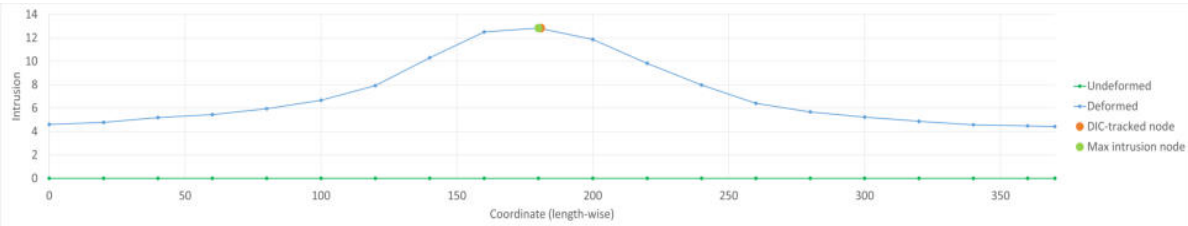

(a) Experimental (V22)

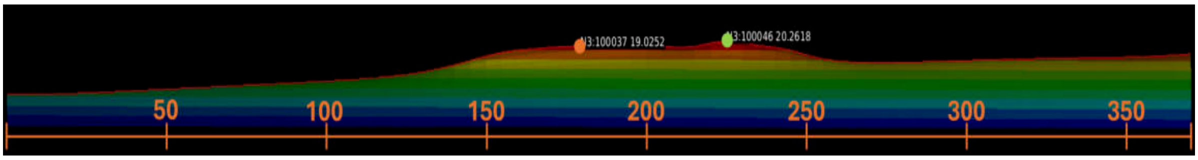

(b) Step 12

Figure C.28: Comparison of profile deformation: Experimental (V22) vs. Simulation, step 12.

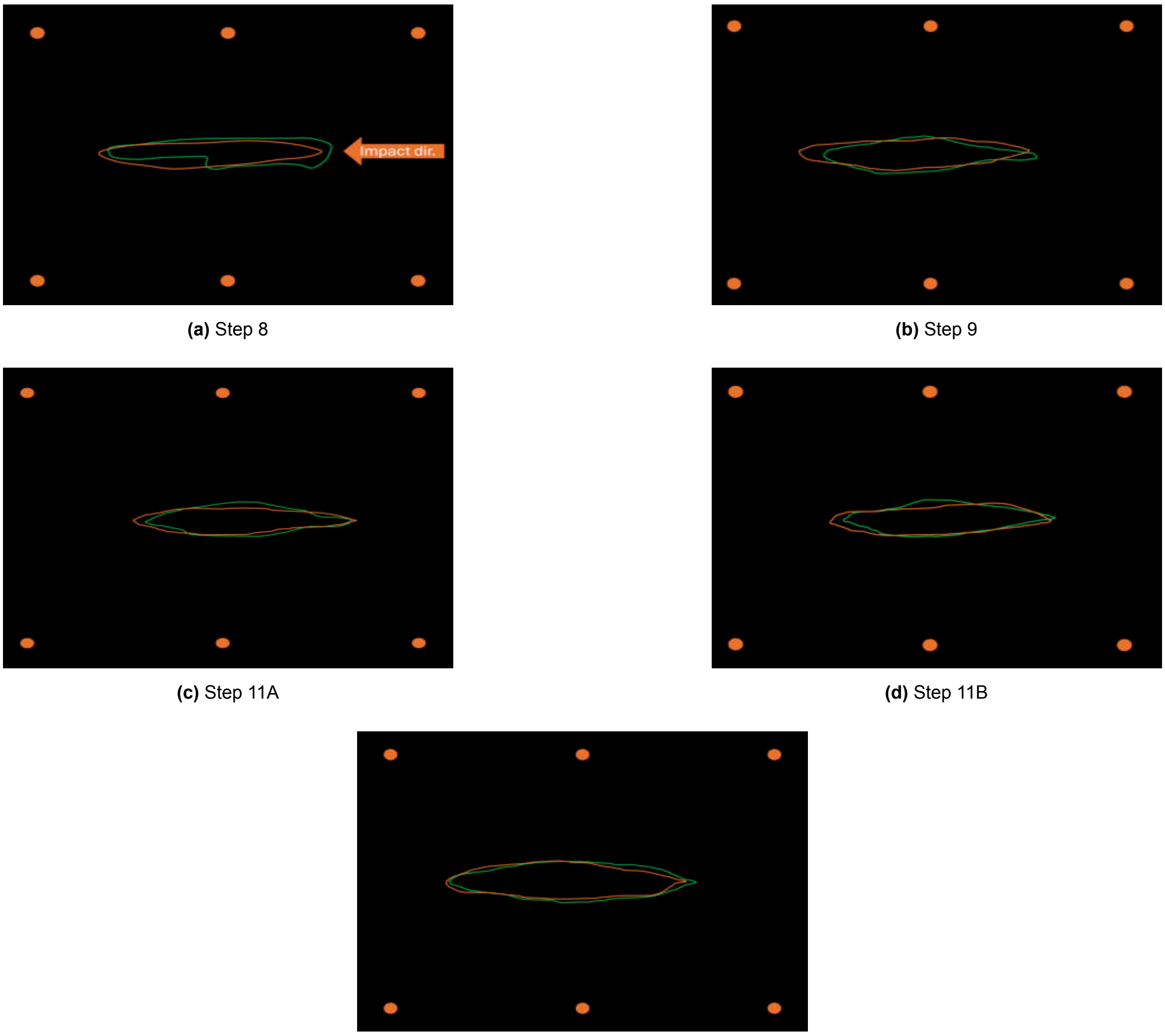

(a) Step 8

(b) Step 9

(c) Step 11A

(d) Step 11B

(e) Step 12

Figure C.29: Comparison of damage patterns: Experimental results (orange envelope) vs. Simulations (green envelope), steps 8 to 12.

C.2.8. EX1: Solutions to Numerical Instabilities

As the goal of this set of simulations is solving the numerical instabilities recorded in Step 8, the analysis will focus on the damage patterns on the protection plates (see Figure C.31); the intrusion of the orange node for each model is checked too, to assess anomalous behaviours (see Figure C.30).

EX1A: CCRIT-Induced Damping

Figure C.31a shows failure all along the plate's edges, plus a large non-physical delamination in the upper portion of the plate, between the top-center and top-right holes, meaning that sudden failure of the tiebreak contact isn't the main responsible for the numerical instabilities.

EX1B: Minimum Timestep Reduction

Figure C.31b shows no numerical issues, although the damage pattern is too big compared to the experimentally measured one. Among all proposed solutions, this results in the smallest intrusion for both peaks (see Figure C.30). Although not completely satisfying, this solution highlights the potential impact of minimum time-step reduction, which could be combined with other solutions to achieve optimal results (see EX1E).

EX1C: Selective Mass Scaling
Figure C.31c shows failure all along the plate's edges and at the plate corners, meaning that selective mass scaling is incapable to fix the numerical issues.

EX1D:Two-Way Contact Formulation
Figure C.31d shows a completely non-physical damage pattern, which results in really high intrusion compared to the other proposed solutions (see Figure C.30). This method is therefore inadequate in solving the issue, although its performance could be improved in combination with a reduction of the minimum time-step (see EX1E)

EX1E: Combination of EX1B and EX1D
Figure C.31e shows a physical damage pattern, meaning that minimum time step reduction can fix most numerical issues for both one-way and two-way contact formulations. Some failures around the holes mostly due to triangular elements remain, although it was shown (see Section C.2.3) that they don't compromise the contact stability; if fixing these failures is deemed critical for any reason, re-meshing and/or special mesh mapping around the holes are suggested.

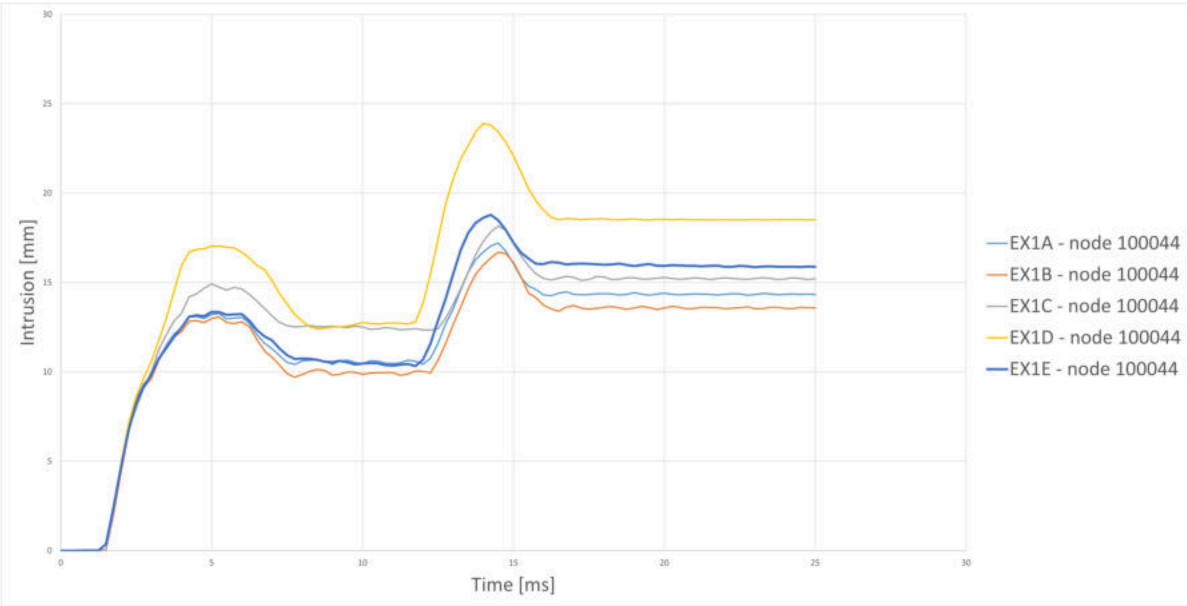

Figure C.30: Intrusion over time for orange node, comparison between the proposed solutions, EX1.

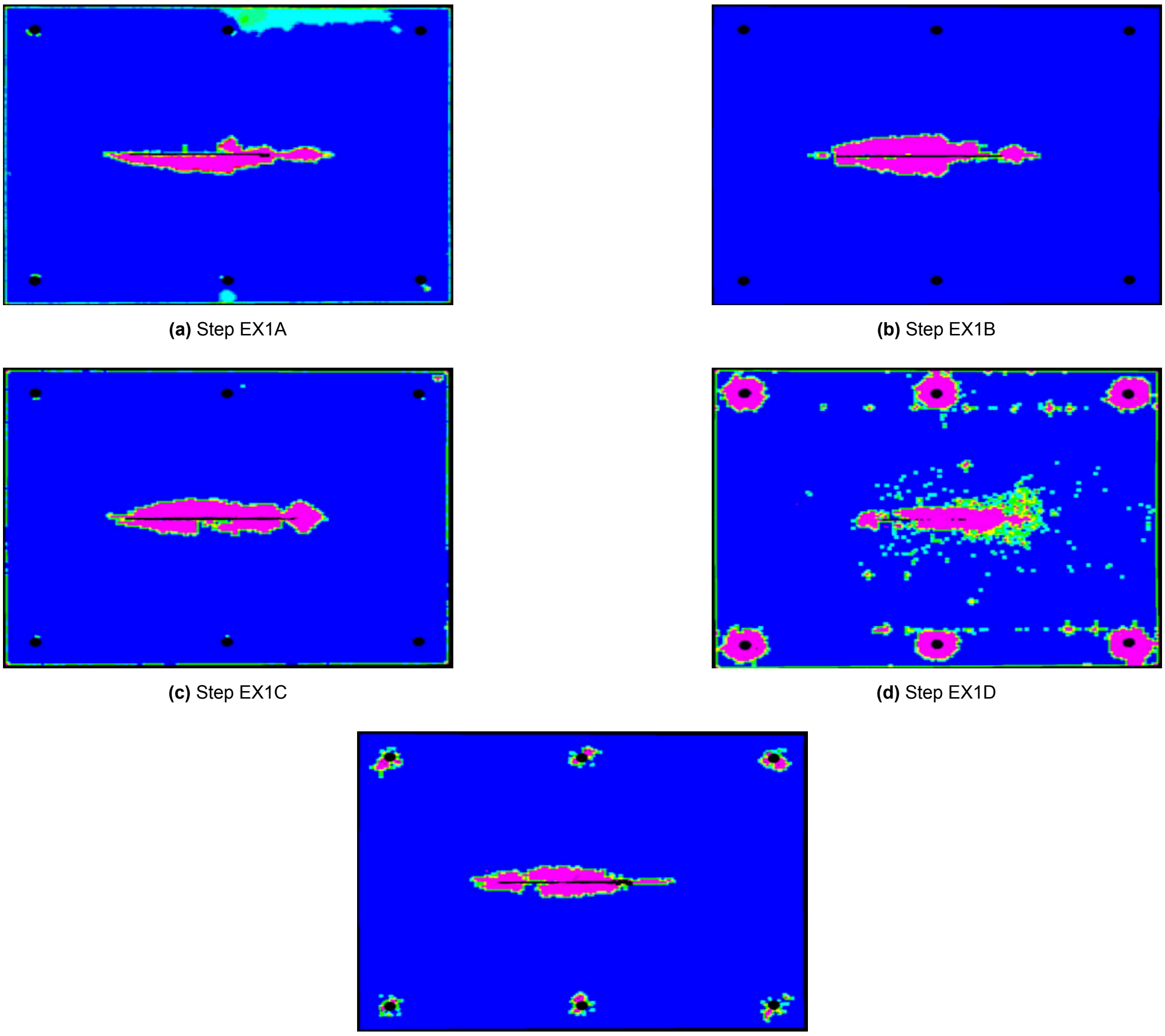

(a) Step EX1A

(b) Step EX1B

(c) Step EX1C

(d) Step EX1D

(e) Step EX1E

Figure C.31: Comparison of damage patterns to assess solutions to numerical instabilities, EX1.

C.2.9. EX2A: New Aluminum Material Card (ALU_2)

Runtime

The total runtime for this model is 11297 s (wall clock), thus being comparable to the finalized model from step 10, from which EX2A only differs for the aluminum plate material model; this is expected as it signals that the new material model doesn't influence the computational effort.

Plastic Deformation Profile and Position of the Maximum Intrusion Node (Aluminum Plate)

The deformation profile at the end of the simulation, along with the position of the maximum intrusion node and the position of the node tracked by the DIC system in experimental tests, are shown in Figure C.32. Compared to the experimental profile (Figure 5.2a), there is a good match for both the impact area and the free edges, and compared to the results with the previous material card, the secondary bump caused by the tail impact is much less pronounced (see Figure C.25d).

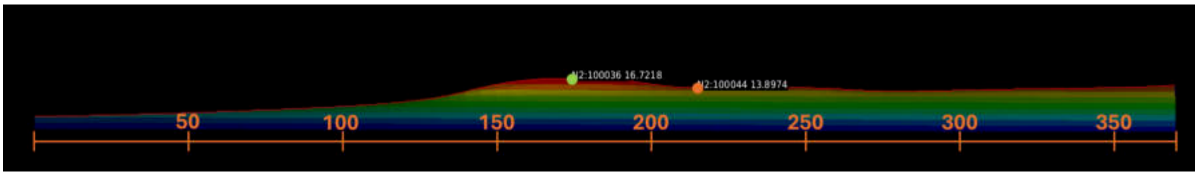

Figure C.32: Profile deformation, EX2A

Intrusion Over Time (Aluminum Plate)

The intrusion over time for the orange node is reported in Figure C.33. Compared to the previous aluminum material model, the new one shows an improvement in both the first and second plastic deformation portions of the plot, as well as a reduction of intrusion for both peaks, and this highlights how the new material model is more accurately capturing the real plate's behaviour.

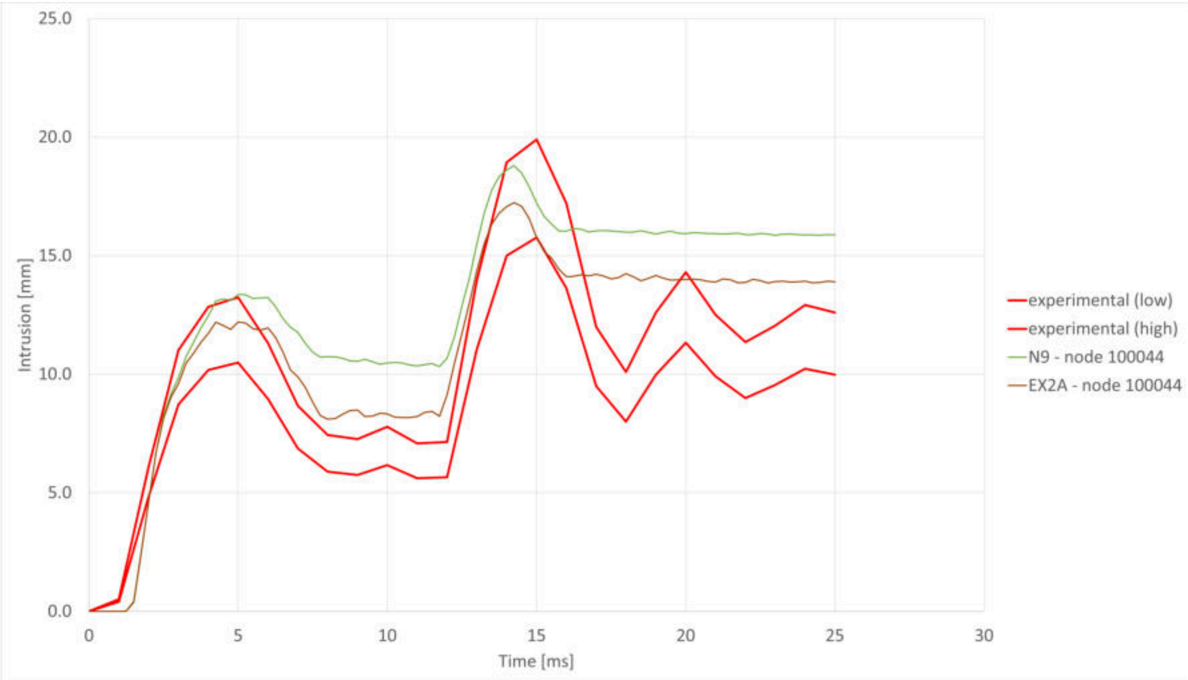

Figure C.33: Intrusion over time for orange node, compared to V31 experimental band, step EX2A

Damage Pattern (Protection Plate)

The damage pattern on the protection plate at the end of the simulation is presented in Figure C.34, and shows a good match for the delaminated area for both length and width, even though a slight mismatch for the front tip remains.

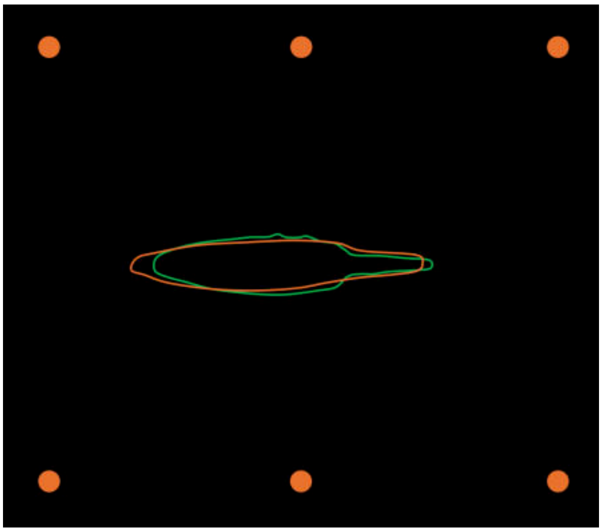

Figure C.34: Comparison of damage patterns: Experimental results (orange envelope) vs. Simulations (green envelope), step EX2A

C.2.10. EX2B: Strain Rate Sensitivity (ALU_3)

Runtime

The total runtime for this model is 11597 s (wall clock), comparable to the previous step and therefore not impacted by the influence of strain rate sensitivity.

Plastic Deformation Profile and Position of the Maximum Intrusion Node (Aluminum Plate)

The deformation profile at the end of the simulation, along with the position of the maximum intrusion node and the position of the node tracked by the DIC system in experimental tests, are shown in Figure C.35. Compared to the experimental profile (Figure 5.2a), the green node shifts to the right edge of the plate, due to the considerable reduction of intrusion at the impact site, caused by the introduced strain-rate sensitivity.

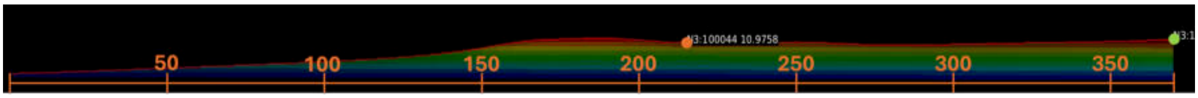

Figure C.35: Profile deformation, EX2B

Intrusion Over Time (Aluminum Plate)

The intrusion over time for the orange node is reported in Figure C.36. Although a substantial improvement in the match with experimental results can be observed, it must be noted that arbitrary Cowper-Symonds coefficients have been chosen to create a "proof of concept" for the importance of strain rate sensitivity for the load-case; in a real use-case, the improvement would have been more modest.

Interestingly, the improvement in the intrusion response translates well to different layups and test versions without the need for a re-calibration of the Cowper-Symonds parameters, as can be seen in Figure C.37, which shows the improvement for V22 when the strain rate sensitive model is used in combination with the scaled up friction coefficient that will be presented in Section C.2.11 .

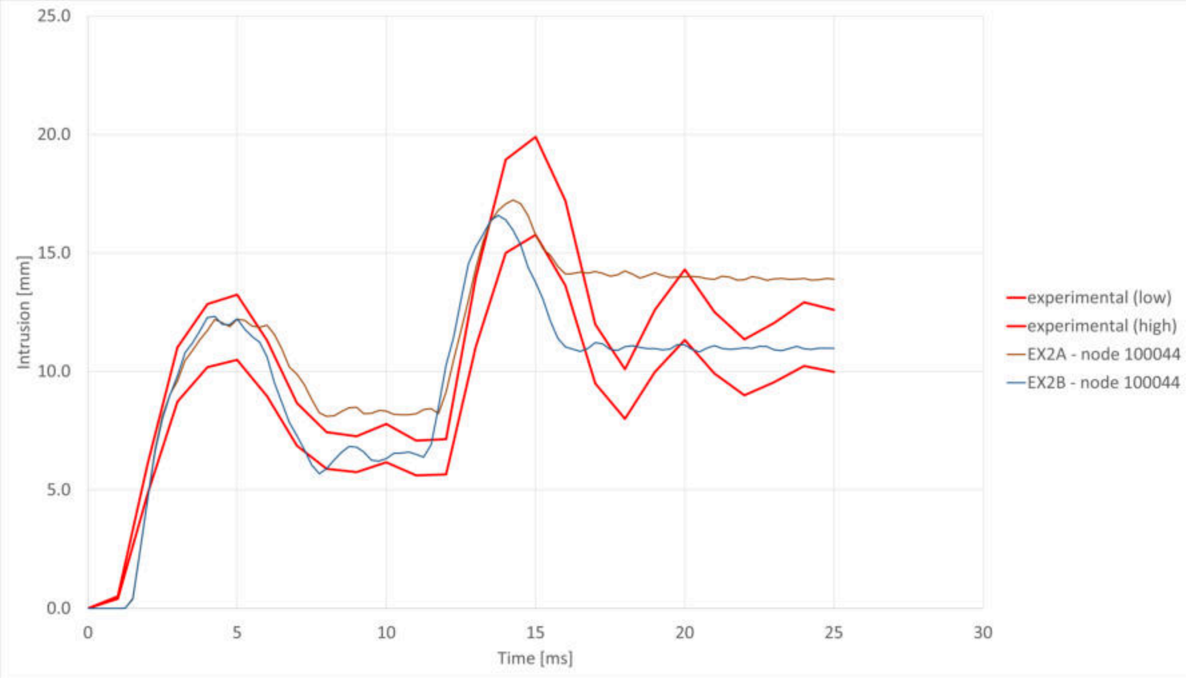

Figure C.36: Intrusion over time for orange node, compared to V31 experimental band, step EX2B

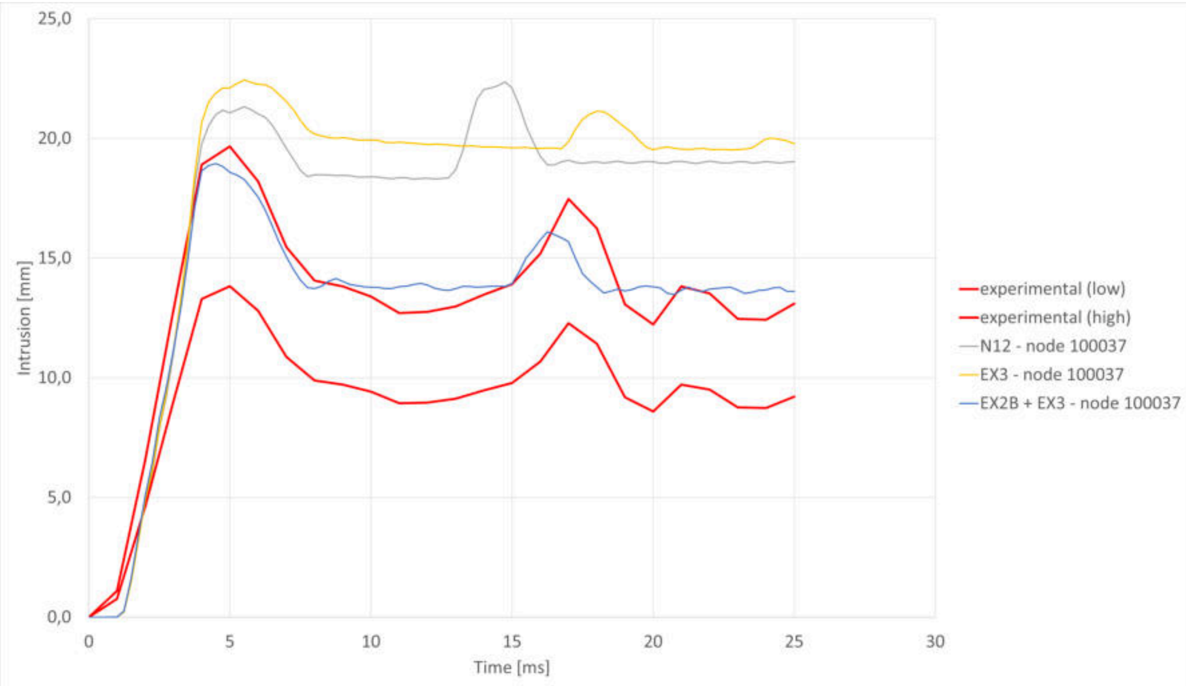

Figure C.37: Intrusion over time for orange node, compared to V31 experimental band and to EX3

Damage Pattern (Protection Plate)

The damage pattern on the protection plate at the end of the simulation is presented in Figure C.38. While still retaining a generally correct delamination shape,a substantial mismatch in the damage length is introduced, but as it will be shown in Section C.2.11, increasing the global friction coefficient can restore the match.

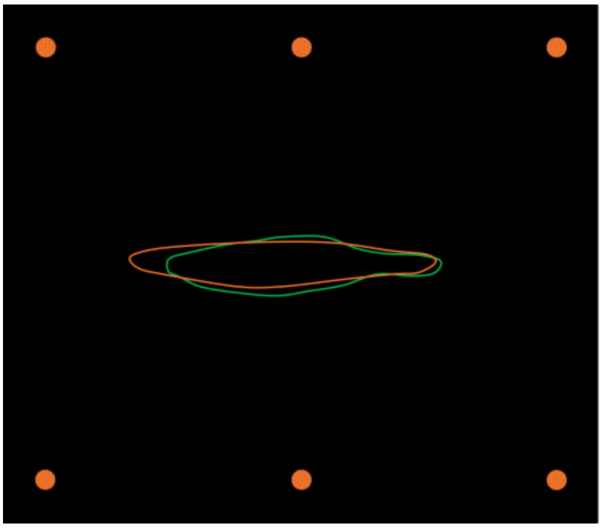

Figure C.38: Comparison of damage patterns: Experimental results (orange envelope) vs. Simulations (green envelope), step EX2B

C.2.11. EX3: Improving on the CARBON Layup Results

Runtime

The total runtime for this model is 17105 s (wall clock). This is comparable to the reference simulation of step 12, as the only difference is an increase in the global friction scaling factor.

Plastic Deformation Profile and Position of the Maximum Intrusion Node (Aluminum Plate)

The deformation profile at the end of the simulation, along with the position of the maximum intrusion node and the position of the node tracked by the DIC system in experimental tests, are shown in Figure C.39. Compared to step 12 (see Figure C.28b), the increase in the friction coefficient resulted in a much better match with the experimentally derived profile in Figure C.28a: [a] the intrusions at the left and right edges are now comparable, [b] no secondary intrusion is now present at 225mm, resulting in [c] a correct position for the green node, slightly to the left of the orange one.

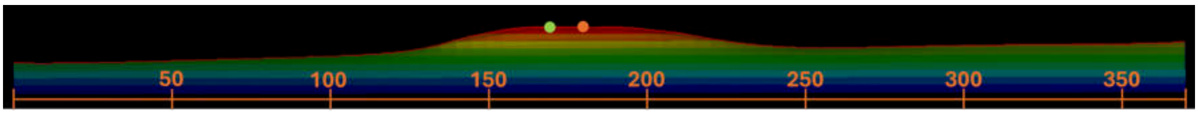

Figure C.39: Profile deformation, EX3

Intrusion Over Time (Aluminum Plate)

The intrusion over time for the orange node is reported in Figure C.40. Although the magnitude of the intrusion is still too high, probably due to errors in the aluminum plate modeling, the shape of the curve is now matching the experimental one: [a] the second peak shifted to the right, and [b] it decreased in magnitude, being now lower than the first one.

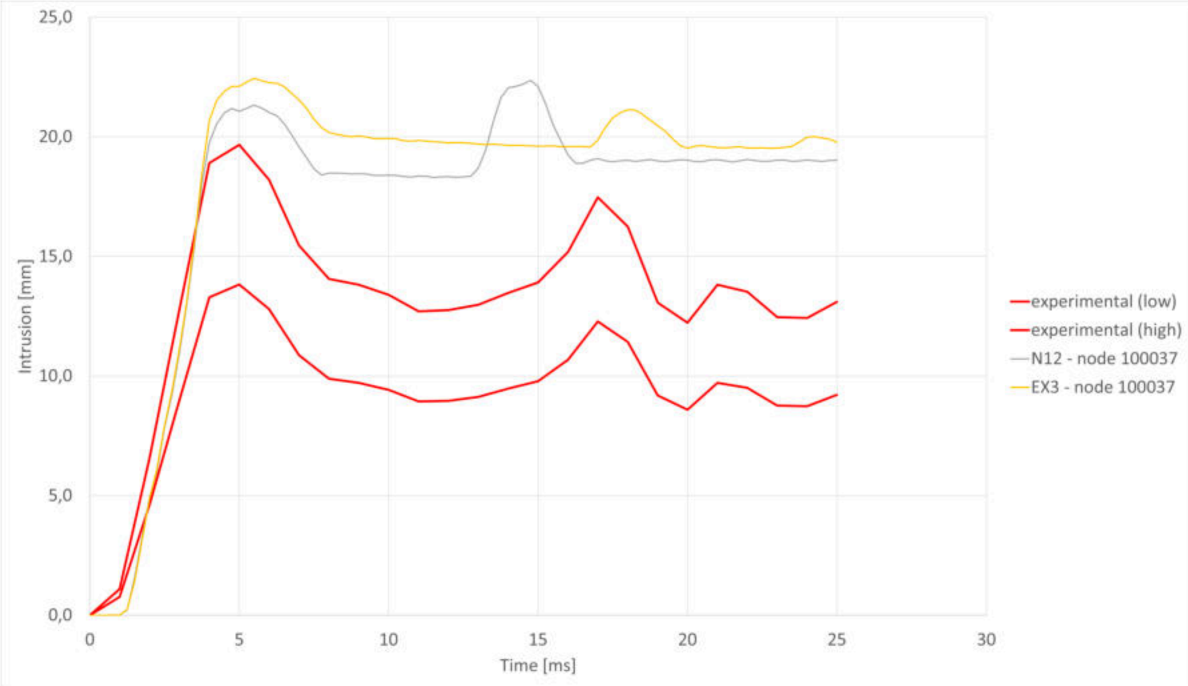

Figure C.40: Intrusion over time for orange node, compared to v22 experimental band and to step 12, step EX3

Damage Pattern (Protection Plate)

The damage pattern on the protection plate at the end of the simulation is presented in Figure C.41. The match with the C-SCAN is still reasonably good, but the left side of the envelope has a straight edge, caused by the impactor head "plowing" through the plate with its front face. This actually happens in the test, and it can be seen from the C-SCAN in Section 3.8a, where the central part of the impact area is completely missing, but there the "plowing" motion ends slighly earlier, thus not producing the aforementioned straight edge.

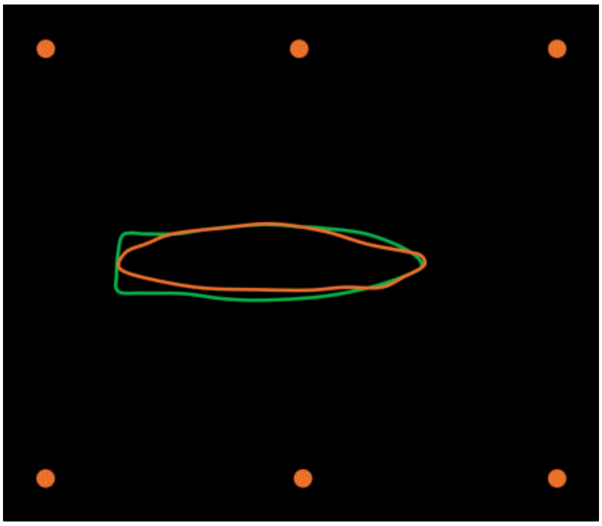

Figure C.41: Comparison of damage patterns: Experimental results (orange envelope) vs. Simulations (green envelope), step EX4

C.3. Delamination Model with GLASS_1

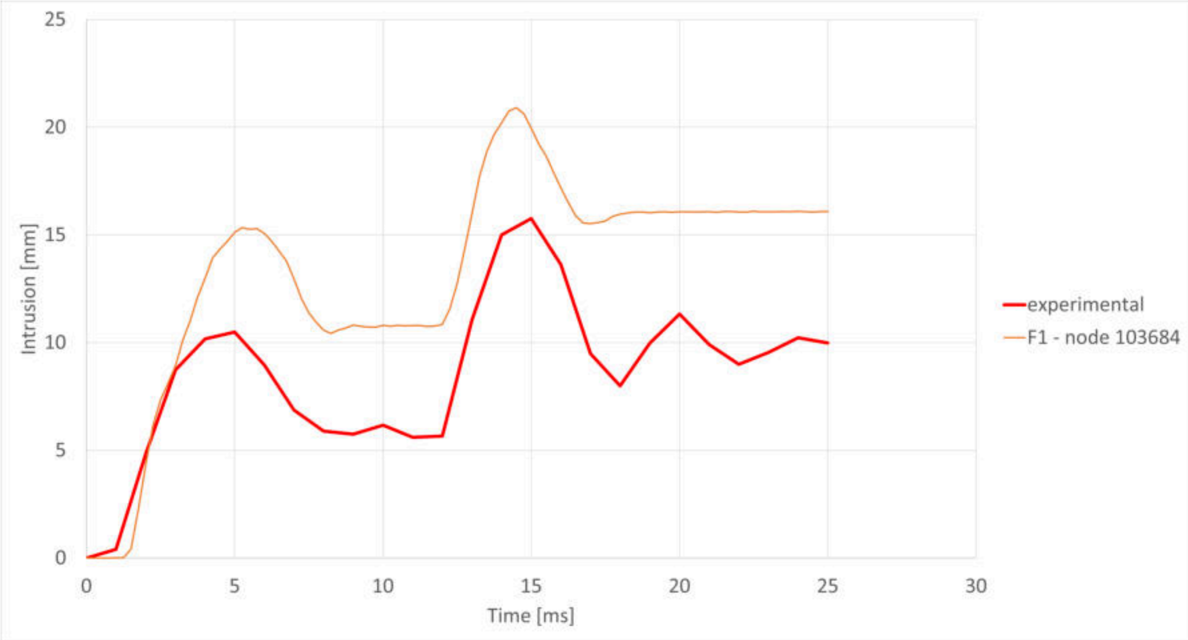

Figure C.42: Intrusion over time for orange node, compared to V31 experimental curve, step F1

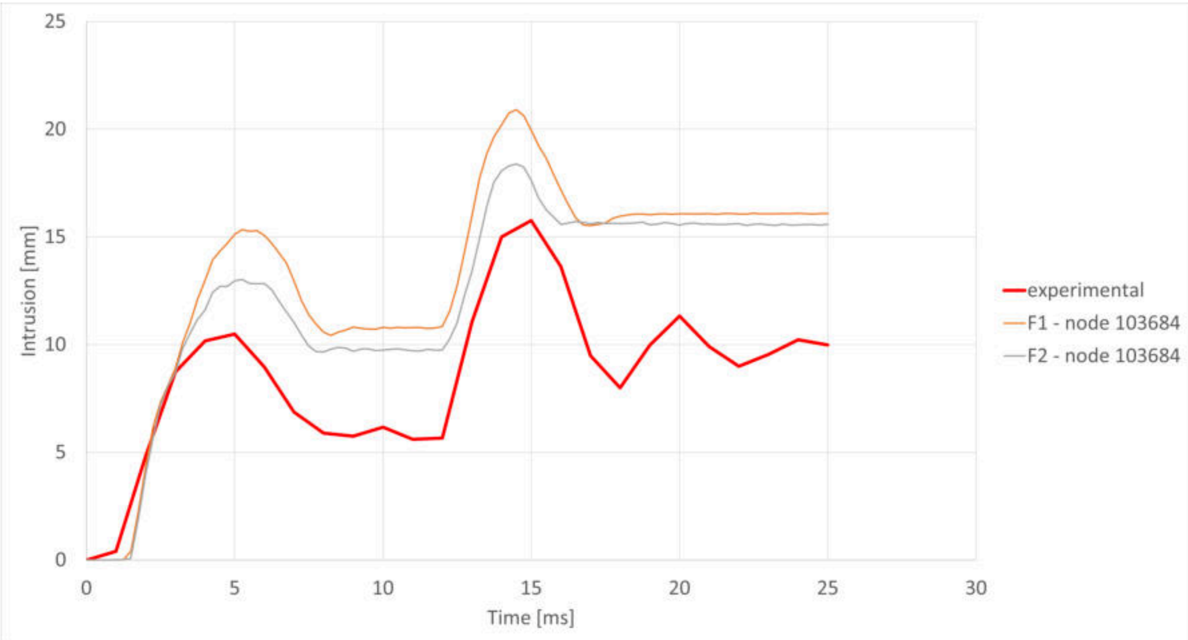

Figure C.43: Intrusion over time for orange node, compared to V31 experimental curve and to the previous step, step F2

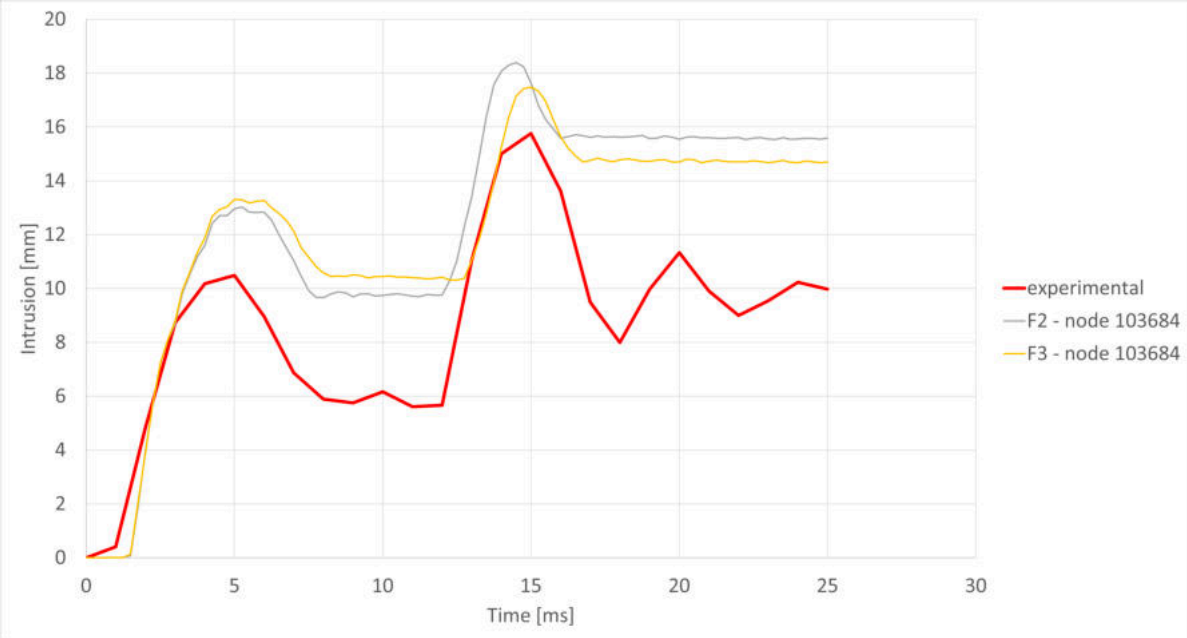

Figure C.44: Intrusion over time for orange node, compared to V31 experimental curve and to the previous step, step F3

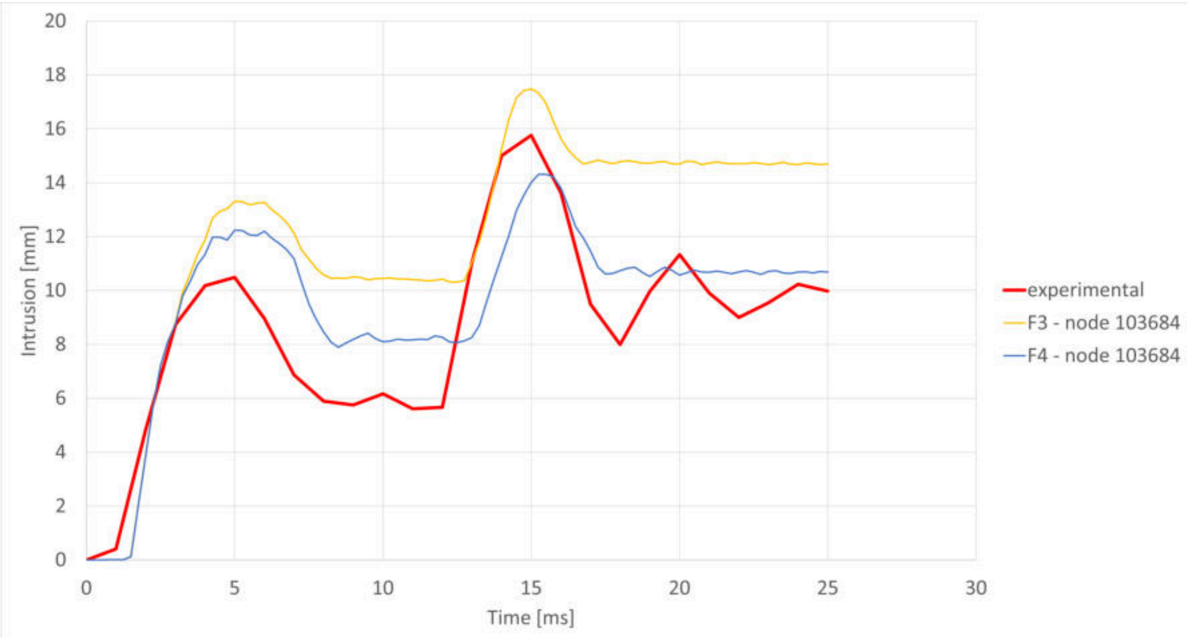

Figure C.45: Intrusion over time for orange node, compared to V31 experimental curve and to the previous step, step F4

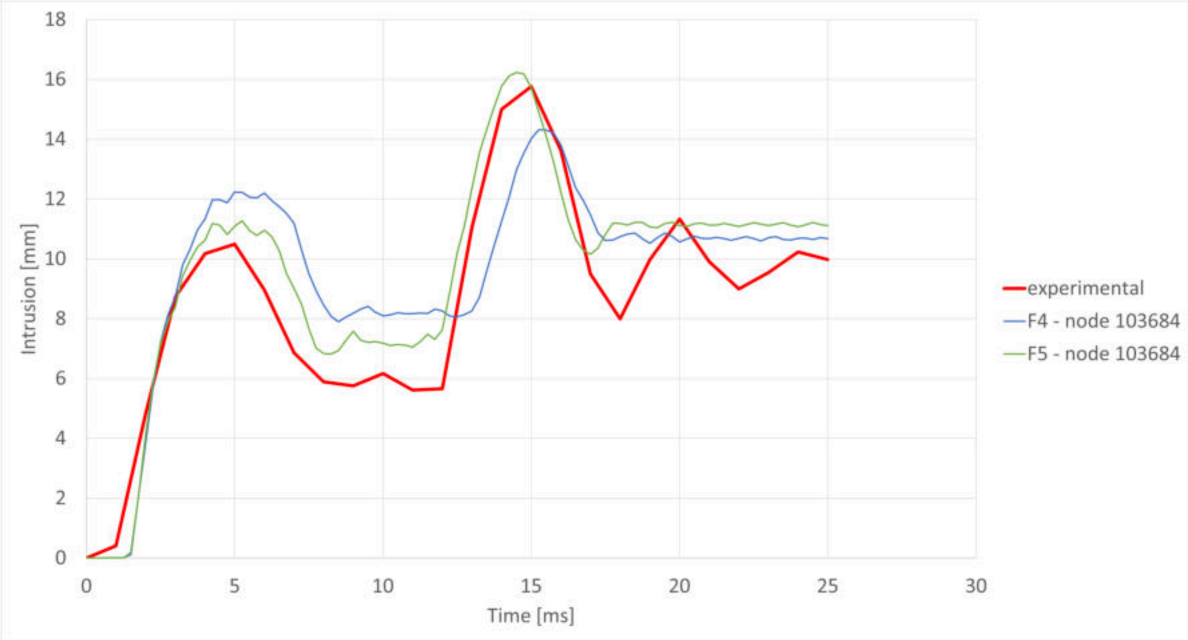

Figure C.46: Intrusion over time for orange node, compared to V31 experimental curve and to the previous step, step F5

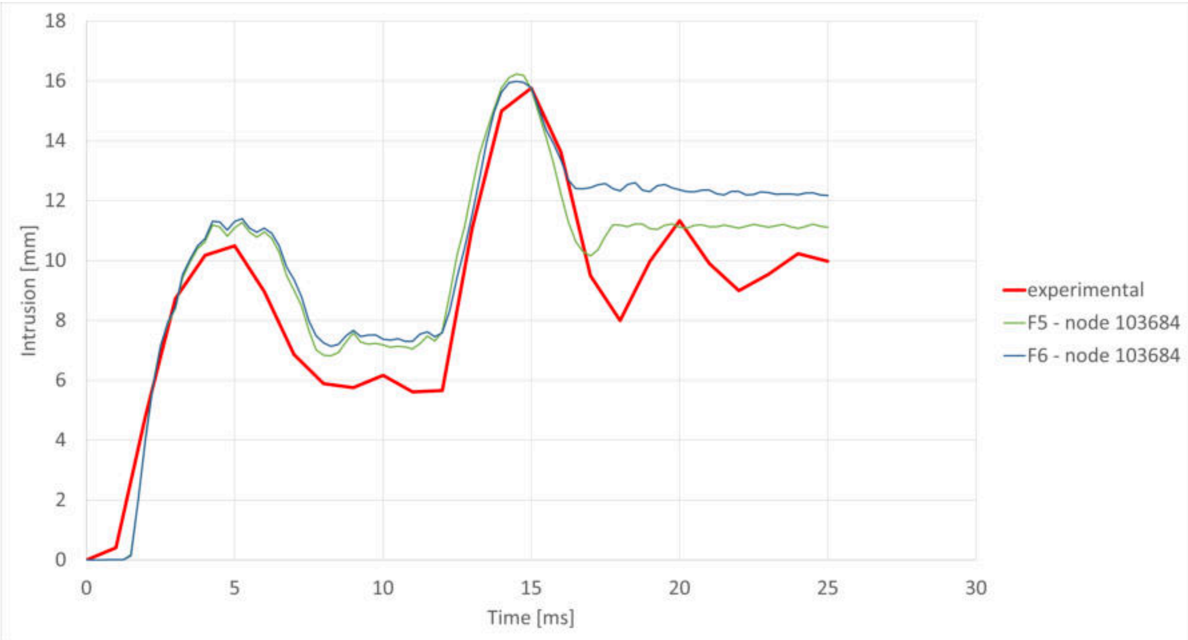

Figure C.47: Intrusion over time for orange node, compared to V31 experimental curve and to the previous step, step F6

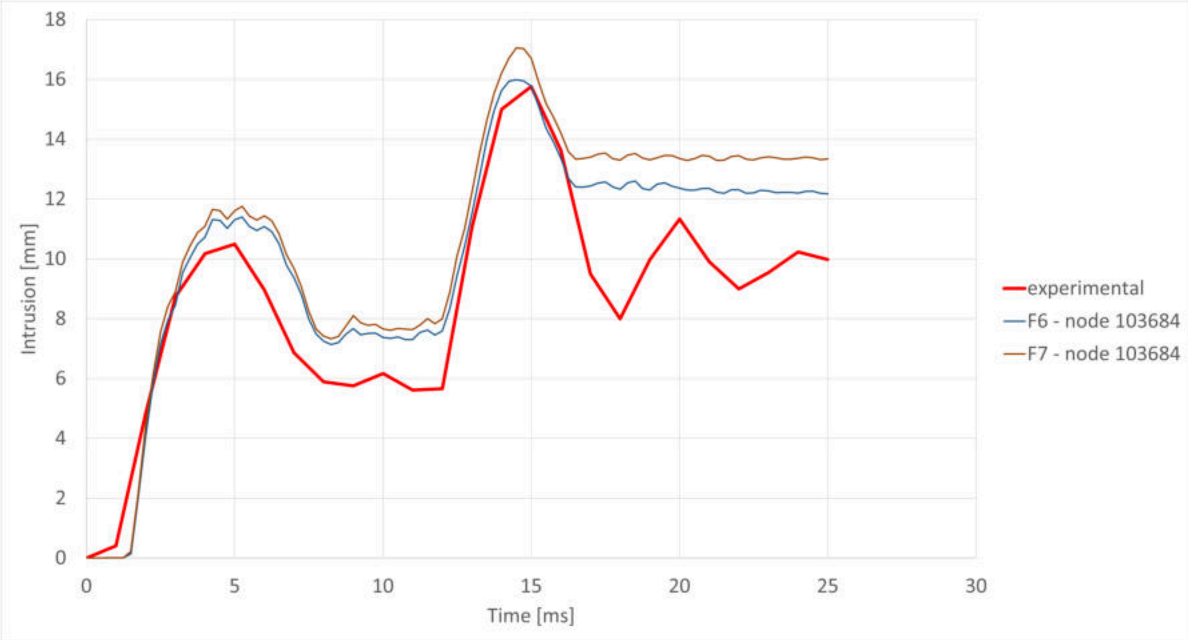

Figure C.48: Intrusion over time for orange node, compared to V31 experimental curve and to the previous step, step F7

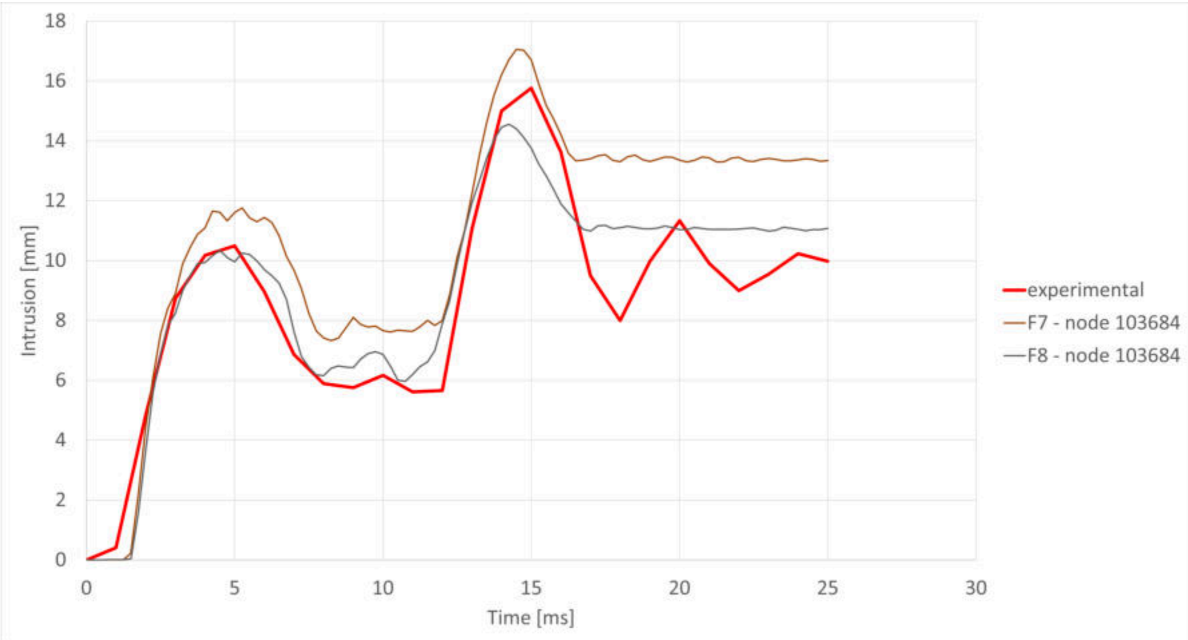

Figure C.49: Intrusion over time for orange node, compared to V31 experimental curve and to the previous step, step F8

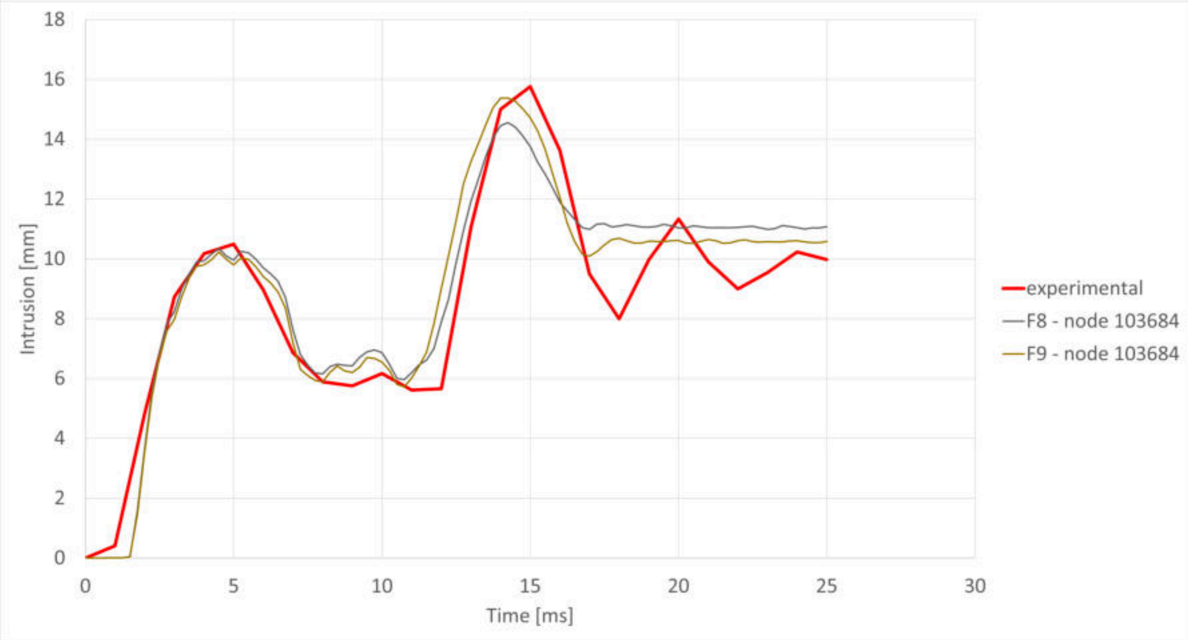

Figure C.50: Intrusion over time for orange node, compared to V31 experimental curve and to the previous step, step F9

D
Supplement to the "Conclusions and Recommendations" Chapter

In Figure 6.1, a comparison of intrusion magnitude between baseline and final models is performed.

In the final model, which accounts for the impactor's secondary dynamics (see Figure 4.17), the chosen node for intrusion tracking in the simulation environment is exactly the one tracked by the DIC-system in experimental tests, and approximately coincides with the first contact point of the impactor with the plate, which is slightly shifted in the positive y-direction, to the side of the plate's centerline (see Figure 4.18).

In the baseline model, since the secondary impact dynamics are not modeled and the impact happens along the plate centerline, tracking the same node wouldn't be acceptable, as it would result in misleadingly low intrusion. Therefore, for the baseline model in Figure 6.1 a node with same x-coordinate but y-coordinate equal to 0 (i.e. , lying on the centerline) is tracked instead, to ensure its coincidence with the first contact point between the plate and the impactor.

For completeness, same-node tracking for all versions (matching the DIC-tracked node) is presented in Figure D.1, still showing a dramatic improvement.

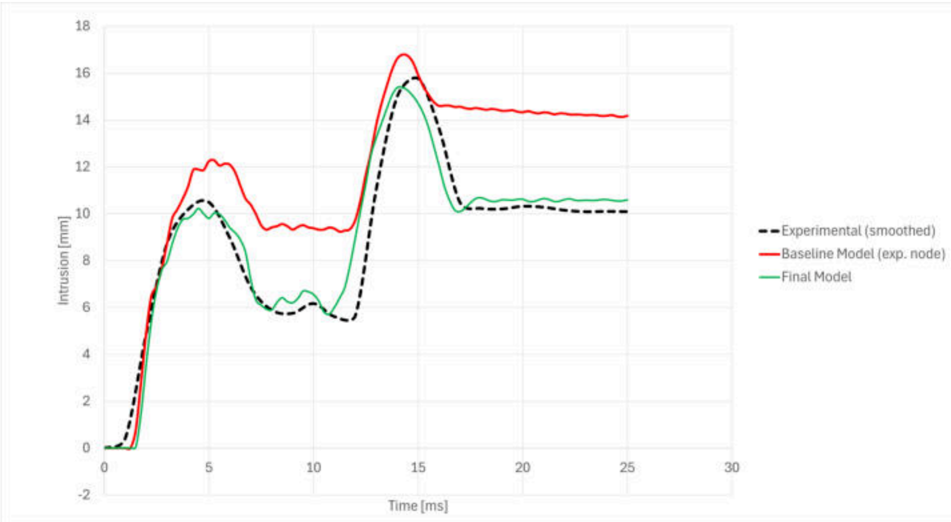

Figure D.1: Intrusion over time with same-node tracking for all models, smoothed experimental curve VS baseline model VS final model

E

LS-Dyna-Specific Modeling

E.1. ONEWAY vs TWOWAY Contact Formulations

It is important to note that for OPTION=6 (and 8), the keyword "AUTOMATIC_ONE_WAY" is recommended, without any further explanation.

In the LS-Dyna support documentation, it is stated that "ONE_WAY" contacts are appropriate when the master side is a rigid body, or in case it is deformable, when it has a coarse mesh and encounters a finely meshed slave surface.

In a one-way contact, only slave nodes are checked for penetration, and this could result in master nodes penetrating the slave segments/elements, while in two-way contacts, both slave and master nodes are checked, preventing penetration at the cost of a higher computational cost. The difference between the two options is clearly illustrated in Figure E.1.

Since in the context of the project, the contact is used to join deformable plies with equal meshes, a regular two-ways contact has been deemed to be more appropriate. To corroborate this idea, a comparison between the two options has been performed for a simple impact load case, and the results are shown in Figure E.2. As expected, the one-way contact doesn't behave properly, while the two-way is capable of handling the scenario. Therefore, the "CONTACT_AUTOMATIC_SURFACE_TO_SURFACE" will be used, and the "ONE_WAY" keyword will be only re-introduced in case of contact stability issues. Note that a reduction in minimum time-step has proven to be helpful in reducing penetrations for the one-way contact.

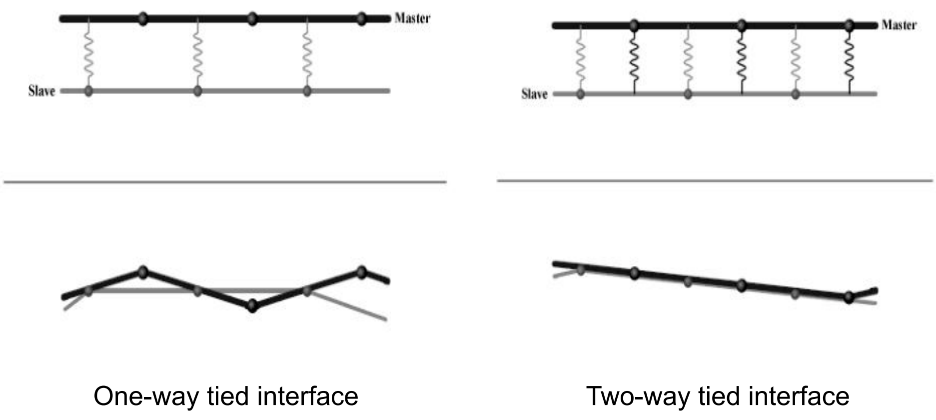

Figure E.1: Comparison between one-way and two-way tied contacts

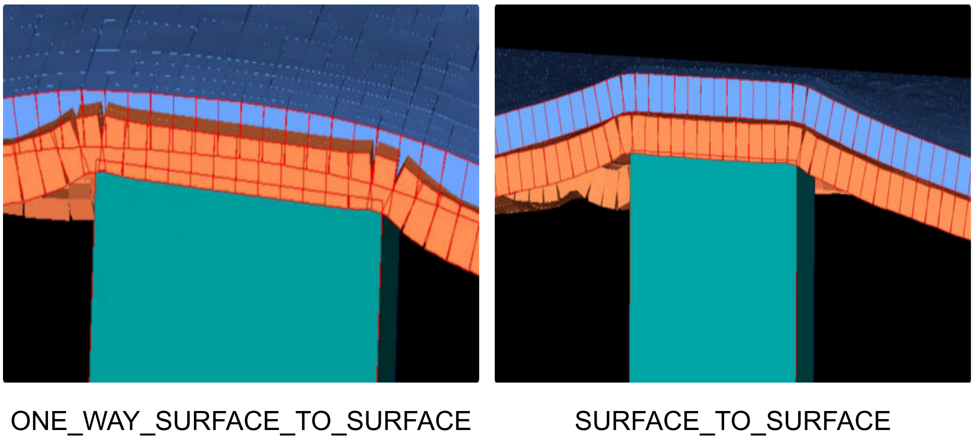

Figure E.2: Comparison of section views of one- and two-ways contacts for a simple impact load case

E.2. Manual Segment Orientation

The parameters SSTYP and MSTYP in the contact card specify the slave segment (or node for SSTYP) set type. The keyword manual advises to use segment sets rather than parts or parts sets, as it gives more control over the definition of the contact segment normal vectors, which should point toward the opposing contact surface to properly distinguish tension from compression.

Usually, in automatic contacts involving shell elements, the contact surfaces are determined by projecting normally from the shell mid-plane a distance equal to half of the contact thickness. Then, at the exterior edge, the contact surface wraps around the shell edge with a radius again equal to half of the contact thickness, thus creating a continuous contact surface with the normal vector always pointing towards the exterior of the shell and therefore towards the opposing contact surfaces.

Notably, in MPP (Massively Parallel Processing), which is used in the project setup, segment normal vectors need to be manually oriented as automatic orientation is disabled even when the "AUTOMATIC" keyword is used. Failing to do so results in incorrect results upon failure.

This requirement presents a topological challenge when modeling multi-layered laminates. For internal plies within a stack, the shell elements must simultaneously interact with the ply above and the ply below. Since a single segment set possesses a unique normal vector direction, it cannot satisfy the MPP orientation requirement for both interfaces simultaneously. To resolve this, a dual-definition strategy was implemented: for each internal ply, two distinct segment sets were defined, allowing independent normal vector orientation toward the respective upper and lower adjacent plies. Validated through extensive testing, this methodology ensures robust contact definition throughout the laminate thickness and prevents numerical instabilities associated with incorrect normal orientations.

F

Derivation of a Monolithic Closed-Form Solution for Anisotropic Plates under Oblique Point Loads

In this appendix, the structural response of anisotropic plates subjected to oblique impact is predicted via an original analytical derivation based on the 1st von Karman large-deflection equation.

The main challenge when modeling an oblique impact is represented by the geometric non-linearity introduced by the interaction of in-plane and out-of-plane load components, which typically requires an iterative solution.

In the proposed approach, by assuming a Navier-type solution with simply supported (ssss) boundary conditions and treating the localized slope at the impact point as a solveable scalar variable, the non-linear coupling is resolved algebraically. This allows for the direct calculation of the displacement field coefficients in a single step, eliminating the need for iterative convergence.

F.1. Derivation

Start from the 1st von Karman equation:

$$D_{11}\frac{\partial^4 w}{\partial x^4} + 2(D_{12} + 2D_{66})\frac{\partial^4 w}{\partial x^2 \partial y^2} + D_{22}\frac{\partial^4 w}{\partial y^4} = -p_x\frac{\partial w}{\partial x} + p_z$$

Assume a solution for a ssss (simply supported all-around) set of BCs:

$$w = \sum_{n=1}^{\infty}\sum_{m=1}^{\infty} A_{mn}\sin(\frac{m\pi x}{a})\sin(\frac{n\pi y}{b})$$

Its derivatives are:

$$\frac{\partial w}{\partial x} = \sum\sum A_{mn}\frac{\pi m \sin(\frac{\pi n y}{b})\cos(\frac{\pi m x}{a})}{a}$$

$$\frac{\partial^4 w}{\partial x^4} = \sum\sum A_{mn}\frac{\pi^4 m^4 \sin(\frac{\pi m x}{a})\sin(\frac{\pi n y}{b})}{a^4}$$

$$\frac{\partial^4 w}{\partial y^4} = \sum\sum A_{mn}\frac{\pi^4 n^4 \sin(\frac{\pi m x}{a})\sin(\frac{\pi n y}{b})}{b^4}$$

$$\frac{\partial^4 w}{\partial x^2 \partial y^2} = \sum\sum A_{mn}\frac{\pi^4 m^2 n^2 \sin(\frac{\pi m x}{a})\sin(\frac{\pi n y}{b})}{a^2 b^2}$$

The point load, with magnitude P, has two components:

$$p_x = P\cos\theta$$
$$p_z = P\sin\theta$$

where θ is the angle of impact. The RHS of the equation then becomes:

$$P(\sin\theta - \cos\theta\frac{\partial w}{\partial x})$$

The load P can be expanded:

$$\sum\sum\frac{4P}{ab}\sin(\frac{m\pi x_0}{a})\sin(\frac{n\pi y_0}{b})\sin(\frac{m\pi x}{a})\sin(\frac{n\pi y}{b})$$

By substituting everything in the equation, A_{mn} can be isolated:

$$A_{mn} = \frac{\frac{4P}{ab}\sin(\frac{m\pi x_0}{a})\sin(\frac{n\pi y_0}{b})}{\frac{D_1\pi^4 m^4}{a^4} + \frac{2(D_{12}+2D_{66})\pi^4 m^2 n^2}{a^2 b^2} + \frac{D_{22}\pi^4 n^4}{b^4}}(\sin\theta - \cos\theta\frac{\partial w}{\partial x})$$

Now $\frac{\partial w}{\partial x}$ needs to be determined. Setting $u = \frac{\partial w}{\partial x}$:

$$u = \sum\sum\frac{\frac{4P}{ab}\sin(\frac{m\pi x_0}{a})\sin(\frac{n\pi y_0}{b})}{\frac{D_1\pi^4 m^4}{a^4} + \frac{2(D_{12}+2D_{66})\pi^4 m^2 n^2}{a^2 b^2} + \frac{D_{22}\pi^4 n^4}{b^4}}(\sin\theta - \cos\theta u)\frac{\pi m\sin(\frac{\pi n y}{b})\cos(\frac{\pi m x}{a})}{a}$$

Groupuing everything (and renaming it T) but $\sin\theta - \cos\theta u$:

$$u = \sum\sum T_{mn}(\sin\theta - \cos\theta u)$$

Now, choosing an arbitrary number of terms M,N for the summation, u becomes a constant, therefore $(\sin\theta - \cos\theta u)$ can be extracted out of the double summation:

$$u = (\sin\theta - \cos\theta u)\sum_{n=1}^{N}\sum_{m=1}^{M}T_{mn}$$

and after some manipulation:

$$u = \frac{\sin\theta\sum_{n=1}^{N}\sum_{m=1}^{M}T_{mn}}{1+\cos\theta\sum_{n=1}^{N}\sum_{m=1}^{M}T_{mn}}$$

Substituting u definition:

$$\frac{\partial w}{\partial x} = \frac{\sin\theta\sum_{n=1}^{N}\sum_{m=1}^{M}T_{mn}}{1+\cos\theta\sum_{n=1}^{N}\sum_{m=1}^{M}T_{mn}}$$

In the case at hand, the load is applied at $x_0 = a/2$, $y_0 = b/2$. For a purely transverse load, the maximum displacement is at $x = a/2$, $y = b/2$. In this case, the combination of p_x and p_z could change the point of maximum displacement: by looking at how A_{mn} is defined, a negative $\frac{\partial w}{\partial x}$ could compensate the reduced effect of p_z farther from the centre of the plate, as long as the angle of impact is small enough.

To sum up, the final expression is:

$$w = \sum_{n=1}^{N}\sum_{m=1}^{M}A_{mn}\sin(\frac{m\pi x}{a})\sin(\frac{n\pi y}{b})$$

with

$$A_{mn} = \frac{\frac{4P}{ab}\sin(\frac{m\pi x_0}{a})\sin(\frac{n\pi y_0}{b})}{\frac{D_1\pi^4 m^4}{a^4} + \frac{2(D_{12}+2D_{66})\pi^4 m^2 n^2}{a^2 b^2} + \frac{D_{22}\pi^4 n^4}{b^4}}(\sin\theta - \cos\theta\frac{\sin\theta\sum_{n=1}^{N}\sum_{m=1}^{M}T_{mn}}{1+\cos\theta\sum\sum T_{mn}})$$

and

$$T_{mn} = \frac{\frac{4P}{ab}\sin(\frac{m\pi x_0}{a})\sin(\frac{n\pi y_0}{b})}{\frac{D_1\pi^4 m^4}{a^4} + \frac{2(D_{12}+2D_{66})\pi^4 m^2 n^2}{a^2 b^2} + \frac{D_{22}\pi^4 n^4}{b^4}} \times \frac{\pi m \sin(\frac{\pi n y}{b})\cos(\frac{\pi m x}{a})}{a}$$

The proposed solution to determine $\frac{\partial w}{\partial x}$ with some placeholder values has been compared to an iterative approach, which has converged to it in a number of iterations $i > 3$, as can be seen in Figure F.1.

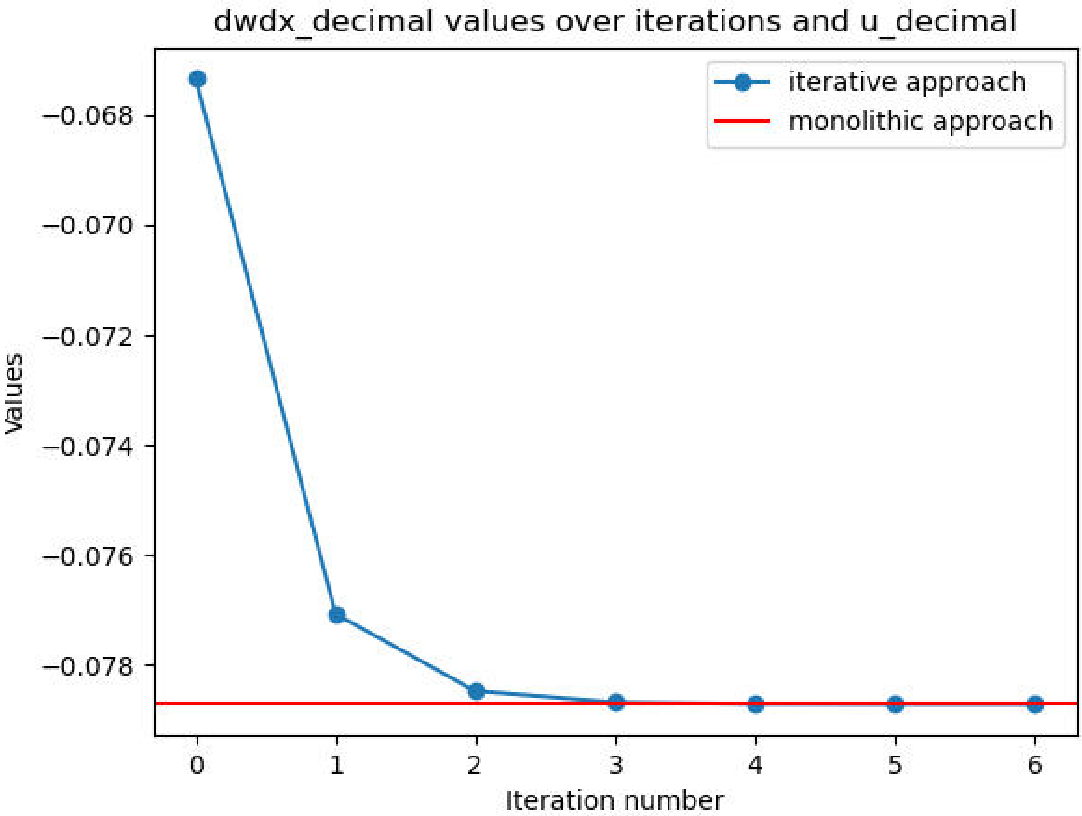

Figure F.1: Convergence plot

After implementing the approach, the displacement field was generated through a Python code. The results are shown in Figures F.2 and F.3.

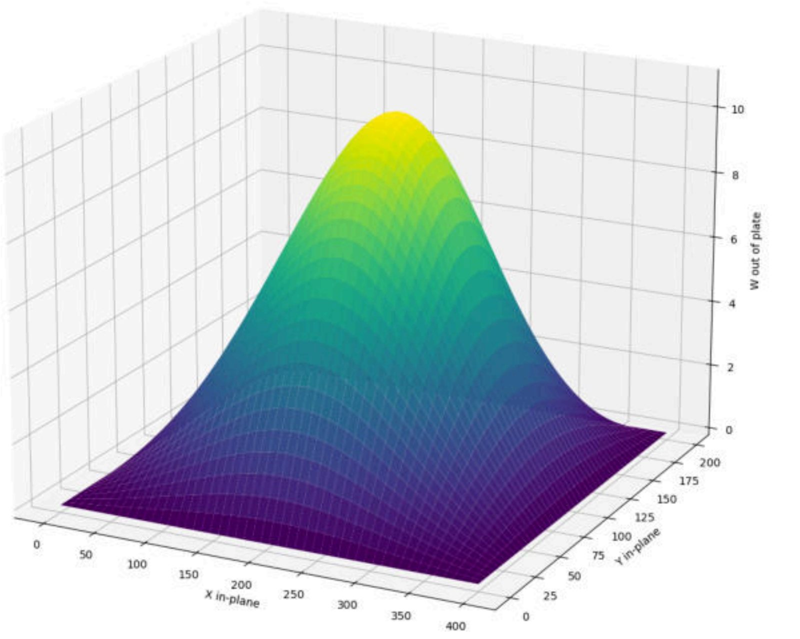

Figure F.2: Displacement field view 1

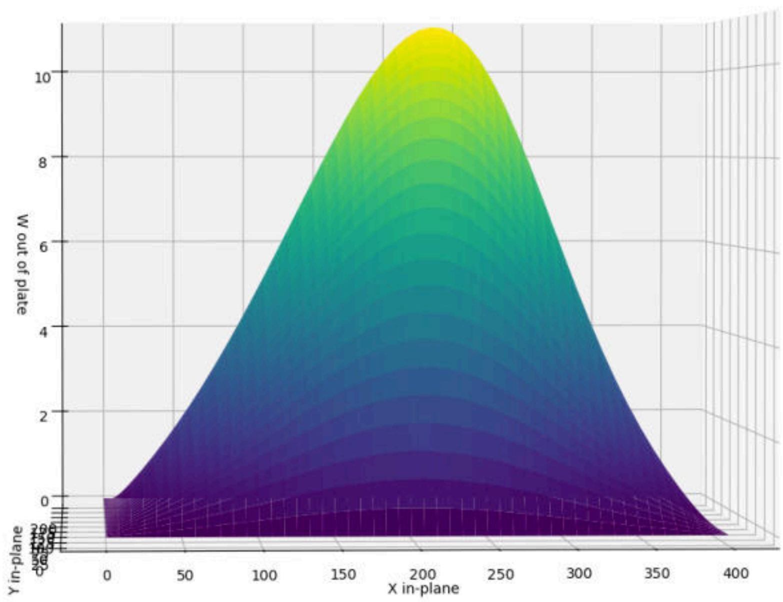

Figure F.3: Displacement field view 2

Note that an alternative solution to the problem, allowing for a scsc configuration clamped at two edges and simply supported at the other two (scsc), could be obtained through the choice of the following shape function:

$$w(x,y) = \sum_{n=1}^{\infty}\sum_{m=1}^{\infty}\Big\{A_{mn}\sin\big(\frac{m\pi x}{a}\big)\Big[\cosh(\lambda_n y) - \cos(\lambda_n y) - \gamma_n(\sinh(\lambda_n y) - \sin(\lambda_n y))\Big]\Big\}$$

with

$$\gamma_n = \frac{\cosh(\lambda_n b) - \cos(\lambda_n b)}{\sinh(\lambda_n b) - \sin(\lambda_n b)}$$

and λ_n coming from solving:

$$\cosh(\lambda_n b)\cos(\lambda_n b) = 1$$

but it would result in a much more complex derivation, which would most certainly require an iterative solution approach.